High-Energy emission from Active Galactic Nuclei

Matteo Cerruti

To cite this version:

Matteo Cerruti. High-Energy emission from Active Galactic Nuclei. High Energy Astrophysical Phenomena [astro-ph.HE]. Université de Paris 7 - Denis Diderot, 2012. English. NNT : . tel-02532715

UNIVERSITÉ DE PARIS-7 DENIS DIDEROT
OBSERVATOIRE DE PARIS-MEUDON
LABORATOIRE UNIVERS ET THÉORIES (LUTH)

ECOLE DOCTORALE D'ASTRONOMIE ET ASTROPHYSIQUE D'ILE-DE-FRANCE

HIGH-ENERGY EMISSION FROM ACTIVE GALACTIC NUCLEI

PhD Thesis

Defended by :

Matteo CERRUTI

Before the jury composed by:

President:	**Etienne PARIZOT**
Referee:	**Laura MARASCHI**
Referee:	**Frank RIEGER**
	Gilles HENRI
	Benoît LOTT
Supervisor:	**Catherine BOISSON**
Supervisor:	**Andreas ZECH**

MEUDON, 21ST OF SEPTEMBER, 2012

Printed in Meudon, September 14, 2012

E quando dottore lo fui finalmente,
non volli tradire il bambino per l'uomo.

Un medico
Non al denaro, non all'amore né al cielo
Fabrizio De André

Contents

List of Figures

List of Tables

Etude de l'émission aux hautes énergies des noyaux actifs de galaxies

Ce manuscrit résume les travaux effectués pendant les trois années de thèse doctorale au sein du LUTh (Laboratoire Univers et Théories) et de la collaboration *H.E.S.S.*.

Le projet de recherche a été l'étude de l'émission aux hautes énergies (rayons X et rayons γ) des Noyaux Actifs de Galaxies (NAG), et a comporté deux parties distinctes: d'un côté l'étude de l'émission en rayons X des galaxies de Seyfert 1 (en s'intéressant particulièrement au problème de l'excès de rayons X-mous, ou *soft-excess*), et d'un autre côté l'étude de l'émission en rayons γ des blazars, en utilisant en particulier les données du réseau de téléscopes de type Cherenkov (pour l'observation de photons aux energies de l'ordre du TeV) *H.E.S.S.*.

Après une courte Introduction sur les NAG et l'astronomie au TeV, nous décrivons tout d'abord l'émission aux rayons X des galaxies de Seyfert (Chapitre 1). Ce Chapitre est une introduction à l'étude détaillée de l'émission en rayons X de deux galaxies de Seyfert 1, *Mrk 509* et *Mrk 841*, presentée dans le Chapitre 2. Une caractéristique importante de l'émission X de ce type de NAG est le *soft-excess*, qui apparaît comme un excès de flux au-dessous de environ 1 keV par rapport à l'extrapolation à basse énergie de la loi de puissance ajustée entre 3-10 keV. Dans ce Chapitre, nous nous concentrons en particulier sur l'interprétation de cette émission, en ajustant les données *Suzaku* avec trois modèles différents: une double Comptonisation, une réflexion sur la partie la plus interne du disque d'accrétion, et une absorption par un vent rélativiste. Alors que pour *Mrk 841* les trois scénarios donnent des résultats statistiquement équivalents, pour *Mrk 509* le scénario avec reflexion est exclu.

La deuxième partie commence par une introduction générale sur les blazars (Chapitre 3), avant de présenter le réseau de téléscope *H.E.S.S.*, ainsi qu'une revue des NAG observés au TeV (Chapter 4).
Nous présentons ensuite l'étude spécifique du blazar émetteur au TeV *1RXS J101015.9 - 311909* (Chapitre 5): l'analyse des observations éffectuées par *H.E.S.S.* et par d'autres observatoires dans l'optique, en rayons-X et rayons-γ (*ATOM*, *Swift* et *Fermi*) nous permet de construire la distribution spectrale d'énergie de la source. L'émission de *1RXS J101015.9 - 311909* est modélisée dans le cadre d'un modèle leptonique, de type synchrotron-self-Compton (SSC).

Les Chapitres suivants sont plus théoriques, et traitent de la modélisation de l'émission des blazars. Les modèles developpés dans la littérature scientifique peuvent être divisés en deux familles: leptoniques et hadroniques, selon que les particules responsables de l'émission soient des paires electrons/positrons ou des protons, respectivement. Concernant les modèles leptoniques, nous avons developpé un nouvel algorithme numérique pour la détermination des paramètres du modèle d'émission de type SSC (Chapter 6). Cette méthode, appliquée comme exemple au cas spécifique de *1RXS J101015.9 - 311909*, montre que, pour un blazar de type HBL (*high-frequency-peaked BL Lac object*), émetteur au GeV et au TeV, l'espace des paramètres du modèle SSC peut être bien determiné, et améliore les contraintes obtenues avec des formules analytiques. Nous pouvons aussi utiliser, sous certaines hypothèses, cet algorithme pour contraindre la distance d'un HBL dont on ne connait pas le redshift (application au cas de *PKS 0447-439*).

Dans le Chapitre 7 nous nous concentrons sur les processus d'émission de type hadronique, en decrivant le développement d'un nouveau code stationnaire lepto-hadronique (qui prend en compte à la fois les processus leptonique et hadronique), et nous présentons une première application à *Mrk 421* et à *PKS 2155-304*. Le code nous permet de modéliser l'émission des blazars dans un scenario soit leptonique soit hadronique, en changeant les paramètres de la région émettrice et des particules présentes. Des scenarios mixtes lepto-hadroniques (dans lesquels l'émission aux hautes énergies est associée aux deux composantes) peuvent être également étudiés dans ce contexte.

Nous terminons, dans le Chapitre 8, avec la modélisation de *3C 454.3*, un blazar de type FSRQ (*flat-spectrum-radio-quasar*), dont le spectre au GeV est décrit par un processus de type inverse Compton sur les photons produits dans la *Broad-Line-Region*.

Les observations conjointes du téléscope *Fermi* (au GeV) et des téléscopes Cherenkov au sol (au TeV, comme *H.E.S.S.*, *MAGIC*, *VERITAS*), ont permit d'observer la composante en rayons-γ des blazars avec une très bonne résolution en énergie. Le nouveau téléscope *H.E.S.S. II* (dont la prémière lumière a été obtenue pendant l'été 2012) va pouvoir améliorer notre connaissance des blazars, en permettant de baisser le seuil d'observation en énergie et donc d'étudier la partie du spectre compris entre *Fermi* et les télescopes de type Cherenkov.

La communauté de l'astronomie au TeV développe actuellement le réseau de nouvelle génération, *CTA* (Cherenkov Telescope Array). Le projet est dans sa phase préparatoire, et les prémiers prototypes sont en construction (comme par exemple le télescope *SST-GATE*, sur le site de l'Observatoire de Meudon). Dans ce contexte, en appendix A est présentée une perspective de détection par *CTA* de blazars au grand redshift.

Preface

In this thesis manuscript we tried to summarize the research work done during the last three years in the high-energy group of the LUTh laboratory, as well as in the *H.E.S.S.* collaboration.
The project deals with the study of high-energy emission from active galactic nuclei (AGN), where, whith *high energy*, we refer here to X and γ-rays. The thesis covers in fact two different aspects of the physics of AGN, firstly the study of the X-ray emission from Seyfert galaxies (radio-quiet AGN), and then of the γ-ray emission from blazars (radio-loud AGN).

We start then by providing a short introduction to the scientific context of AGN physics (by presenting the unified AGN model), as well as of TeV astronomy.
In the first part we first describe the problem of the soft-X-ray excess in Seyfert galaxies (Chapter 1), before entering in the details of the study of *Suzaku* observations of two particular objects (*Mrk 509* and *Mrk 841*, Chapter 2), presenting the data analysis and their modelling.

The second part starts with an introduction on the blazar physics (Chapter 3), before showing the results achieved by the *H.E.S.S.* telescope array on AGN (Chapter 4). A detailed study has been done on a particular blazar detected at TeV energies (*1RXS J101015.9 - 311909*), and is presented in Chapter 5.

The following chapters are more theoretical, and discuss the modelling of the observed blazar emission. In particular, in Chapter 6 we discuss the constrains on the synchrotron-self-Compton model, presenting a new numerical algorithm to determine the best-fit solution, while in Chapter 7 we present a new stationary lepto-hadronic code, which can be used to model the blazar emission in leptonic, hadronic and mixed scenarios.

In Chapter 8 we present the problem of the spectral break observed in the GeV spectrum of *3C 454.3*, and we model it consistently in an external-inverse-Compton scenario.
Finally we present a perspective for the detection of high-redshift sources with the future telescope CTA (Appendix A).

Introduction

Contents

In this Chapter we describe the general scientific context of this work. In Section 0.1 we provide the historical background of the discovery of quasars and active galactic nuclei, and we present the current unification model. An important part of this thesis deals with the study of TeV emission from AGN, and largely benefits from observations taken by the *H.E.S.S.* experiment. For this reason, in Section 0.2 we present the basis of TeV astronomy, providing an introduction to the detection technique and describing the current generation of telescopes.

0.1 Active galactic nuclei

With the term active galaxy nucleus (AGN) we refer to any kind of galactic nucleus showing signs of activity related to accretion onto a super-massive black hole. A galaxy hosting an AGN is then called *active galaxy*. The observational signatures of activity can be different, and include detection of strong emission lines in the optical spectrum[1], strong radio-emission (often in the form of bipolar jets), broad-band continuum spectrum, rapid variability. The AGN class is not homogeneous, and is composed by a huge variety of objects, which differ in shape, luminosity, spectrum and temporal variability. These differences are understood today in the context of the unification scenario, which will be presented later. Before, we describe briefly the history of AGN observations, and the zoology of the different observational classes.

---

[1] The measurement of the line ratios is used to determine the excitation mechanism, and in particular, to discriminate between normal HII regions and photo-ionisation by power-law continuum, which is characteristic of AGN (see Baldwin et al. 1981).

0.1.1 The discovery of quasars

Soon after the release of the first catalogs of radio astronomical sources (like the *Cambridge* catalog of radio sources, Edge et al. 1959), the attention was driven to powerful, very compact radio-sources. Their optical counterparts were identified as faint point-like sources, which showed strong variability and strong emission line in their optical spectrum. They where thus named quasi-stellar object (quasar, or QSO). One of the most important discoveries in the astronomy of the XX century was that the measurement of the redshift of these newly-identified object was suprisingly high (see for example Schmidt 1963, for the case of *3C273*): once the Doppler redshift excluded (mainly through the non-detection of blue-shifted quasars), the cosmological redshift [2] was accepted as the explanation of the observed shift in frequency, constraining the quasars as powerful extra-galactic sources. In fact, the high measured distance implies an appearent luminosity wich can reach 10^{48}erg s^{-1}.

The new question became then, what is the origin of such high luminosity? It can be easily shown (see e.g. Peterson 1997; Kembhavi & Narlikar 1999) that chemical reactions cannot provide such an energy, nor nuclear ones (which are responsible for the thermal emission from stars). The only source which can provide an amount of energy consistent with the observed luminosity is the graviational force. This solution implies, however, that the mass of the compact object responsible for the emission is of the order of $10^7 - 10^9\ M_\odot$. General relativity imposes that such an object is a black hole, and, in order to differentiate it from the black holes resulting from stellar collapse (with $M_\bullet = O(M_\odot)$), is called super-massive black holes (SMBH).
The basic idea is that the gravitational potential energy of the material orbiting around the SMBH is converted into thermal emission through friction and viscosity in the accreting material, which forms an accretion disc around the central object. The same physical situation, on a different scale, is encountered in galactic black holes accreting material from a companion giant star (X-ray binaries).

An important step towards the understanding of quasars, was the discovery of nearby active galactic nuclei. They have been detected as nearby galaxies (mostly part of historical catalogs, as the Messier Catalog (Messier 1781) or the New General Catalog (NGC, Dreyer 1888)) which show a luminosity peak at their center. An example is shown in Fig. 1. Another unique feature is that their optical spectrum is characterised by emission lines with unusual intensity ratios with respect to the one observed in normal galaxies, where the emission lines come from the contribution of HII regions. In addition, these emission lines can be significantly broader than in normal galaxies, with a full-width-half-maximum in the range 5000-10000 km s^{-1} (for a recent review, see Véron-Cetty & Véron 2000). Their peculiarity was first noticed by Seyfert (1943), whose name remained to define the class of the Seyfert galaxies (which will be presented in more details in Chapter 1).

The question becomes than, are quasars and AGN linked? And in which way? The answers is yes, they are, and it will be discussed in the unification scheme Section. The idea is that Seyfert galaxies are low-luminosity AGN, observed only in nearby galaxies, while quasars are high-luminosity AGN, which outshine the emission of the associated galaxy. Before going into the details of the unification scenario, we provide some observational basis of all the different kinds of AGN.

---

[2] The Hubble's law, relating the redshift to the distance was empirically discovered only a few decades before, in 1929 (Hubble 1929), and the cosmological origin of the redshift was not firmly established, yet.

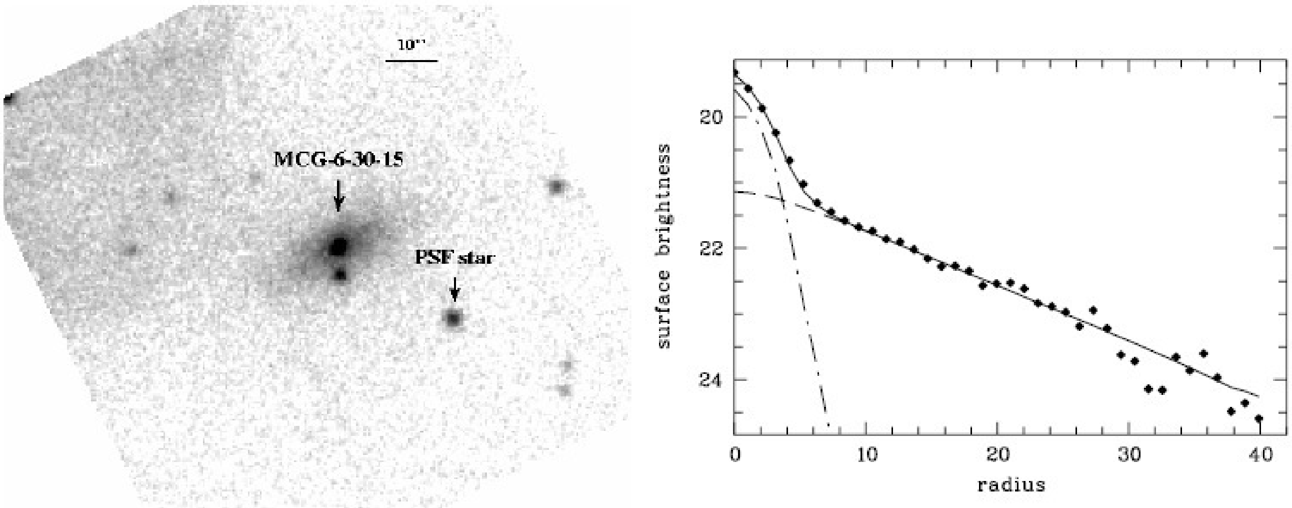

Figure 1: *Left:* optical image of the *Seyfert 1* galaxy *MCG - 6 - 30 - 15*. *Right:* surface brightness of the object as a function of the integration radius, showing the contribution from the host galaxy (dashed line) and from the active nucles (dashed-dotted line). Taken from Arévalo et al. (2005).

0.1.2 The AGN zoo

The classification of AGN can be quite complicated at a first glance, and the reason is mainly its historical evolution. We have thus classes of AGN which merged during the last decades, new classes which were introduced, some others which were abandoned. The class of blazars, for example, which will be deeply discussed in the second Part of this thesis, is not a homogeneous group, and is composed by highly variable quasars (sometimes called Optically Violent Variable quasars, OVV) and BL Lacertae objects (BL Lac). We try to describe here, in a simple (and not exhaustive) way, the different kind of AGN that can be encountered, providing the most recent name.

The most general classification of AGN is based on their radio flux (Kellermann et al. 1989). If their measured flux at 5 GHz is more than ten times their optical flux, they are called *radio-loud* AGN, while if it's lower they are called *radio-quiet* AGN. As we will se later, this dichotomy represents one of the aspects of the unification scenario which remain unclear.

Radio-quiet AGN are called Seyfert galaxies (from Seyfert 1943), and they are distinguished in type-one Seyfert galaxies (or, simply, Seyfert 1), and type-two Seyfert galaxies (Seyfert 2). The observational threshold between the two sub-classes is the width of the emission lines observed in the optical spectrum: if we observe only narrow emission lines (of the order of hundreds km s^{-1}) we call them Seyfert 2, while if we also see broad emission lines (of the order of thousands km s^{-1}) we call them Seyfert 1.
The distinction between the two kind of Seyfert galaxies is not a true dichotomy, in the sense that we have observed intermediate Seyfert, which are then called Seyfert 1.5. In general, a Seyfert galaxy is nowadays identified by a continous index spanning the range $1.X$ to 2.0, indicating the amount of broad versus narrow line observed. However, a class of Seyfert galaxies which does not follow this simple schema exists, like the *Narrow-Line-Seyfert-1* galaxies (NLS1, Osterbrock & Pogge 1985), which show a Seyfert-1 spectrum plus unusually narrow HI lines, with strong FeII emission and weak forbidden lines. More details on Seyfert galaxies will be given in Chapter 1.
Quasars share the same spectral properties of Seyfert 1 galaxies, but they have a higher luminosity. They can thus be seen as the brighter version of Seyfert 1 galaxies, being easily detected despite their high dis-

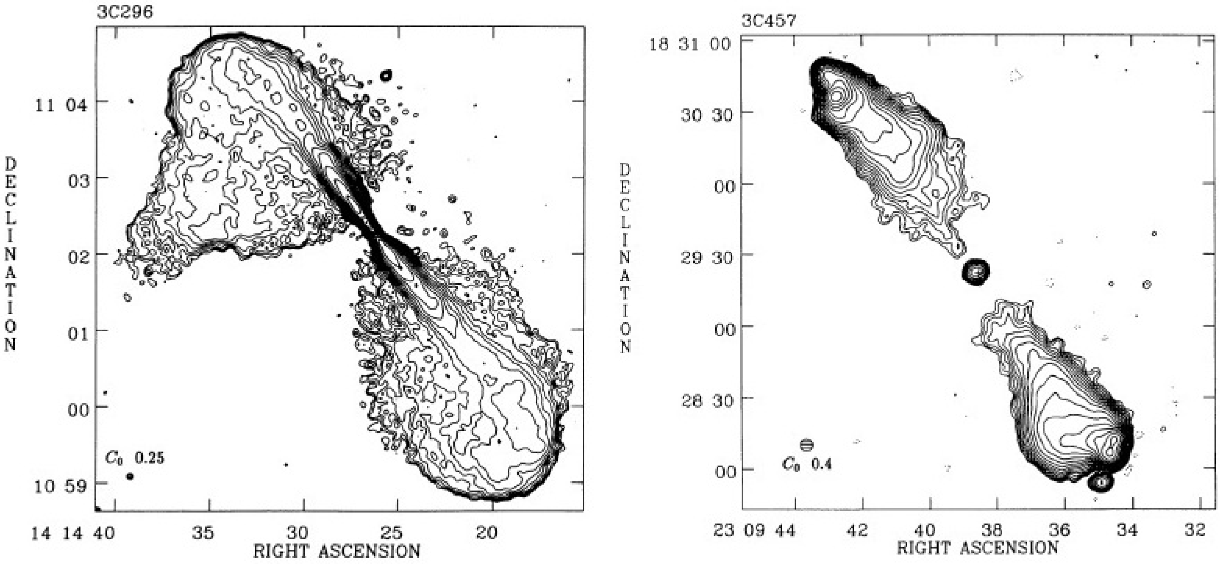

Figure 2: Example of the different morphology observed in radio-galaxies. At the left, the radio image (at 20 cm) of the FR I radio-galaxy *3C296*, at the right of the FR II radio-galaxy *3C457*. Adapted from Leahy & Perley (1991)

tance. Hereafter we will thus adopt the term quasar to indicate an AGN whose host galaxy is not observed.

The archetype of radio-loud AGN are radio-galaxies. A radio-galaxy is defined as a radio-source whose optical counterpart is a resolved galaxy. Their radio morphology is characterized by a relativistic jet, which emits non-thermal emission (synchrotron radiation) in a wide range of frequencies, from radio to γ-rays. The radio-galaxies are divided in two sub-classes according to the morphology of their radio emission: if it is dominated by the core they are called *FR I* (from Fanaroff & Riley 1974), while if it is dominated by distant hotspots in the jet they are called *FR II* (the two symmetric hotspot representing the shock-front between the relativistic jet and the inter-galactic medium). This morphological dichotomy (shown in Fig. 2) corresponds to a luminosity dichotomy, with FR II radio-galaxies brighter than FR I.

If instead the host galaxy of the radio-source is not resolved, we call it generally *radio quasar*. According to the spectral index in the radio band, we can call them *Flat-Spectrum-Radio-Quasar* (FSRQ) or *Steep-Spectrum-Radio-Quasar* (SSRQ) if the index α [3] is lower or higher than 0.5.

Radio-galaxies and quasars both show emission lines in the optical spectrum. If instead it is characterized by a continuum, non-thermal distribution, the AGN is called *BL Lac* object (from the name of the first object of this kind observed, the previously-thought variable-star *BL Lacertae*; the threshold for an object being classified as *BL Lac* is that the equivalent width of the emission lines in the spectrum has to be lower than 5 Å, see Angel & Stockman (1980)). The term *blazar* (merging of BL Lac and quasar, but also reminding of *"to blaze"*) is adopted to refer to BL Lac objects and OVVs, which are considered two sub-classes of the same family, characterised by rapid variability and high and variable polarization. It is nowadays established that FSRQs also belong to the blazar class (Fugmann 1988), as they share the same properties of the OVVs. More details on blazars will be presented in Chapter 3.

---

[3] Spectral index in F_ν, the flux spectral density

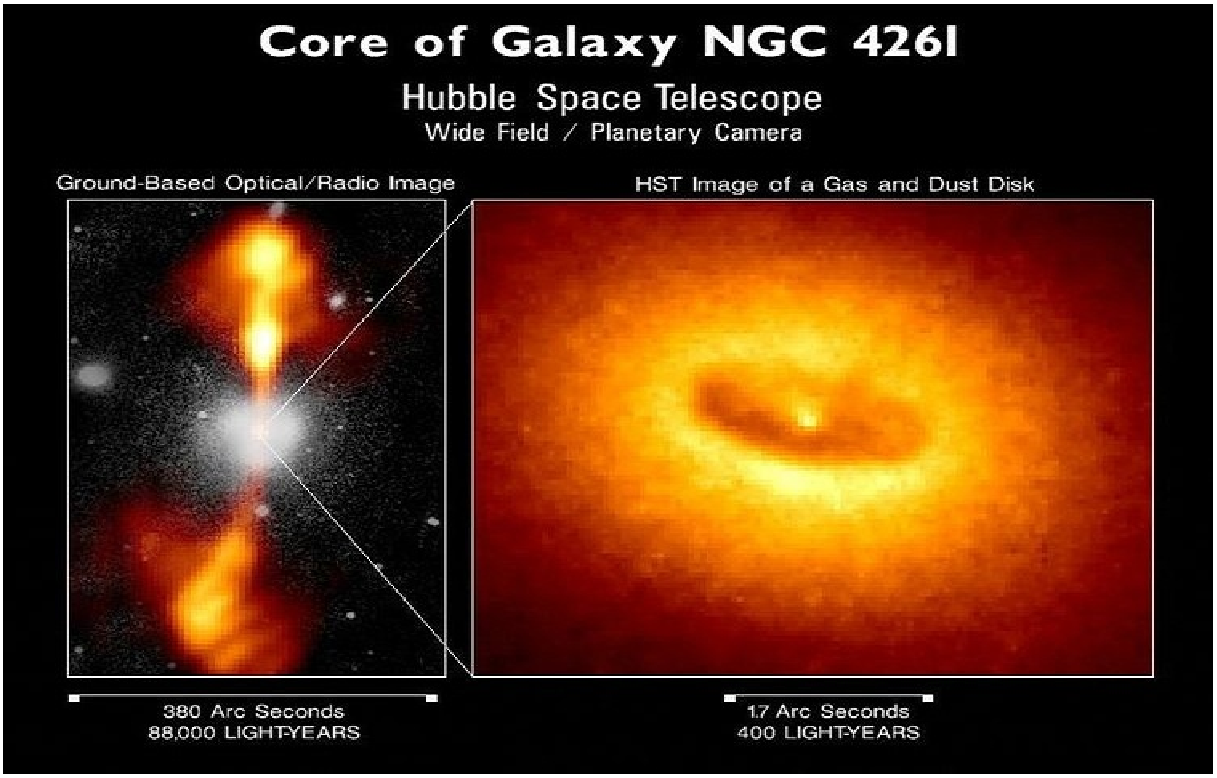

Figure 3: The active galactic nucleus *NGC 4261*. *Left:* optical image of the galaxy with, in false-color, the relativistic jets observed in radio. *Radio:* zoom on the inner part, showing the dust torus obscuring the central engine of the active galactic nucleus. (Credit HST/NASA/ESA, adapted from Jaffe et al. (1993))

0.1.3 The unification model

The unification model, developed in the 1980s, (for a review see Antonucci 1993; Urry & Padovani 1995) tries to explain the different kind of observed AGN in a consistent framework. The basic scenario is the presence, at the center of the system, of a central engine, the SMBH, which accretes matter in the form of an accretion disc. Part of the incoming matter is expelled in the form of a pair of polar, relativistic jets, which correspond to the jet observed in radio-galaxies.
The mechanism of the production of jets in AGN is one of the open-question in XXI century astrophysics. It seems clear nowadays that the production of jets is possible only in the presence of a strong magnetic field, which collimates the outflow, but the details of this mechanism remain unclear (for a recent review, see e.g. Camenzind 2005). The presence of the jets is considered as a necessary and sufficient condition for the observation of an AGN as radio-loud: if the jets are present we will see it as a radio-loud AGN, while if the system does not show relativistic jets, we will see it as a radio-quiet AGN.
This scenario explains thus the radio-dichotomy of AGN. It is important to underline, however, that this dichotomy is not fully explained nor theoretically supported, and remains a weak spot of the theory. Several authors claimed that the presence/absence of jets is linked to the spin of the central black hole (see e.g. Tchekhovskoy et al. 2010), but this hyopthesis has not been confirmed yet.

The second key-ingredient of the unification scenario, is a dust torus located on the same plane of the accretion disc, at a parsec-scale distance from the central black-hole. This affects the observation of the AGN because, if we see the system edge-on, the central region would be obscured by the torus, while if we observe it face-on, we can directly see the accretion disc and the inner core of the system.

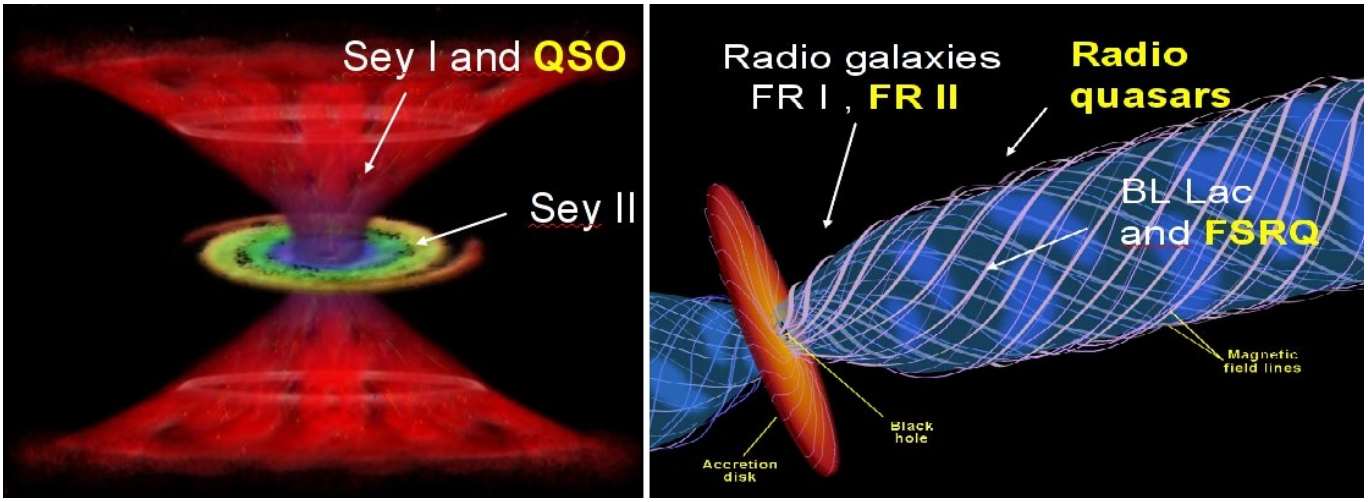

Figure 4: Simplified scheme of the unified model of active galactic nuclei. *Left*: radio-quiet AGNs. The dusty torus is not shown, while the outflow represents a disk wind. *Right*: radio-loud AGNs, characterized by the presence of a relativistic jet.

The emission line observed in the optical spectrum are thought to be produced by clouds illuminated by the thermal emission from the accretion disc. The width of these lines is explained by Doppler broadening, and is thus linked to the distance of the cloud from the center of the gravitational potential: narrow-emission lines map the farthest emission regions (narrow-line regions, NLRs), while broad-emission lines map the emission regions closest to the black hole (broad-line regions, BLRs).
If the observation of the central regions is obscured by the torus, we will thus see only the NLRs, while, if we observe the AGN face-on we will be able to detect the emission from the BLRs. This scenario explains thus by a simple orientation effect the difference between Seyfert 1 galaxies and Seyfert 2 galaxies, naturally taking into account the intermediate objects.
The observational proofs of this interpretation are mainly two: the first, indirect, is the detection of broad-lines in Seyfert 2 galaxies when observed in polarized light. This is explained by considering that what we are observing in this case is the emission from BLRs scattered in the direction of the observer. The second proof is the direct observation of the dusty torus, like in the famous study of the nearby AGN *NGC 4261*, showed in Fig. 3 (Jaffe et al. 1993).

0.1.4 Silent super-massive black holes

The most important confirmation of the unification model of AGN comes from our own galaxy. In fact, it is now unanimously accepted that the very center of the Mily Way (called $SgrA^{\star}$) hosts a SMBH of $10^6\ M_{\odot}$, whose presence is detected indirectly by the orbital motion of stars in its gravitational potential. In Fig. 5 (taken from Eisenhauer et al. 2005) we shows an image of the measured orbital motion of six stars around $SgrA^{\star}$, together with the measurement of their radial velocity. This observation shows that even non-actif galaxies can harbour a SMBH at their center, which does not show any sign of activity because it is not currently accreting matter.

Another important observation is the recent detection (Su et al. 2010), by the *Fermi-LAT* telescope (observing the sky in γ-rays, between 100 MeV and 100 GeV), of a pair of γ-ray lobes in our galaxy (called *"Fermi bubbles"*), symmetric with respect to the galactic center (see Fig. 6). The origin of this newly-discovered component is currently under-debate, but one of the possibility is that it represents an

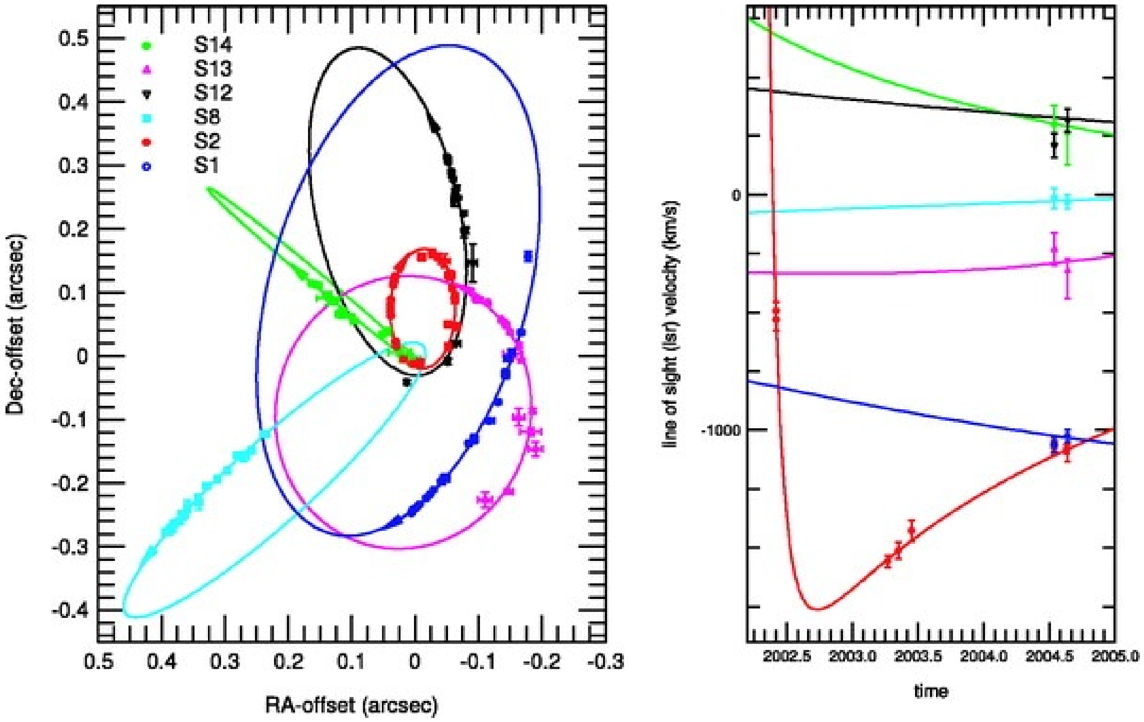

Figure 5: *Left:* orbital motion of stars around *SgrA**. *Right:* radial velocity of the six stars considered (same colour as for the left plot). Taken from Eisenhauer et al. (2005).

echo of a past activity of the Milky Way center. This would thus confirm that an AGN is the visible effect of accretion onto a SMBH, and that it can be turned on and off according to the matter reservoir.

0.2 TeV astronomy

TeV astronomy, which studies photons with an energy of the order of magnitude of the Tera-electonVolt, is nowadays a firmly-established part of astronomy, and is considered as an autonomous branch thanks to its particular detection technique (for a review, see for example Weekes 2003), which will be briefly presented in this Section.

The term γ-ray astronomy is used to describe the study of photons above $\approx$ 100 keV (i.e., more energetic than X-rays). There is however a distinction between medium-energy γ-rays (ME, $E \in$ [100 keV, 100 MeV]), high-energy γ-rays (HE, $E \in$ [100 MeV, 100 GeV]) and very-high-energy γ-rays (VHE, $E \in$ [100 GeV, 100 TeV]). In the following, we will adopt VHE astronomy as a synonym of TeV astronomy. The difference between ME/HE and VHE astronomy is more than a simple practical distinction between the photon energy: in fact, while for $E <$ 100 GeV the detection is done using space-telescopes which directly intercept the γ-ray photon, measuring its energy and incoming direction, above 100 GeV the observation is done with ground-based telescopes, and it is indirect.
What is observed is indeed the emission from the electro-magnetic shower triggered by the interaction of the TeV photon with the Earth atmosphere. The first process taking place is the pair production of an electron and a positron as a result of the interaction of the γ-ray with the atmosphere. The two leptons, by interaction with the atmosphere, emit bremsstrahlung radiation, which then pair-produces again. The characteristics of the shower (number of pairs produced, altitude and length of the shower) depend on the photon energy. If the electron-positron pairs composing the cascade are super-luminal in the atmo-

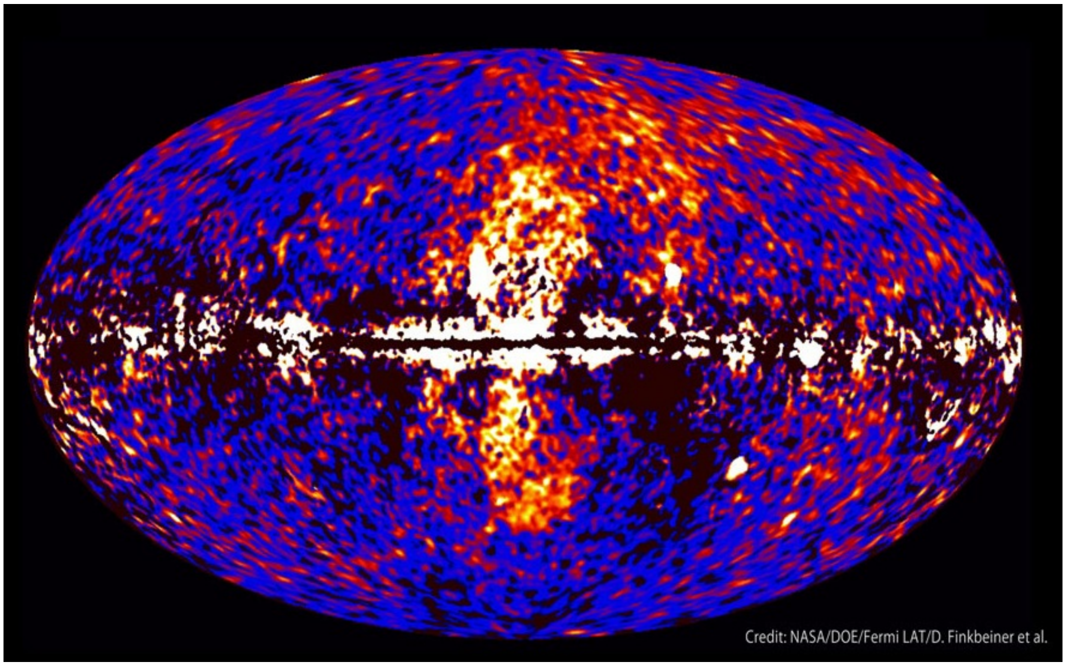

Figure 6: The Fermi bubbles in the Milky Way. The image represents the sky in galactic coordinates (the plane representing the Milky Way disc). Credits NASA/DOE/Fermi LAT/D.Finkbeiner et al.

sphere (i.e. their speed v is higher than c/n, where n is the refractive index of the medium), they emit Cherenkov light, which is observed on the ground. The energy and the direction of the incoming γ-ray is then reconstructed, on the basis mainly of the shape of the observed image and its intensity. The main problem of this detection technique is the background, which is represented by all the showers triggered by cosmis rays. It is however possible to discriminate between a photon-shower and a hadron-shower on the basis of the shape of the observed Cherenkov light, given the fact that a photon-shower is much more compact, as illustrated in Fig. 7. More details on the data analysis of TeV data, specifically for the case of the *H.E.S.S.* telescope array , will be provided in Section 4.

We recall here the basis of the Cherenkov emission, which is the basis of the TeV astronomy. When a charged particle crosses a dielectric medium, it induces a polarization in the surrounding molecules, which then radiate photons. If the particle is moving with a speed lower than the speed of light in the medium (c/n), the induced polarization is symetrical, and no effective radiation is emitted. The situation is different if the particle is travelling faster than the speed of light: in this case, the disturbance is asymmetrical (in the direction of propagation of the particle), and a net effect is produced. As shown in the sketch presented in Fig. 8, the different contributions produced along the path sum up constructively in a cone, characterized by an angle ϑ whose value is uniquely determined by the refractive index of the medium (if $\beta \approx 1$) by $\cos\vartheta = 1/n$. The physical situation is in analogy to the one of acoustic waves, when an object travels at a speed higher than the speed of the sound, producing a Mach cone of acoustic waves.
The Cherenkov light has its peak emission in blue/ultra-violet (the spectrum is characterised by a $1/\lambda^2$ distribution), and it is responsible, for example, for the blue luminosity of the water-pool in nuclear reactors.

The VHE observatories (commonly abbreviated IACTs, for Imaging Atmospheric Cherenkov Telescopes) are thus optical telescopes looking at the blue Cherenkov light emitted by the interaction of the

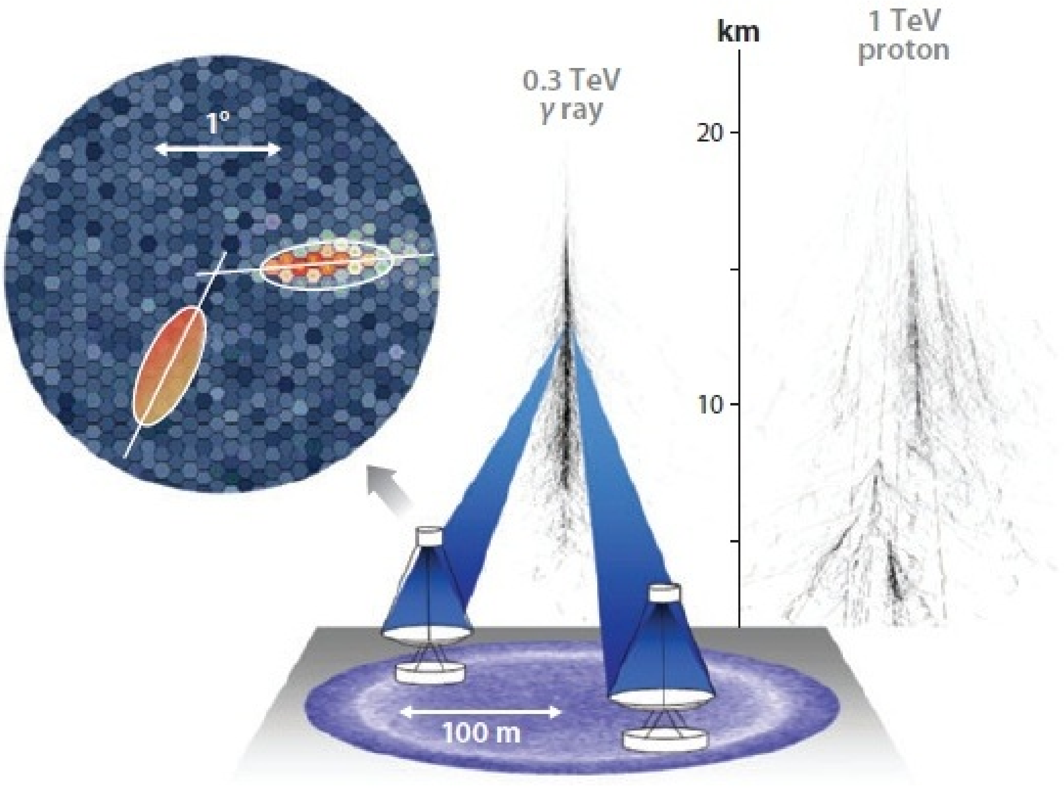

Figure 7: Scheme of the detection technique of Cherenkov telescopes. The left inset shows the observed Cherenkov light produced by the shower triggered by the TeV photon. For comparaison, the right part shows a shower triggered by a proton. (Taken from Hinton & Hofmann (2009))

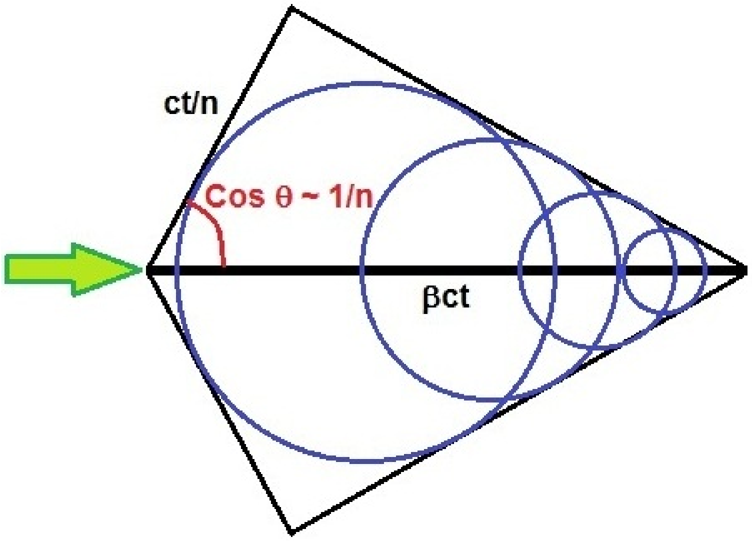

Figure 8: Diagram of the production of a cone of Cherenkov light by a relativistiv particle, going from the left to the right.

photon with the atmosphere. This emission has however two characterstics which challenge its detection: it is very faint and lasts for few nano-seconds. The detectors have thus to respond very fast, collecting at the same time enough photons to permit the characterization of the shower. On the other hand, a good spatial resolution is not required, given the fact that we are interested only in the overall image of the shower. The optimal solution (in term of costs) is a large segmentated mirror (i.e. composed by several blocks, allineated on the support structure) while the camera is made up of clusters of photo-multipliers. One of the peculiarity of TeV astronomy which is worth mentioning is that the measurement of the Cherenkov light is affected by the brightness of the sky, and, in particular, it is usually not worth to observe in presence of Moon-light. This affects significantly the useful observing time of a TeV observatory.

The first important success in TeV astronomy came in 1989, when the *Whipple* telescope (Cawley et al. 1990) detected the Crab nebula as the first TeV source (Weekes et al. 1989). For the work presented in this thesis, it is important to recall the first extragalactic source observed at TeV, *Mrk 421*, by Punch et al. (1992) (by the *Whipple* collaboration, as well). Among that generation of VHE telescopes, it is worth mentioning the *Hegra* (HEGRA Collaboration et al. 1999) and *CAT* (Barrau et al. 1998) telescopes, built respectively in Spain and France.

0.2.1 The current generation of IACTs

The current generation of IACTs is characterized mainly by stereoscopy: the observatory is composed by at least two telescopes, which detect the Cherenkov light at the same time, significantly improving the reconstruction of the direction of the incoming photons and the overall sensitivity.
There are nowadays three competitive TeV telescope arrays in the world (shown in Fig. 9 and 10):

- *H.E.S.S.* (High Energy Stereoscopic System)
  is a system of four identical IACTs of 13 m of diameter each, located in the Khomas Highlands, in Namibia. It has been built by a collaboration mainly composed by French and German institutions, and is operative since 2004.

- *MAGIC* (Major Atmospheric Gamma-ray Imaging Cherenkov telescope)
  is composed by a couple of different IACTs built in two different phases: the first one is operative since 2004, while the second has been completed in 2009. It is located in the Canary islands, and is supported mainly by German, Italian and Spanish institutions. The second telescope represents today the biggest operative IACT (17 m), and allows this system to observe at energies down to 25 GeV (see next section).

- *VERITAS* (Very Energetic Radiation Imaging Telescope Array System)
  is composed by four identical IACTs, in Arizona. Operative since 2007, it is the successor of *Whipple*, and is supported by American institutions.

It is important to underline that the three observatories do not observe the same part of the sky, *MAGIC* and *VERITAS* being located in the Northern hemisphere, and *H.E.S.S.* being located in the Southern hemisphere. In particular, *H.E.S.S.* benefits from the view of the central region of the Milky Way: the TeV galactic survey performed by *H.E.S.S.* (Aharonian et al. 2005a; Chaves et al. 2008) represented a major result in TeV astronomy, leading to the detection of dozens of new sources, some of them still unidentified.

Figure 9: *Left:* the two telescopes of the *MAGIC* observatory in the Canary islands. *Right:* the four-telescope array of *VERITAS*, in Arizona. (Credits: the *MAGIC* and *VERITAS* collaborations.)

Figure 10: The new telescope of the phase II of *H.E.S.S.*, built in the middle of the four-telescope array of *H.E.S.S.* I. (Credits: the *H.E.S.S.* collaboration.)

0.2.2 The future of TeV astronomy

H.E.S.S. II

The *H.E.S.S.* telescope array, in its actual configuration of four 13 m IACTs, has a low-energy threshold of roughly 100 GeV. The measurement of the lower energies is limitated mainly by the faintness of their associated Cherenkov emission and by the cosmic-ray background: to detect them it is thus mandatory to increase the collecting surface. A current issue in γ-ray astronomy is that HE and VHE telescopes do not overlap in energy. In fact, the *Fermi* satellite (launched in 2008, and observing the GeV universe in an all-sky mode), starts loosing detecting efficiency at energies of the order of 100 GeV, exactly when *H.E.S.S.* starts being sensitive. The part of the spectrum in-between the two instruments is thus poorly known, given the fact that both telescopes are at their respective thresholds. To decrease the low-energy threshold, the *H.E.S.S.* collaboration has built a fifth telescope of 28m of diameter (more than twice the current *H.E.S.S.* telescopes, see Fig. 10), placed at the middle of the array. In this new configuration (*H.E.S.S. II*), the low-energy threshold is expected to be at roughly 20 GeV, significantly overlapping the *Fermi-LAT* energies. The fifth telescope will provide of course benefit also for the already studied range of energies, improving the overall sensitivity of *H.E.S.S.*.

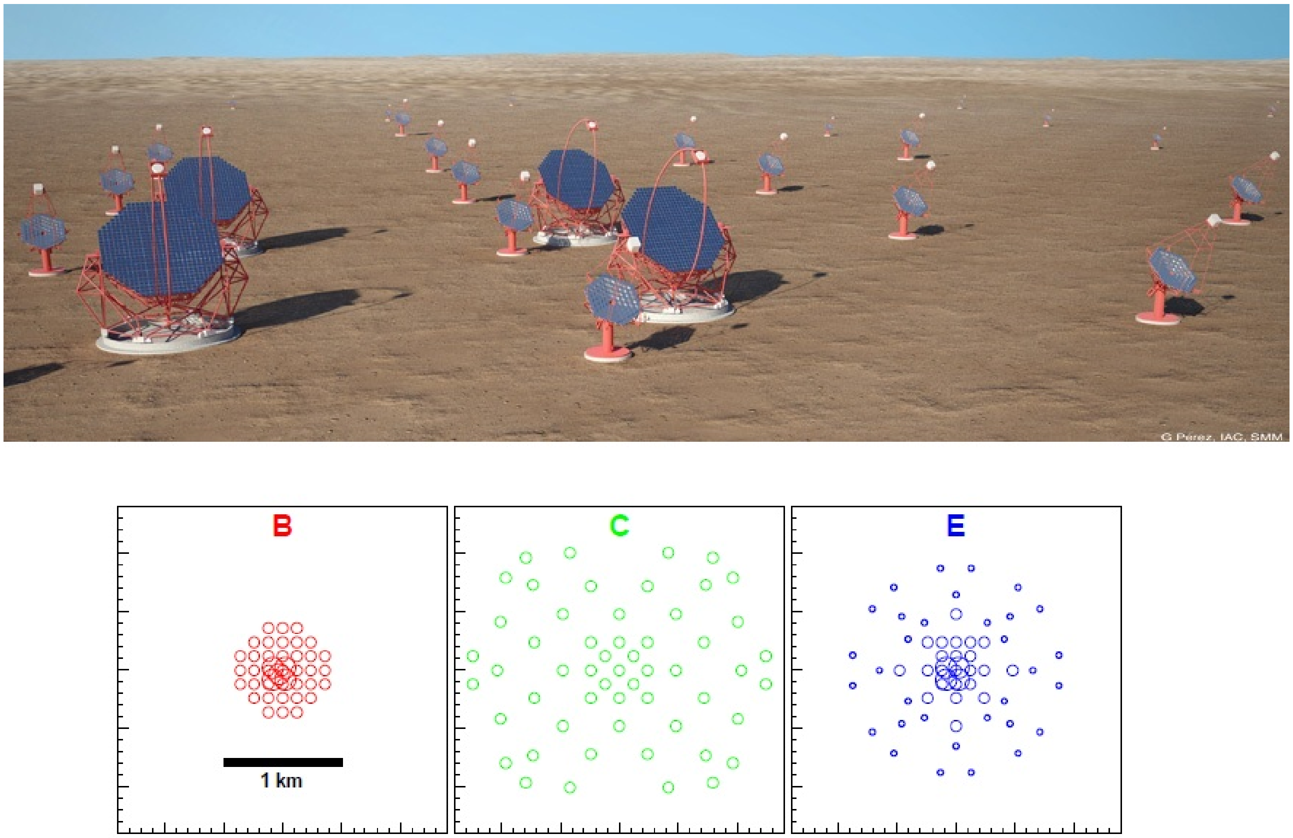

Figure 11: *Top:* rendering of the future *CTA* observatory, with four Large-Size-Telescopes (LSTs) in beetween a grid of Mid-Size-Telescopes (MSTs). Several Small-Size-Telescopes (SSTs) can be seen in the background. (Credits: the *CTA* consortium) *Bottom:* example of three different array configuration under study for the *CTA* telescope. The size of the circles is proportional to the size of the telescopes used (taken from Actis et al. 2011); configuration B, LSTs and MSTs; configuration C, MSTs only; configuration E, LSTs, MSTs and SSTs.

The official inauguration of this new phase of *H.E.S.S.* is planned at the end of September. Considering that at the beginning the observing time would be devoted to the characterization of the instrument, the first scientific results are expected for 2013.

CTA

At the same time that the current generation of IACTs is providing a huge scientifical outcome, establishing TeV astronomy as a solid science, the community is already preparing the next generation of telescopes. The different collaborations running the three competitive instruments (*MAGIC*, *H.E.S.S.* and *VERITAS*) decided to merge, putting their efforts together to conceive, develop and build the TeV observatory of the next decades, *CTA* (*Cherenkov Telescope Array*, Actis et al. 2011). Conceived as an open observatory (while the current observatories are private), *CTA* will consist of several dozens of telescopes, detecting photons from 30 GeV to 300 TeV, with a sensitivity one order of magnitude higher than current IACTs. It will be composed by three different kind of telescopes: few Large-Size-Telescopes (LSTs, with a diameter of 24 m), which cover the lowest energies, and represent the center of the array; several Mid-Size-Telescopes (MSTs, similar in dimension to *H.E.S.S.*), which cover the central part of the spectrum, around the TeV; several Small-Size-Telescopes (SSTs, with a diameter of a few meters), placed more sparsely in the array and covering the highest energies. Some possibilities of the exact configuration of the array (which has not been defined yet) are shown in Fig.11. The project is currently in its preparatory phase, and the first prototypes of the different parts of the array (telescope structures, cameras, mirrors) are being studied. In order to have a good coverage of the sky, the plan is to build two sites, one in the southern hemisphere (more devoted to galactic sources, given the visibility of the central region of the Milky Way), and one in the northern hemisphere (more devoted to extra-galactic sources). However, the choice of the two sites has not been made yet. If the expected schedule will be respected, *CTA* is planned to be fully operational in the next decade (2018), providing new and exciting results in the field of γ-ray astronomy.

Prototyping *CTA*: the GATE project

We present here, briefly, the prototype for the *CTA* small-size-telescopes currently in development in the Paris Observatory, as a result of a collaboration between different laboratories in the Paris region. The project, named *GATE* (for GAmma-ray Telescope Elements), is characterised by a new kind of design with respect to the Davies-Cotton one, adopted in the current generation of IACTs. It will consists, in fact, of a two-mirror telescope, in the so-called Schwarzschild-Couder (SC) configuration. The primary mirror will have a diameter of four meters. The main goal of the prototype is thus to show that a SC design can be efficiently built and used for the TeV astronomy.

The project, whose construction is expected to be completed in 2013, will be fully equipped (with mirrors and camera), and will remain in the Meudon campus for teaching puroposes.

A rendering of the *GATE* telescope once completed, is shown in Fig. 12

Figure 12: Rendering of the *GATE* project, prototype for the small-size-telescopes in the *CTA* array. The main mirror has a diamter of four meters

Part I

Radio-quiet active galactic nuclei

Chapter 1

Seyfert 1 galaxies and the problem of the soft excess

Contents

1.1 Introduction

In this Chapter we provide an introduction on Seyfert galaxies, presenting first their observational properties in visible light, at the basis of their spectroscopic classification 1.2.1, as well as the observation in polarized light, which represented an important step for our comprehension of active galactic nuclei. We then enter in more details into the X-ray emission from Seyfert 1 galaxy discussing their general continuum spectrum (see Section 1.3.1), the iron Kα emission line (Section 1.3.2), the soft X-ray excess (Section 1.3.3) and the warm absorber (Section 2.4.1). For consistency, we also briefly discuss the X-ray emission from Seyfert 2 galaxies (see Section 1.4).

This Chapter represents an introduction to the work on modelling of the *Suzaku* spectra of the Seyfert 1 galaxies *Mrk 509* and *Mrk 841* presented in Chapter 2.

1.2 Seyfert galaxies

As discussed in the previous Chapter (Section 0.1.2), Seyfert galaxies are a class of AGN characterised by their radio-quietness (ratio of 5GHz-to-optical flux lower than 10), and by the fact that the host galaxy is clearly detected (otherwise they would be called, by definition, quasars). They are thus observed in nearby galaxies. These two characteristics make Seyfert galaxies an interesting class of AGN: the absence of relativistic jets (which dominate the emission in radio-loud AGN) permits us to better observe the inner core of the AGN, studying physical details that are hidden in radio-loud sources; their proximity permits us to observe them with higher photon statistics and spatial resolution compared to the luminous and distant quasars.

1.2.1 Type 1 and type 2

Seyfert galaxies are classified in type 1 and type 2 on a spectroscopic basis: if the emission line observed in the optical spectrum are narrow, we call them Seyfert 2, while if a broad component is present as well, we call them Seyfert 1. More correctly (see e.g. Khachikian & Weedman 1974), the distinction between the two classes is made regarding the relative width of the Balmer lines to the forbidden lines: if they have the same width, it is called Seyfert 2, while if the Balmer lines are broader, it is called Seyfert 1.
As already said, this classification is not a clear dichotomy and according to the strength of the broad component we can have intermediate Seyfert galaxies (with an index going from 1.0 to 2.0). In Fig. 1.1 we show an example of optical spectra from two Seyfert galaxies, showing the different aspect of their emission lines.
A clue in the comprehension of AGN, came from observations of Seyfert 2 galaxies in polarized light (see e.g. Antonucci & Miller 1985): as shown in Fig. 1.2 for the case of *Mrk 348*, the polarized spectrum of a Seyfert 2 galaxy looks indeed like the spectrum of a Seyfert 1. In the framework of the unified model of AGN (see Section 0.1.3), this effect is explained by considering that the emission from the BLR, hidden by the torus in the Seyfert 2 galaxies, emerges along the polar axis and is then scattered towards the observer (the polarization carrying the information on the scattering angle).

The classification scheme of Seyfert galaxies is however not so simple. A first issue comes from the fact that some Seyfert galaxies showed mutation in their broad component (see for example Cohen et al. (1986) for the case of *Mrk 1018*, or Aretxaga et al. (1999), for the case of *NGC 7582*): this effect could be explained by considering that the obscuring torus is patchy, and can sometimes reveal the hidden nucleus of a type 2 object, modyfing the ratio of broad and narrow emission lines.
Another aspect is that there is an important part of Seyfert galaxies which cannot be classified as type 1, nor type 2. Their spectrum is similar to a Seyfert 1 (including high-ionization lines, like FeVII and FeX, which are not present in Seyfert 2 galaxies), but they show strong permitted narrow lines. Given their peculiarity they have been classified outside the standard Seyfert 1-2 classification, and they are known as Narrow-Line Seyfert 1 (NLS1, Osterbrock & Pogge 1985).
Even though in the following they will not be discussed any more, it is important to recall here that their importance in the understanding of AGN physics grew significantly in the latest decades, and they are nowadays of particular interest in high energy astrophysics, given their strong soft X-ray emission and rapid variability (see e.g. Boller et al. 1996). Recently, they have also been established as a new class of γ-ray emitter in the GeV range by the *Fermi* telescope (Abdo et al. 2009c).

The observational classification of Seyfert galaxies is done in optical wavelenghts for historical reasons. However, the different optical properties reflect different spectral characteristics in X-rays. In the following we concentrate on the X-ray emission from Seyfert 1 galaxies, describing the key elements of the spectrum. A brief discussion of the X-ray spectrum of Seyfert 2 galaxies will be provided in Section 1.4.

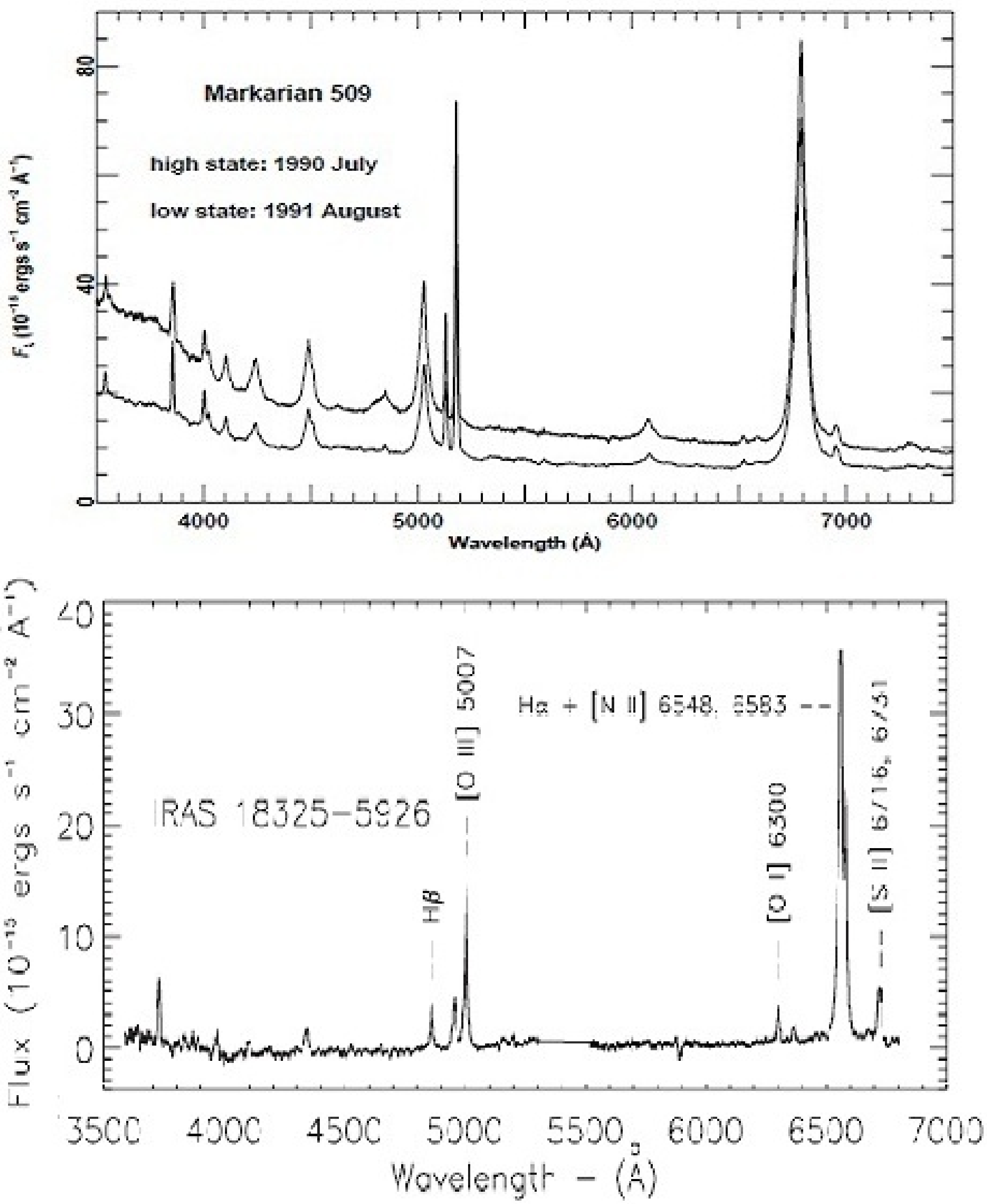

Figure 1.1: Example of optical spectra from different Seyfert galaxies. *Top:* optical and UV spectrum of the Seyfert 1 galaxy *Mrk 509* (whose X-ray spectrum will be deeply studied in Chapter 2), showing the characteristic broad-emission lines. The two spectra have been taken in different period (one year of interval), showing the continuum and line variability. See in particular the vairation of the broad HeII line (4686 Å). Taken from Carone et al. (1996). *Bottom:* optical and UV spectrum of the Seyfert 2 galaxy *IRAS 18325-5926*, showing narrower emission line with respect to the top plot. Adapted from Trippe et al. (2010).

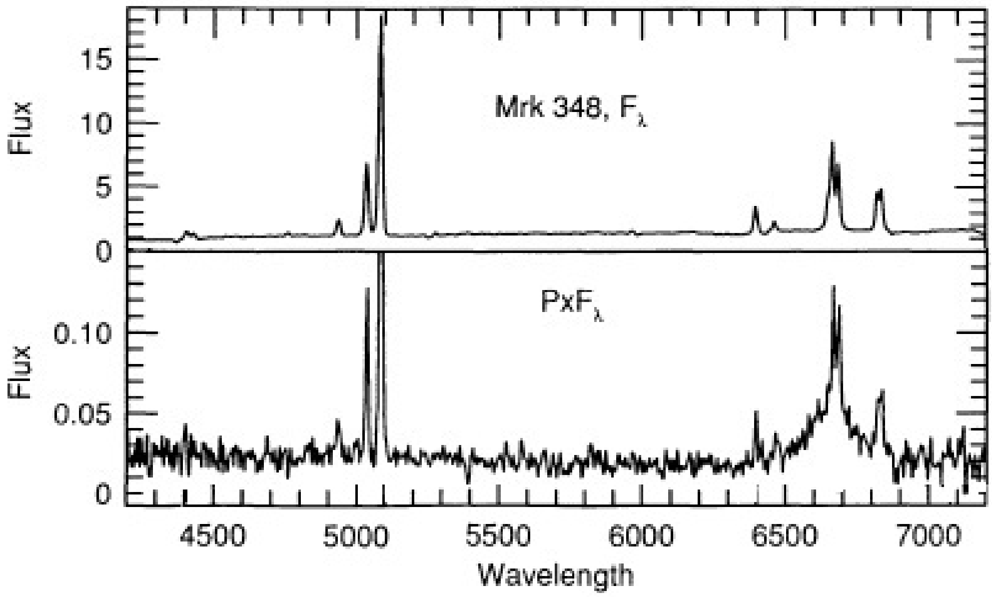

Figure 1.2: *Top:* spectrum of the Seyfert 2 galaxy *Mrk 348*, showing the characteristic narrow emission lines. *Bottom:* spectrum of the polarized emission, showing the broad component. Adapted from Miller & Goodrich (1990).

1.3 The X-ray spectrum of Seyfert 1 galaxies

The X-ray spectrum of Seyfert 1 galaxies can be well described by the following components:

- an underlying power-law continuum
- the Fe Kα line and the Compton bump
- the soft excess
- the warm absorber

1.3.1 The X-ray continuum

From the very beginning of X-ray astronomy it was found that the X-ray emission from Seyfert 1 galaxies was characterised by a non-thermal power-law distribution, with a photon index comprised between 1.2 and 2.0 (with a mean value of 1.56 ± 0.04, as measured recently by Cappi et al. 2006, , using the *XMM-Newton* satellite).
Soft X-ray photons (for energies below 1 keV) are absorbed in the interaction with the neutral material in our own galaxy, preventing us from observing the energies between UV and X-rays. The observed continuum is indeed a power-law with exponential absorption: $E^{-\Gamma}$ $\exp[-N_H \cdot \sigma(E)]$, where N_H is the hydrogen column density between the source and the Earth, and $\sigma(E)$ the photo-electric cross-section.

The origin of this power-law emission is thought to be an inverse Compton process by a thermalized population of electrons in a hot ($kT \approx 100$ keV) and optically thin ($\tau \approx 1$) region (called *corona*, see

Haardt & Maraschi 1993, as well as Fig. 1.7 for a schematic view), which scatters the thermal photons from the accretion disc. This view is also consistent with the detection of a high-energy cut-off around 100 keV (Gondek et al. 1996), which reflects the maximum energy of the electrons in the emitting region. However, the origin of this corona (its production mechanism) is not understood, nor the exact geometry (its shape and location with respect to the other components of the AGN).

1.3.2 The Fe Kα line and the Compton bump

A characteristic of the X-ray spectrum of Seyfert galaxies is the presence of the iron Kα emission line at energies around 6.4 keV. This feature, together with a hardening of the power-law continuum at energies above 10 keV (which can be seen as a "bump" in the hard-X-rays), is explained as the reflected emission of the primary corona continuum over the disc and the molecular torus. The physical processes responsible of the reflected spectral distribution are mainly Compton scattering and fluorescence (for a more detailed review on the calculation of the reflected spectrum, see e.g. Kahn et al. (2005, Chapter 3)). The shape of the Fe Kα can be complex: first of all, it can be produced by different kinds of iron ionization state, which provide contributions at slightly different energies (from 6.4 keV for neutral iron, to 6.65 keV for FeXXIV; for this reason, the detection of a narrow 6.4 keV emission line is usally associated to reflection on cold material, as the molecular torus); second, when it is produced by reflection of the inner regions of the accretion disc, its shape can be significantly modified by the relativistic effects near the SMBH, resulting in both a broadening of the line, and in the formation of a red-wing (which is of primary importance, providing an access to the value of the SMBH spin, see Tanaka et al. (1995); Nandra et al. (1997) and Fig. 1.3).

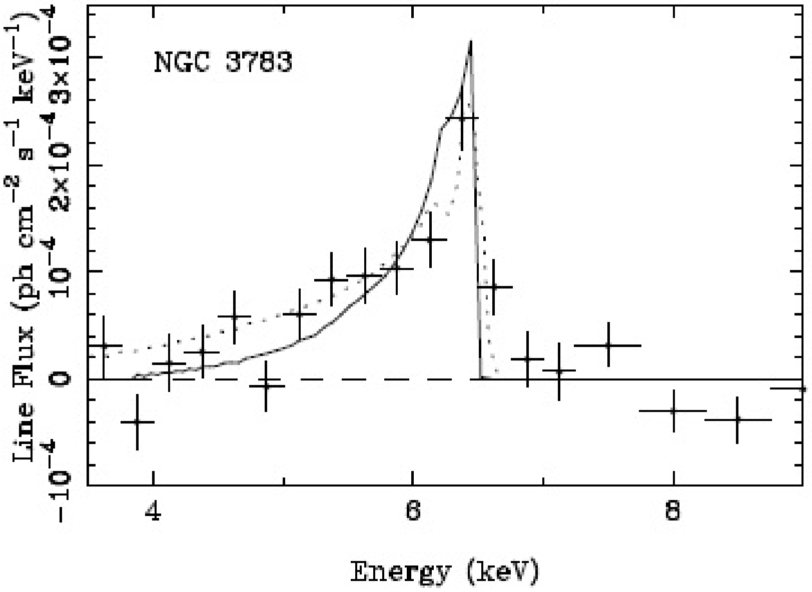

Figure 1.3: Fe Kα emission line in *NGC 3783*, with the red-wing clearly visible. The bolded and dashed lines represent the best-fit solutions assuming a Schwarzschild and a Kerr geometry, respectively. Taken from Nandra et al. (1997).

1.3.3 The soft X-ray excess

The soft-X-ray excess represents an important feature in the Seyfert 1 X-ray spectrum, always observed, even though variable in both shape and strength. It appears as a featureless excess of emission above the low energy extrapolation of the 2-10 keV best-fit power law. Detected since the 80s (Pravdo et al. 1981; Arnaud et al. 1985), the origin of this component is still nowadays, about three decades after the discovery, one of the major open questions in AGN research (see e.g. Turner & Miller 2009).

Historically associated with the high energy tail of the accretion-disc black-body radiation, many authors (Czerny et al. 2003; Gierliński & Done 2004; Piconcelli et al. 2005; Crummy et al. 2006) have shown that modelling with a thermal continuum infers a characteristic ”temperature” higher than expectations (Shakura & Sunyaev 1976) that remains remarkably constant across a range of AGN despite a wide spread in black hole mass and AGN luminosity. Moreover, in bright and variable AGN the soft excess does not follow the expected black-body luminosity-temperature relation (Ponti et al. 2006). Various studies have shown that the ratio of the soft excess, at 0.5 keV, to the extrapolation of the high-energy power-law emission has a very small scatter (Piconcelli et al. 2005; Miniutti et al. 2009), which is very different from what is observed in galactic black holes in the bright soft state, dominated by the disc black-body emission (e.g. Done et al. 2007).

The soft-excess shape seems to be related to the luminosity of the source. As shown in Fig. 1.4 (in which six different soft-excess shapes are shown, in order of increasing luminosity), faint sources show a sharp rise at energies less than 1 keV, while more luminous sources show a smoother spectrum, with the soft-excess starting already at 2 keV.

We describe now briefly the three competitive models developed to describe the soft-excess: in the next Chapter they will be more deeply discussed for the specific case of *Mrk 509* and *Mrk 841*.

The double Comptonization model

The first idea investigated to explain the soft-excess was Comptonisation that might occur in the upper layer of the accretion disc (Czerny et al. 2003; Gierliński & Done 2004; Sobolewska & Done 2007). This model represents a natural extension of the disc-corona model (it assumes that there are indeed two Comptonisation regions, the hot and optically thin corona, responsible of the power-law continuum, and a second, colder, Comptonisation region, responsible of the soft-X-ray emission) and may explain the featureless shape of the soft excess.

The main issue of this model is that it is difficult to explain in such a scenario the constancy of the soft-excess temperature, while the black-hole mass (and the accretion disc temperature) spans a large range of values. The feedback between the coronal disc irradiation and the disc external-layers may provide however a mechanism to stabilize both the soft excess temperature and emission ratio relative to the power-law emission.

The blurred reflection model

The observed constancy of the soft excess temperature seems to suggest a nature tied to atomic processes, which can naturally explain its universal ”temperature”.

The first possibility is reflection of the power-law continuum produced by the corona over the accretion disc. The physical mechanism is the same as for the production of the Fe Kα line and the hard-X-ray bump, but this time the reflection is done on the inner regions of the accretion disc. If the upper layer of the accretion disc is ionized, the disc Compton reflection component will contain many X-ray lines

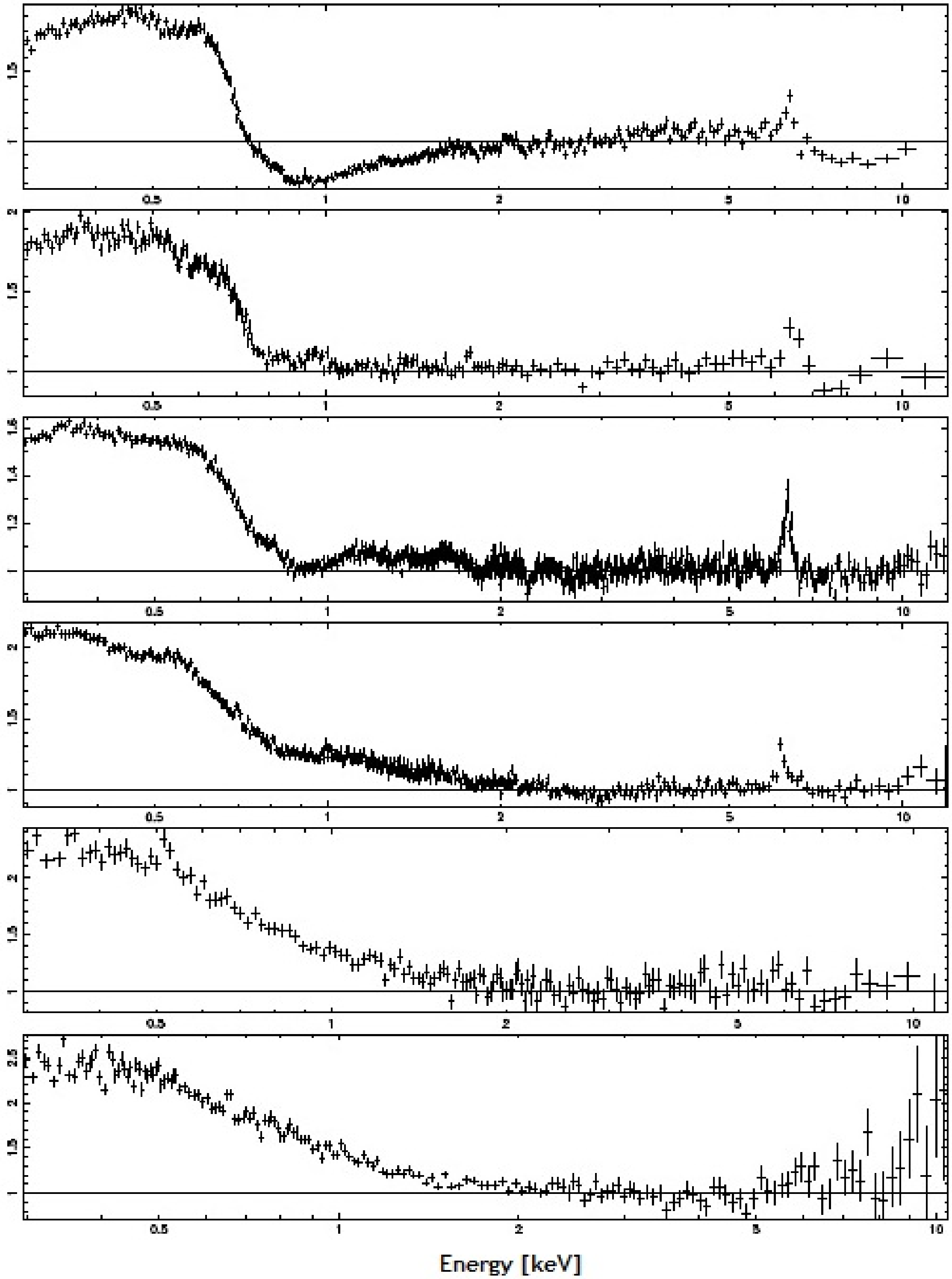

Figure 1.4: Example of six different soft X-ray excess in Seyfert 1 galaxies. From top to bottom, in order of increasing 2-10 keV luminosity, *MCG-6-30-15*, *Mrk 766*, *NGC 5548*, *Mrk 509*, *1H 0419-577* and *PKS 0558-504*. Taken from Pounds & Reeves (2002).

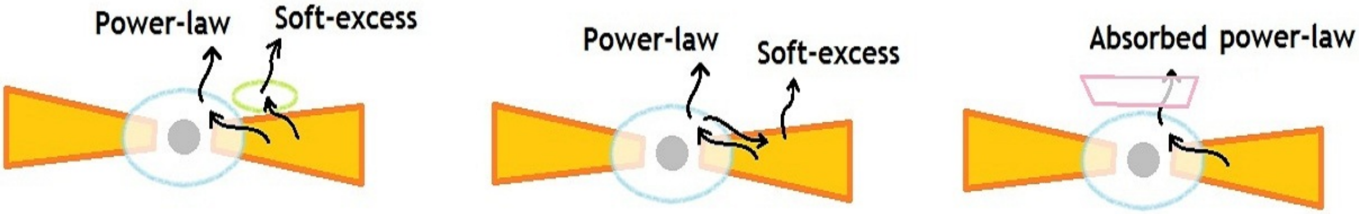

Figure 1.5: Schema of the different models explaining the soft X-ray excess. From left to right: double Comptonization, blurred reflection, smeared absorption. The different part of the diagrams are: SMBH, accretion disc (yellow), hot corona (blue), second corona (green, for the first model only), outflowing absorber (pink, last model).

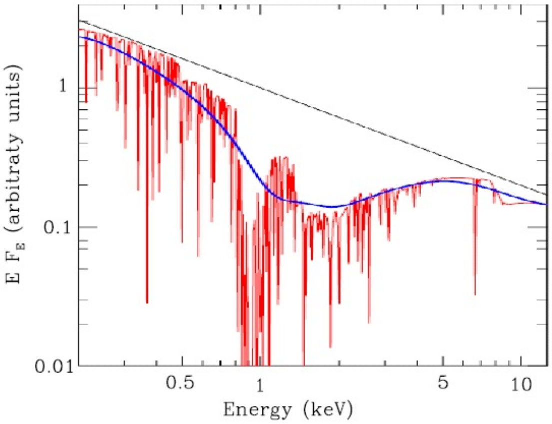

Figure 1.6: Representation of how an ionised absorption can reproduce the soft-excess. The black line represents the intrinsic power-law emission (with $\Gamma = 2.7$; the red line represents the absorbed emission; the blue line represents the absorbed emission when the smearing is taken into account. Taken from Gierliński & Done (2004).

(Ross & Fabian 2005) that will be broadened by the relativistic motion of the material on the surface of the accretion disc, forming a featureless continuum (Crummy et al. 2006).

The smeared absorption model

An alternative, based as well on atomic processes, is absorption by an ionised medium, which can imprint its main features in the soft X-ray band. If the absorber is moving relativistically (for example, in the form of a disc wind) it may, as well, produce a featureless curved continuum and reproduce the soft excess. In this scenario, the soft-excess would be indeed an absorption feature, and not an emission component, coming from the incorrect estimation of the intrinsic power-law spectral index produced in the hot corona (see Gierliński & Done 2004, , and Fig. 1.6).
Numerical simulations indicate however that, to reproduce the excess, the velocities of such a wind have to be extremely high (Schurch & Done 2008), suggesting that the flow has to be clumpy and/or only partially covering the source, or associated with a magnetically driven jet.

1.3.4 The warm absorber

The last component of the X-ray spectrum of Seyfert 1 galaxies we introduce, are the absorption features generated by the so-called 'warm absorber'. These absorption lines are present in the soft-X-ray part

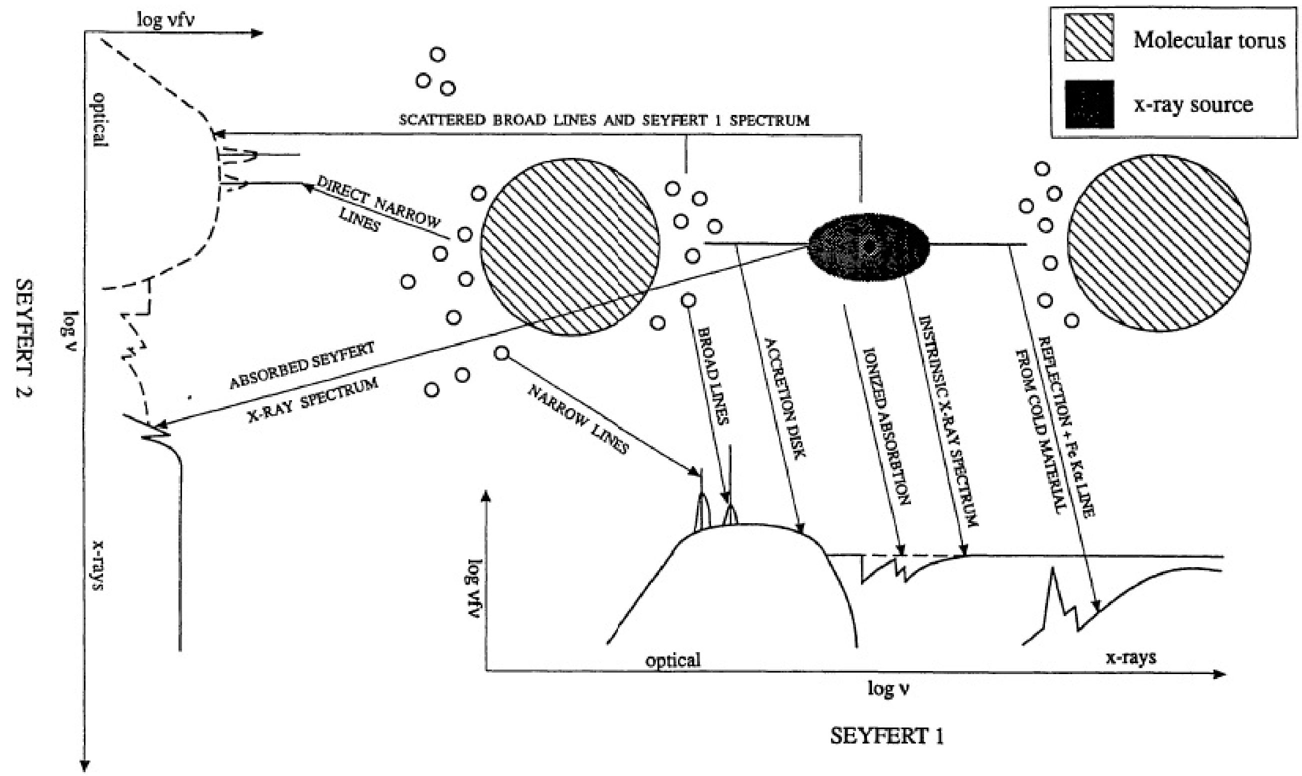

Figure 1.7: Schema of the visible-to-X-ray emission observed in Seyfert 1 and Seyfert 2 galaxies. The key-ingredients are the same: continuum emission from the hot corona, reflection over the distant region of the accretion disc (and on the torus), absorption by ionized gaz, emission from broad and narrow line regions. For Seyfert 2 galaxies, the presence of the torus hiddens the inner region of the system, and the observed X-ray continuum is heaviliy absorbed. Please notice that the soft-X-ray excess component is not considered in this plot. The orizontal plot shows the broad-band spectrum observed in Seyfert 1 galaxies, while the vertical plot shows the braod-band spectrum observed in Seyfert 2 galaxies. Taken from Mushotzky et al. (1993).

of the spectrum, and are associated with an ionised medium (which explains the adjective *warm*). The current generation of X-ray satellites, with the excellent energy resolution provided by *XMM-Newton* and *Chandra*, permits a thorough study of the warm absorber properties, revealing a complex scenario, with multiple-phase absorbers (see also Section 2.4.1), occasionally blue-shifted with respect to the observer (i.e. associated with an outflow), and showing time variability in both ionisation and covering-factor. For a review of the status of our knowledge on the warm-absorber, see e.g. Turner & Miller (2009) and referencese therein.

In the next Chapter we will discuss the results achieved on the warm absorber observed in the Seyfert 1 galaxies *Mrk 509* and *Mrk 841*, but it is important to note that *Suzaku* is not the best instrument to study such a component, given its relatively-low energy resolution. In particular to better constrain the warm absorber parameter, we will make use of the results obtained with the more performant *RGS* instrument on-board *XMM-Newton*.

1.4 The X-ray spectrum of Seyfert 2 galaxies

While the X-ray spectrum of Seyfert 1 galaxies will be studied in deeper detail in the next Chapter, in which we present an analysis and modelling of the *Suzaku* observations of two well known Seyfert 1, (with a particular interest in the interpretation of their soft-excess), the Seyfert 2 galaxies will not be discussed any more in this thesis. It is worth then to present here, briefly, their main spectral characteristics. In Fig. 1.7 we present a skecth of a radio-quiet AGN, indicating the different emitting regions, as well as the associated contribution in the visible-to-X-ray spectrum (taken fom Mushotzky et al. 1993). The obscuring torus, which plays a fundamental role in differentiating the observed visible spectrum between Seyfert 1 and 2 galaxies, hiddens as well the X-ray corona (responsible of the X-ray continuum emission), and the accretion disc.

However, the torus starts becoming transparent to X-rays above energies of the order of $\approx$ 5 keV: the observed spectrum is thus a Seyfert-1-like spectrum at hard X-rays (power-law emission plus Fe Kα line and Compton bump), while it is significantly absorbed in the soft X-ray part. However, the extrapolation of the hard-X-ray best-fit model at lower energies, shows evidence of a soft-X-ray excess. This excess is however completely different from the soft-excess observed in Seyfert 1 galaxies, and is explained (similar to the observation of broad-lines in the polarized optical spectra) as the X-ray primary continuum scattered to the line of sight.

The population of Seyfert 2 galaxies detected in X-rays is however not homogeneous, and their spectrum strongly depends on the amount of absorption present (see e.g. Cappi et al. 2006): we call Compton-thin the sources absorbed by column densities N_H lower than 10^{24} cm^{-2}, and Compton-thick the sources absorbed by column densities higher than this value. It is important to note that for heavily Compton-thick Seyfert galaxies, the direct emission can be absorbed up to several tens of keV: the observed spectrum below 10 keV is thus entirely due to reprocessed emission, resulting in a relatively flat spectrum. In this case it becomes difficult to correctly identify them as Compton-thick AGN, and, in this context, is fundamental the development of new and better detectors in the hard-X-ray domain (hundreds of keV), like *NuSTAR* (Harrison et al. 2010) and *Astro-H* (Takahashi et al. 2010), which will be operative in the near future.

Chapter 2

Suzaku broad-band observations of *Mrk 509* and *Mrk 841*

Contents

2.1 Introduction

In this Chapter we describe the analysis done on six different *Suzaku* observations taken between 2006 and 2007 on two well-known Seyfert 1 galaxies: *Markarian*[1] *509* (*Mrk 509*) and *Mrk 841*. In Section 2.2, we detail the data reduction of the *Suzaku* data and we present the serendipitous detection of the blazar *PKS 1502+106* (see Section 2.2.1). In Section 2.3.1, we study the light curves of *Mrk 509* and *Mrk 841*; in Section 2.3.2 and 2.3.4 we analyse and discuss the soft and hard X-ray excess; in Section 2.3.3, we concentrate on the Fe $K\alpha$ narrow emission line detection in *Mrk 841*. The Section 2.4 is devoted to the

---

[1] The Markarian catalog (see Markarian (1967) and following associated papers, or Mazzarella & Balzano (1986) for a review) has been composed as a sample of objects with blue excess and strong ultra-violet continuum, and contains mostly radio-quiet active galactic nuclei.

Table 2.1: Summary of the *Suzaku* observations on *Mrk 509* and *Mrk 841*. The columns report the observations IDs, the aim point used, the starting date and the effective exposure. For a discussion on the aim point, see Section 2.2.

Mrk 509				
	ID	Aim Point	Start	Exposure (s)
obs.1	701093010	HXD	2006-04-25	24580
obs.2	701093020	XIS	2006-10-14	25960
obs.3	701093030	XIS	2006-11-15	24450
obs.4	701093040	XIS	2006-11-27	33090
tot				108080

Mrk 841				
	ID	Aim Point	Start	Exposure (s)
obs.1	701084010	HXD	2007-01-22	51790
obs.2	701084020	HXD	2007-07-23	50930
tot				102720

broad-band modelling of the *Suzaku* spectra of *Mrk 509* and *Mrk 841*, while the discussion on the physical interpretation is presented in Section 2.5. The plots showing the broad-band fits of the spectra, and the table containing the physical parameters of the models can be found at the end of the Chapter. The work presented in this Chapter, in a shortened version, has appeared in 2011 in Astronomy and Astrophysics (Cerruti et al. 2011).

As discussed in Chapter 1.3.3, the current scenarios proposed to explain the soft-X-ray excess are three: a double Comptonisation (Section 2.4.1), a blurred reflection on the inner region of the accretion disc (Section 2.4.2), and a smeared absorption by a relativistic wind (Section 2.4.3). These different models are degenerate in the 0.5-10 keV band but still predict different amounts of hard X-ray emission. In addition, these models predict different variability behaviours in the soft and hard energy band and, thus, the measurement of the high energy flux may help us to disentangle them. To this aim, with *Suzaku* (which, among the current-generation X-ray telescopes, provides the best-resolution spectrum up to the highest energies) we observed *Mrk 509*, the brightest Seyfert 1 galaxy in the hard X-ray sky (17-60 keV), with an important soft excess but no strong warm absorber component (Sazonov et al. 2007), and *Mrk 841*, one of the first AGN in which a soft excess has been discovered (Arnaud et al. 1985). Information about the four *Mrk 509* observations and the two observations of *Mrk 841* are given in Table 2.1.

Located at a redshift of $z = 0.0344$ (Fisher et al. 1995), *Mrk 509* was first observed at X-ray energies with *Ariel V* (Cooke et al. 1978), and then studied with several X-ray telescopes. Using *HEAO-1* Singh et al. (1985) detected its soft excess for the first time, a detection that was later confirmed with *EXOSAT* (Morini et al. 1987), in addition to the detection of a Fe $K\alpha$ emission line. Using *Ginga* Singh et al. (1990) revealed a hardening of the power law at energies greater than 10 keV; *BeppoSAX* observations (Perola et al. 2000) suggested a power-law cut-off at 70 keV and revealed information about the warm absorber (Dadina et al. 2005), which since has been studied in depth by Smith et al. (2007) and Detmers et al. (2010), with *XMM-Newton/RGS* data. Ponti et al. (2009) presented the most complete study to date of the Fe K complex, using *XMM-Newton* data and the same *Suzaku* observations we present here. For

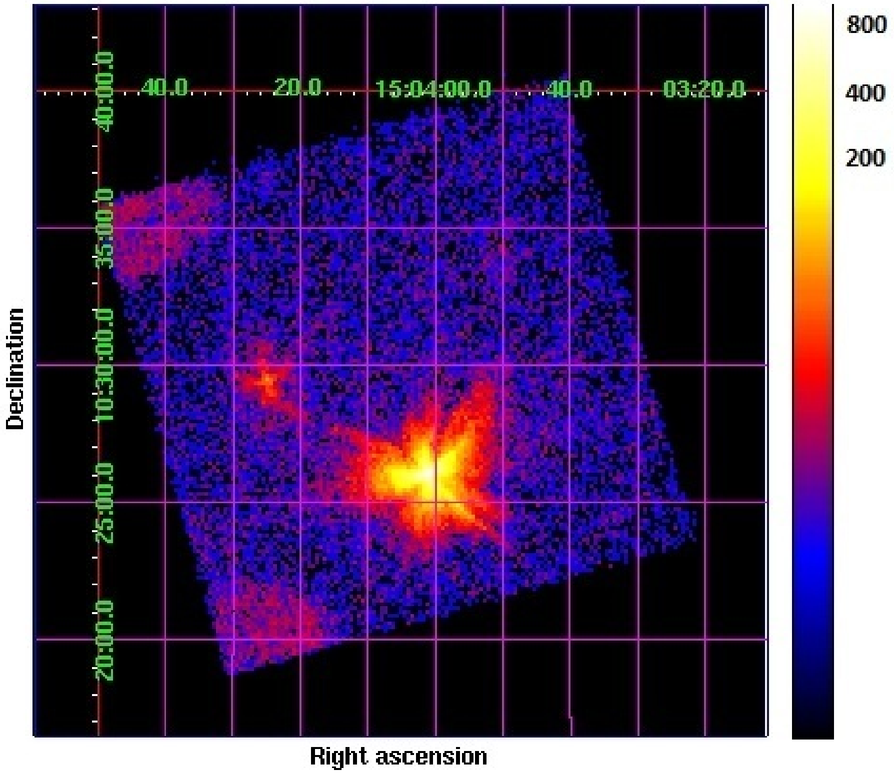

Figure 2.1: *Suzaku/XIS0* image of *Mrk 841* (first observation): the brightest source is *Mrk 841* and the fainter one is consistent with *PKS 1502+106*; the two calibration spots are visible in the top and bottom left corners.

this reason, for *Mrk 509* we study only the broad-band emission, and no further discussion of the Fe K complex is presented. Recently, Kaastra et al. (2011) carried out a multi-wavelength campaign of this source, using data from seven different satellites and observatories (from infra-red to hard X-rays, see Kaastra et al. (2011) and references therein).

The bright Seyfert 1 galaxy *Mrk 841* (z = 0.0365) has a soft excess that was first detected by *EXOSAT* (Arnaud et al. 1985). As for *Mrk 509*, *Mrk 841* has been extensively studied. George et al. (1993) provided the first evidence of Fe $K\alpha$ emission-line detection and broad-band variability. In a sample of 24 type 1 AGN bserved by *ASCA* (Reynolds 1997), *Mrk 841* belongs to sources for which a ”statistically significant soft excess” is observed. More recent observations were performed by *BeppoSAX* (Bianchi et al. 2001) and *XMM-Newton* (Petrucci et al. 2007; Longinotti et al. 2010). Petrucci et al. (2007) studied in detail Fe K complex variability, while Longinotti et al., using *XMM-Newton/RGS* data, investigated the warm absorber structure. Even though the goal of this project was to investigate the broad-band X-ray spectrum of this typical Seyfert 1 galaxies, in Section 2.3.3 we also discuss the Fe $K\alpha$ narrow emission-line detection, comparing our results with previous observations of the source.

2.2 Data reduction

The X-ray satellite *Suzaku*, which was used to perform these observations, is a joint *NASA/JAXA* project, and represent today the X-ray telescope wich covers the broadest energy-band, reaching several hundreds of keV. It is, thus, the most suitable telescope in order to study the high energy part of the Seyfert 1 galaxy spectrum, constraining the power-law emission coming from the hot corona.
It carries two main instruments: *XIS* (Koyama et al. 2007), a soft (0.2-12 keV) X-ray Imaging Spectrometer, and *HXD* (Takahashi et al. 2007), a Hard X-ray Detector that covers the higher energy domain (10-500 keV).

The *XIS* instrument is composed of four CCD cameras (it is thus an imaging detector, providing an X-ray image of the sky): three of them (*XIS0,2,3*) are front-illuminated (*FI*), while one (*XIS1*) is back-illuminated (*BI*). Owing to an instrumental failure, *XIS2* is unavailable for observations performed after November 9, 2006: for uniformity between observations, we did not consider data from this instrument. Event files from version 2.0.6.13 of the *Suzaku* pipeline processing were used, with standard screening criteria, and data were then reduced using version 6.7 of *HEASoft*[2]. Spectra and light curves were extracted using *XSelect*, version 2.4a. The chosen extracting region is large enough (r>150 arcsec) to avoid calibration problems (as suggested in the *Suzaku* ABC Guide [3]). The background was extracted from a region (circular for the observations taken with the *HXD* aim point, or annular for the observations taken with the *XIS* aim point[4]) in the same image, respecting the same geometrical constraints as for the source. Response matrices and ancillary response files were generated for each *XIS* using *xisrmfgen* (version 2009-02-28) and *xissimarfgen* (version 2009-01-08) tools. The two *FI* spectra were added using *mathpha* with the *'POISS-3'* error propagation method, which represents a mean value between the two extreme error values *'POISS-1'* and *'POISS-2'* (see *mathpha* user's guide [5] and references therein). Response files were added using *addrmf*, version 1.21, and *addarf*, version 1.2.6. A single *XIS* lightcurve was obtained by summing up the three *XIS0,1* and *3* background-subtracted lightcurves, using *XRonos*, version 5.22.

The *HXD* instrument is composed of two detectors: *PIN* (Positive Intrinsic Negative diodes; 10-60 keV) and *GSO/BGO* (Gadolinium Silicate/Bismuth Germanate crystals; 50-500 keV). In this paper, we present data from *PIN* only, since no significant signal was detected from *GSO*. For *HXD/PIN*, non-X-ray instrumental background (NXB) and response matrices provided by the *HXD* instrument team were used. An additional component for the CXB (cosmic X-ray background) (Boldt & Leiter 1987) was included and added to the NXB using *mathpha*, version 4.1.0. Spectra were corrected for dead time, using *hxddtcor*, version 1.50, and the background exposure time was increased by a factor of ten, following the *Suzaku* ABC Guide. For *Mrk 841* observations, *PKS 1502+106* (see section 2.1) is in the *PIN* field of view, and its flux, as extrapolated from *XIS* observations, was added with *mathpha* to the background.

Each spectrum was rebinned according to the following procedure [6]: for *Suzaku/XIS* we checked the true energy resolution of each instrument, extracting the spectrum of the calibration spots in the CCD

---

[2] `http://heasarc.nasa.gov/lheasoft`

[3] `http://heasarc.gsfc.nasa.gov/docs/suzaku/analysis/abc/`

[4] If the observation is taken with the *XIS* aim point, the source is centered at the center of the *XIS* detector, while if the observation is taken with the *HXD* aim point, the source would be shifted with respect to the *XIS* image center

[5] `http://heasarc.gsfc.nasa.gov/docs/heasarc/caldb/docs/memos/ogip95008/ogip95008.pdf`

[6] We thank Matteo Guainazzi for having provided the script used in this data analysis (the original script has been modified in order to be used for the *Suzaku* data format and energy resolution values). A public version of this script, for *XMM-Newton* data, is currently available in the *SAS* data-analysis software (*specgroup* command).

camera (see Fig. 2.1), and measuring the energy and the FWHM (full width at half maximum) of the Mn $K\alpha$ line; with these values, and using equation (1) given in Koyama et al. (2007), we get the true *XIS* energy resolution as a function of energy; for *PIN*, we used energy resolution values given in Takahashi et al. (2007); we then rebinned the data to have five bins for each energy resolution element. To use a χ^2 minimization algorithm, we imposed a minimum number of counts per bin: this second rebinning affects the first and the last bins of the spectra only, while in the other channels the condition of five bins per resolution element is always dominant. We chose a minimum of 30 (for *Mrk 841*) and 50 (for *Mrk 509*) counts per bin, leading to a similar number of bins for both sources. We considered *XIS/FI* data in the energy band 0.6-10 keV, and *XIS1* data in the range 0.5-8.5 keV; *XIS* data comprised between 1.62 and 1.82 keV were ignored owing to a known calibration problem around the Si K edge[7]; *PIN* data below 15 keV were ignored, and the last *PIN* significant bin is at $\approx$ 33 keV for *Mrk 841* and $\approx$ 38 keV for *Mrk 509*.

We also studied the summed spectra of the sources, adding *XIS* and *PIN* data from different observations. For *Mrk 509*, the first observation was not included in the summed spectrum, because it was performed with an aim point different than the others. Source and background spectral files from different observations were added using the same procedure described above for the sum of *XIS/FI* spectra.
To take into account the relative normalization between different instruments during the fitting, models for each instrument data were multiplied by a constant, as indicated by Maeda et al. (2008) [8]. More precisely, the value of this constant was left free to vary in the allowed range ($\pm 1\sigma$) determined by Maeda et al. (2008). Spectral fitting was performed with *XSpec*, version 12.5.1. Parameter errors in both text and tables are given at the 90% confidence level. We assume a flat cosmology (required for the conversion of flux in luminosity) with $H_0 = 70$ km s^{-1}Mpc^{-1} and $\Omega_\Lambda = 0.73$.

2.2.1 Contaminating source: *PKS 1502+106*

Figure 2.1 shows the *Suzaku/XIS0* image of the first observation of *Mrk 841*. The brightest source at the *HXD* aim point position is *Mrk 841*, while a second bright source appears in the field of view (at a distance of about 7′ from *Mrk 841*), that is coincident with *PKS 1502+106*. This source, situated at $z = 1.839$ (Smith et al. 1977), was recently classified as a blazar by Abdo et al. (2010c).
We extracted the spectrum of this source following the same procedure discussed in the previous section: Fig. 2.2 shows the *XIS* spectrum of PKS 1502+106. We fitted the spectrum with a simple power law absorbed by galactic material (model *wabs*powerlaw* in *Xspec*, with $N_H = 2.36 \cdot 10^{20}$ cm^{-2}, Dickey & Lockman (1990)). The best-fit photon index is $\Gamma = 1.32 \pm 0.08$ ($\tilde{\chi}^2 = \chi^2/$ (degrees of freedom (DOF))=71/86). The source (absorbed) flux in the 0.5-2 keV and 2-10 keV bands is $2.2^{+0.3}_{-0.3}$ and $7.5^{+0.6}_{-0.7} \cdot 10^{-13}$ergs cm^{-2} s^{-1}, respectively. The 2-10 keV luminosity is $1.8^{+0.2}_{-0.1} \cdot 10^{46}$ergs s^{-1}. In the past, PKS 1502+106 was observed to have a photon index Γ varying between 1.4 and 1.9 and a 2-10 keV flux in the range $4.9 - 6.54 \cdot 10^{-13}$ergs cm^{-2} s^{-1} (George et al. 1994; Akiyama et al. 2003; Watanabe et al. 2004). An outburst was observed by Fermi and Swift (Abdo et al. 2010c), with $F_{0.3-10keV} = 2.18 \cdot 10^{-12}$ergs cm^{-2} s^{-1}, and $\Gamma = 1.54$. The *Suzaku* observation detected PKS 1502+106 during quite a high state, but not during an outburst (its light curve does not show any significant variability). However, the power-law index is consistent with a low state of the source.

This source falls within the field of view of the *PIN* instrument, which, as a non-imaging detector,

---

[7] `http://heasarc.nasa.gov/docs/suzaku/analysis/sical.html`

[8] `http://www.astro.isas.ac.jp/suzaku/doc/suzakumemo/suzakumemo-2008-06.pdf`

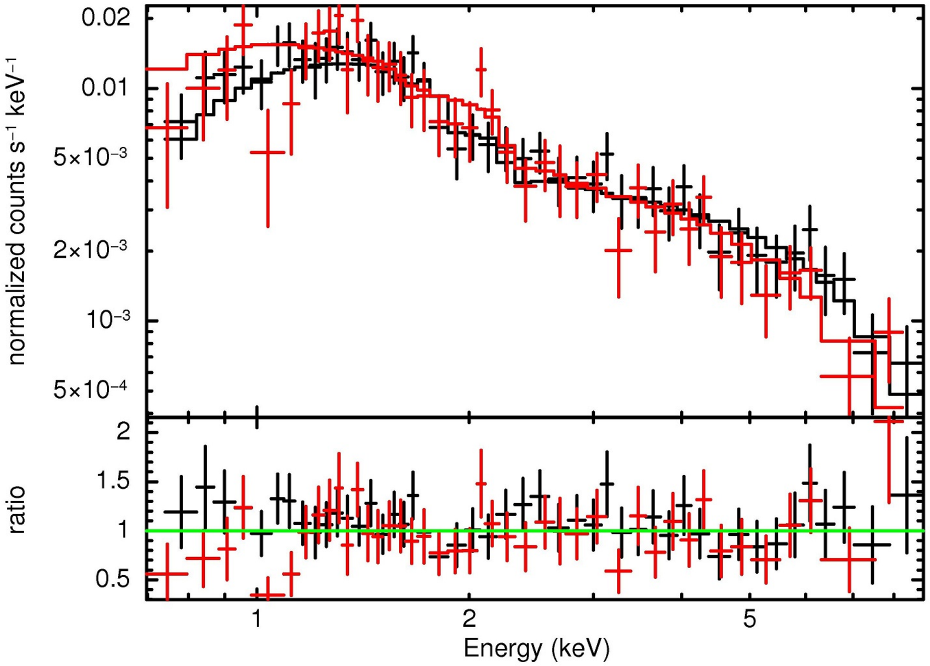

Figure 2.2: *PKS 1502+106* spectrum (observer frame) as seen by *Suzaku/XIS/FI* (black) and *XIS1* (red). Data were fitted with a power-law model absorbed by galactic material (see section 2.1): data-to-model ratio is shown in the bottom plot.

would measure the photons from *PKS 1502+106* together with the ones from *Mrk 841*. The extrapolated flux in the 12-60 keV band is $2.5 \cdot 10^{-12}$ergs cm^{-2} s^{-1}. This component was included in the *PIN* background.
During the second observation, PKS 1502+106 falls off the CCD image of *Mrk 841*, but it remains in the *PIN* field of view: we subtracted from *PIN* data the same spectrum evaluated for the first observation.
No bright X-ray sources are observed in the *XIS* field of view of *Mrk 509*.

2.3 Data analysis

2.3.1 Light Curves

XIS light curves of *Mrk 509* and *Mrk 841* are shown in Fig. 2.3. Due to the *Suzaku* orbit, the targets, periodically occulted by Earth, cannot be observed continuously and light curves are composed by several blocks of a few kiloseconds each. As no significant variability appears at this time scale, we decided to rebin the data to one bin per observation window. Light curves were extracted in two energy bands, a soft (0.5-3 keV) one and a hard (3-10 keV) one, and a count-rate hardness ratio ($h = hard/soft$) was evaluated. *PIN* light curves are always compatible with a constant flux.

During the first observation of *Mrk 509*, the source was in the *HXD* aim point, which provides a lower ($\approx 10\%$) effective area and a lower number of counts per second than for the *XIS* aim point (which was used for the three other observations). For this reason, the lightcurve of obs.1 has to be corrected for this systematic error when compared to the other observations. Taking into account this effect, *Mrk 509*

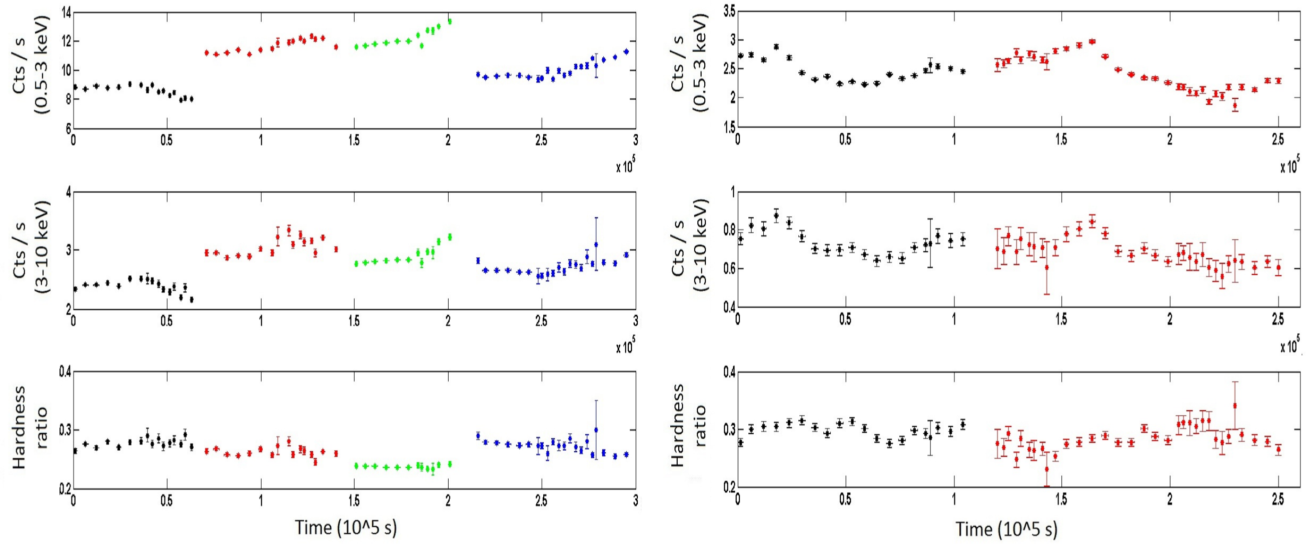

Figure 2.3: *Mrk 509* (left) and *Mrk 841* (right) light curves. Different observations are shown in different colours (one-black, two-red, three-green and four-blue). From top to bottom: 0.5-3 keV light curve (in units of counts per second); 3-10 keV light curve and hardness ratio (3-10/0.5-3). Gap between observations is arbitrary (see Table 2.1).

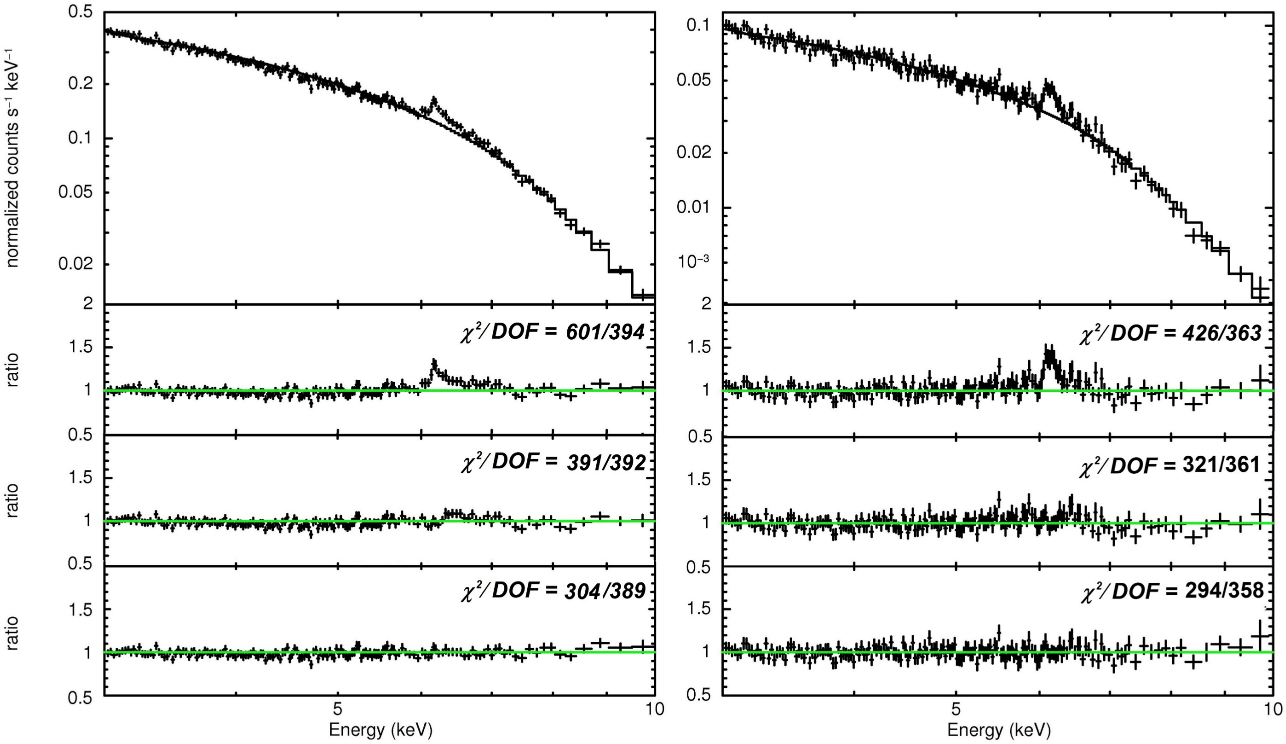

Figure 2.4: *XIS* data between 3 and 10 keV of the sum of *Mrk 509* (left) and *Mrk 841* (right) observations : data are first fitted with a power law (ignoring the 6-7 keV energy band, upper panel and first ratio plot); then two narrow gaussian lines (for the Fe $K\alpha$ and $K\beta$ emission lines, see section 3.2) are added to the fit (second ratio plot); a broad ($\sigma > 0$) Fe emission line is finally considered (third and last ratio plot). Only *FI* data are shown, as they have the best resolution around the Fe $K\alpha$ emission line, but the fit was performed using both *FI* and *XIS1* data. The energy on the abscissa is in the observer frame. The data were rebinned for clarity purposes.

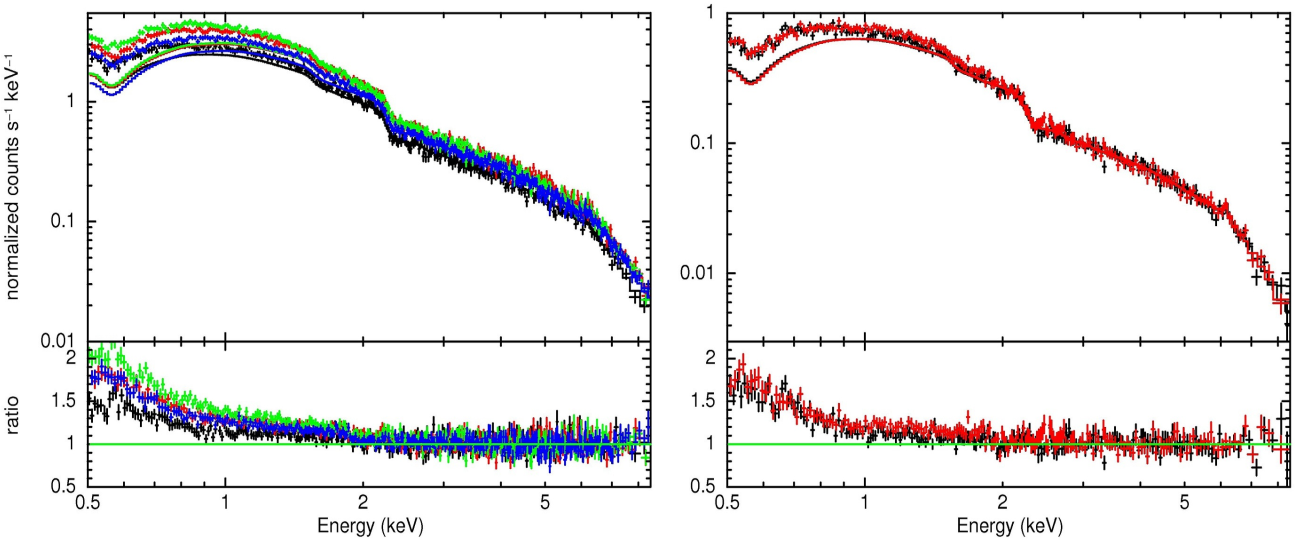

Figure 2.5: *Mrk 509* (left) and *Mrk 841* (right) soft excess: data from 3 to 10 keV are fitted with a power law plus three gaussian emission lines (see Table 2.2), and the model is then extrapolated to lower energies. Galactic absorption is taken into account. Only *XIS1* data are shown, as they extend down to 0.5 keV, but the analysis was performed using both *FI* and *XIS1* data; the colour code for the different observations is as in Fig. 2.3. The energy on the abscissa is in the observer frame. The data were rebinned for clarity purposes.

presents a variability[9] of $\approx 25\%$ between the four observations in the soft energy band, but within a single observation the flux variation is only 11-14%, reaching 20% only during the last observation. In the hard energy domain, the variability is $\approx 16\%$ between observations and $\approx 15\%$ (but 20% during the fourth observation) on 10^5s timescale.

The value of the hardness ratio during obs. 1, 2 and 4 is compatible with a constant (the mean values are $h = 0.27^{+0.01}_{-0.01}$, $0.26^{+0.01}_{-0.01}$ and $0.27^{+0.01}_{-0.01}$, respectively). During the third observation h has instead a lower value ($0.24^{+0.01}_{-0.01}$). Miyazawa et al. (2009) analysed the temporal and spectral variability of a sample of 36 AGN observed by *Suzaku*. The four observations of *Mrk 509* we present here, are part of this sample, and they found a correlation between the fluxes in the soft and the hard energy band, consistent with the nearly constancy of the hardness ratio, though the lower value of h during the third observation increases the dispersion in the correlation plot.

The two *Mrk 841* observations have an almost equal mean flux value, but the source shows variability on time scale of 10^5s (26 and 46% in the soft X-ray domain, and 32 and 42% in the hard X-ray domain, for the two observations respectively). For this source, too, the hardness ratio is nearly constant, and we measure a mean value of $h = 0.29^{+0.02}_{-0.02}$.

Given the low variability observed in *Mrk 509* and *Mrk 841* light curves, and in order to improve the signal-to-noise ratio, in the following we study the summed spectra as well as individual observations for phenomenological models.

---

[9] Defined as the greatest fluctuation (*Max-min*) divided by the mean value.

Table 2.2: Best fit parameter values for the model *powerlaw* + *zgauss* + *zgauss* + *zgauss*, considering *XIS* data between 3 and 10 keV. The three gaussian functions model the Fe $K\alpha$ and $K\beta$ narrow emission lines (with $\sigma = 0$) and the broad Fe K emission line. Fe $K\beta$ emission line was frozen in energy ($E_{K\beta} = 7.06$ keV) and in normalization (imposed equal to 0.15 times the $K\alpha$ line normalization). Γ is the power law photon index; the power law normalization C_Γ is the number of photons keV^{-1} cm^{-2} s^{-1} at 1 keV; the line normalization parameters $C_{K\alpha}$ and C_{br} are the integrated number of photons cm^{-2} s^{-1} in the line; σ_{br} is the line width expressed in keV; EqW is the line equivalent width expressed in eV; the flux F, evaluated between 3 and 10 keV, is given in units of ergs cm^{-2} s^{-1}. For the summed spectra, the results of a *XIS* (above 3 keV) + *PIN* fit are reported as well (last line): the R_{pexrav} parameter represents the *pexrav* reflection scaling factor (see Section 3.3).

Mrk 509												
Obs.	Γ	C_Γ (10^{-3})	$E_{K\alpha}$ (keV)	$C_{K\alpha}$ (10^{-5})	$EqW_{K\alpha}$ (eV)	E_{br} (keV)	C_{br} (10^{-5})	σ_{br} (keV)	EqW_{br} (eV)	R_{pexrav}	F (10^{-11})	χ^2/DOF
1	$1.80^{+0.05}_{-0.04}$	$12.5^{+0.8}_{-0.6}$	$6.42^{+0.09}_{-0.09}$	$0.9^{+0.9}_{-0.8}$	16^{+18}_{-15}	$6.44^{+0.17}_{-0.16}$	$6.2^{+3.6}_{-2.7}$	$0.44^{+0.28}_{-0.17}$	126^{+79}_{-78}		$3.45^{+0.02}_{-0.03}$	329/386
2	$1.79^{+0.04}_{-0.03}$	$13.4^{+0.2}_{-0.3}$	$6.47^{+0.06}_{-0.06}$	$1.6^{+0.8}_{-0.7}$	28^{+19}_{-18}	$6.51^{+0.17}_{-0.18}$	$4.6^{+3.0}_{-2.2}$	$0.41^{+0.30}_{-0.18}$	86^{+50}_{-61}		$3.78^{+0.02}_{-0.02}$	375/366
3	$1.86^{+0.05}_{-0.04}$	$14.4^{+0.4}_{-0.7}$	$6.41^{+0.05}_{-0.05}$	$1.7^{+0.9}_{-0.8}$	30^{+19}_{-17}	$6.55^{+0.25}_{-0.14}$	$5.7^{+1.8}_{-1.8}$	$0.44^{+0.29}_{-0.14}$	112^{+43}_{-45}		$3.60^{+0.03}_{-0.02}$	344/352
4	$1.80^{+0.04}_{-0.03}$	$12.1^{+0.7}_{-0.6}$	$6.42^{+0.03}_{-0.03}$	$1.8^{+0.7}_{-0.7}$	35^{+15}_{-15}	$6.71^{+0.21}_{-0.14}$	$6.7^{+3.2}_{-2.4}$	$0.52^{+0.25}_{-0.20}$	145^{+75}_{-65}		$3.39^{+0.02}_{-0.02}$	396/378
2+3+4	$1.84^{+0.03}_{-0.02}$	$13.5^{+0.5}_{-0.4}$	$6.43^{+0.03}_{-0.03}$	$1.7^{+0.4}_{-0.5}$	31^{+6}_{-6}	$6.63^{+0.11}_{-0.09}$	$6.6^{+2.2}_{-1.7}$	$0.50^{+0.17}_{-0.12}$	135^{+48}_{-45}		$3.50^{+0.01}_{-0.02}$	304/389
+*PIN*	$1.88^{+0.05}_{-0.05}$	$14.0^{+0.6}_{-0.8}$	$6.43^{+0.03}_{-0.03}$	$1.7^{+0.5}_{-0.5}$	33^{+9}_{-14}	$6.69^{+0.16}_{-0.13}$	$6.1^{+3.8}_{-1.4}$	$0.56^{+0.34}_{-0.17}$	126^{+29}_{-67}	$0.4^{+0.2}_{-0.2}$	$3.50^{+0.02}_{-0.02}$	319/405

Mrk 841												
Obs.	Γ	C_Γ (10^{-3})	$E_{K\alpha}$ (keV)	$C_{K\alpha}$ (10^{-5})	$EqW_{K\alpha}$ (eV)	E_{br} (keV)	C_{br} (10^{-5})	σ_{br} (keV)	EqW_{br} (eV)	R_{pexrav}	F (10^{-11})	χ^2/DOF
1	$1.77^{+0.08}_{-0.05}$	$3.77^{+0.20}_{-0.19}$	$6.39^{+0.02}_{-0.03}$	$1.0^{+0.3}_{-0.3}$	58^{+26}_{-22}	$6.03^{+0.36}_{-0.31}$	$2.7^{+2.7}_{-0.9}$	$0.74^{+0.32}_{-0.31}$	156^{+105}_{-119}		$1.10^{+0.03}_{-0.03}$	303/341
2	$1.75^{+0.06}_{-0.05}$	$3.66^{+0.10}_{-0.25}$	$6.38^{+0.04}_{-0.04}$	$0.7^{+0.3}_{-0.4}$	39^{+32}_{-26}	$6.26^{+0.18}_{-0.17}$	$2.3^{+1.1}_{-0.9}$	$0.40^{+0.22}_{-0.16}$	131^{+87}_{-80}		$1.11^{+0.03}_{-0.03}$	259/323
1+2	$1.77^{+0.05}_{-0.04}$	$3.80^{+0.08}_{-0.21}$	$6.38^{+0.02}_{-0.02}$	$0.9^{+0.2}_{-0.2}$	50^{+19}_{-17}	$6.22^{+0.16}_{-0.19}$	$2.7^{+0.9}_{-0.7}$	$0.54^{+0.27}_{-0.15}$	150^{+66}_{-64}		$1.11^{+0.03}_{-0.03}$	294/358
+*PIN*	$1.88^{+0.10}_{-0.05}$	$4.18^{+0.60}_{-0.16}$	$6.37^{+0.03}_{-0.01}$	$0.9^{+0.2}_{-0.2}$	44^{+17}_{-18}	$6.14^{+0.24}_{-0.31}$	$1.6^{+1.6}_{-0.9}$	$0.54^{+0.35}_{-0.23}$	< 158	$1.3^{+0.8}_{-0.3}$	$1.11^{+0.03}_{-0.03}$	295/374

2.3.2 Soft Excess

We start the analysis considering the *XIS* 3-10 keV energy band. We model the data using a power law plus two narrow gaussian functions (model *zgauss* in *XSpec*, assuming $\sigma = 0$) for the Fe Kα and Kβ narrow emission lines (assuming $E_{K\beta} = 7.06$ keV and imposing its normalization factor $C_{K\beta}$ equal to 0.15 $C_{K\alpha}$ (Palmeri et al. 2003)). An excess of emission is clearly observed around 6.4 keV (see Fig. 2.4) and adding a broad emission line significantly improves the fit (F-test probability equal to $4 \cdot 10^{-21}$ and $7 \cdot 10^{-7}$ for the summed *Mrk 509* and *Mrk 841* data set, respectively). Table 2.2 shows the best fit results. The detection of a Fe broad emission line in *Suzaku* observations is consistent with the results shown in the FERO (Finding Extreme Relativistic Objects) survey (de La Calle Pérez et al. 2010), which studied, using *XMM-Newton* data, the relativistic Fe Kα emission lines in Seyfert 1 galaxies, including *Mrk 509*. Ponti et al. (2009) studied in detail the Fe K complex in *Mrk 509*, using the same *Suzaku* observations presented here: in particular, they showed that a broad Fe line (with parameters consistent with our values given in Table 2) represents the best-fitting model, compared to a possible blend of narrow Fe lines.
For *Mrk 841*, we tested as well the possibility that a blending of H-like and He-like lines of Fe can be responsible of the broad line observed : however, this model (two narrow gaussian lines, with energies fixed to 6.67 and 6.97 keV, plus the 6.4 and 7.06 Fe lines, as described above), does not improve significantly the goodness of the fit (F-test probability equal to 0.1 for the summed data-set).

Mrk 509 shows variability in the 3-10 keV flux (it is comprised between 3.39 and $3.78 \cdot 10^{-11}$ ergs cm^{-2} s^{-1}), while the slope is consistent, within errors, with a constant (the two extreme values are $1.79^{+0.04}_{-0.03}$ and $1.86^{+0.05}_{-0.04}$ for the second and the third observation, respectively); *Mrk 841* observations are quite similar (Γ = 1.75-1.77 and F = 1.10-1.11 $\cdot 10^{-11}$ ergs cm^{-2} s^{-1}), as discussed in the previous section.

It is useful to compare these results to past observations. *BeppoSAX* (De Rosa et al. 2004) detected *Mrk 509* in two quite different states, at $F_{2-10\ keV}$ = 2.7 and 5.7 $\cdot 10^{-11}$ ergs cm^{-2} s^{-1} with Γ = 1.80-1.59 respectively (for comparison the 2-10 keV flux of *Mrk 509* during the four *Suzaku* observations varies between 4.3 and 4.8 $\cdot 10^{-11}$ ergs cm^{-2} s^{-1}, setting these observations in an intermediate state); *XMM-Newton* (Smith et al. 2007) observed the source in a even lower state at $F_{0.5-10\ keV} = 2.6 \cdot 10^{-11}$ ergs cm^{-2} s^{-1}. *Mrk 841* was observed by *XMM-Newton* (see Petrucci et al. 2007) at $F_{3-10\ keV}$ = 0.8-1.3 $\cdot 10^{-11}$ergs cm^{-2} s^{-1} with Γ = 1.30-1.95. Compared to these values, the source was in an intermediate state during *Suzaku* observations; in the past *Mrk 841* was seen in a quite low state by Pounds et al. (1994) (simultaneous *Ginga* and *ROSAT* observations) with $F_{2-10\ keV} = 7.9 \cdot 10^{-12}$ ergs cm^{-2} s^{-1}.

Extrapolating the power law fit between 3 and 10 keV to low energies, an excess of photons is observed: in Fig. 2.5 we report *XIS1* spectra for *Mrk 509* and *Mrk 841*, and for each observation; the bottom panel shows the data-to-model ratio. The galactic absorption was taken into account following Dickey & Lockman (1990), using $N_H = 4.11 \cdot 10^{20}$cm^{-2} for *Mrk 509* and $N_H = 2.34 \cdot 10^{20}$cm^{-2} for *Mrk 841*. The soft excess shape is remarkably similar for the two Seyfert galaxies, and for *Mrk 509* a spectral variability is observed at low energies.

As a first qualitative study, we model the 0.5-10 keV spectrum with a broken power law (plus three gaussian emission lines, with parameters fixed as in Table 2.2, and galactic absorption, fixed at values given above) in order to evaluate soft excess slope (Γ_s) and energy break E_b. As shown in Table 2.3, this model does not give a good fit to our data : the soft spectrum between 0.5 and 3 keV shows clear signature of curvature and cannot be described by a power law.

Table 2.3: Best fit parameter values for the broken power law model. *XIS/FI* data between 0.6 and 10 keV and *XIS1* data between 0.5 and 8.5 keV were considered. The power law normalization C_h is the number of photons keV^{-1} cm^{-2} s^{-1} at 1 keV.

Mrk 509					
Obs.	Γ_s	E_b (keV)	Γ_h	$C_h(10^{-3})$	χ^2/DOF
1	$2.24^{+0.08}_{-0.05}$	$1.02^{+0.07}_{-0.09}$	$1.87^{+0.01}_{-0.01}$	$13.8^{+0.2}_{-0.4}$	743/726
2	$2.16^{+0.02}_{-0.02}$	$1.83^{+0.09}_{-0.08}$	$1.86^{+0.01}_{-0.01}$	$18.0^{+0.1}_{-0.1}$	849/677
3	$2.29^{+0.01}_{-0.01}$	$1.74^{+0.06}_{-0.07}$	$1.93^{+0.01}_{-0.01}$	$19.3^{+0.1}_{-0.1}$	902/652
4	$2.12^{+0.01}_{-0.01}$	$1.96^{+0.09}_{-0.10}$	$1.84^{+0.01}_{-0.01}$	$15.6^{+0.1}_{-0.1}$	936/689
2+3+4	$2.19^{+0.01}_{-0.01}$	$1.77^{+0.04}_{-0.04}$	$1.89^{+0.01}_{-0.01}$	$17.3^{+0.1}_{-0.1}$	1248/721

Mrk 841					
Obs.	Γ_s	E_b (keV)	Γ_h	$C_h(10^{-3})$	χ^2/DOF
1	$2.44^{+0.06}_{-0.08}$	$1.02^{+0.06}_{-0.04}$	$1.82^{+0.01}_{-0.01}$	$4.09^{+0.07}_{-0.07}$	686/651
2	$2.40^{+0.09}_{-0.08}$	$0.96^{+0.06}_{-0.04}$	$1.87^{+0.01}_{-0.01}$	$4.21^{+0.12}_{-0.13}$	604/613
1+2	$2.44^{+0.06}_{-0.06}$	$1.00^{+0.04}_{-0.03}$	$1.85^{+0.01}_{-0.01}$	$4.18^{+0.08}_{-0.08}$	804/694

2.3.3 Fe Kα emission line in *Mrk 841*

We present here the analysis of the Fe $K\alpha$ emission line in *Mrk 841*. Ponti et al. (2009) already presented a thorough study of the iron K complex in *Mrk 509*.

A narrow ($\sigma = 0$) Fe $K\alpha$ emission line was observed in past *Mrk 841* observations, and, in particular, Petrucci et al. (2007) claimed that this narrow component is roughly constant in time, in agreement with a remote reflection scenario. We tested this hypothesis fitting the 3-10 keV *XIS* data with a power law plus a *narrow* Gaussian emission line, with σ fixed to zero, as done by Petrucci et al. (2007). In Fig. 2.6 we report the contour plots of line flux versus line energy, for the two *Suzaku* observations, and we compare them to Petrucci et al. (2007) results (*XMM/Newton*, observations from 2001 to 2005). The line flux is in agreement with what had been found by Petrucci et al. (2007), and no variability is observed. Line energy, in the source frame, is consistent with iron $K\alpha$ for both observations.

2.3.4 Hard Excess

Extrapolating the 3-10 keV best fit power law to high energies, considering *PIN* data, a hard excess appears as well (see Figure 2.7). This feature is well explained by introducing a distant reflection by cold material, which accounts at the same time for the Fe $K\alpha$ narrow emission line and the high energy bump (see Chapter 1). In order to quantify the amount of reflected emission required, we fitted the summed *PIN* and *XIS* (above 3 keV) data with a power law (plus three gaussian lines, as described in the previous section) plus *pexrav* (Magdziarz & Zdziarski 1995), a model which describes reflection from neutral material. *Pexrav* free parameters are the reflection scaling factor R_{pexrav} (which is equal to 1 for a source isotropically illuminating the disc); the illuminating power law high energy cut-off E_c (frozen at 100 keV, given the fact that it is not detected in the *Suzaku* data up to $E \approx$ 30-40 keV; see also Section 1.3.1); the abundances (fixed equal to solar values) and the disc inclination angle ϑ (frozen at 30 degrees). For the summed spectra we obtain $R_{pexrav} = 0.4^{+0.2}_{-0.2}$ and $1.3^{+0.8}_{-0.3}$ for Mrk 509 and Mrk 841, respectively. Adding the neutral reflection component slightly modifies the best fit parameters of the broad Fe emission line,

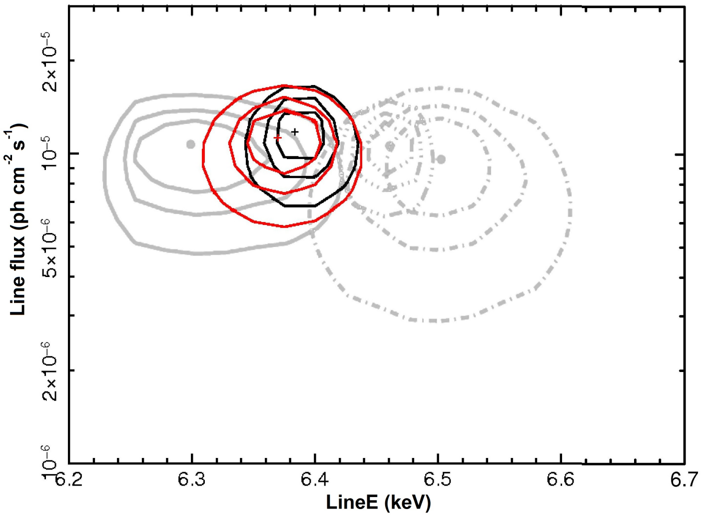

Figure 2.6: Contour plots (in black for obs.1, and in red for obs.2) of line-flux versus line-energy (source frame) for the narrow emission Gaussian line in *Mrk 841*. The three confidence levels are for 68, 90 and 99%, respectively. In grey are superimposed the contour plots of 2001-2005 *XMM/Newton* observations (see Petrucci et al. 2007, , Fig. 9)

.

in particular its equivalent width. Best fit parameters are given in Table 2.2.
Pexrav has the advantage that it gives directly the information about the reflected fraction R_{pexrav}, but it does not evaluate the narrow Fe $K\alpha$ emission line produced. We then decided to use *reflext*, a modified (and not public) version of the *reflion* model (an older version of *reflionx* (Ross et al. 1999; Ross & Fabian 2005); see section 3.6). Unlike the *reflion*, in which the ionisation parameter ξ is comprised between 10 and 10^4 erg cm s^{-1}, in *reflext* the ξ parameter space was extended as low as 1 erg cm s^{-1}. Using *reflext* the evaluation of the reflected fraction is less accessible, but the Fe $K\alpha$ narrow emission line and the high energy bump are intrinsically tied.

In the following we add *reflext* with parameters $Fe/Fe_{\odot} = 1$, $\Gamma_{reflext} = \Gamma$ and $\xi = 1$ erg cm s^{-1}. Its normalization parameter $C_{reflext}$ was frozen such that the flux of the model in the narrow Fe $K\alpha$ emission line reproduces the observed line flux. As the intensity of the reflected emission depends on the slope of the illuminating continuum, we evaluated the value of $C_{reflext}$ which reproduces the observed line flux as a function of Γ; we fitted the result with a polynomial function, and we fixed the *reflext* normalization as a function of Γ.

The fitted relation between $C_{reflext}$ and Γ required to explain the narrow Fe Kα line via the *reflext* model is:

$$C_{reflext} = 0.001122 - 0.0007476\,\Gamma - 0.0001564\,\Gamma^2 + 0.0001410\,\Gamma^3 \tag{2.1}$$

for the summed spectra of *Mrk 509*, and

$$C_{reflext} = -0.004432 + 0.007333\,\Gamma - 0.004045\,\Gamma^2 + 0.0007567\,\Gamma^3 \tag{2.2}$$

for the summed spectra of *Mrk 841*.
These equations are used directly in *Xspec*, which can handle any analytical relation between different parameters.

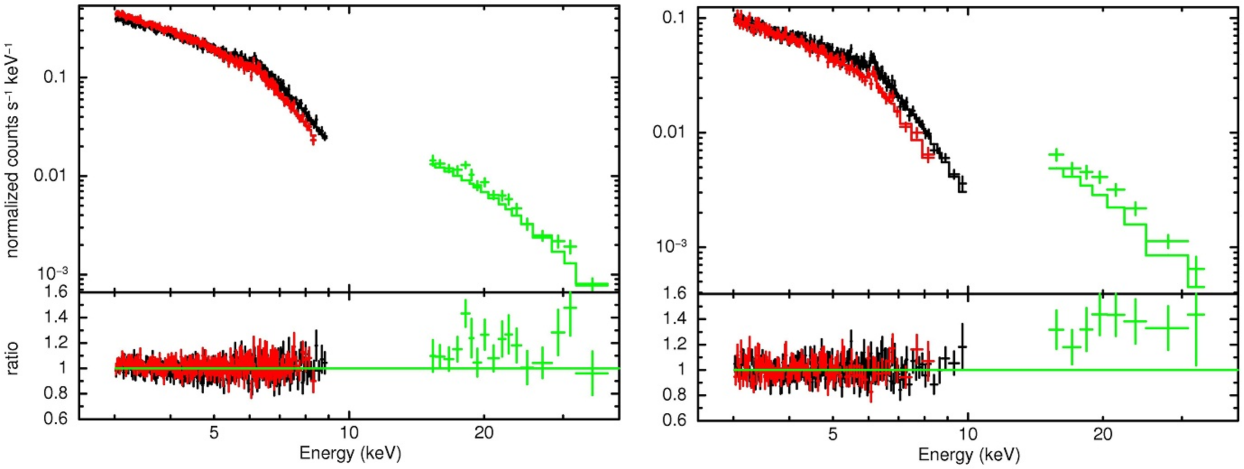

Figure 2.7: *Left:* hard X-ray excess of *Mrk 509*. *Right:* hard X-ray excess of *Mrk 841*. The fit is performed in the 3-10 keV energy range (see Table 2.2), and then extrapolated to higher energies, including the *PIN* data.

2.4 Modelling of the broad-band spectrum

In the following we concentrate on the broad-band (0.5-30 keV) spectral fitting of *Mrk 509* and *Mrk 841* data with three different physical models : a double Comptonisation, a blurred reflection and a smeared absorption. As only weak flux variability is observed between individual *Mrk 509* observations, and as no significant variability is observed between individual *Mrk 841* observations, we perform and discuss the broad-band spectral analysis for the summed spectra only (unless explicitly mentioned).

2.4.1 Double Comptonisation model

In the standard disc-corona scenario (Haardt & Maraschi 1993, , see also Chapter 1), the power law high energy emission is explained as a Comptonisation of thermal photons emitted by the black hole accretion disc. Electrons producing this inverse Compton effect have temperature $kT_e \approx 100$ keV and low optical depth, $\tau \approx 1$. One possibility to easily explain the soft excess is that there is a second warm Comptonisation region, with lower temperature and higher optical depth, which modifies the black-body emission from the accretion disc, scattering UV photons up to soft X-ray energies. A physical interpretation of this ”second corona” can be a warm skin on the disc surface (Janiuk et al. 2001), or a transition region between an outer disc and an optically thin inner flow (Magdziarz et al. 1998).

We used *NTHComp* (Życki et al. 1999), part of *XSpec* models, to simulate Comptonised spectra: this model solves the Kompaneets equation, and the output spectrum is parametrtised by the electron temperature kT_e and the spectral index Γ; seed photons come from an accretion disc spectrum, parametrised by kT_{disc}, the temperature at the inner radius. The electron temperature of the corona producing the high energy emission (subscript h), kT_h, can be constrained only via the high energy cutoff: as we do not observe it in our data, we fixed it at 100 keV. For the soft Comptonisation region (subscript s), we cannot fit at the same time Γ_s and kT_s, and, following Gierliński & Done (2004), we fixed $\Gamma_s = 2$.
The exact value of kT_{disc} does not affect the fit as long as it is lower than our energy domain: we chose $kT_{disc} = 45$ eV. We added *reflext* to our model to describe the reflection from distant material, with normalization parameter frozen as described above, plus two gaussian functions for the Fe $K\beta$[10] and the Fe

---

[10] The Fe Kα line is consistently modelled by the *reflext* model, as discussed in Section 2.3.4

K_{broad} emission lines, as in Table 2.2 (for the *XIS* + *PIN* fit). Best fit results are given in Table 2.4.

The double Comptonisation model was studied in detail by Gierliński & Done (2004): they fitted a sample of 26 AGN showing that the cold Comptonisation region has a remarkably constant temperature $< kT_s >= 0.12$ keV with $\sigma = 0.02$ keV, despite large variations in black hole mass and AGN luminosity. The model they used was *NTHComp*, too. The values we found for *Mrk 509* and *Mrk 841* during Suzaku observations are in agreement with their results. We remind here that the exact value of kT_s depends on the assumption done for Γ_s: the only physical parameter which can be constrained (when the high energy cut-off is not observed) is the Comptonisation parameter y, defined as $4kT/(mc^2) \cdot Max(\tau, \tau^2)$, where τ is the plasma optical depth. The Γ parameter represents the asymptotic power law function which describes the Comptonised spectrum, and can be expressed as

$$\left(2.25 + \frac{4}{y}\right)^{0.5} - 0.5 \tag{2.3}$$

which is equal to 2 for $y = 1$. The most important result obtained by Gierliński & Done (2004) is not the exact value of kT_s, but its constancy in AGN samples.

Following Gierliński & Done (2004), we evaluated the soft excess strength, R_{GD}, defined as the ratio of the unabsorbed 0.3-2 keV flux in the cool and hot Comptonised components: it is equal to $0.23^{+0.04}_{-0.05}$ for *Mrk 509* and $0.28^{+0.08}_{-0.04}$ for *Mrk 841*, setting our sources in the lowest part of the Gierliński & Done (2004) sample.

Additional contribution of the warm absorber

Considering the χ^2 values, the double Comptonisation model does not provide a good fit to data. In fact, for both sources, the presence of a warm absorber was confirmed, and its features could explain residuals to the fit. The most complete studies on the warm absorber of these two objects were done using *XMM/RGS* data by Smith et al. (2007) and Detmers et al. (2010) for *Mrk 509*, and by Longinotti et al. (2010) for *Mrk 841*.

Smith et al. detected a three-phase warm absorber in *Mrk 509*: a low ionisation component ($\log \xi \approx 0.89$ and column density $N_H \approx 7.9 \cdot 10^{20}\mathrm{cm}^{-2}$), an intermediate ionisation phase ($\log \xi \approx 2.14$, $N_H \approx 7.5 \cdot 10^{20}\mathrm{cm}^{-2}$) and a high ionisation one ($\log \xi \approx 3.26$, $N_H \approx 55 \cdot 10^{20}\mathrm{cm}^{-2}$). Detmers et al. confirmed the presence of three different components in the warm absorber: they found a low ionisation phase ($\log \xi \approx 0.6$, $N_H \approx 1.0 \cdot 10^{20}\mathrm{cm}^{-2}$), an intermediate phase ($\log \xi \approx 1.95$, $N_H \approx 10.5 \cdot 10^{20}\mathrm{cm}^{-2}$), and a high ionisation phase ($\log \xi \approx 3.2$, $N_H \approx 80.0 \cdot 10^{20}\mathrm{cm}^{-2}$).

A multi-phase warm absorber was found in *Mrk 841*, too, by Longinotti et al., with an intermediate ionisation component ($\log \xi \approx$ 1.5-2.2, $N_H \approx$ 12-39 $\cdot 10^{20}\mathrm{cm}^{-2}$) and a higher ionisation phase ($\log \xi =$ 2.8-3.3 and $N_H \approx$ 76-300 $\cdot 10^{20}\mathrm{cm}^{-2}$).

We tested the presence of the warm absorber using the model *zxipcf* (Reeves et al. 2008), part of *XSpec* models, which has as free parameters the ionisation parameter $\log \xi$, the column density N_H, the covering factor f and the redshift z. We started our study by multiplying the double Comptonisation model by one *zxipcf* component, with $f = 1$ and $z = z_{object}$. For *Mrk 509*, we find $\log \xi_{WA} = 2.19^{+0.05}_{-0.05}$ and $N_{H,WA} = 17^{+2}_{-2} \cdot 10^{20}\mathrm{cm}^{-2}$, values which are consistent with the intermediate ionisation phase found by Smith et al. and Detmers et al.. For *Mrk 841*, we find $\log \xi_{WA} = 2.3^{+0.1}_{-0.1}$ and $N_{H,WA} = 17^{+4}_{-4} \cdot 10^{20}\mathrm{cm}^{-2}$, consistent with the intermediate ionisation phase in Longinotti et al.. Adding *zxipcf* always improves the goodness of the fit, as confirmed by a F-test: the null hypothesis probabilities are $7 \cdot 10^{-44}$ (for *Mrk 509*)

and $1 \cdot 10^{-13}$ (for *Mrk 841*).
We then tried to add a second absorber (subscript 2). For *Mrk 509*, we find that a two-phase warm absorber is statistically preferred (the associated F-test probability is $5 \cdot 10^{-5}$) and we measure $\log \xi_{WA,2} = 2.7^{+0.4}_{-0.1}$, $N_{H,WA,2} = 7^{+9}_{-2} \cdot 10^{20}\mathrm{cm}^{-2}$, $\log \xi_{WA,1} = 1.7^{+0.1}_{-0.1}$ and $N_{H,WA,1} = 8^{+2}_{-1} \cdot 10^{20}\mathrm{cm}^{-2}$. For the high ionisation phase, *XMM/RGS* data showed also a warm absorber flow velocity blueshifted relatively to the galaxy: we then fixed $z_{WA,2}$ at the value found by Detmers et al. ($z_{WA,2} = 0.0334$, corresponding to $v = -290$ *km s*$^{-1}$).
For *Mrk 841* adding a second absorber does not improve the goodness of the fit and the absorber parameters are badly constrained: we then fixed $\log \xi_{WA,2} = 3.3$, equal to the value measured by Longinotti et al. during the 2001 *XMM* observation of *Mrk 841*.
Best fit results are given in Table 2.4 and plotted in Figs. 2.9 and 2.10 (left panel). We tested the presence of a three-phase warm absorber in *Mrk 509*, but the goodness of the fit worsens, even fixing the warm absorbers parameters at the values measured by *XMM/RGS*.

Zxipcf can take into account a covering factor f<1, to describe partial covering absorbers. We tested the effect of this parameter on a one-phase warm absorber. For *Mrk 509*, leaving f free to vary, it decreases down to 0.3, while $N_{H,WA}$ increases, reaching $3 \cdot 10^{22}\mathrm{cm}^{-2}$; the new fit is statistically better than the one with $f = 1$ (the null hypothesis probability is equal to $1 \cdot 10^{-7}$). For *Mrk 841* the best fit result is always consistent with $f = 1$ (we can only set a lower limit: $f > 0.7$). Despite the better fit obtained with f<1 for *Mrk 509*, we decided to use and study the $f = 1$ case in order to compare our results to *XMM/RGS* results (and for consistency between the analysis of our two sources). In any case there is a degeneracy between f and N_H, and leaving f free affects the values of ξ and T_s and, consequently, the physical interpretation of our results. In the next sections, we will always use $f = 1$, with a reminder that, for *Mrk 509*, thawing f always leads to a better fit.

In both sources, *XMM/RGS* data revealed an OVII emission line at $E \approx 0.56$ keV. We tested the presence of this emission adding a narrow ($\sigma = 0$) gaussian line to the model (the fit was performed using data below 10 keV, without *reflext*, which produces an OVII emission line as well (see below)).
For *Mrk 509* we find a significant better fit (F-test probability = $4 \cdot 10^{-9}$) for the fourth observation, while for the other observations and for the summed spectra the goodness of the fit is not improved. However, it should be noted that at 0.56 keV we do not have the *XIS/FI* detectors (which start at 0.6 keV), and that we are at the energy edge of *XIS1*: the energy resolution is quite low (the emission line is defined by one bin only) and we cannot confirm if this statistically significant improvement of the fit corresponds to a true emission line detection.
For *Mrk 841*, adding a gaussian OVII emission line does not improve the goodness of the fit in any individual observation or in the summed spectrum.
The origin of this emission line is thought to be the warm gas itself but, on the other hand, we expect OVII emission from colder reflection, too. In particular, Ebrero et al. (2010) showed, for the Seyfert 1 Mrk 279, that the *reflext* code (for $\log \xi < 1.43$) produces an OVII line emission flux which exceedes the observed OVII line flux by a factor of 10 or more. For *Mrk 509* and *Mrk 841*, such excess is not present: the line flux produced by *reflext* (with $\log \xi = 0$) is equal to $2.1 \cdot 10^{-4}$ cm^{-2} s^{-1} for *Mrk 509* (compared to $2.7 \cdot 10^{-4}$ cm^{-2} s^{-1} found by Detmers et al.), and to $7.2 \cdot 10^{-5}$ cm^{-2} s^{-1} for *Mrk 841* (compared to $(6.4 \pm 5.3) \cdot 10^{-5}$ cm^{-2} s^{-1} found by Longinotti et al. in the January 2005 *XMM/RGS* observation).

Gierliński & Done (2004) performed their fits without testing the presence of a warm absorber in their data. Looking at Table 2.4 we can see that, adding *zxipcf*, kT_s increases from 0.13-0.14 keV to 0.19-0.21 keV, becoming only marginally consistent with Gierliński & Done (2004) results.

2.4.2 Blurred reflection model

The constancy and universality of soft excess temperature is difficult to explain in a double Comptonisation scenario, for objects with different black hole masses (Gierliński & Done 2004); instead it is expected if some atomic processes are at work. If the reflection from the accretion disc is ionised, and if emission lines are broadened by relativistic velocity near the black hole, this component can explain the soft excess as well.

We used the *reflionx* model (Ross et al. 1999; Ross & Fabian 2005), convolved with the *kdblur* model (Laor 1991), to describe the disc ionised reflection. For the relativistic blurring we assumed $R_{in} = 1.235\ R_G$ (the last stable orbit for a near extremal Kerr black hole with parameter $a = 0.998$, (Thorne 1974)), $R_{out} = 100\ R_G$, $\vartheta = 30$ degrees, and disc emissivity index $\beta = 3$ (Laor 1991); for *reflionx* we fixed iron abundance equal to the solar value, leaving ξ and the normalization free. Following what we did in the Section 2.4.1, we added a neutral reflection from distant material (*reflext*, with normalization parameter fixed as a function of Γ, as described in Section 3.3), a narrow gaussian line (for the Fe $K\beta$[11] emission line) and a two-phase warm absorber totally covering the source (*zxipcf*), with ionisation parameter and column density left free to vary within the error bars of the values found using a double comptonisation continuum (see Section 3.5.1). A broad emission feature around 6.4 keV is expected from the blurred reflection on the accretion disc, so no broad emission line was included in the model. Best fit results are given in Table 2.5.

The R parameter, which gives information about the reflected flux fraction, as defined by Crummy et al. (2006), is the ratio of the unabsorbed reflected component (*reflionx*) flux on the total (excluding *reflext*) unabsorbed flux in the 0.3-12 keV energy band. For a flat disc illuminated by an isotropic source we evaluated a value of $R \approx 0.5$ for a high ionisation state ($\log \xi > 3.5$), while for lower ionisations the reflection fraction decreases, reaching 0.4 for $\log \xi = 3$, 0.2 for $\log \xi = 2$ and 0.1 for $\log \xi = 1.5$.

This model is widely used in literature: Crummy et al. (2006) analysed a sample of 34 type 1 AGN, fitting their *XMM-Newton* observations with *reflion* model (an older version of *reflionx*). For the R parameter, they found one third of the sources having no power law component ($R = 1$), while in the rest of the sample R is almost equally distributed between 0.25 and 0.8. Our values, comprised between 0.15 and 0.18, are quite low compared to this result. In particular, *Mrk 841* is included in their sample, and they found $R = 0.67 \pm 0.17$. This value is different from what was found by Petrucci et al. (2007), in a dedicated paper on *XMM-Newton* observations, including the one studied by Crummy et al. (2006), for which they found $R = 0.3$. In their paper Petrucci et al. (2007) computed indeed R', defined as the reflected fraction evaluated in the energy band 0.1-1000 keV, and including warm absorption; for consistency, we have re-evaluated R using their best fit parameters. In our model we have frozen all *kdblur* parameters. We tried to thaw β, but its best fit value is always consistent with 3. Crummy et al. (2006) performed their fits leaving all, but R_{out}, *kdblur* parameters free to vary: with such a large number of parameters, best fit values become less well constrained, with several parameters pegged at lower or higher limits (as can be seen in Crummy et al. (2006), Table 3) and a physical interpretation of these results is not obvious. The results from Petrucci et al. (2007) for *XMM-Newton* observations of *Mrk 841* were $1.59 \leq \Gamma \leq 2.45$, $2 \leq log\ \xi \leq 2.5$ and $\beta \approx 4$ (but in one observation they found $\beta > 8.6$), with a reflection fraction R' varying between 0.30 and 0.43.

The best fit result for *Mrk 509* is not good ($\tilde{\chi}^2 = 1.25$) and some residuals are clearly observed between 6 and 7 keV (see Fig. 2.8). First we tried to thaw the inner radius and the inclination angle of the accretion disc: the fit is significantly improved (F-test probability = $1 \cdot 10^{-4}$) and we measure $R_{in} < 1.7\ R_G$

---

[11] The Fe Kα line is consistently modelled by the *reflext* model, as discussed in Section 2.3.4

and $\vartheta = 38^{+2}_{-3}$ degrees. However, this cannot take into account all the residuals observed near the Fe Kα line. An excess of emission in the Fe Kα complex could be due to iron abundance higher than the solar value: we tried to thaw this parameter but the best fit results are always consistent with Fe/Fe$_\odot$ = 1. Adding a broad gaussian line, the fit is significantly improved (the null hypothesis probability is 10^{-29}). We measure $E_{0,broad} = 6.9^{+0.1}_{-0.1}$ keV, $C_{broad} = 10^{+1}_{-1} \cdot 10^{-5}$ photons cm^{-2} s^{-1} and $\sigma_{broad} = 0.8^{+0.3}_{-0.2}$ keV, with an equivalent width of 255^{+85}_{-66} eV (see Table 2.5 and Fig.2.9, middle panel).

For Mrk 841, a good fit to the data is already provided by the first model (all *kdblur* parameters frozen at the values described above, and absence of a broad emission line), but the fit is improved when ϑ is left free to vary, and we found $\vartheta = 41^{+3}_{-4}$ degrees (F-test probability equal to $4 \cdot 10^{-4}$). Adding a broad emission line at the Fe K complex energy does not improve the goodness of the fit (F-test probability = 0.1 compared to the fit with ϑ thawed) (see Table 2.5 and Fig.2.10, middle panel).

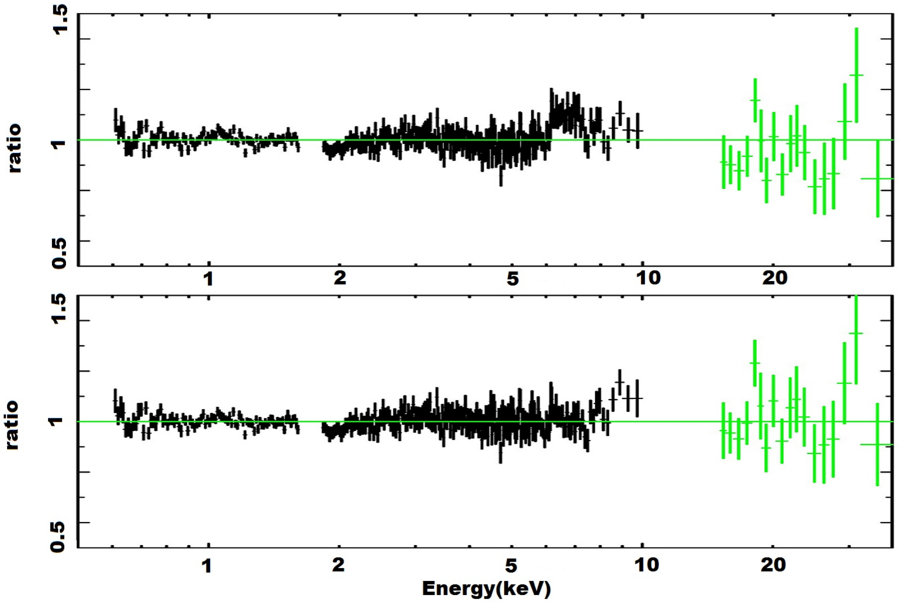

Figure 2.8: Ratio plot obtained for the fit of *Mrk 509* data with a blurred reflection model with (bottom) or without (top) a broad emission Kα line (see section 3.6). *XIS/FI* data are in black, while *HXD/PIN* data are in green. For clarity, the data were rebinned, and *XIS1* data are not shown in this plot.

2.4.3 Smeared absorption model

An alternative model to explain the soft excess is a relativistically smeared absorption: high velocities can blur all atomic features, producing a curved continuum spectrum. This absorption could represent an outflowing disc wind, as shown by Murray & Chiang (1997). We used *swind* (Gierliński & Done 2004), part of *XSpec* models, to describe this component: a *XSTAR* (Bautista & Kallman 2001) grid (calculated assuming $\Gamma = 2.4$ and microturbulent velocity of 100 km/s) is convolved with a Gaussian function with width $\sigma = v/c$. Free parameters of *swind* model are the column density N_H, the ionisation parameter ξ and the velocity dispersion σ. As for the ionised reflection model, we added a neutral reflection (*reflext*), a narrow gaussian line for the Fe $K\beta$ emission line and a two-phase warm absorber (*zxipcf* model). As no broad Fe emission line is included in the model, we also added a broad emission line with parameters fixed as in Table 2.2 (for the *XIS* + *PIN* fit). Best fit results are shown in Table 2.6 and Figs. 2.9 and 2.10, right panel.

For both sources the values of σ are always pegged at the highest authorized value ($v = 0.5\ c$), and we can only give lower limits. It is interesting to cite the results of a fitting without *zxipcf*: σ decreases down to ≈ 0.3 (it is equal to $0.29^{+0.01}_{-0.02}$ and $0.28^{+0.03}_{-0.02}$ for *Mrk 509* and *Mrk 841*, respectively). We can compare our results for *Mrk 841* with Petrucci et al. (2007), who tested the same model for *XMM-Newton* observations: their best fit values for *swind* model are $2.4 \leq \log \xi \leq 3.5$, $0.9 \leq N_H \leq 4.4 \cdot 10^{23}\mathrm{cm}^{-2}$ and σ consistent with 0.3 (but > 0.4 in two cases). The values of N_H and ξ we found are in agreement with these results.

This model was studied by Middleton et al. (2007), who analysed the same AGN sample used by Crummy et al. (2006). They found that, in half of their sample, σ is pegged at 0.5, and that, in general, it has a typical value > 0.3. Their ξ and N_H best fit values do not have large dispersion: $\log \xi$ varies between 2.5 and 3.7, with lower values ($\log \xi < 3$) for their Narrow-Line Seyfert 1 (NLS1) galaxy sample; N_H values are comprised between $5 \cdot 10^{22}$ and $5 \cdot 10^{24}$, with, once again, values lower than $1.5 \cdot 10^{23}$ restricted to NLS1 galaxies. The intrinsic power law spectral index varies between 2.0 and 3.4, with a clear difference between the softer NLS1s and the harder broad-line AGN. The values we found are in agreement with these global results, but Γ is only marginally compatible with the results obtained by Middleton et al. (2007). The evaluation of Γ is important since it affects the soft excess strength and shape, and then *swind* parameters. In order to test if *PIN* data have an effect in the evaluation of Γ, we tried to fit *XIS* data alone, but the best fit values of Γ are compatible with the broad-band fit.

2.5 Discussion

Mrk 509 and *Mrk 841* are two bright Seyfert 1 galaxies, well known for their soft X-ray excess, their iron $K\alpha$ emission line and their spectral variability. We presented here the analysis of new *Suzaku* observations: four of *Mrk 509* (from April, 2006 to November, 2006), and two of *Mrk 841* (January and July, 2007). The soft excess is clearly present in both sources, with a flux ≈ 2 times higher than the 3-10 keV power law extrapolation at 0.5 keV. Pounds & Reeves (2002) analysed a sample of six Seyfert 1 galaxies, showing that a variety of soft excess shapes exists, correlated with AGN luminosity: our sources during *Suzaku* observations can be described as 'Gradual Soft Excess' galaxies, according to Pounds and Reeves terminology (i.e. a smooth excess, starting at roughly 2 keV, see Chapter 1 and Fig. 1.4). We can compare our results to past observations (Pounds et al. 2001; Pounds & Reeves 2002; De Rosa et al. 2004; Petrucci et al. 2007): a soft excess 2 times higher than the power law extrapolation at 0.5 keV is common for both sources, even though *Mrk 841* during *XMM-Newton* observations showed a stronger soft excess, 2.5-3 times higher than the power law, and the soft excess of *Mrk 509* during obs.1 is quite low, similar to what was observed during the highest state in *BeppoSAX* observations (De Rosa et al. 2004).

Comparing our observations to statistical studies of the soft excess (Gierliński & Done 2004; Crummy et al. 2006; Middleton et al. 2007), we confirm that both sources were detected during a weak soft excess state, setting them always in the lower part of the sample: for the double Comptonisation model, the "soft excess strength" (R_{GD}, as defined by Gierliński & Done (2004)) of *Mrk 509* and *Mrk 841* during our observations is comprised between 0.23 and 0.28, while the sample by Gierliński & Done (2004) has a typical value of 0.4-0.6; in the reflection model, we found a R parameter comprised between 0.15 and 0.18, quite low compared to the reflected flux fractions of Crummy et al. (2006).

Both sources show a hard excess at energies greater than 10 keV. This excess is weak compared to what was observed by *Suzaku* in three other Seyfert 1 galaxies (Walton et al. 2010), though they are rather extreme exemples of hard excesses.

A narrow Fe $K\alpha$ emission line is detected in both sources, consistent with a reflection by remote and cold material (i.e. the dust torus or the farthest regions of the accretion disc). For *Mrk 841* we compared our results to previous *XMM-Newton* observations, showing that the line flux is constant in time. For *Mrk 509* Fe K complex emission, we refer to Ponti et al. (2009). A broad Fe K emission line is observed as well, with equivalent width $\approx$ 150 eV in both sources.

We detected a two-phase warm absorber in *Mrk 509* data, with log $\xi_{WA,1} \approx 1.7$ and log $\xi_{WA,2} \approx 2.7$, values which are lower than what were found by Smith et al. and Detmers et al.. We do not see in the *Suzaku* data the low ionisation phase (log $\xi = 0.6 - 0.9$) of the absorber detected by *XMM/RGS*. For *Mrk 841* we found a low ionisation warm absorber with log $\xi_{WA,1} \approx 2.2$, consistent with the lower ionisation phase in the two-phase absorber described by Longinotti et al. (2010), and we froze the high ionisation parameter log $\xi_{WA,2} = 3.3$. For *Mrk 509*, considering a warm absorber covering factor lower than 1, always improves the fit.

We analysed the broad-band spectra of the two sources considering the double Comptonisation model: it correctly fits the data ($\tilde{\chi^2} \approx 1.09$ for *Mrk 509*, and $\tilde{\chi^2} \approx 1.00$ for *Mrk 841*), but the constancy of the temperature of the cold Comptonisation region in statistical studies of Seyfert 1 galaxies is not explained by current physical models of accretion disc atmospheres, and thus disfavours this model.
We then fitted the broad-band spectrum with the two competitive models aimed to explain the soft excess with atomic processes: a blurred reflection and a smeared ionised absorption.
For *Mrk 509*, we need to add a broad emission line in order to correctly fit the data, and we obtain $\tilde{\chi^2} \approx$ 1.04-1.02 for the blurred reflection and the smeared absorption model, respectively.
The physical origin of this emission is not clear: for the reflection model, a broadened emission line is already included in the code we used, and it is difficult to explain why we do need some more reflection at $E \approx 6.4$ keV. Interestingly, this result suggests that the reflection model correctly describes the soft excess shape and strength, but it underestimates the broad emission at Fe K complex energies.
For the smeared absorption model we do not include any reflection from the accretion disc, and the fact that we need to add a broad emission line is less critical: the *swind* code assume a simple power law emission as input for the smeared absorption, and the presence of residuals in the Fe K complex region means that the continuum spectrum absorbed by the wind does include, indeed, some reflected component.
For *Mrk 841* no extra-emission in the reflection model is required, while a broad gaussian emission line is needed in the absorption model: each model gives a good fit to the data, and none of them can be invalidated ($\tilde{\chi^2} \approx 1.04$ for the two models).

Suzaku data, characterised by a good energy resolution in a large energy domain (0.5-60 keV), seemed to be able to constrain the intrinsic power law photon index at high energies, and then to favor one model over another. The best fit models show that, while in the soft X-ray domain the models are degenerate, in the hard energy band they do not superpose any more and we could, in principle, distinguish between them, but the *PIN* signal-to-noise ratio is still too low to constrain the fit. For the sum of *Mrk 509* observations, we can estimate from the best fit model in the hard X-ray domain a flux $F_{17-60keV}$ = 4.47, 4.81 and $4.27 \cdot 10^{-11}$ ergs cm^{-2} s^{-1} and $F_{14-150keV}$ = 7.64, 8.07 and $7.66 \cdot 10^{-11}$ ergs cm^{-2} s^{-1} for the double Comptonisation, the blurred reflection and the smeared absorption model, respectively; for the sum of *Mrk 841* observations we obtain $F_{17-60keV}$ = 1.94, 2.15 and 1.67 · 10^{-11} ergs cm^{-2} s^{-1} and $F_{14-150keV}$ = 3.47, 3.72 and 3.06 · 10^{-11} ergs cm^{-2} s^{-1} for the three models, respectively. These values can be compared with the *INTEGRAL* (Krivonos et al. 2010) and *Swift/BAT* (Cusumano et al. 2010) detections of our sources: *INTEGRAL* detected *Mrk 509* at $F_{17-60keV} = 5.90 \cdot 10^{-11}$ ergs cm^{-2} s^{-1} and *Mrk 841* at $F_{17-60keV} = 3.07 \cdot 10^{-11}$ ergs cm^{-2} s^{-1}; *Swift/BAT* observed a flux in the 14-150 keV energy band equal to 8.5 · 10^{-11} ergs cm^{-2} s^{-1} for *Mrk 509* and 2.9 · 10^{-11} ergs cm^{-2} s^{-1} for *Mrk 841*. The differences in the predicted high-energy fluxes show that a simultaneous broad-band observation with adequate signal-to-noise ratio would be able to distinguish between the different models.

Statistical studies of AGN can help in solving the problem of the origin of the soft excess. The discovery of the remarkably constant temperature of the cold Comptonisation region, despite the fact that AGN luminosity and black hole mass span several decades, is hardly explained in a double Comptonisation scenario. Our kT_s values are in agreement with the results by Gierliński & Done (2004), but it is interesting to note that adding a warm absorber (which was not included in the Gierliński & Done (2004) analysis) affects kT_s best fit values.

Reflection and absorption models, linked to atomic processes, can easily explain the low spread in the soft excess temperature.
The blurred reflection model fits the *Suzaku* data well for *Mrk 841*, while for *Mrk 509* we need an extra-emission at Fe K energies, which is difficult to explain. The model does not need a high reflection fraction R, seen in several other cases, which may be explained by a huge light bending effect (Miniutti & Fabian 2004) close to the black hole.
It is of course possible that different processes are at work at the same time : in this scenario (which is difficult to test in a stationary framework due to the high number of free parameters involved) the broad emission observed in *Mrk 509* could be due to standard ionised reflection on the accretion disc, while Comptonisation or smeared absorption should be responsible for the soft excess below 1 keV (see Patrick et al. (2011)).

However, the smeared absorption model has the weakness that the velocity dispersion required to fit the soft excess is very high, reaching $c/2$, which corresponds to extremely relativistic terminal velocities for the wind. Numerical simulations (Schurch & Done 2008) show that disc winds have $\sigma < 0.1c$, very low compared to *swind* model results. A possible way out could be a magnetically driven wind, partially covering the source. It is important to underline that *swind* takes into account only the absorption by the wind, but if we consider its emission, too, (Chevallier et al. 2006; Schurch & Done 2006) the fit requires a lower smearing velocity and a lower column density. A possible concern of the *swind* model is that the absorption is evaluated assuming an incident power law spectrum with $\Gamma = 2.4$, not consistent with the Γ best fit values of our observations.
The Fe broad line excess we observe in both sources suggests that, even in an absorption scenario, we need some reflected emission from the inner regions of the accretion disc. A broad Fe K emission line can also be reproduced by recent disc wind models (Sim et al. 2010), with lower outflow velocity (0.1c). Alternatively, the continuum X-ray emission from the hot corona can deviate from a powerlaw when measured over a broad energy band, showing an intrinsic curvature which was not taken into account in our modeling.

Variability studies can disentangle different models: in the blurred reflection scenario, variability can be explained by changes in the height of the corona above the disc, but this picture implies a strong continuum-reflected component correlation which was not observed. In the smeared absorption model, spectral variability is more easily explained by variation in the absorber physical parameters, or in its covering factor. Unluckily, neither of our sources showed a strong variability during *Suzaku* observations, and we could not use temporal information to better constrain our models.

Future X-ray observatories, and in particular *Astro-H* (Takahashi et al. 2010) and *NuSTAR* (Harrison et al. 2010), with higher sensibility and energy resolution in the hard X-ray domain, will be able to better constrain the spectrum, casting light on the physical origin of the soft excess in Seyfert 1 galaxies.

Table 2.4: Best fit parameter values for the double Comptonisation model, with (second row) or without (first row) a two-phase warm absorber. Γ_S and kT_H are frozen at values 2 and 100 keV, respectively. Distant reflection is modelled using *reflext*, whose normalisation parameter is frozen in order to reproduce the observed Fe $K\alpha$ line (see Section 3.3). Two gaussian functions are included in the model, for the narrow Fe $K\beta$ and the broad Fe K emission line, with parameters frozen as in Table 2.2. *NTHComp* normalization parameters C are in units of keV^{-1} cm^{-2} s^{-1} at 1 keV; warm absorber column density N_H is given in units of cm^{-2}, and ionisation parameter ξ in units of erg cm s^{-1}. Frozen parameters are marked by (F). The last two columns give the chi squared value over the number of degrees of freedom and the associated probability.

Mrk 509										
Obs.	kT_S (keV)	C_S (10^{-3})	Γ_H	C_H (10^{-3})	$N_{H,WA,1}(10^{20})$	$log\ \xi_{WA,1}$	$N_{H,WA,2}(10^{20})$	$log\ \xi_{WA,2}$	χ^2/DOF	prob
2+3+4	$0.127^{+0.006}_{-0.003}$	$0.9^{+0.2}_{-0.1}$	$1.96^{+0.01}_{-0.01}$	$15.8^{+0.1}_{-0.1}$	-	-	-	-	1077/737	$3 \cdot 10^{-15}$
2+3+4	$0.206^{+0.005}_{-0.006}$	$3.8^{+0.2}_{-0.2}$	$1.92^{+0.01}_{-0.01}$	$15.1^{+0.2}_{-0.2}$	8^{+2}_{-1}	$1.7^{+0.1}_{-0.1}$	7^{+9}_{-2}	$2.7^{+0.4}_{-0.1}$	800/733	0.04
Mrk 841										
Obs.	kT_S (keV)	C_S (10^{-3})	Γ_H	C_H (10^{-3})	$N_{H,WA,1}(10^{20})$	$log\ \xi_{WA,1}$	$N_{H,WA,2}(10^{20})$	$log\ \xi_{WA,2}$	χ^2/DOF	prob
1+2	$0.137^{+0.13}_{-0.06}$	$0.35^{+0.10}_{-0.05}$	$1.82^{+0.01}_{-0.01}$	$4.00^{+0.04}_{-0.08}$	-	-	-	-	769/707	0.005
1+2	$0.19^{+0.01}_{-0.01}$	$0.85^{+0.11}_{-0.11}$	$1.80^{+0.01}_{-0.01}$	$3.92^{+0.06}_{-0.07}$	14^{+4}_{-7}	$2.2^{+0.2}_{-0.3}$	< 41	3.3 (F)	705/704	0.48

Table 2.5: Best fit parameter values for the blurred reflection model. Distant reflection is modelled using *reflext*, whose normalisation parameter is frozen in order to reproduce the observed narrow Fe $K\alpha$ line (see Section 3.3). A gaussian function is included in the model, for the narrow Fe $K\beta$ emission line, with parameters frozen as in Table 2.2. For *Mrk 509*, the best fit results including a broad gaussian emission line are also shown. *reflionx* and power law normalization parameters C are in units of keV^{-1} cm^{-2} s^{-1} at 1 keV; ionisation parameter ξ is given in units of erg cm s^{-1}; the line normalization parameter C_{broad} is the integrated number of photons cm^{-2} s^{-1} in the line; σ is the line width expressed in keV. The R parameter is defined as the ratio of the flux of the unabsorbed reflected component on the total unabsorbed flux (evaluated between 0.3 and 12 keV). The two-phase warm absorber parameters are constrained within the range evaluated with the double Comptonisation model (Table 2.4). The last two columns give the chi squared value over the number of degrees of freedom and the associated probability.

Mrk 509										
Obs.	Γ	$C(10^{-3})$	$\log \xi$	$C_{reflionx}(10^{-6})$	$E_{broad}(keV)$	$C_{broad}(10^{-5})$	$\sigma_{broad}(keV)$	R	χ^2/DOF	prob
2+3+4	$2.041^{+0.004}_{-0.004}$	$15.9^{+0.1}_{-0.1}$	$1.54^{+0.14}_{-0.06}$	$11.5^{+2.2}_{-2.9}$	-	-	-	$0.16^{+0.03}_{-0.04}$	915/733	$5 \cdot 10^{-6}$
2+3+4	$2.039^{+0.007}_{-0.005}$	$15.9^{+0.1}_{-0.1}$	$1.73^{+0.03}_{-0.02}$	$6.1^{+0.7}_{-1.1}$	$6.9^{+0.1}_{-0.1}$	10^{+1}_{-1}	$0.8^{+0.3}_{-0.2}$	$0.15^{+0.01}_{-0.02}$	756/730	0.25
Mrk 841										
Obs.	Γ	$C(10^{-3})$	$\log \xi$	$C_{reflionx}(10^{-6})$	$E_{broad}(keV)$	$C_{broad}(10^{-5})$	$\sigma_{broad}(keV)$	R	χ^2/DOF	prob
1+2	$1.89^{+0.02}_{-0.01}$	$3.9^{+0.1}_{-0.1}$	$1.80^{+0.09}_{-0.05}$	$1.9^{+0.04}_{-0.05}$	-	-	-	$0.18^{+0.04}_{-0.05}$	730/704	0.24

Table 2.6: Best fit parameter values for the smeared absorption model. Distant reflection is modelled using *reflext*, whose normalisation parameter is frozen in order to reproduce the observed Fe $K\alpha$ line (see Section 3.3). For both sources, two gaussian functions are included in the model, for the narrow Fe $K\beta$ and the broad Fe K emission line, with parameters frozen as in Table 2.2. Power law normalization parameter C is in units of keV^{-1} cm^{-2} s^{-1} at 1 keV; wind column density N_H is given in units of cm^{-2}, and ionisation parameter ξ in units of erg cm s^{-1}. The two-phase warm absorber parameters are constrained within the range evaluated with the double Comptonisation model (Table 2.4). The last two columns give the chi squared value over the number of degrees of freedom and the associated probability.

Mrk 509							
Obs.	Γ	$C(10^{-3})$	$N_H(10^{22})$	$log\ \xi$	σ	χ^2/DOF	prob
2+3+4	$2.06^{+0.01}_{-0.01}$	$23.8^{+0.3}_{-0.5}$	18^{+2}_{-1}	$3.29^{+0.03}_{-0.02}$	> 0.45	748/732	0.33

Mrk 841							
Obs.	Γ	$C(10^{-3})$	$N_H(10^{22})$	$log\ \xi$	σ	χ^2/DOF	prob
1+2	$1.97^{+0.02}_{-0.02}$	$6.25^{+0.07}_{-0.12}$	12^{+3}_{-3}	$3.10^{+0.10}_{-0.09}$	> 0.46	732/703	0.21

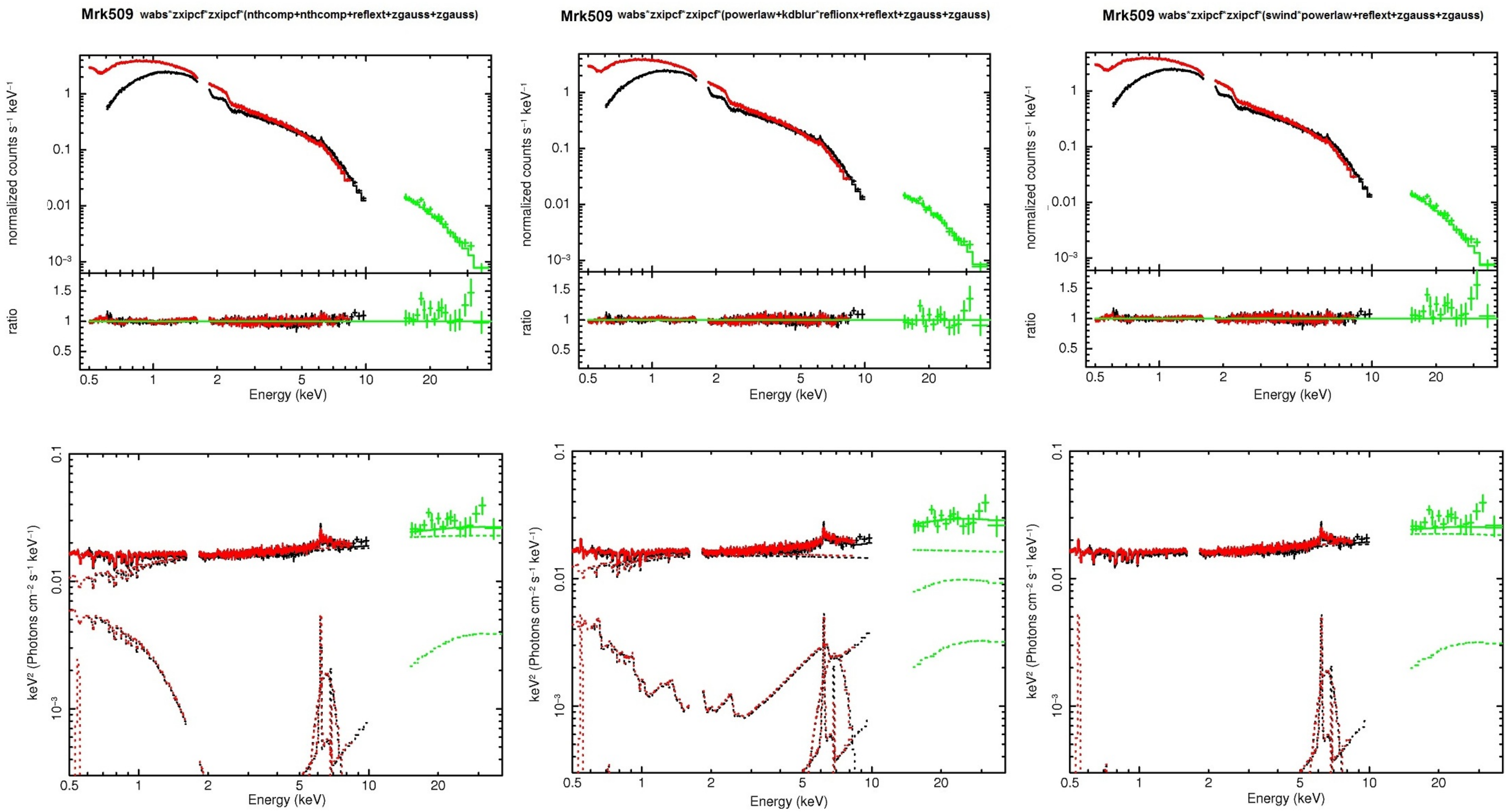

Figure 2.9: Top: *Mrk 509* data (sum of *Suzaku* observations) and, in the subplot, data-to-model ratio. Bottom: unfolded data. Colour code for the different *Suzaku* instruments: *XIS/FI*-black, *XIS1*-red and *HXD/PIN*-green. Three different models are shown, from left to right: double Comptonisation, blurred reflection and smeared absorption. Solid lines correspond to the best fit model, and thin dashed lines to the model different components. For the three models a broad emission line component is required. The energy on the abscissa is in the observer frame. The data were rebinned for clarity purposes.

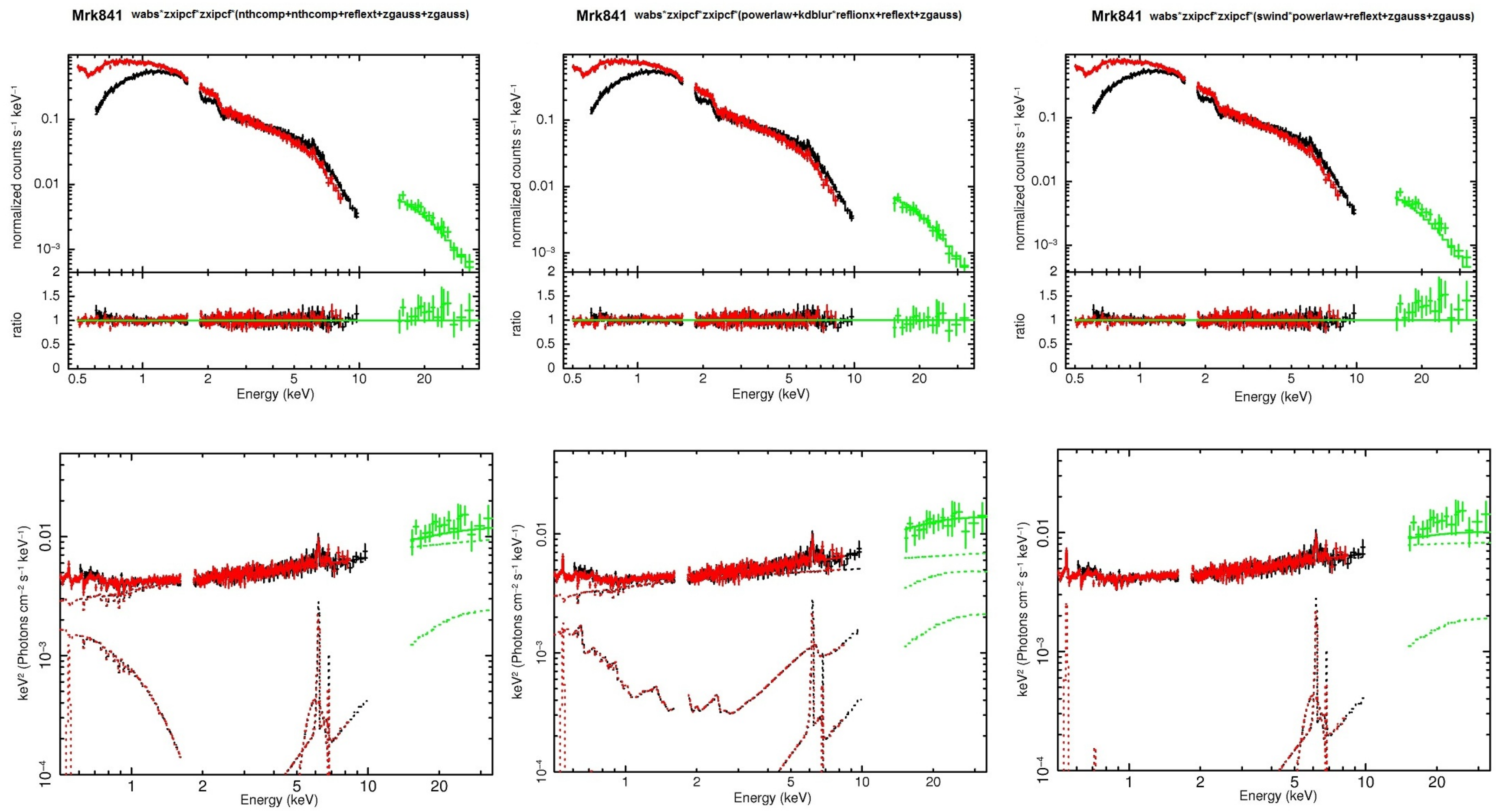

Figure 2.10: Top: *Mrk 841* data (sum of *Suzaku* observations) and, in the subplot, data-to-model ratio. Bottom: unfolded data. Colour code for the different *Suzaku* instruments: *XIS/FI*-black, *XIS1*-red and *HXD/PIN*-green. Three different models are shown, from left to right: double Comptonisation, blurred reflection and smeared absorption. Solid lines correspond to the best fit model, and thin dashed lines to the model different components. A broad emission line component is added for the double Comptonisation and the smeared absorption model only. The energy on the abscissa is in the observer frame. The data were rebinned for clarity purposes.

Part II

Radio-loud active galactic nuclei

Chapter 3

Blazars and emission models

Contents

3.1 Introduction

In this Chapter we introduce the class of blazars, describing first their observational properties, as well as the differences between the different sub-classes (Section 3.2). The theoretical modelling of the broad band emission is described in Sections 3.3 and 3.4, for the leptonic and hadronic scenarios, respectively. In Section 3.5 we discuss the TeV horizon related to the absorption by the extragalactic background light.

3.2 Blazars

As presented in the Introduction, in the framework of the AGN unified model, blazars are considered as radio-loud AGN whose relativistic jet points in the direction of the observer. The non-thermal emission from the jet thus dominates the broad-band spectrum, and is reponsible for the high degree of polarization and the rapid variability observed (see e.g. Strittmatter et al. 1972; Stein et al. 1976; Moore & Stockman 1981). Their spectral energy distribution (SED) is also peculiar, being comprised of two bumps, the first one peaking at low energies (infraread to soft-X-rays), the second one peaking in γ-rays (up to the TeV for the most extreme sources).

Historically, the class of blazar comes from the unification of the BL Lac objects and the OVVs. It is nowadays unanimously accepted that the OVV class is basically coincident with the FSRQs (radio sources characterised by a flat spectrum, see Introduction), and the class of blazars is thus considered as

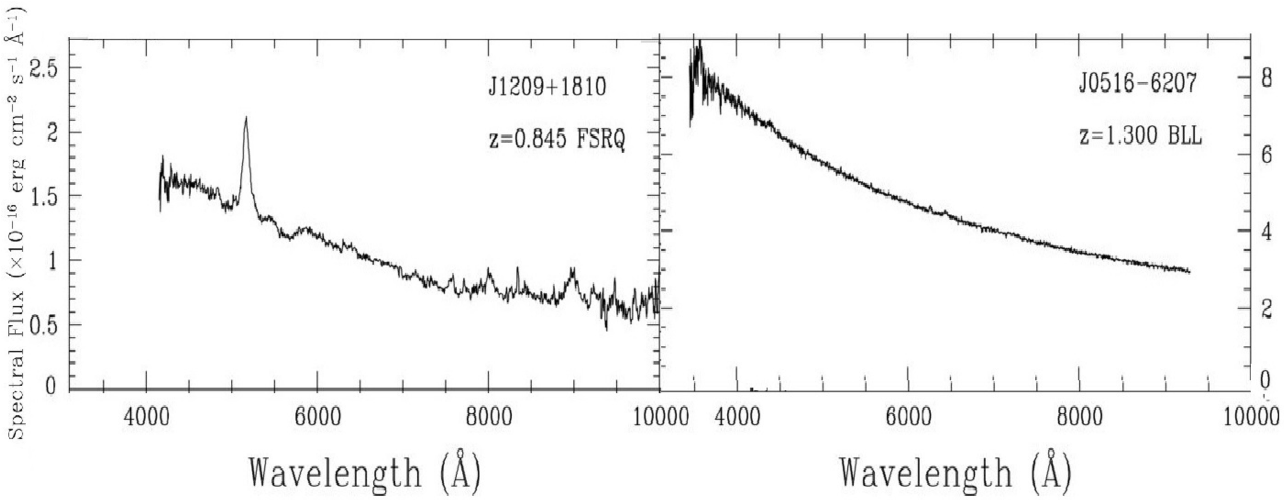

Figure 3.1: Example of optical spectra of blazars. *Left*: spectrum of the FSRQ *1FGL J1209.7+1806*. *Right*: spectrum of the BL Lac object *PKS 0516-621* (*1FGL J0516.7-6207*). Taken from Shaw et al. (2012).

composed by the two sub-classes of BL Lac and FSRQs.
The classification criterion is the presence (or absence) of emission lines in the optical spectrum (Angel & Stockman 1980): if their equivalent width is higher than 5Å the source is classified as a FSRQ, otherwise (when the optical spectrum is continuum) as a BL Lac. An example of the two different optical spectra is shown in Fig. 3.1.
However, this classification is not unambigous: some objects classified as BL Lac showed sometimes broad emission lines (see e.g. the case of BL Lac, Madejski et al. 1999), supporting the similarity of the classes of FSRQs and BL Lacs.

There are however several other differences among these two sub-classes: first, the luminosity function is not the same, with the FSRQs significantly brighter than the BL Lac objects (Padovani 1992). Another important difference is in the redshift distribution: while the FSRQs distribution peaks around $z = 1.0$, BL Lacs are located much closer, and are found mainly at $z < 0.6$ (see e.g. Massaro et al. 2009). The last important difference comes from the SED: while FSRQs show always a low-frequency peak of the first bump (located in infrared-visible light), BL Lacs can be characterised by both a low-frequency or a high-frequency (UV to X-rays) peak (see e.g. Abdo et al. 2010a).

The unification model consistently explains the difference in luminosity, which reflects the difference observed in the jet structure of radio-galaxies (FR I and II): in this context, the bright FSRQs are considered as FR II radio-galaxies observed in the direction of the jet, while BL Lac objects correspond to the fainter FR I radio-galaxies (Urry & Padovani 1995).
The redshift distribution could be biased by a common problem in the study of blazars: the absence of features in the optical spectrum of BL Lac objects challenges the measurement of their redshift. The sample of BL Lacs could thus be affected by incompletness. As an example, in the *Fermi* catalog of AGNs, the 40% of sources classified as BL Lacs does not have a redshift estimation (Ackermann et al. 2011).

The SED characteristics, and in particular the energy of the first peak, is also used to discriminate

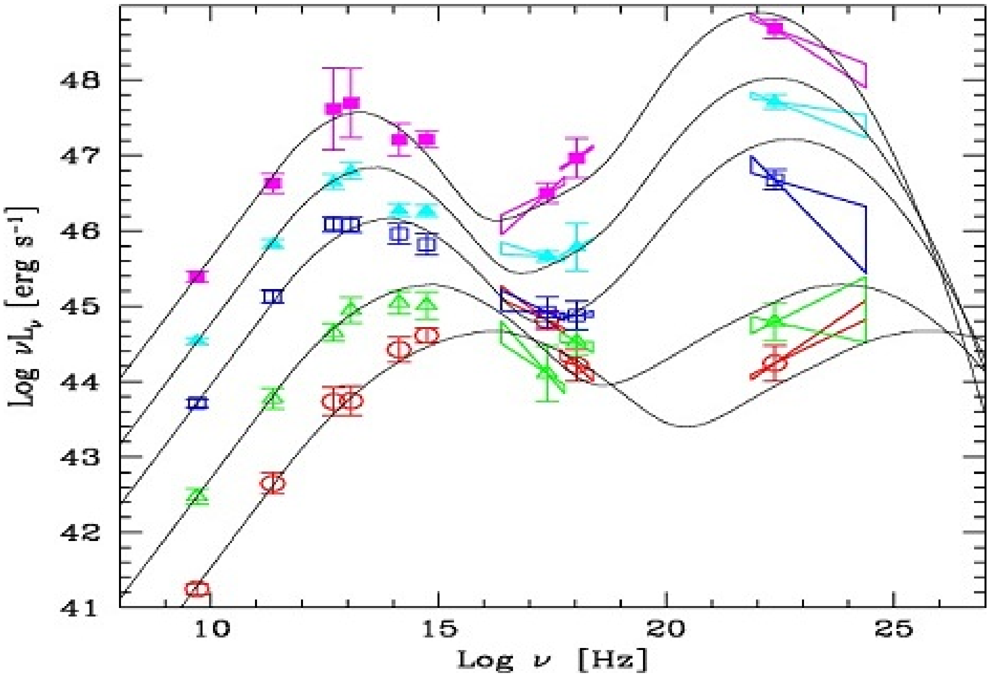

Figure 3.2: The *blazar sequence*, as originally presented by Fossati et al. (1998).

among BL Lac objects (Padovani & Giommi 1995): we thus differentiate between a low-frequency-peaked BL Lac (LBL) and a high-frequency-peaked BL Lac (HBL)[1]. When the peak of the first bump is located right in visible/UV light, the object is called intermediate-frequency-peaked BL Lac object (IBL). This classification, done on the basis of the peak of the first component, corresponds also to another observational classification, which divides the BL Lac accordingly to whether their are observed in X-ray surveys (X-ray selected BL Lac, XBLs) or radio surveys (radio selected BL Lac, RBLs): in fact, HBLs are more likely XBLs, while LBLs are more likely RBLs.

The X-rays spectrum is also different: while HBLs are characterised by a spectral index softer than 2.0, LBLs show harder spectral indices, given the fact that what is observed is already the rising part of the high-energy bump. The measurement of the X-ray spectrum can thus be used as well to differentiate among them (see e.g. Padovani et al. 1997).

The *Fermi* satellite has put new constraints on the high-energy peak, showing the same behaviour (though inverted, giving that in this case what is measured is the spectrum below the peak) in the GeV energy range (Ghisellini et al. 2009; Abdo et al. 2010b): in this case the HBLs are characterised by a spectral index generally harder than 2.0, while the LBLs show a spectral index softer than 2.0 (similar to FSRQs).

Interestingly, the differences between the different BL Lac objects also correspond to a luminosity difference, with the LBLs generally brighter than HBLs: this would imply an evolution of the SED as a function of the luminosity, with the energy of the peak decreasing as the luminosity increases (the so called *blazar sequence*, see Fossati et al. (1998) and Fig. 3.2). The FSRQs naturally fit in this sequence, representing the high-luminosity part of the sample. A unifying scheme which explains the observed blazar sequence in the context of leptonic models (see next Section) has been proposed by Ghisellini

---

[1] More correctly, the original name were high and low-energy cut-off BL Lac objects. This original classification was extended later into the high/low frequency peaked BL Lacs. They can be sometimes abbreviated into LSPs and HSPs, which stand for low/high synchrotron peaked BL Lacs, making reference to the synchrotron origin of the first bump, which we will introduce in the next section. The couples LBL/LSP and HBL/HSP can be considered as synonyms.

et al. (1998). In this case the blazar sequence would be due to the decreasing importance of external radiation field from FSRQs to HBLs.

The existence of the blazar sequence has been widely discussed in the scientific literature, and it has been claimed that it could be due to an observational bias. Padovani et al. (2003); Caccianiga & Marchã (2004); Padovani et al. (2006, 2012) presented the detections of low-luminosity/low-frequency peaked and high-luminosity/high-frequency peaked blazars, which thus break the blazar sequence. According to Nieppola et al. (2008) the blazar sequence could be an artefact of the Doppler boosting, while for Giommi et al. (2012) it would be due in fact to a selection effect, resulting mainly from the fact of ignoring the blazars without redshift estimation (which are the ones with the strongest continuum).

3.3 Leptonic models

The emission from blazars is dominated by the non-thermal emission of the relativistic jet. Shocks inside the jet are thought to be responsible of the emission (see e.g. Marscher & Gear 1985), which is associated to an overdensity moving inside the jet with a bulk Lorentz factor Γ_{bulk}. When observed under a small angle ϑ, Γ_{bulk} translates into a high Doppler factor value, defined as

$$\delta = \frac{1}{\Gamma_{bulk}(1 - \cos\vartheta)} \tag{3.1}$$

The Doppler factor affects the observed emission by both shifting the frequencies and increasing the intensity (which is multiplied by a factor δ^3, which represents the so-called *Doppler boosting*).
Another important observational effect of relativistic jets observed in a direction close to the jet axis is the detection of the super-luminal motion of the projected component of the velocity. This effect has been observed in several blazars (see for example the case of *3C 273*, Pearson et al. 1981) and can be considered as an important proof of the unification scenario.

The low-energy bump of the blazar SED is ascribed to a synchrotron emission[2] by electrons and positrons in the emitting region, which is thus supposed to be filled with a magnetic field. The particle distribution required to fit the data is in most cases a broken-power-law function, where the break is reponsible for the peak observed in the SED.
A power-law function is expected as a result of shock acceleration: the simplest first order *Fermi* acceleration implies a spectral index of 2.0, even though more detailed evaluations increase the range of expected values (see Longair 1994).

A break in the power-law distribution is indeed expected in the presence of synchrotron emission. The energy losses are in fact energy-dependent, and induce a softening of the particle distribution above a certain value $\gamma_{break} = f(B, R)$[3], where R is the size of the emitting region. The theoretical break in the particle distribution is equal to one (for a standard injection function characterised by $\Gamma = 2.0$ we would thus expect an index equal to 3.0 after the break). However, the observations consistent with such a break

---

[2] We do not provide here the details of the equations describing the emission processes nor the radiation transfer, which can be found in several books on the argument (as Rybicki & Lightman 1979; Longair 1994; Dermer & Menon 2009). In the following we will provide equations only when needed. In particular we will discuss more extensively the emission processes in the context of the developement of the lepto-hadronic code described in Chapter 7.

[3] See Section 7.2.6.

are rare, and we usually observe stronger breaks. This aspect is not fully understood, and reflects the fact that the injection/cooling mechanisms are more complicated than this simple scenario: in particular it could be explained, for example, by considering more complex (inhomogeneous) injection terms, energy-dependent escape from the emitting region, non-linear cooling effects, or could represent, more generally, the fact that the homogeneous one-zone model is too simplistic.
It is thus common to consider the two spectral indices as free parameters, and to test a posteriori the self-consistency of the model with respect to a pure synchrotron cooling.

The synchrotron emission from this blob-in-jet cannot explain the emission at radio wavelengths. Moreover, at these energies the emission from the extended jet is expected (and observed), and is supposed to be dominant. We consider thus a two-zone scenario, in which the radio emission is ascribed to the external regions of the jet, while the synchrotron emission from the blob starts dominating the SED at higher energies (infrared to visible). This scenario also accounts for an apparent observational inconsistency: the measurement of the Doppler factor in radio is usually much lower than the one required by the modelling of the high-energy component. This fact can be easily taken into account by considering that the emitting regions observed are not the same (see e.g. Lyutikov & Lister 2010).

By now we have considered a model in which the emitting region is homogeneous (in both the magnetic field and the particle population). However, inhomogeneous models have also been proposed (see e.g. Ghisellini et al. 1985; Maraschi et al. 1992; Katarzyński et al. 2003; Boutelier et al. 2008). In this case the emitting region is considered as being the basis of the jet, whit the magnetic field and the particle density decreasing as a function of the distance.

3.3.1 Synchrotron-Self-Compton (SSC)

So far, we concentrated on the origin of the low energy bump of the blazar SED, which is unanimously ascribed to synchrotron emission. Concerning the high energy bump, several models have been proposed.
The synchrotron-self-Compton (SSC) model considers as resposible for the γ-ray emission an inverse Compton scatter between the leptons in the emitting region and their own synchrotron emission (see e.g. Konigl 1981; Inoue & Takahara 1996; Katarzyński et al. 2001).

An important effect occouring in the emitting region is the pair production of leptons, after interaction of the γ-rays with the low-energy photon field. This translates into an absorption of the flux in the VHE energy band, and an injection of secondary pairs in the emitting region. However, for the SSC model the emission from these secondaries pairs is usually negligible (contrary to the absorption).
An important point concerns the energy budget of the emitting region. In particular, to describe the observed SED, the model requires a particle energy content higher than the magnetic one, far from equipartition.

In this thesis we made use of the original stationary SSC code developed by Katarzyński et al. (2001). The blazar emitting region is considered as spherical, and filled with a homogeneous magnetic field and a population of primary electrons and positrons, desribed by a broken power-law function. This code was used as the basis for the different works described in the second part of this thesis.

The stationary one-zone SSC model, despite its simplicity provides a good description of the SED of HBLs, as can be shown in Fig. 3.3. However, the SSC model fails in general to provide a good representation of the SED of low-frequency-peaked blazars (LBLs and FSRQs), as discussed recently, for example, by Ghisellini et al. (2011). An example of the modelling of the SED of a HBL in a SSC scenario will be provided in Chapter 5, in which we describe the observations of the BL Lac object *1RXS J101015.9 - 311909*.

3.3.2 External-Inverse-Compton (EIC)

An alternative to the SSC scenario is represented by the External-Inverse-Compton (EIC) models, in which the low energy photon field scattered by the leptons in the emitting region is not due to their own synchrotron emission, but has an external origin (see e.g. Sikora et al. 1994).
In particular, for FSRQs it is natural to consider as external field the strong broad-lines observed in the optical spectrum. Other contribution can come from the accretion disc or the dusty torus.

EIC models have been shown to succesfully model the SED of LBLs and FSRQs. In Fig.3.4 we report an example of modelling of the SED of the FSRQ *3C 454.3* in an EIC scenario. We will come back to the external Compton in Chapter 8.

3.4 Hadronic models

In leptonic models, the emission is dominated by the electrons and positrons in the emitting region. Protons can be present in the region, but only in the form of a cold, non-relativistic population.
If the protons are instead relativistic, and if the magnetic field in the emitting region is of the order of tens of Gauss (several order of magnitudes higher than the values required in leptonic models), their synchrotron emission can become dominant, and reproduce the observed high energy bump of the SED. This kind of scenario is generally called *hadronic* model, or *proton-synchrotron* model (see e.g. Mannheim 1993; Mücke & Protheroe 2001).
The hadrons in the emitting region can interact with the low-energy photon field represented by the synchrotron emission of primary leptons (p-γ interaction): the two main interaction channels are the Bethe-Heitler pair production (p+$\gamma \rightarrow p' + e^{+} + e^{-}$) and the photo-meson production (p+$\gamma \rightarrow p' + n^{0}\pi^{0} + n^{+}\pi^{+}n^{-}\pi^{-}$). The synchrotron emission from this secondary particles (muons and electrons/positrons coming from the pion decay) can also be important, and the high energy bump can thus be explained as the sum of these different contributions. In Chapter 7 we describe the development of a new lepto-hadronic code, and the details of the computation of p-γ interactions, as well as emission from secondary particles will be provided.
In blazar hadronic modelling the p-p interactions are usually neglected, given the low density of the emitting region (in contrast such a process is important in denser environments such as supernova remnants). However, it can become important in case of heavier jets, as in the recent hadronic modelling of the emission from radio-galaxies by Reynoso et al. (2011).

Similarly to the leptonic EIC model, we can also consider hadronic models in which the low energy photon field target of the p-γ interactions is represented by external photons, as described by Dermer & Atoyan (2001). Alternative models consider the interaction between neutrons *escaping* the emitting region and external photons as source of the emission (see e.g. Dermer et al. 2012). Another interesting possibility which is worth mentioning is the interaction of clouds or stars with the relativistic jet: in this case the emission is dominated by p-p interactions and can describe the rapid flaring activity observed in blazars (see Barkov et al. 2012, for an application to *PKS 2155-304*).

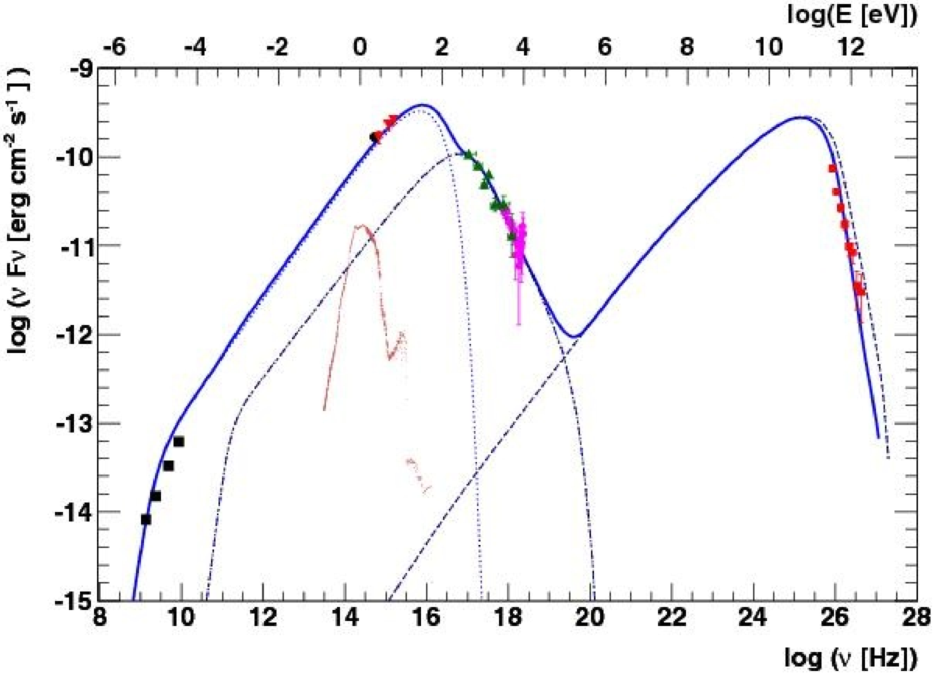

Figure 3.3: The SED of the BL Lac object *PKS 2155-304*, modelled in a SSC scenario. The synchrotron emission from the extended jet (dotted line) is reponsible of the low-energy part of the SED. The host galaxy contribution is shown by the red curve. Taken from Abramowski et al. (2012a).

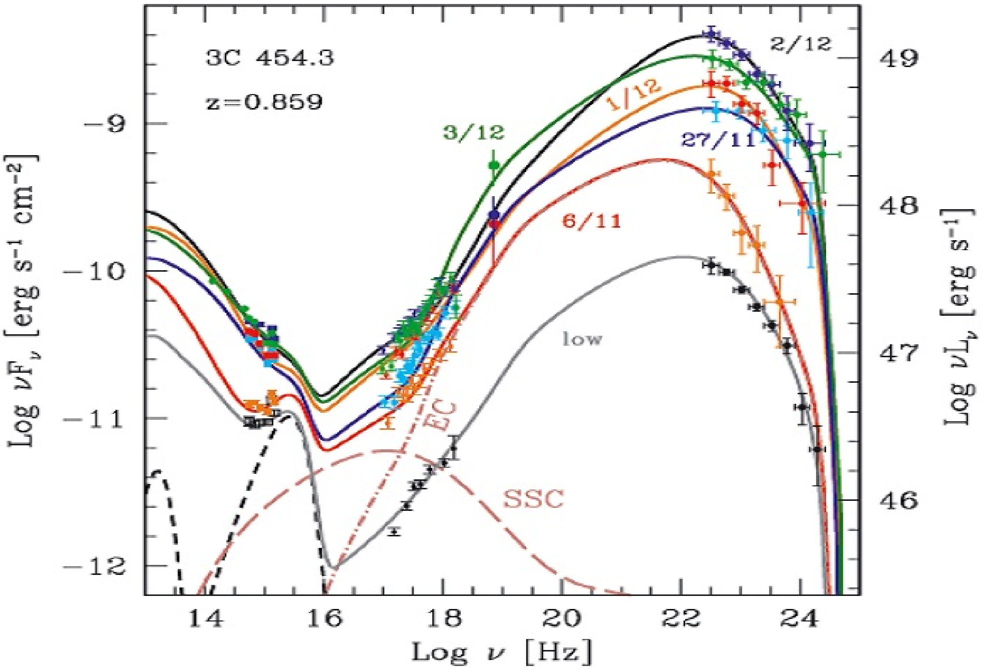

Figure 3.4: The SED of the FSRQ *3C 454.3*, modelled in a EIC scenario, for low and flaring states (each color represents a different observing period, which is indicated by the date near the respective curve). Taken from Bonnoli et al. (2011).

The interest in hadronic models comes also from the multi-messenger link with both the neutrino astronomy and the physics of cosmic rays. Hadronic interactions implies in fact the production of neutrinos, which could be detected using the Earth as a target with the current neutrino telescopes (as *ANTARES* (Ageron et al. 2011), or *IceCube* (IceCube Collaboration et al. 2006)). On the other hand, if hadronic models are confirmed, they would imply acceleration of hadrons up to $E \geq 10^{18}$ eV, stronlgy suggesting AGN as the sources of the ultra-high-energy cosmic rays (UHECR) observed on Earth.

3.5 The TeV horizon

The TeV photons emitted by the source interact with the diffuse low energy photon field (Extra-galactic Background Light, EBL) represented by the thermal emission from dust and stars, producing a pair of leptons (see e.g. Salamon & Stecker 1998, and the sketch in Fig. 3.5). This interaction affects the observed VHE flux in the form of an absorption which becomes important for energies above the TeV (for observations of blazars. For very high redshift sources such as GRBs (γ-ray bursts) the absorption can be significant also below the TeV). The probability of interaction increases with the distance, and thus the absorption is most important for high redshift sources: the TeV astronomy is thus limited by the horizon defined by the absorption on the EBL. Nowadays the most distant objects detected at VHE are at a redshift of roughly 0.5 (as *3C 279*, *PG 1553+113* and *KUV 00311-1938*, see next Chapter).

If the EBL strength and spectral shape are known, the intrinsic spectrum of the source can be reconstructed. However, our knowledge of the EBL is limited by several effects: it is in particular difficult to disentangle the emission from the zodiacal light and our own galaxy from the true extra-galactic background. An efficient way to measure the EBL comes from the galaxy counts, but it represents only a lower limit (see e.g. Dole et al. 2006).
On the other hand, the measurement of the TeV spectrum can be used to define an upper limit on the EBL, assuming that the intrinsic spectral index of the source is not harder than 1.5. The lower and upper limits are in agreement between each other, constraining a narrow range of accepted values which defines the EBL spectrum. In Fig. 3.6 we show the constraints on the EBL, including both galaxy-count measurements and VHE upper limits.
In the study of TeV sources we usually do not de-absorb the VHE data, but we include instead the EBL absorption in the models. An exception is represented by the study of *Mrk 421* provided in Chapter 7.

There is a wide choice of EBL models in literature (see e.g. Franceschini et al. 2008; Kneiske & Dole 2010; Domínguez et al. 2011). We use in the following the model by Franceschini et al. (2008), which is in agreement with the most recent limits provided by VHE observations (Aharonian et al. 2006d).

The pairs produced in the γ-γ absorption are not lost. In particular they can scatter a photon from the Cosmic Microwave Background (CMB), creating a new γ-ray photon, which pair-produces again, forming a pair-cascade. The emission from the cascade would be observed as a secondary component in the GeV energy range (thus detectable with *Fermi-LAT*). However, the presence of an inter-galactic magnetic field affects this component: in particular the effect is a broadening of the cascade and thus a reduction of the cascade emission component along the line-of-sight. Given the fact that such a secondary component has not been seen yet, observations with *Fermi-LAT* of TeV detected blazars can thus be used to put lower limits on the inter-galactic magnetic field (see e.g. Neronov & Vovk 2010; Taylor et al. 2011). This effect implies also the possibility that the γ-ray emission from blazars is not point-like, but extended, in a form of a pair-halo (see e.g. Aharonian et al. 1994). However, up to now, no evidence of such halos has been observed.

In the following we consider that this effect is negligible: we assume thus that the inter-galactic magnetic field is high enough that the emission from the cascade is suppressed, and significantly lower than the source emission.

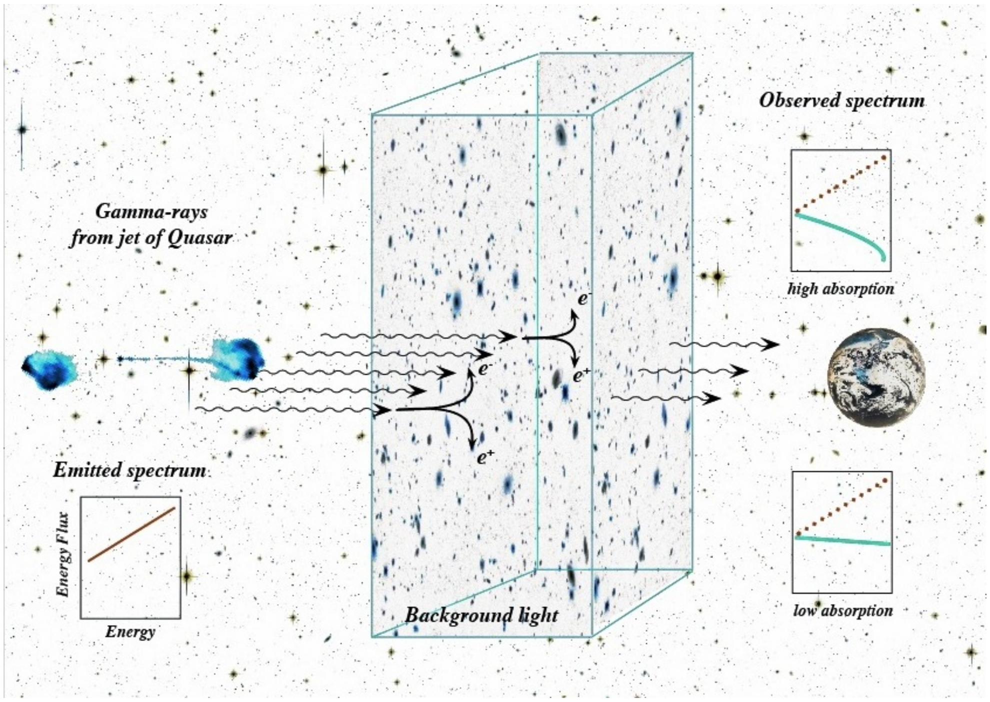

Figure 3.5: Schema of the absorption of γ-ray photons by the extra-galactic background light. Credits: the *H.E.S.S.* collaboration (adapted from).

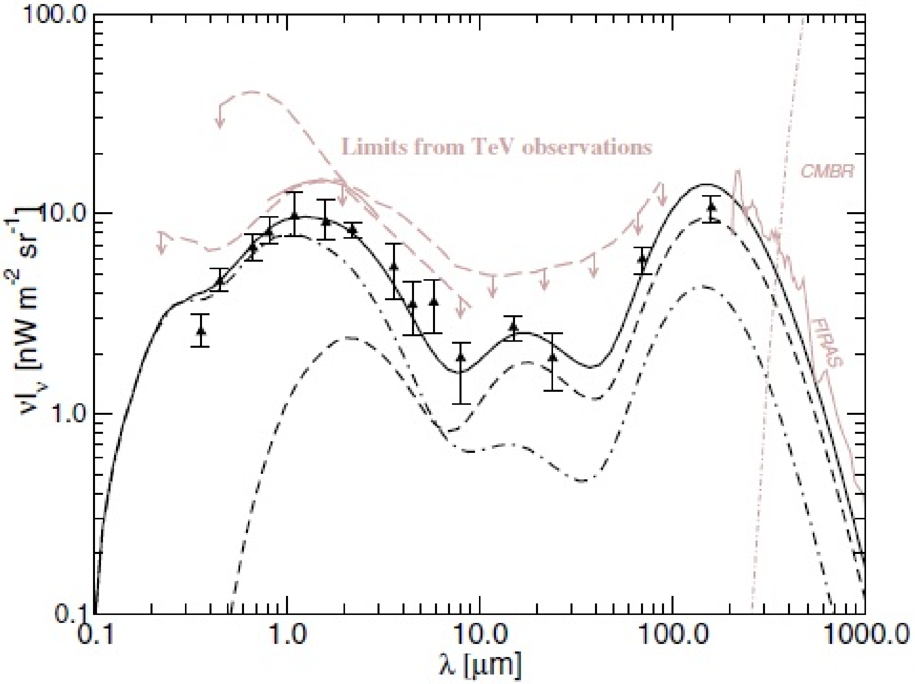

Figure 3.6: Extra-galactic background light lower limits (from galaxies counts: data points and black solid line) and upper limits (from TeV observations, pink lines). Taken from Kneiske & Dole (2010).

Chapter 4

Blazars at TeV with *H.E.S.S.*

Contents

4.1 Introduction

This Chapter is devoted to observations of TeV emission from AGN with *H.E.S.S.*. Before presenting the results, we introduce briefly the *H.E.S.S.* telescope array (Section 4.2), and the data analysis (Section 4.3). The round-up of *H.E.S.S.* AGN observations (Section 4.4) will include a brief presentation of the latest detections. The upper limits on undetected AGN are provided in Section 4.5.

4.2 The High Energy Sterescopic System (*H.E.S.S.*)

The *H.E.S.S.* telescope array represents one of the three leading TeV observatories in the world, together with *MAGIC* and *VERITAS*. The basis of TeV astronomy have been recalled in the Introduction; we present here some more details on the *H.E.S.S.* telescope array itself.

Figure 4.1: *Left*: view of one of the *H.E.S.S.* telescopes, showing the structure, the segmented mirror (in the left part can be seen a missing mirror, replaced by the CCD camera used for the pointing corrections), and the building covering the camera during day-time. *Right*: view of one of the *H.E.S.S.* cameras, showing the cover (on the left), equipped with a LED panel, used for the calibration of the PMs. Taken from Guy (2003).

The system, as used up to now[1], is composed by four identical telescopes, with a diameter of 13m, located on the corners of a 120m-side square. The system is located at an altitude of 1800 m above mean sea level, in the Khomas Highlands, Namibia, roughly 100 km south-west of the capital Windhoek.

The mount of the telescopes, shown in Fig. 4.1 is altazimuth, and the design adopted for the optics is the Davies-Cotton one (Davies & Cotton 1957, orginally developed for solar-concentrators): the mirror is not monolithic, but is composed of 380 spherical sub-mirrors, aligned on the spheroid defined by the mount.[2]. The focal lenght between the spheroid and the camera is 15 m. In each telescope, two mirrors are replaced by two CCD cameras, used for the pointing correction.
During 2010 and 2011, the mirrors of the four telescopes of the *H.E.S.S.* instrument have been recoated, significantly ameliorating their reflectivity which was degrading since the starting of *H.E.S.S.* operations in 2004. This operation was done telescope per telescope, resulting in a three-telescope configuration during this period.

The *H.E.S.S.* camera, shown in Fig. 4.1, is composed of 960 photo-multipliers (PMs), arranged in 60 sub-units of 16 PMs each (*drawers*). Each drawer is independent from the others, both in terms of structure and electronics.
Each PM is associated to a Winston cone, used as a light concentrator and for rejecting photons coming from an angle higher than 30° with respect to the PM's normal.
The fast electronics of the camera is adapted to the very fast (ns) Cherenkov flashes that we want to measure. A detailed description of the electronic trigger can be found in Guy (2003).
The field-of-view of the detector is 5°, required to capture complete images of the showers up to the highest energies. It is also particularly interesting for the Galactic survey and the observation of extended galactic sources.
The mean point-spread-function (PSF, defined as the 80% containement radius) of a single mirror is 0.4 mrad. The PSF of the entire instrument depends on the off-axis position of the source, and on the eleva-

---

[1] The fifth telescope has been already built, and the inauguration of the *H.E.S.S. II* phase is planned for September 2012, see the Introduction.

[2] The normals to the mirrors are however not aligned with the spheroid normal. For a comparison of the performances of different designs, see Schliesser & Mirzoyan (2005)

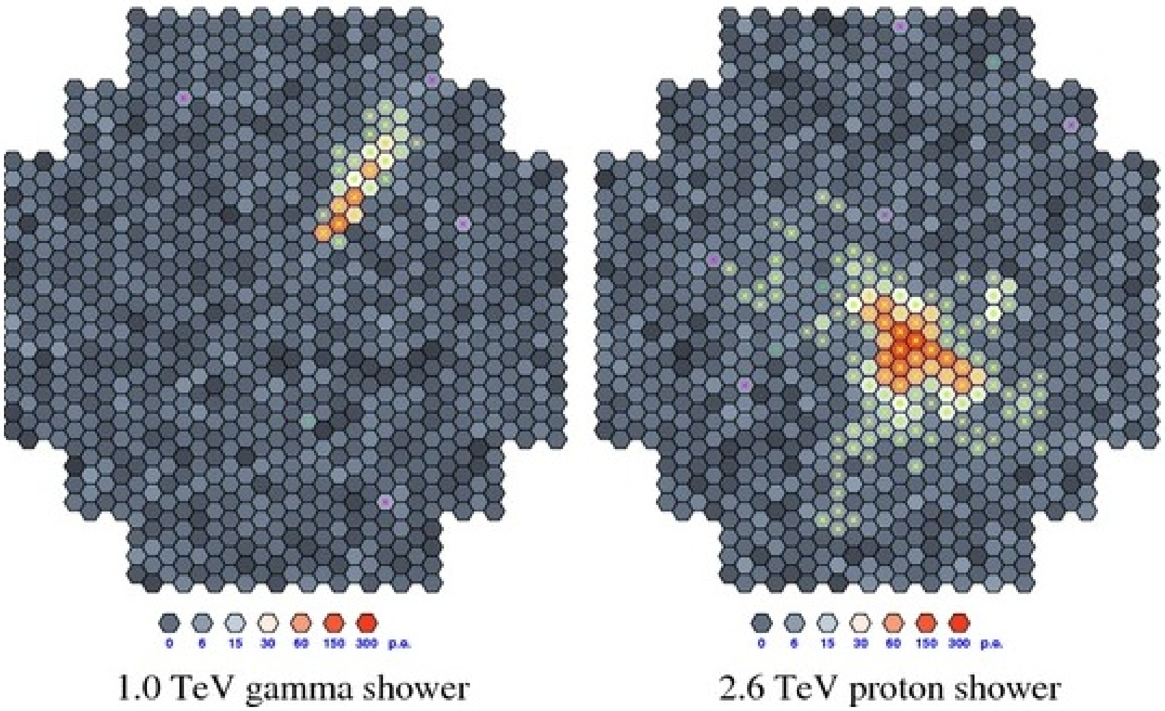

1.0 TeV gamma shower

2.6 TeV proton shower

Figure 4.2: Example of photon-triggered (left) and hadron-triggered (right) Cherenkov light. Taken from Völk & Bernlöhr (2009).

tion angle of the telescope. It is however smaller than the size of a camera pixel.
The angular resolution of the system, which depends on the uncertainty in the reconstruction of the shower, is roughly 0.1° (Aharonian et al. 2004).

Some observing time is dedicated to *calibration runs*, required to correctly calibrate the images of the Cherenkov showers. The *pedestal* run is performed with the camera lid closed, and consists in a measurement of the electronic output in absence of Cherenkov light; the *single photo-electron* run is performed measuring the light emitted by dedicated calibration LED pulsers, located in front of the PMs of the camera (see Fig. 4.1); the *flat-field* run consists of measuring the signal from LED flashers mounted on the telescope dishes, illuminating the camera in a homogeneous way. For more details on the *H.E.S.S.* calibration, see Aharonian et al. (2006a).
The calibration of the *H.E.S.S.* data is done off-line, once the acquired signal is transferred to Europe. It is done indipendantly by two groups, one in Heidelberg, the other in Paris, in order to perform a cross-check, and compare the different results.

4.2.1 The *ATOM* optical telescope

Located on the *H.E.S.S.* site, close to the five Cherenkov telescopes, *ATOM* (Automatic Telescope for Optical Monitoring)[3] is an optical telescope dedicated to the observation, in visible light, of variable γ-ray sources, and to the monitoring of AGN. It is of primary importance for blazar physics, because it provides a follow-up in visible of the TeV targets, assuring almost simultaneous multi-wavelength observations.

---

[3] The telescope is run by the *Landessternwarte* in Heidelberg. For more details see Hauser et al. (2004).

The telescope, a Cassegrain reflector characterised by a primary-mirror diameter of 75 cm and a focal length of 600 cm, is completely automated, performing observations in different filters (B,V,R, and I, as defined by Bessell 1990) which are retrieved the day after.
The calibration is done in a differential way, by looking at reference stars in the same field-of-view of the AGN, and the true magnitude value is then computed. The used extraction region has an aperture of 4".
The *ATOM* telescope also provides alerts for flares, as soon as a scheduled source shines above a pre-defined threshold.

Results from the *ATOM* telescope are used systematically in the AGN papers of the *H.E.S.S.* collaboration, and an example can be found for the case of *1RXS J101015.9 - 311909*, presented in Chapter 5.

4.3 *H.E.S.S.* data analysis

Once calibrated, the data are ready to be analysed, reconstructing the energy and position of the incoming photons. There are currently several analysis packages, which are used independently as cross-checks. The softwares used during this thesis are the ones developed within the *H.E.S.S.* collaboration in France: *HAP* (for *HESS Analysis Package*, developed at the APC laboratory and in Germany), and *ParisAnalysis* (developed at the LLR laboratory).
These two codes represent the general framework within which the analysis is performed (run-selection, sky-map calculation, spectral and timing analysis,...), but there exist other different methods of signal reconstruction. We will describe briefly here the three different signal-reconstruction algorithms that have been used in this thesis:

- the Hillas analysis (Hillas 1985)
- the Model analysis (de Naurois & Rolland 2009)
- the Multi-Variate analysis (Becherini et al. 2011b)

The Hillas analysis (Hillas 1985) is nowadays the standard analysis in IACTs, and consists in reconstructing the direction and energy of the photon by looking at the geometrical quantities of the shower image on the camera. In particular, the shower image is fitted to an ellipse, defined by the direction of the major axis, the length of the major and minor axis, and the position with respect to the camera center. The combination of the four images coming from the different telescopes are used to determine the best value of the arriving direction of the γ-ray (see Fig. 4.3). The integrated luminosity in the ellipse is used to evaluate the energy of the incoming γ-ray.
As discussed in the Introduction, the main problem in TeV astronomy is the background composed by the showers generated by cosmic-rays (which are much more numerous than the γ-rays we are interested in). They can be however discriminated from the γ-rays by looking at the radial distribution of the Cherenkov light, which is much broader for hadronic showers, as shown in Fig. 4.2. We can then define a threshold value (a *cut*) on the angular distribution to discriminate between a γ-ray like or a hadron-like shower.

The Model analysis (developed by Le Bohec et al. (1998) and improved for the specific case of *H.E.S.S.* by de Naurois & Rolland (2009)) is based on the comparison of the observed images with a grid of simulated images, as a function of the incoming photon direction and energy, zenith and azimuthal observing angle, and the depth of the first interaction with the atmosphere : each image is then fitted,

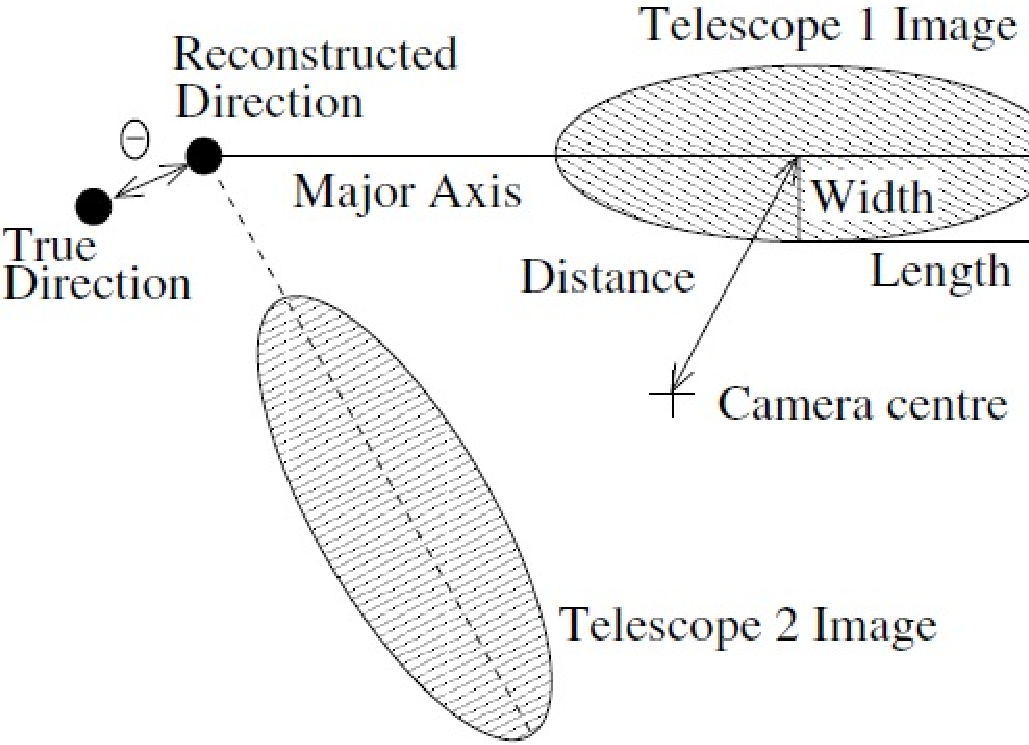

Figure 4.3: Basic parameters used in the standard Hillas analysis. In this case only the images from two telescopes are considered. Taken from Aharonian et al. (2006a).

providing direct access to the γ-ray photon parameters, and selecting (on the basis of the goodness of the fit) only the γ-ray candidates.[4]
The Model-3D analysis (Lemoine-Goumard et al. 2006), not used in this thesis, compares the Cherenkov images with the models coming from a three-dimensional modelling of the γ-ray shower, and is specifically developed for the *H.E.S.S.* stereoscopical data.

The third kind of analysis is a Multi-Variate analysis (MVA), which combines several parameters into a decision tree, improving the photon-hadron discrimination. Two different MVA analysis are available within the *H.E.S.S.* collaboration: the one developed by Ohm et al. (2009), which makes use of the standard Hillas parameters, and the one developed by Becherini et al. (2011b) (*Paris-MVA*), which makes use of both Hillas and Model-3D variables, significantly improving the sensitivity.

The Hillas and the Paris-MVA analysis are used in the framework of the HAP package, while the Model analysis is used in the ParisAnalysis package.

The preliminary step of the *H.E.S.S.* data-analysis is the run selection. The idea is to have a homogeneous data-set, discarding all the observations affected by bad or variable weather, or by technical problems. To do this, several discriminants can be considered: for the weather stability, a good estimator is given by the radiometer installed on each telescope, which are sensible, for example, to clouds crossing the field-of-view; for the image quality, we ask that the fraction of broken-pixels in the camera is lower than a certain threshold. Another aspect which can be chosen is the number of telescopes used in the observations: we can decide to work with a homogeneous set of 4-telescope runs, or to merge the 3 and

---

[4] For more details on this analysis see also Brun (2012) (in French).

4-telescope observations. For more details on the *H.E.S.S.* run-selection, see Aharonian et al. (2006a). Once the run-list is defined, we can proceed with the reconstruction of the γ-ray emission of a given source.

For the three analysis presented, an important point is that there is not a unique configuration of cuts which are applied in the photon-hadron discrimination, but we can choose between different configurations. The main difference is in the threshold of the charge contained in the γ-ray flagged image. For the HAP-Hillas analysis, there are three different configurations, named *loose*, *standard*, and *hard*, with a charge-threshold equal to 40, 60 and 120 photo-electrons, respectively.
For the Model analysis the situation is the same, but the *hard* configuration is called *faint*.
For the Paris-MVA analysis, the number of configurations is higher, defined for 40, 60, 80, 110 and 150 photo-electrons.

The charge threshold also somehow defines the low-energy threshold of the reconstructed spectrum, given the fact that faint showers are related to low-energy photons: the choice of the *loose* configuration is thus adapted to soft-spectrum sources (as, for example, distant AGN, whose spectrum is predicted to be particularly soft due to EBL absorption), while the *hard* configuration is adapted to hard-spectrum sources. On the other-hand, the *loose* cuts are more permissive, and the photon-hadron discrimination is worst. Generally an analysis is performed for all the different configuration, selecting the cuts which better allow an analysis of the source (but making sure that the detection is confirmed by different analysis, and is not a spurious signal from a single analysis-chain).

The first step of the data analysis is the computation of the significance of the signal detected from one source. In order to do this, it is fundamental to extract also a background signal, above which the significance of the source emission is calculated. There is a choice of different background substraction methods[5]: we present here the most standard background selection, used for point-like sources[6].
A *H.E.S.S.* observation is not performed with the target centered in the field-of-view, but it is explicitely mis-centered by 0.5° (*wobble* observation, see Aharonian et al. 2006a). The background region is then chosen symmetricaly to the source region (*reflected* background). In this way, the acceptance (the sensitivity of the instrument, which varies rapidly as a function of the offset with respect to the center of the field-of-view) of the two regions is the same. To improve the statistic of the background signal, multiple background regions are chosen (multiple-reflected background), on a circle of radius 0.5° around the pointed position (see Fig. 4.4).
Given that the acceptance is the same, the background signal has to be rescaled only by the higher geometrical area of the background region,[7] when compared to the source signal. This rescaling factor, named α, is equal, for the multiple-reflected background, to the inverse of the number of background regions used.

The *Reflected background* is not the unique choice for the *H.E.S.S.* analysis: an alternative is the *Ring background* method (showed as well in Fig. 4.4), in which the background region is defined as a continuous ring around the source. In the following, however, we will always work with the *Reflected background*.
The significance of the detection is then computed, using the formula computed by Li & Ma (1983). As

---

[5] In the *H.E.S.S.* and IACTs jargon, source and background regions are called ON and OFF, respectively.

[6] For extended sources, the choice of the source and background regions is much more complicated, and can even be performed with dedicated observations, if the source extension is large.

[7] It is thus the same as the *BACKSCAL* value defined in X-ray data-analysis.

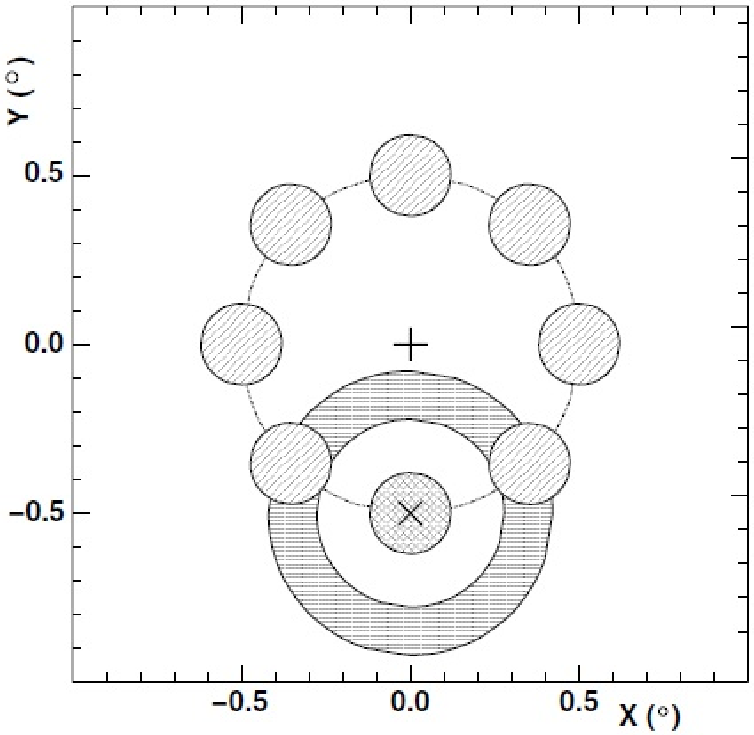

Figure 4.4: Definition of the background regions used in the analysis of *H.E.S.S.* data. The source position is marked with a cross, the pointing position is marked with a plus. The diagonal-filled regions represent the regions used in the *Reflected-background* method, while the horizontal-filled regions represent the *Ring-background* method. Taken from Aharonian et al. (2006a).

usual in high-energy physics, the threshold for a detection to be claimed is 5 σ (which corresponds to a chance probability of $\approx 10^{-7}$ that the observed signal corresponds to a fluctuation of the background). An interesting property is that, for a steady source, the significance is expected to grow following the square-root of the observing time: this relation is important if one wants to know whether a hot-spot in the field-of-view is likely a source candidate, and in this case to compute the expected observing time required to reach the 5 σ detection, or whether a source is variable (before computing the light-curve), by looking at strong deviations from the expected square-root function.

Another useful information is the angular distribution of photons expressed in ϑ^2 (with respect to the position of the source we are interested in) which, when fitted with the *H.E.S.S.* PSF, can be used to test whether the excess is consistent with a point-like source.

Once the reconstruction of the γ-ray photons coming from the source is completed, it is possible to perform a spectral analysis of the emission. The computation of the spectrum is done using the *forward-folding* technique, widely used in high-energy astrophysics. The spectrum we measure with our instrument (in X-rays as well in γ-rays) is not the spectrum emitted by the source, but is the result of the convolution of the intrinsic spectrum with the response function of our instrument (as well as the exposure-time, which can be not homogeneous in the region we are interested in). The main problem comes from the fact that the response-function matrix is not-invertible, and we cannot easily compute the intrinsic spectrum from the observed one. The solution is to assume *a priori* the source intrinsic spectrum, convolve it by the simulated response function, compute the expected observed spectrum, and

Table 4.1: Comparison between the *Hillas* and the *Model* analysis of the 2010 observations of *PKS 2155-304*, for different configurations (see Section 4.3).

Live time	standard		loose		hard/faint	
	σ_{Hillas}	σ_{Model}	σ_{Hillas}	σ_{Model}	σ_{Hillas}	σ_{Model}
23.2	31	49	23	56	19	37

Table 4.2: Comparison between the spectral analysis of the 2010 observations of *PKS 2155-304*, performed using the *Hillas* and the *Model* reconstruction methods (see Section 4.3).

	$Hillas_{standard}$	$Model_{standard}$
Γ	3.36 ± 0.13	3.52 ± 0.09
ϕ_{1TeV} $[10^{-12}$ cm^{-2} s^{-1} TeV$^{-1}]$	1.80 ± 0.16	1.91 ± 0.12

compare this estimation with the measure we have. We then need a statistical tool to determine whether the simulated spectrum and the observed one are in good agreement: in the *H.E.S.S.* data-analysis this is done by computing a likelihood function (see Piron 2000; Piron et al. 2001), which is then maximised as a function of the model parameters, providing the best solution.

The comparison between two different models is then performed by comparing the two maximum-likelihood values obtained.

Given the much lower number of photons that we have at VHE with respect to X-rays, it is difficult to study in detail the spectral distribution of TeV photons, and usually a power-law function represents the best-fit model for the TeV data (of extra-galactic sources). For the brightest sources it is possible, however, to study intrinsic curvature, or to test the presence of a high-energy cut-off.

The best-fit solution is usually plotted as an error-band at the 1-σ confidence level (which, for a power-law, is represented by a bow-tie); residuals to the fit can also be shown, by computing the differences between the expected and measured photon (for *H.E.S.S.* data, residual points corresponding to 3σ are usually shown).

It is also interesting to study variability behaviour of sources: while for faint sources statistics is usually too low to perform variability studies, bright sources (as *PKS 2155-304*, see Section 4.4) have revealed interesting flaring behaviour, of primary importance for our understanding of blazar physics.

The light-curve is computed by integrating the number of photons above a given threshold, and in a given time period. To compute the flux we need however the information on the spectral shape of the photons coming from our source, so we first perform the spectral fit on the overall data-set, and we then use this result to compute the light-curve (this assumes that the source varies only in flux, and not in spectral shape). In *H.E.S.S.* we study light-curves using three different standard time-bins: either run-by-run (integrating each observation on its own, which lasts 28 minutes), night-by-night (when multiple observations have been taken in the same night), or period-by-period (integrating the observations performed during a month). For bright and flaring sources, the time-binning required to characterise the temporal variability can be adapted, studying time-scales smaller than a single observation.

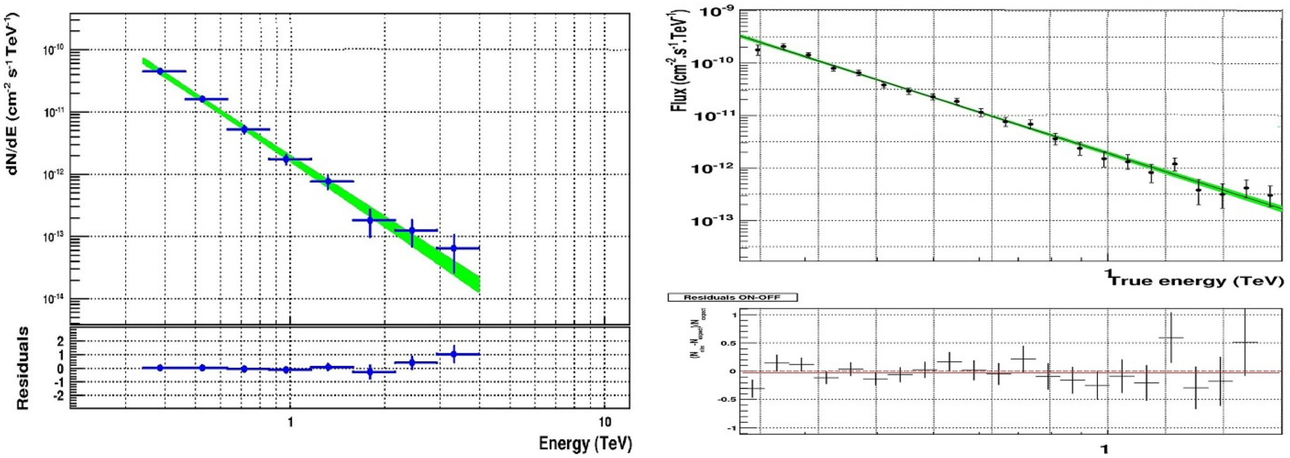

Figure 4.5: Spectral analysis of *H.E.S.S.* data of *PKS 2155-304*, as observed in 2010 (see Table 4.1). *Left:* spectral fit obtained using the *HAP* analysis package, with the *Hillas* analysis in the *standard* configuration; *Right:* spectral fit obtained using the *ParisAnalysis* package, with the *Model* analysis in the *standard* configuration.

4.3.1 Comparison of different analysis chains

In this Section we present a comparison between different analysis chains and reconstruction methods used in the *H.E.S.S.* collaboration. This step is mandatory before any *H.E.S.S.* publication, as it provides a cross-check for a source detection, or a spectral study.

We consider the BL Lac object *PKS 2155-304*, one of the brightest sources in the TeV sky, detected at high significance in few hours, even during low state. We concentrate in particular on the observations performed with *H.E.S.S.* in 2010, and we analyse them using both the HAP package, with the Hillas reconstruction method, and the ParisAnalysis package, with the Model reconstruction method. The run selection has been performed in HAP, and the same final run-list has been used for all the analysis. The data-set is composed of 52 runs, for a total live-time of $\approx$ 23 hours. For both reconstruction methods, we did the analysis using the three available configurations (*standard*, *loose*, *hard/faint*). In Table 4.1 we provide the information about the detection significance with the different analysis and configurations. As can be seen, the *Model* analysis is much more performant compared to the standard Hillas one, resulting in an increase of more than 10 σ for all the configurations.

This translates to a higher number of photons available for the spectral analysis, and thus a better evaluation of the spectral index (i.e. a smaller uncertainty). For a fit with a power-law function, performed using the results obtained with the *standard* configuration, we obtain, for the *Hillas* analysis, a value of $\Gamma = 3.36 \pm 0.13$, while for the *Model* analysis, a value of $\Gamma = 3.52 \pm 0.09$.

In this case, we can use the results obtained with the *Hillas* analysis as a true cross-check. For fainter sources we use as cross-checks two analysis with a similar sensitivity, as the *Model* and the *Paris-MVA*. An example, presented in detail in Chapter 5, is on *1RXS J101015.9 - 311909*: in this case, the result achieved with the *Hillas* analysis is a 5.2σ detection, using the *standard* configuration (2.3σ using the *loose* configuration), and the best-fit spectral index is 4.00 ± 0.80, with a statistical error significantly greater than the results achieved with the *Model* and *Paris-MVA* analysis (0.43 and 0.40, respectively).

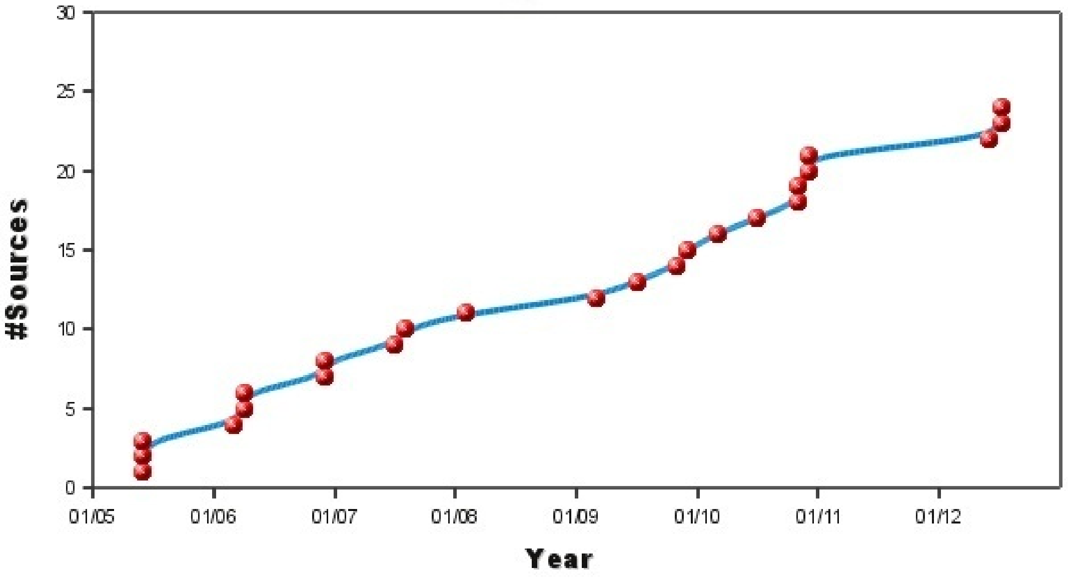

Figure 4.6: Number of extragalactic sources detected by *H.E.S.S.* as a function of time.

4.4 The *round-up* of *H.E.S.S.* AGN

The list of the twenty-four extra-galactic sources detected by *H.E.S.S.* is presented in Table 4.3: apart from the starburst galaxy *NGC 253* [8], all are radio-loud AGN. Among them are two radio-galaxies, one FSRQ, one LBL and twenty HBLs, which represent by far the dominant sub-class of AGN in the *H.E.S.S.* extra-galactic sky.
The number of detected extra-galactic sources as a function of time is shown in Fig. 4.6: the two steps in the detection number occouring in December 2009 and July 2012 represent the 2010 Texas symposium, and the Gamma 2012 symposium, respectively, during which new detections were announced.

In this Section we present a summary (a *round-up*) of the *H.E.S.S.* discoveries, emphasizing the outcomes in terms of our understanding of blazar physics, as well as the open questions.
In *H.E.S.S.*, the *round-up* represents the continous monitoring of *H.E.S.S.* AGN observations (with the delay imposed by the calibration of the data), updating the results from already known sources and following the evolution of *promising* sources. I was in charge of the *round-up* for the first two years of this thesis.

4.4.1 Radio-galaxies

Radio-galaxies are the only class of non-blazar AGN detected at VHE energies. Only five sources of this kind have been detected: *M87* (Aharonian et al. 2006e; Acciari et al. 2009a; Abramowski et al. 2012b) and *Cen A* (Aharonian et al. 2009c) by the *H.E.S.S.* collaboration, *NGC 1275* (Aleksić et al. 2012), *IC 310* (Aleksić et al. 2010) and *3C 66B* (Aliu et al. 2009) by the *MAGIC* collaboration. However, only three of them are confirmed, given the fact that *IC 310* has been proposed as a weakly-beamed blazar (Rec-

---

[8] Starburst galaxies do not present an active nucleus, but show an enhanced star formation with respect to normal galaxies. Higher star-formation means higher supernovae rate, which translates into higher cosmic ray flux inside the galaxy. The γ-ray emission comes from p-p collisions between cosmic rays and the local inter-stellar medium.

	Redshift	Ref.
Starburst Galaxies		
NGC 253	8.14×10^{-4}	Acero et al. (2009); H.E.S.S. Collaboration et al. (2012a)
Radio Galaxies		
M 87	0.0044	Aharonian et al. (2006e); Acciari et al. (2009a) Abramowski et al. (2012b)
Centaurus A	0.00183	Aharonian et al. (2009c)
FSRQs		
PKS 1510-089	0.36	Wagner & H.E.S.S. Collaboration (2010)
BL Lacs		
SHBL J001355.9-185406	0.095	Hofmann (2010b)
KUV 00311-1938	> 0.51 Pita et al. (2012)	Becherini et al. (2012)
RGB J0152+017	0.08	Aharonian et al. (2008c)
1ES 0229+200	0.14	Aharonian et al. (2006d)
PKS 0301-243	0.26	Wouters et al. (2012)
1ES 0347-121	0.188	Aharonian et al. (2007a)
1ES 0414+009	0.287	H.E.S.S. Collaboration et al. (2012b)
PKS 0447-439	> 0.176	Zech et al. (2011)
PKS 0548-322	0.069	Aharonian et al. (2010)
1RXS J101015.9-311909	0.143	H.E.S.S. Collaboration et al. (2012c)
1ES 1101-232	0.186	Aharonian et al. (2007c)
Mrk 421	0.031	Aharonian et al. (2005b)
1ES 1312-423	0.105	Becherini et al. (2011a)
PKS 1440-389	0.065(?)	Hofmann (2012)
AP Lib	0.049	Hofmann (2010a); Fortin et al. (2010)
PG 1553+113	0.43 – 0.58 Danforth et al. (2010)	Aharonian et al. (2006c, 2008a)
HESS J1943+213	> 0.14	H.E.S.S. Collaboration et al. (2011a)
PKS 2005-489	0.071	Aharonian et al. (2005c) H.E.S.S. Collaboration et al. (2011c)
PKS 2155-304	0.116	Aharonian et al. (2005d,e, 2007b) Aharonian et al. (2009a,b) H.E.S.S. Collaboration et al. (2010b) Abramowski et al. (2012a)
H 2356-309	0.165	Aharonian et al. (2006b) H.E.S.S. Collaboration et al. (2010a)

Table 4.3: Extra-galactic sources detected by *H.E.S.S.* up to July 2012, listed in order of type and Right Ascension.

tor et al. 1999), and the VHE emission from *3C 66B* is not clearly disentangled from the nearby blazar *3C66A*. All the three are FR I radio-galaxies (see Introduction), and are located quite nearby compared to the blazars detected at VHE.

The origin of the TeV emission from radio-galaxies is an open question, and several models have been proposed. The minimal variation approach consists in considering that the emission mechanism is the same as for blazars: a solution has been thus found by Lenain et al. (2008) by considering that at the basis of the jet can exist emitting regions moving in the direction of the observer, being affected by the same Doppler boosting as in blazars.
Alternative models consider the black-hole magnetosphere as responsible of the TeV emission (see e.g. Rieger & Aharonian 2008), or a hadronic origin (Reimer et al. 2004, similar to the proton-synchrotron model of blazar, discussed in Chapter 7).

In Fig. 4.7 we show the *H.E.S.S.* sky-map of *M87* and *Cen A*, with superimposed the respective radio-contours. It is important to underline that what is shown for both cases are not the extended giant radio-lobes (at a degree scale), but the more compact kilo-parsec radio-structures. The giant radio-lobes as source of the detected TeV emission are clearly excluded by the data.
A key for the understanding of the origin of the VHE emission is variability: multiwavelength campaigns, and measurement of the correlation between different energy bands, can help in associating the γ-ray emitting region to a particular structure in the kilo-parsec radio jet. The most complet result today is the work presented by Abramowski et al. (2012b), in which an overview over the last 10 years of MWL monitoring of *M87* is presented.
Another aspect is whether the emitting region is point-like or diffuse: the current-generation of IACT did not detect any extension in the radio-galaxy emission, but the expected capabilities of *CTA* will permit to put stronger constraints on this point.

4.4.2 FSRQs

Flat-Spectrum-Radio-Quasars represent the brightest sub-class of blazars (compared to the BL Lac objects). As discussed in Chapter 3, the current view is that their parent population is represented by the *FR II* radio-galaxies (while *FR I* radio-galaxies represent the parent population of BL Lac objects).

Their SED shows a low-frequency peak for the synchrotron bump (which peaks in infrared), while the high-energy bump peak is located in the MeV energy range (the measured *Fermi* spectral index is higher than 2.0). Given the fact that their redshift distribution peaks around $z = 1.0$ (while BL Lac objects are more commonly found at $z < 0.6$, Massaro et al. 2009), their TeV emission is heavily absorbed by γ-γ pair production on the EBL. For both their SED and redshift characteristics, their detection at VHE remains challenging for the current generation of IACTs.

Up to now, only three FSRQs have been detected at TeV energies: *3C 279* (MAGIC Collaboration et al. 2008) and *PKS 1222+21*[9] (Aleksić et al. 2011), by the *MAGIC* collaboration, and *PKS 1510-089*, detected by *H.E.S.S.* in 2010 (Wagner & H.E.S.S. Collaboration 2010).
The detection of *PKS 1222+21* has been of particular interest for the understanding of the physics of blazars given the extreme variability observed (detection of a flare at VHE, with a doubling time of less

---

[9] also known under the name *4C 21.35*

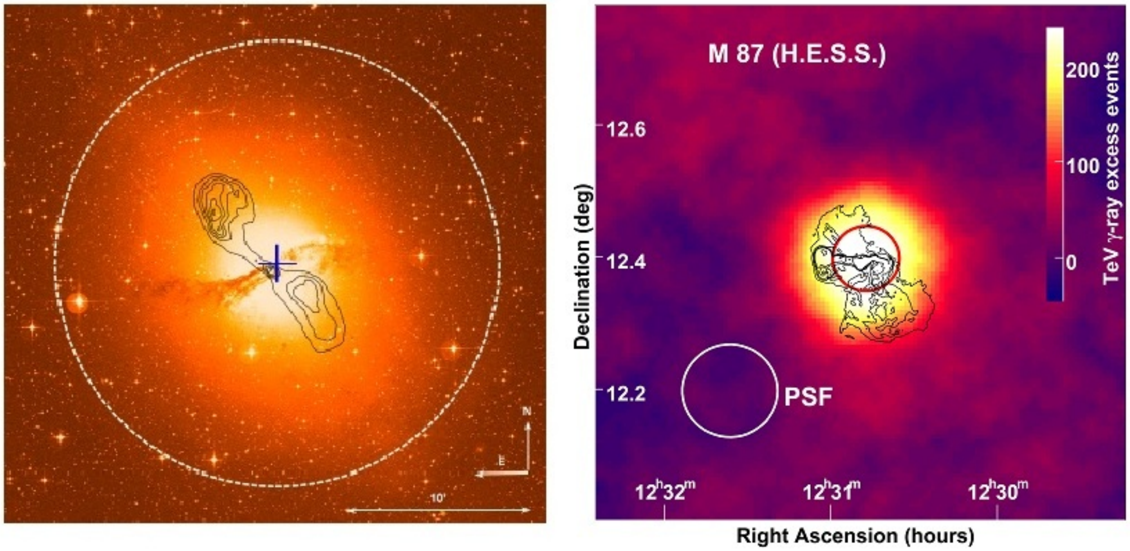

Figure 4.7: *Left*: Optical image of *Cen A* overlaid with radio contours (black, VLA, Condon et al. 1996), VHE best fit position with 1-σ statistical errors (blue cross), and VHE extension upper limit (white dashed circle, 95% confidence level). Taken from Aharonian et al. (2009c). *Right*: Smoothed TeV -ray excess map of *M87* as measured by *H.E.S.S.*. The size (68% containment radius) of the *H.E.S.S.* point spread function (PSF) is also indicated. The red circle indicates the intrinsic extension upper limit (99.9% confidence level) of 3 arcmin of the TeV γ-ray excess corresponding to 13.7 kpc in M87. The contour lines show the 90 cm radio emission (Owen et al. 2000). Adapted from Aharonian et al. (2006e).

than 10 minutes), which challenges the standard leptonic models. The variability time-scale implies in fact an emitting region size smaller than 2.5×10^{14} $(\delta/10)cm$; assuming that this size is related to the section of the conical jet, this implies a location of the emitting region close to the black hole (at only a few gravitational radii), but this would imply a location inside the broad-line region, resulting in a significant absorption by γ-γ pair production which is not observed (see Tavecchio et al. 2011, for a discussion of the problem, and for possible explanations in terms of EIC modelling). Alternative explanations have been proposed, such as secondary emission from cascades initiated by ultra-high energy cosmic rays emitted by the source (Dermer et al. 2012), or existence of photon-axion oscillations [10] (Tavecchio et al. 2012).

The FSRQ *PKS 1510-089* was detected by *H.E.S.S.* during a flaring activity state in both the GeV range (triggered by the *Fermi-LAT* collaboration) and in optical light (triggered by the *ATOM* telescope) during 2009. The source is detected at $\approx 9\sigma$ in roughly 15 hours of observing time. No significant variability was however observed in the *H.E.S.S.* data. The associated publication is currently in preparation.

4.4.3 LBLs

Low-frequency peaked BL Lac objects represent a rather uncommon class of AGN detected at VHE. As discussed in Chapter 3, even though they are more luminous than HBLs, their TeV emission is less important: given the fact that their high-energy bump peaks at lower energies (of the order of magnitude

---

[10] The TeV photon, oscillating into an axion, does not pair-produce on the low energy photon field, and can then escape the emitting region.

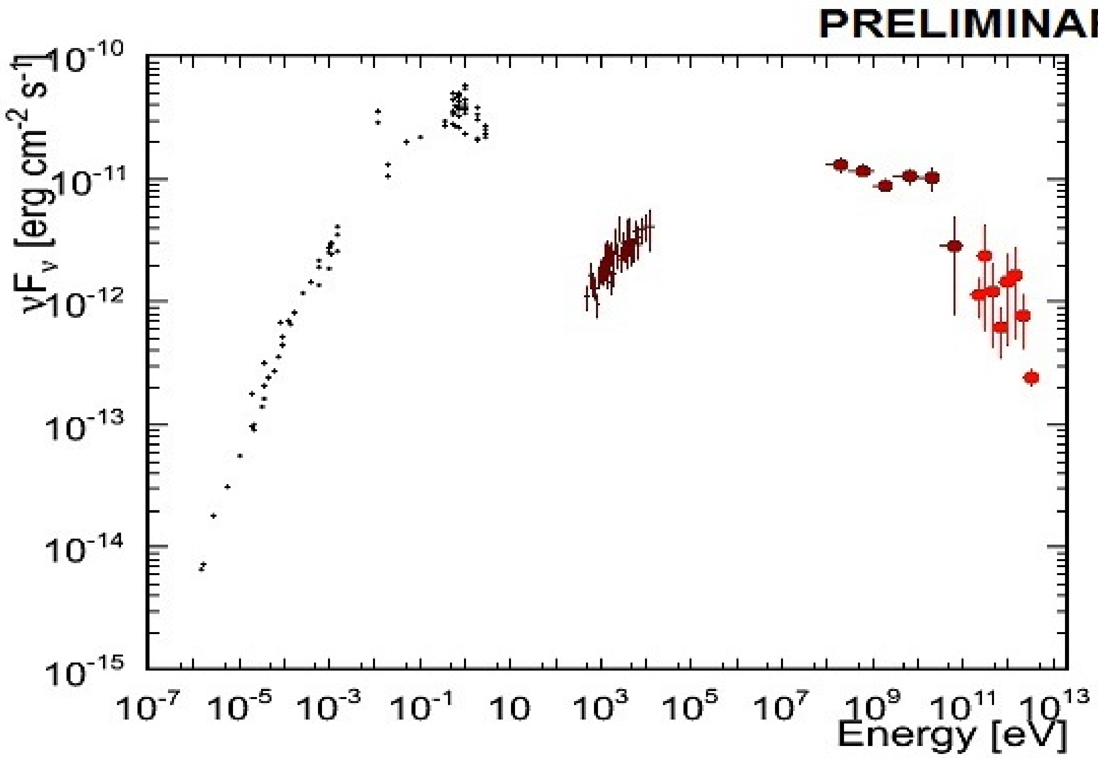

Figure 4.8: Spectral Energy Distribution of *AP Lib*. See Fortin et al. (2010) for details.

of 100 MeV), the part of the spectrum accessible to IACTs is the rapidly decreasing tail of the inverse Compton bump.

Up to now, only three LBLs have been detected at VHE: the eponymous *BL Lacertae* (Albert et al. 2007b) and *S5 0716+714* (Anderhub et al. 2009), by the *MAGIC* collaboration, and *AP Librae*, whose detection has been announced by the *H.E.S.S.* collaboration in 2010 (Hofmann 2010a).

The source was observed by *H.E.S.S.* following its detection at GeV energies by *Fermi-LAT*(with an integrated 0.3-300 GeV flux of $(1.9 \pm 0.1) \times 10^{-8}$ ph cm^{-2} s^{-1}, and a spectral index of 2.1 ± 0.1, see Fortin et al. (2010)): the TeV emission from the source was detected at 7σ in 11 hours of observation, with a flux corresponding to $\approx 2\%$ of the Crab nebula. The spectral index of *AP Lib* is (surpisingly) relatively hard, being equal to 2.5 ± 0.2.

The SED of *AP Lib*, shown in Fig. 4.8, is characterised by a very broad high-energy bump, covering almost nine orders of magnitudes (from keV to TeV). The broadness of such a component is all the more impressive as the synchrotron bump is quite narrow. In particular, this kind of SED cannot be modelled in a one-zone SSC scenario, and might be explained by considering external-Compton components or hadronic scenarios.

4.4.4 HBLs

High-frequency peaked BL Lac objects represent by far the largest class of AGN in the TeV sky (see the updated TeV Catalog [11], or Funk (2012) for a recent review on the γ-ray sky). Taking into account

---

[11] `http://tevcat.uchicago.edu/`

the results obtained by the *MAGIC* and *VERITAS* collaborations, the number of HBLs detected as TeV emitter approaches 40.

Among the *H.E.S.S.* HBLs, *PKS 2155-304* is the brightest and one of the most studied. It is regularly observed by *H.E.S.S.* since 2004, and is used as a bright point-like source for analysis tests. The most striking result is the impressive TeV flare detected in 2006 (Aharonian et al. 2007b), during which the source exceeded the Crab nebula flux by seven times, showing variability on a time-scale of few minutes. As for *PKS 1222+21*, this extreme variability implies an emitting region smaller than 4.65×10^{13} $(\delta/10)$ cm. This extremely small emitting region implies a small value of the gravitational radius of the central SMBH, and thus a low mass, of the order of 10^8 $M_\odot$ (for δ of the order of 10), which does not agree with the mass estimate through the measurement of the host galaxy luminosity. The solution would be to consider a high value of δ, of the order of 100. For a modelling of the flaring behaviour of *PKS 2155-304* in a standard one-zone SSC approach, see Katarzyński et al. (2008) or Abramowski et al. (2012a), who performed a multi-wavelength study of *PKS 2155-304*, modelling both low and flaring state of the source. Other models, which go beyond the SSC scenario, have been however proposed. Among them, it is worth mentioning the inhomogeneous model by Boutelier et al. (2008), the jets-in-jet scenario by Narayan & Piran (2012), the binary SMBH model by Rieger & Volpe (2010), or the star-jet interaction proposed by Barkov et al. (2012). The giant flare was used also to test for Lorentz-invariance break (variation of the value of the speed of light as a function of the photon energy), as presented by H.E.S.S. Collaboration et al. (2011b).

Another interesting result comes from the sources *1ES 1101-232*, *1ES 0229+200*, *1ES 0347-121* and *1ES 0414+009*. These HBLs share the same spectral property: when corrected for the EBL absorption, their TeV spectrum shows a spectral index $\Gamma < 2$, indicating that *H.E.S.S.* is currenlty measuring the rising part of the high-energy bump. This particular class of HBLs, with an inverse Compton bump peaking at energies $E > 1$ TeV is commonly referred to as *Extreme*-HBL (E-HBL in the following, even though this name is not unanimously used in literature; E-HBL can be used also to refer to a HBL showing a *synchrotron* peak around the keV). Such a high energy bump cannot be accounted for by a simple SSC scenario. A possible solution is to consider a high value of the minimum electron energy (Katarzyński et al. 2006; Kaufmann et al. 2011), but this adds a new free parameter (if $\gamma_{e;min}$ is low-enough, it does not play a role in the modelling, see Chapter 6). Hadronic or mixed lepto-hadronic models as presented in Chapter 7 may be applied to constrain the energy distribution of E-HBL.

The brightness of HBLs at VHE energies is also fundamental for non-AGN physics: the measurement of their TeV spectral distribution is used to determine the absorption induced by the EBL (see Section 3.5), and for this reason the detection of distant HBLs ($z > 0.5$, like *PG 1553+113*, discovered by *H.E.S.S.*, Aharonian et al. 2006c, , or *KUV 00311-1938*, presented in the next Section) is a primary goal of TeV astronomy. Distant HBLs are also used to test non-standard physics, like the existence of axions (de Angelis et al. 2007).

Finally, it is worth mentioning here the case of *HESS J1943+213*, a point-like source detected by *H.E.S.S.* in the Galactic survey, which is interpreted as the first TeV-discovered BL Lac object seen through the Milky Way (H.E.S.S. Collaboration et al. 2011a). The association with an AGN is confirmed by Leahy & Tian (2012) even though this interpretation is not unique (see Gabanyi et al. 2011)).

4.4.5 Latest *H.E.S.S.* results on blazars

We present now the latest results achieved by *H.E.S.S.* on blazars, and in particular the detection of TeV emission from *KUV 00311-1938* (among the farthest BL Lac object ever observed at TeV, of primary interest for the EBL studies), from *PKS 0301-243* (at z=0.26), and from *** ****-*** (the first serendipitous detection of an extra-galactic source by *H.E.S.S.*). The detection of the first two sources has been announced at the recent *GAMMA2012* symposium.
In April 2012 the detection of TeV emission from the BL Lac object *PKS 1440-389* was announced by the *H.E.S.S.* collaboration (Hofmann 2012). Up to now only preliminary analysis has been performed, and this result will not be discussed in the following.

KUV 00311-1938

The BL Lac object *KUV 00311-1938* is observed by the *H.E.S.S.* telescope array since 2009, as part of a search of TeV emission from high redshift sources. A tentative redshift for this source (z=0.61) was given by Piranomonte et al. (2007), as part of the optical survey of the *SHBL* catalog (catalog of high frequency peaked BL Lac objects, selected according to their high X-ray and radio flux Giommi et al. 2005). This redshift value (classified by the authors themselves as *tentative*) should not be considered as certain, even though is the redshift adopted in the 2FGL catalog (The Fermi-LAT Collaboration 2011).

An indipendent measurement of the redshift of *KUV 00311-1938* has been obtained (Pita et al. 2012) using the *X-Shooter* spectrograph on the VLT at ESO (Vernet et al. 2011). A lower limit of z>0.51 (through the detection of a MgII doublet of absorption lines, associated to an absorber located anywhere between the Earth and the AGN) is set. *KUV 00311-1938* is thus one of the farthest TeV detected sources (the farthest TeV sources detected so far being the FSRQ *3C 279* (MAGIC Collaboration et al. 2008), at z=0.536, and *PG 1553+113*, at $z \in [0.43, 0.58]$, (Danforth et al. 2010)).

H.E.S.S. observations, performed up to Autumn 2011 (for a total live-time of more than 60 hours) show a (preliminary) 6σ detection with the *Model* analysis, with *loose* cuts (adapted for the detection of soft sources, see Fig. 4.9 and 4.10). The spectrum of the source (shown in Fig. 4.11) is indeed soft (preliminarily evaluated at $\Gamma = 4.4 \pm 1.0$), which is at least for a large part due to the huge EBL absorption expected for such a high redshift.

The *Fermi-LAT* source associated with *KUV 00311-1938* has a spectral slope $\Gamma = 1.75 \pm 0.05$, suggesting a classification as a HBL (Abdo et al. 2010b). The detection of this new HBL in the TeV sky was announced at the recent *GAMMA2012* meeting, in Heidelberg (Becherini et al. 2012).

PKS 0301-243

The BL Lac object *PKS 0301-243* has been observed with *H.E.S.S.* between 2009 and 2011. The first direct measurement of the redshift of this source was obtained by Pita et al. (2012), who determined $z = 0.266$. This measurement is in agreement with the first estimation made by Falomo & Ulrich (2000), who suggested a resdhift of $z = 0.26$, thanks to the observation of some companion (non-actif) galaxies .

The source has been detected by *Fermi-LAT* as a bright GeV emitter (it is part of the *0FGL* catalog, the preliminary sample of bright GeV sources released by the *Fermi* collaboration, Abdo et al. 2009a). Its spectral index, in the more recent *2FGL* catalog, is $\Gamma = 1.94 \pm 0.04$. The source also showed flaring

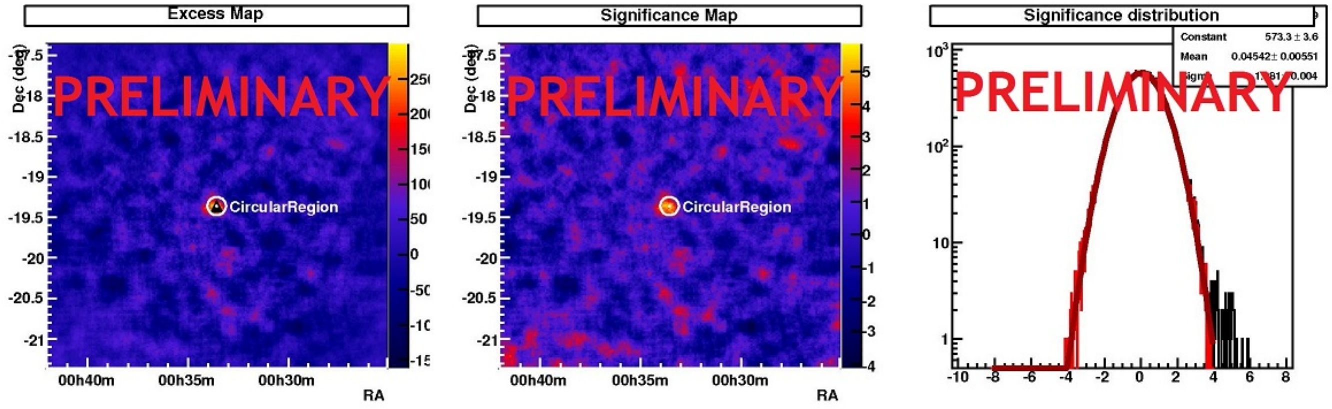

Figure 4.9: *H.E.S.S.* sky map centered on *KUV 00311-1938*. The three plots represent the excess sky-map (in number of photons), the significance sky-map, and the significance distribution, where the ON-region component is plotted in black, the OFF-region component is plotted in red, and the fit over the OFF-region component with a gaussian function is represented by the tick red-line, with the fit parameter showend in the top-right corner.

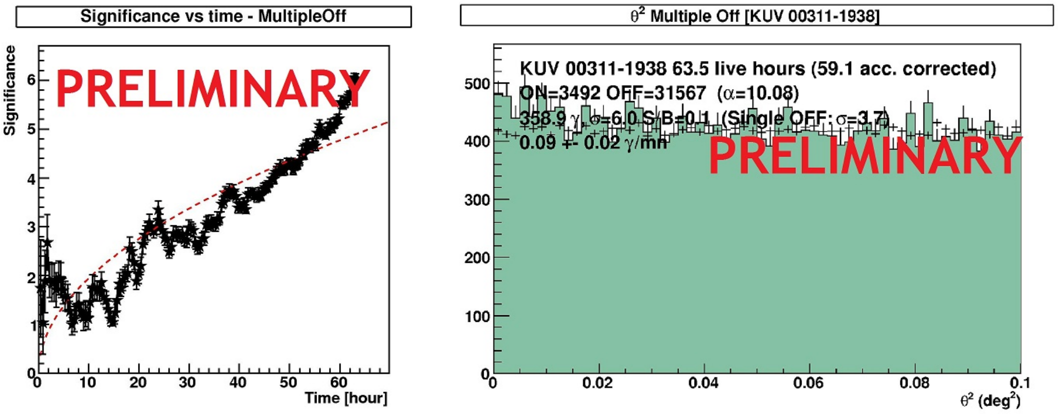

Figure 4.10: *Left:*Significance over time for *KUV 00311-1938*. *Right:* Theta-squared plot centered at the nominal position of *KUV 00311-1938*. Evaluated using the *Model* analysis with loose cuts.

activity during 2010 (Cannon 2010), reaching a flux ≈ 40 times higher than the steady GeV flux (unluckily, the target was not observable by *H.E.S.S.* during that period). Observations performed with the *Swift* X-ray satellite (Gehrels et al. 2004), showed that the source was also flaring at these energies.

The observations performed with the *H.E.S.S.* telescope array, for a total live-time of ≈ 40 hours, clearly reveal the TeV emission from the source, which is detected at more than 10σ (preliminary). The sky-map as seen by *H.E.S.S.* and the theta-squared plot are shown in Fig. 4.12 and 4.13.
As for *KUV 00311-1938*, the relatively high redshift of the source allows to put additional constrains on the EBL strength, and was publicily announced at the *GAMMA2012* symposium (Wouters et al. 2012).

*** ****-***

An analysis performed using the *Model* reconstruction techniques (presented in Section 4.3) on past *H.E.S.S.* observations of the BL Lac object *** ****-*** (not detected as TeV emitter, see Aharonian

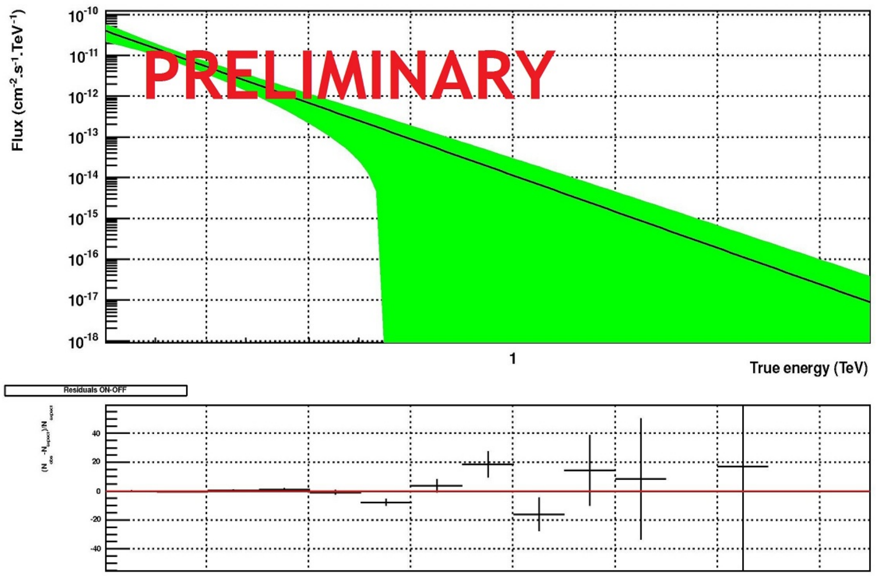

Figure 4.11: Spectrum of *KUV 00311-1938*, computed using the *Model* analysis, with loose cuts. The black-line represent the best-fit model; the green-band represent the $1-\sigma$ confidence band. *Bottom plot:* residuals to the fit.

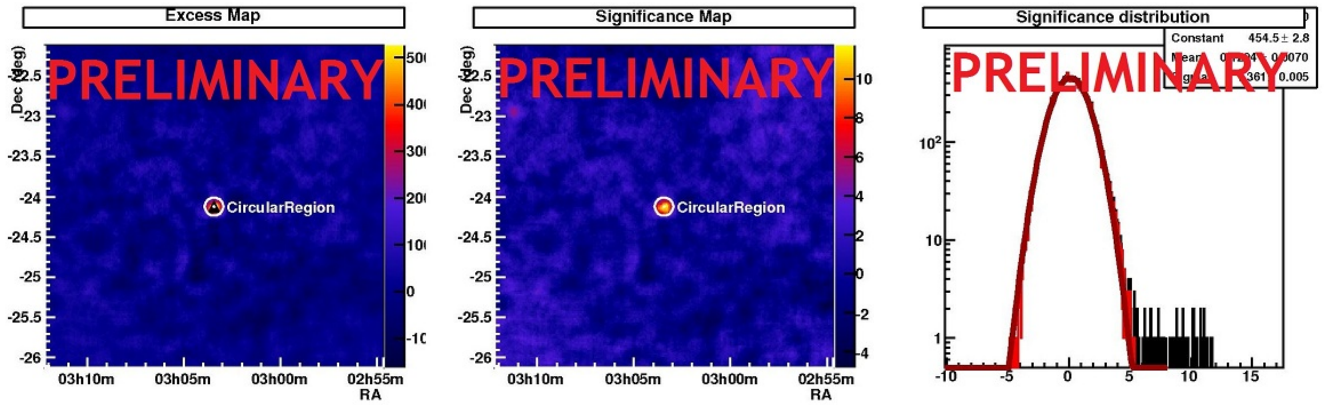

Figure 4.12: *H.E.S.S.* sky map centered on *PKS 0301-243*. The three plots represent the excess sky-map (in number of photons), the significance sky-map, and the significance distribution, where the ON-region component is plotted in black, the OFF-region component is plotted in red, and the fit over the OFF-region component with a gaussian function is represented by the tick red-line, with the fit parameter showend in the top-right corner.

et al. 2008b) revealed the presence of a hot-spot in the field of view (see reconstucted sky map in Fig. 4.14).

The dataset is composed of 21 runs (after quality cuts) taken in 2004 and 2006. The live-time on the hot-spot, corrected for the acceptance, is 3.1h.

The position of the hot-spot is consistent with the X-ray source *** ****-*** (also known as *** ****-***), classified as a blazar (Thomas et al. 1998) at a redshift of *.** (from the 6dF survey (Jones et al. 2009), even though this is the only value in the literature, and has not been confirmed yet). The _Fermi-LAT_ source _2FGL J****.*-****_ has been recently associated with this BLLac object (The Fermi-LAT Collaboration 2011).

An analysis centered at the nominal position of *** ****-*** shows that the hot-spot stands out at 6.0

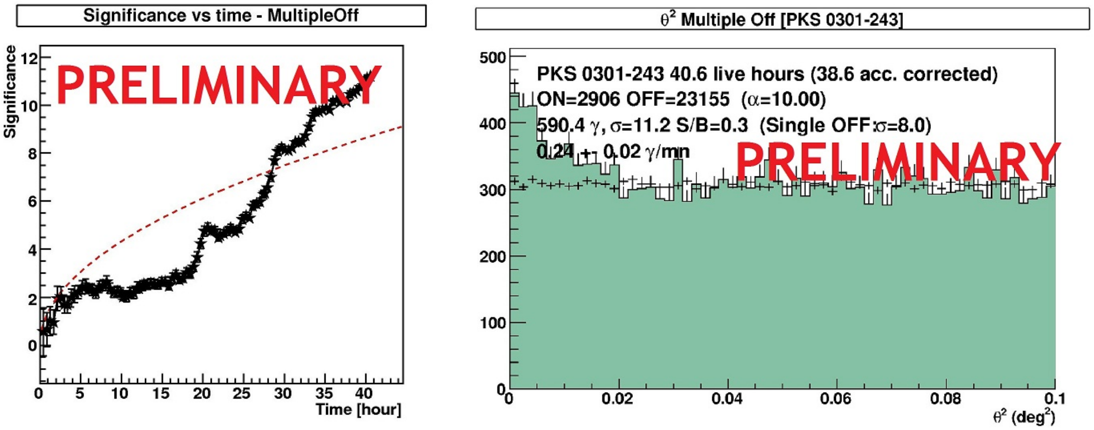

Figure 4.13: *Left:*Significance over time for *PKS 0301-243*. *Right:* Theta-squared plot centered at the nominal position of *PKS 0301-243*. Evaluated using the *Model* analysis with loose cuts

standard deviations (preliminary, not corrected for trials[12]) using *standard* cuts. In Fig. 4.14 and 4.15 we report, for the *standard* analysis, the theta squared plot, the evolution of the significance as a function of time and the sky map, respectively.
The spectrum of the source (Fig. 4.16) is well described by a power law function. The lightcurve (Fig. 4.17) is compatible with a constant, and no variability has been observed between 2004 and 2006.

This serendipitous detection (the first true one; the BL Lac object *1ES 1312-423* has been observed in the field-of-view of *Cen A*, but its detection was expected, and it has just benefitted of the large observation campaign on the nearby radio-galaxy) was followed by a new observation campaign in Autumn 2011 [13]: with the new data-set, composed of 16 hours of observations (the live-time corrected for the acceptance is 9 hours), the source stands out at more than 8σ (preliminary, not corrected for trials. However, the source is observed at more than 5σ using the pointed data-set only, the significance of the detection being certain).

The *Fermi-LAT* source associated with *** ****-*** has a spectral slope $\Gamma = *.* \pm *.*$, suggesting a classification as an *BL (Abdo et al. 2010b).

---

[12] The significance of the detection has to be corrected for the probability of observing such excess anywhere in the sky-map (the so-called *look-elsewhere* effect, see e.g. Gross & Vitells 2010).

[13] Indeed, the *Fermi* source associated with this BL Lac object was pointed out as potential target for IACTs indipendently from the serendipitous detection of the hotspot coincident with *** ****-***, and was scheduled for observations as a low-priority target. The discovery of the hot-spot was followed by a new proposal (accepted), asking for upgrading the source as a high-priority one.

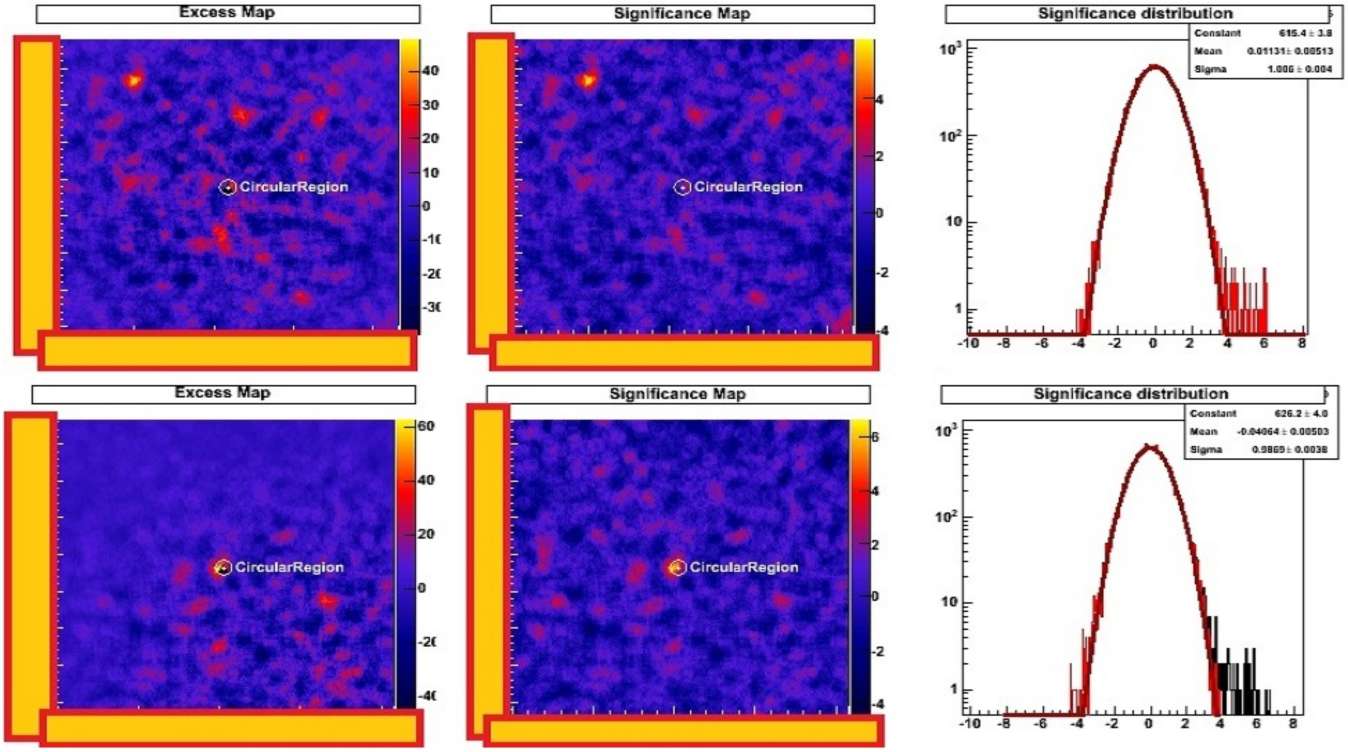

Figure 4.14: *Top:H.E.S.S.* sky map centered on *** ****-***. *Bottom:H.E.S.S.* sky map centered on *** ****-***. The three plots represent the excess sky-map (in number of photons), the significance sky-map, and the significance distribution, where the ON-region component is plotted in black, the OFF-region component is plotted in red, and the fit over the OFF-region component with a gaussian function is represented by the tick red-line, with the fit parameter showend in the top-right corner. Evaluated using the *Model* analysis with std cuts.

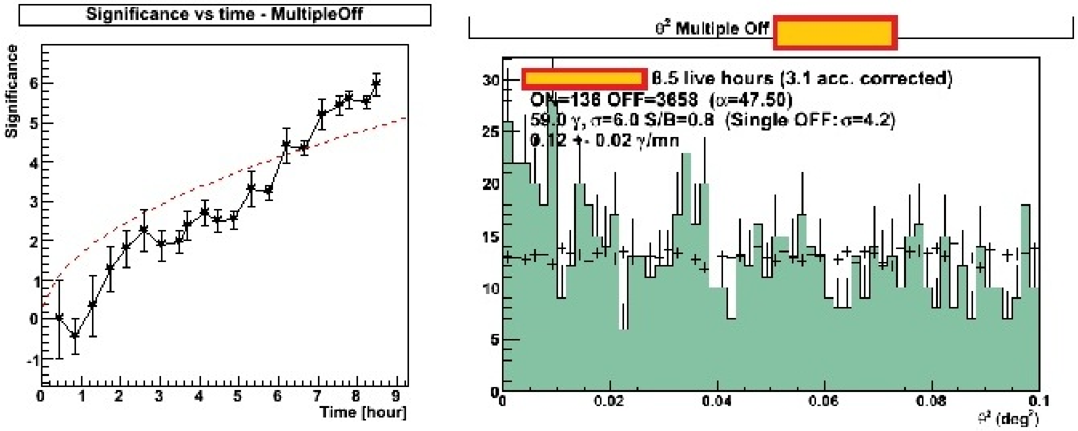

Figure 4.15: *Left:*Significance over time for *** ****-***. *Right:* Theta-squared plot centered at the nominal position of *** ****-***. Evaluated using the *Model* analysis with std cuts.

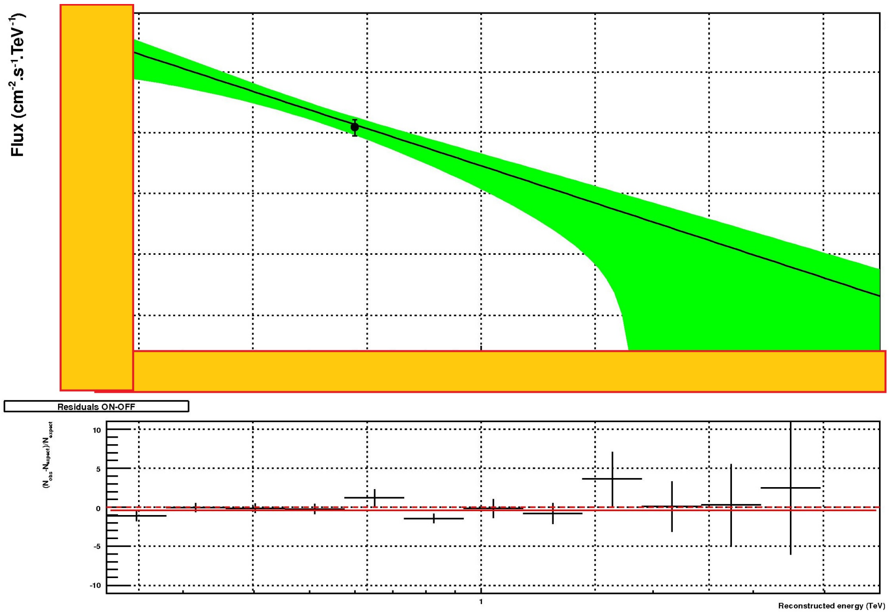

Figure 4.16: Spectrum of *** ****-***, computed using the *Model* analysis with std cuts.The black-line represent the best-fit model; the green-band represent the $1-\sigma$ confidence band. *Bottom plot:* residuals to the fit.

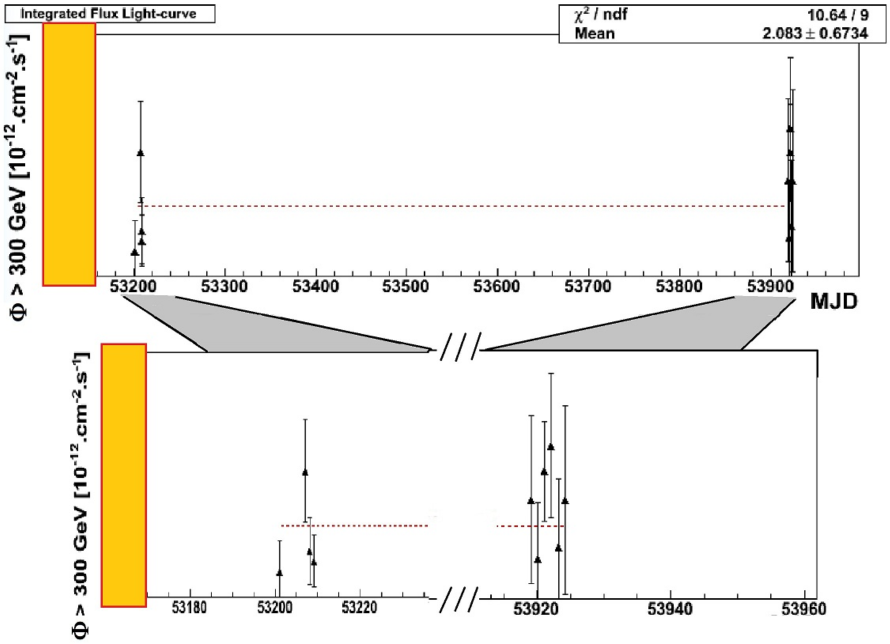

Figure 4.17: Lightcurve (night-by-night) of *** ****-*** during past *H.E.S.S.*observations. The red dotted line represents the fit of the observations with a constant function.)

4.5 Upper limits on undetected AGN

Since the beginning of scientific operations in 2004, the *H.E.S.S.* system observed a large number of AGN which do not reveal any clear emission of TeV γ-rays. A non-detection can be as important as a detection, providing interesting upper-limits on the flux, thus constraining the emission models.

An upper-limit is provided as an integral flux above a given threshold (it thus has units of $\mathrm{cm}^{-2}\ \mathrm{s}^{-1}$): the threshold used is provided directly by the analysis, and is calculated as the energy at which the effective area corresponds to a given fraction of the maximum effective area (0.1 in the following).

The upper-limit value also depends on the assumption done for the spectrum of the source: for AGN we consider a power-law with an index of 3.0 (Aharonian et al. (2008b) showed that this parameter affects the evaluation of the upper-limit only at the 10% level if we consider an uncertainty of 0.5 on the photon index).

The *H.E.S.S.* collaboration already published two papers on upper-limits on AGN observations (Aharonian et al. 2005f, 2008b) performed from 2004 to 2007.

In Table 4.4 we provide the evaluation of the upper-limits (at the 99% level) obtained with the *Model* analysis (*Standard* configuration), for sources observed up to 2011 (excluding the sources which are considered as *promising*).

Source	RA	dec	z	Type	E_{th}	$I(> E_{th})$
Mrk 1501	00 10 31.01	+10 58 29.50	0.089	Seyfert 1	0.33	0.433111
1FGL J0022.2-1850	00 22 17	-18 50 48	-	Unid	0.22	1.19447
1FGL J0030.7+0724	00 30 43	+07 24 12	-	Unid	0.33	1.17556
PKS 0048-097	00 50 41.32	-09 29 05.21	1.53	BL Lac	0.22	0.778848
1ES 0145+138	01 48 29.721	+14 02 17.77	0.13	BL Lac	0.33	2.38888
BWE 0210+1159	02 13 05.18	+12 13 10.91	0.25	BL Lac	0.40	0.455944
3EG J0215+1123	02 16 00	+ 11 22 48	-	Unid	0.40	0.44218
1RXS J023733.9-360330	02 37 34.01	-36 03 32.4	-	BL Lac	0.27	1.64273
NGC 1068	02 42 40.77	-00 00 47.84	0.0038	Seyfert 2	0.22	1.9421
RBS 413	03 18 51.79	+18 45 33.84	0.19	BL Lac	0.29	0.700994
RBS 421	03 25 41.09	-16 46 16.9	0.29	BL Lac	0.22	1.40075
1ES 0323+022	03 26 13.91	+02 25 14.74	0.15	BL Lac	0.22	0.86995
1RXS J033311.8-361942	03 33 09.6	-36 19 40	0.31	BL Lac	0.22	0.413507
PKS 0352-686	03 52 57.55	-68 31 16.8	0.087	BL Lac	0.59	0.271238
3C 120	04 33 11.10	+05 21 15.22	0.033	Seyfert 1	0.27	2.2547
1ES 0507-040	05 09 38.2	-04 00 46.0	0.31	BL Lac	0.22	2.01068
Pictor A	05 19 49.74	-45 46 43.70	0.034	Seyfert 1	0.22	1.22068
PKS 0521-365	05 22 57.98	-36 27 30.85	0.055	BL Lac	0.22	3.12878
EXO 0556.4-3838	05 58 06.20	-38 38 27.0	0.302	BL Lac	0.22	1.93076
PKS 0558-504	05 59 46.78	-50 26 39.3	0.14	Seyfert 1	0.33	0.650075
RGB J0812.0+0237	08 12 01.90	+02 37 32.60	-	BL Lac	0.27	6.46594
Hydra A	09 18 05.65	-12 05 43.99	0.055	LINER	0.22	2.66013
RGB J1117+202	11 17 06.25	+20 14 07.4	0.14	BL Lac	0.40	1.19083
NGC 3783	11 39 01.721	-37 44 18.60	0.0096	Seyfert 1	0.18	3.00122
RBS 1049	11 54 04.56	-00 10 09.6	0.25	BL Lac	0.27	3.09236
1ES 1218+30.4	12 21 21.92	+30 10 36.83	0.184	BL Lac	0.18	0.890967
3C 273	12 29 06.69	+02 03 08.66	0.16	Quasar	0.22	1.45812
3C 279	12 56 11.17	-05 47 21.52	0.54	Quasar	0.22	1.57925
1ES 1440+122	14 42 48.23	+12 00 39.93	0.16	BL Lac	0.27	1.95393
Arp 220	15 34 57.272	+23 30 10.48	0.018	Seyfert	0.49	0.366891
PKS 2004-447	20 07 55.18	-44 34 44.27	0.24	Seyfert 1	0.32	0.605505
SHBL J213135.4-091523	21 31 35.45	-09 15 22.70	0.449	BL Lac	0.22	0.826658
NGC 7213	22 09 16.26	-47 09 59.95	0.006	Seyfert 1	0.27	1.70825
PG 2209+184	22 11 53.89	+18 41 49.86	0.07	Seyfert 1	0.49	0.849506
3C 445	22 23 49.5	-02 06 13	0.056	Seyfert 1	0.22	2.22225
RBS 1888	22 43 41.6	-12 31 38	0.23	BL Lac	0.22	1.02441
3EG J2248+1745	22 48 57.6	+17 46 12	-	Unid	0.40	0.976687
HS 2250+1926	22 53 07.37	+19 42 34.59	0.28	Seyfert 1	0.49	0.385247
2QZ J225453.2-272509	22 54 53.225	-27 25 09.23	0.33	BL Lac	0.18	1.7565
NGC 7469	23 03 15.674	+08 52 25.28	0.016	Seyfert 1	0.27	1.86209
PKS 2316-423	23 19 05.92	-42 06 48.69	0.056	BL Lac	0.22	0.998839
2FGL J2339.6-0532	23 39 51	-05 30 42	-	Unid	0.22	1.13104
1ES 2343-151	23 45 38.2	-14 49 28	0.22	BL Lac	0.18	0.609062

Table 4.4: Upper limits on the AGN observed by *H.E.S.S.*, listed in order of Right Ascension. *Unid* in the classification column refers to unidentified γ-ray sources. The threshold energy E_{th} is given in TeV; the upper limits ($I(> E_{th})$) are in units of 10^{-12} cm^{-2} s^{-1}.

Chapter 5

A specific case : *1RXS J101015.9 - 311909*

Contents

5.1 Introduction

In this Chapter we present and discuss the detection of VHE γ-ray emission from the BL Lac object *1RXS J101015.9 - 311909* (Section 5.2). In order to fully describe the spectral energy distribution (SED) of this object, an analysis of multi-wavelength data has been performed, in particular using public data from the *Fermi-LAT* and *Swift* satellites, and optical data from the *ATOM* telescope (Section 5.3). The modelling of the SED using a stationary one-zone synchrotron-self-Compton (SSC) model is presented in Section 5.4.

1RXS J101015.9 - 311909 was detected for the first time as a bright X-ray source with the *Rosat* X-ray telescope (1RXS being the acronym for the first *Rosat* X-ray Survey catalog, in which the source has been presented for the first time, Voges et al. (1999)). The 0.1 to 2 keV flux measured with *Rosat* (with observations performed in 1990/91) was 2.9×10^{-11} erg cm^{-2} s^{-1}
The X-ray object was associated by Bauer et al. (2000) and Giommi et al. (2005) to a radio source and an infrared/optical galaxy (known as *NVSS J101015-311906* and *2MASX J10101597-3119088*, respectively). Giommi et al. also identified the BL Lac nature of the object, including it in their SHBL (Sedentary High-frequency-peaked BL Lac object) catalog, under the name *SHBL J101015.9-311908*.
Piranomonte et al. (2007) analysed the optical counterparts of the SHBL catalog, measuring for the first time the distance of *1RXS J101015.9 - 311909* through the detection in the optical spectrum of absorption

year	MJD$_{start}$	MJD$_{end}$	N_{runs}	Live-Time	zen	N_{ON}	N_{OFF}	N_{γ}	σ
2006	54090.09	54090.11	1	0.43	12.7	17	126	5.5	1.5
2007	54142.95	54238.79	35	14.52	11.7	551	4835	111.5	4.9
2008	54475.07	54535.92	12	5.37	10.1	136	1291	18.6	1.6
2009	54832.06	54976.79	36	15.26	14.4	457	3968	96.2	4.6
2010	55265.90	55299.84	29	12.80	13.6	255	2466	30.8	1.9
Tot.	54090.09	55299.84	113	48.70	12.9	1416	12686	262.7	7.1

Table 5.1: Summary of good-quality data of *H.E.S.S.* observations of *1RXS J101015.9 - 311909* over the years 2006-2010. The columns represent the observation year, the beginning and end of the observations (expressed in modified julian day), the number of runs, the total live-time (in hours), the mean zenith angle (in degrees), the number of source (N_{ON}) and background (N_{OFF}) events, the number of excess events (N_{γ}) and the significance of the detection (in standard deviations). For the entire data-set, the observation off-set is 0.5°, and the background normalization (α factor) is 0.09.

features associated to its host galaxy : the redshift of the source is evaluated at $z = 0.143$.
In 2011 the *Fermi* collaboration announced the detection of GeV emission from *1RXS J101015.9 - 311909* after two years of data taking, including the source in the 2FGL catalog (Second Fermi Gamma-ray LAT catalog, The Fermi-LAT Collaboration (2011)) under the name *2FGL J1009.7-3123*.

Costamante & Ghisellini (2002) proposed a simple criterium for the selection of TeV-emitter-candidate HBLs, based on their radio and X-ray flux. The basic idea is that in order to efficiently produce TeV photons through an inverse Compton process, both high energy electrons and soft photons are needed, the first ones being estimated through the X-ray flux of the source, the second through its radio flux (even though with contamination from the external regions of the jet). Therefore, if one considers two sources with the same X-ray flux, the most-likely TeV emitter should be the one with the highest radio flux.
As *1RXS J101015.9 - 311909* fulfilled the criteria given by Costamante & Ghisellini, being in the top-right part of the plot X-ray-flux vs. radio-flux, and given the relatively weak EBL (Extra-galactic Background Light) absorption expected for the redshift of the source, *H.E.S.S.* started observing *1RXS J101015.9 - 311909* in 2006, integrating data up to 2010.
The detection of the source has been announced at several conferences (the first time at the *Texas* symposium, in December 2010 (Becherini et al. 2011a), then at the ICRC 2011 conference (Cerruti 2011)) before the publication in a refereed journal (H.E.S.S. Collaboration et al. 2012c, ; corresponding authors: Yvonne Becherini, myself and Jean-Philippe Lenain). In this Chapter we provide a more detailed account of the work.

5.2 Detection of TeV emission with *H.E.S.S.*

Observations of *1RXS J101015.9 - 311909* were carried out with the *H.E.S.S.* array in a campaign of 64 hours of observations performed from 2006 to 2010. After a run selection based on hardware and weather quality selection-criteria (as discussed in Aharonian et al. 2006a), the total live-time of observations is roughly 48.7 hours. The mean zenith angle of the run-list is 12.9°, with a pointing offset of 0.5° with respect to the nominal position of the source (*wobble* observation mode, see Aharonian et al. 2006a). Details on the data-set (divided per year of observation) are given in Table 5.1.

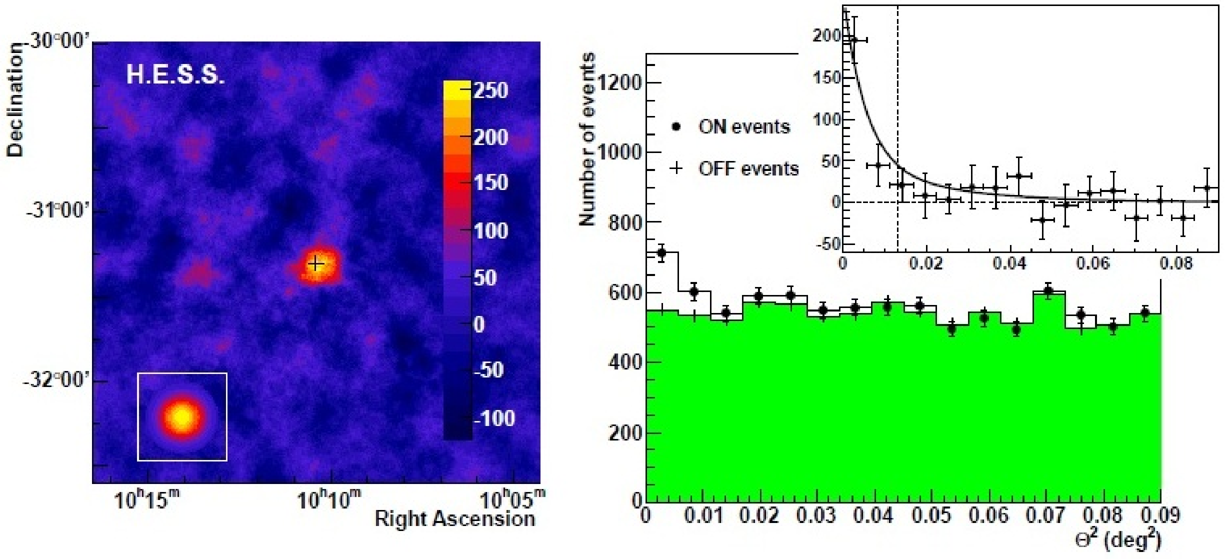

Figure 5.1: *Left*: Excess map of *1RXS J101015.9 - 311909* as seen by *H.E.S.S.*. The gamma-ray excess has been oversampled with the 68% containement radius of the PSF (which is equal to 0.116° for these analysis cuts). The black cross represents the nominal position of the source. The inset shows the expected excess distribution from a point-like source.
Right: Angular distribution (ϑ^2) of source (ON) and normalized background (OFF) events centered at the nominal position of *1RXS J101015.9 - 311909*. The inset shows the distribution of excess events at the fitted position of the source, fitted (black line) by the PSF. The containement radius at 68% of the PSF is 0.116° and is shown by the dashed vertical line.

The analysis of the gamma-ray emission from *1RXS J101015.9 - 311909* has been carried out with the enhanced (with respect to the standard Hillas analysis, Aharonian et al. 2006a) analysis algorithm described in Becherini et al. (2011b) (see also Section 4.3). The analysis configuration with a charge value threshold of 40 photoelectrons has been used. The VHE γ-ray emission is detected with a significance of 7.1σ, using the *Reflected* background method (see Aharonian et al. 2006a, and Section 4.3).
In the left plot of Fig. 5.1 the excess map of *1RXS J101015.9 - 311909* is shown, while in the right plot the angular distribution of events for both ON-source and normalized OFF-source events is reported. The background is flat, and the excess of emission at the nominal position of the source is clearly observed. A fit to the excess events of a point-like source model convolved with the *H.E.S.S.* point-spread-function (PSF) yields a position $\alpha_{2000} = 10^h10^m15.03^s \pm 3.77^s_{stat} \pm 1.56^s_{sys}$ and $\delta_{2000} = -31^\circ18'18.4'' \pm 14.6''_{stat} \pm 20''_{sys}$, consistent with the positions of the radio and X-ray sources (see Fig. 5.3).
A cross-check has been performed using the *ParisAnalysis* package, which contains the *Model* analysis developed by de Naurois & Rolland (2009). The analysis, perfomed using the same run-list as for the *MVA* analysis, and *loose* cuts, yields a 7.9σ detection, with an excess of 434 photons (see Fig. 5.2).

5.2.1 Spectral and temporal analysis

The time-averaged VHE γ-ray spectrum of *1RXS J101015.9 - 311909*, derived using the forward-folding technique described in Section 4.3, is shown in the left plot of Fig. 5.4. The data are well-fitted by a power-law function $dN/dE = \phi_0 \cdot (E/1\ \mathrm{TeV})^{-\Gamma}$, with normalization factor $\phi_0 = (1.87 \pm 0.66_{stat} \pm 0.37_{sys}) \times 10^{-13}\ \mathrm{cm^{-2}\ s^{-1}\ TeV^{-1}}$ and photon index $\Gamma = 3.08 \pm 0.43_{stat} \pm 0.20_{sys}$. The differential flux

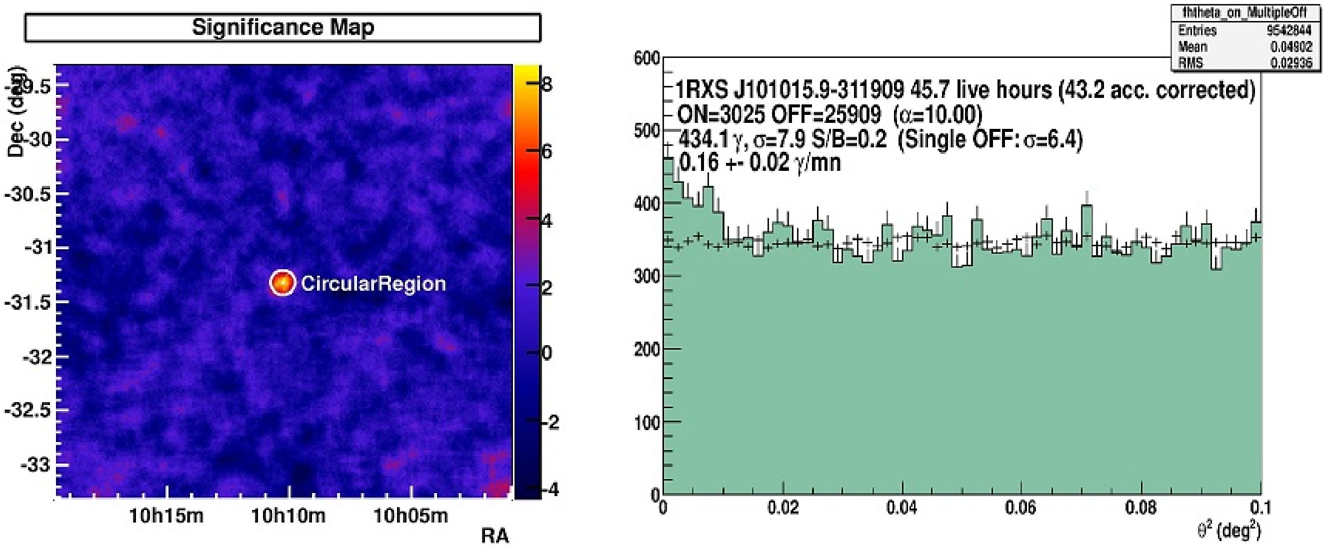

Figure 5.2: *Left*: Excess map of *1RXS J101015.9 - 311909* as seen by *H.E.S.S.*with the *ParisAnalysis* package. This result represents a cross-check with respect to the published result.
Right: Angular distribution (ϑ^2) of source (ON; filled histogram) and normalized background (OFF; black crosses) events centered at the nominal position of *1RXS J101015.9 - 311909*, obtained with the *ParisAnalysis*. This result represent a cross-check with respect to the published result.

at the decorrelation energy (see Chapter 4) (in this case E_{dec} = 510 GeV) is $\phi_{E_{dec}} = (1.47 \pm 0.31_{stat} \pm 0.29_{sys}) \times 10^{-12}$ cm^{-2} s^{-1} TeV^{-1} while the integral flux above the analysis threshold E_{th} = 200 GeV is $\phi\,(E > E_{th}) = (2.35 \pm 0.64_{stat} \pm 0.47_{sys}) \times 10^{-12}$ cm^{-2} s^{-1}, corresponding to roughly 0.8% of the Crab nebula.
The cross-check performed with the *Model* analysis is completely consistent with the published spectrum. A fit performed assuming a power-law hypothesis yields a normalization factor $\phi_0 = (1.50 \pm 0.58_{stat}) \times 10^{-13}$ cm^{-2} s^{-1} TeV^{-1} and a photon index $\Gamma = 3.17 \pm 0.40_{stat}$ (see Fig. 5.5).

The *H.E.S.S.* light-curve is shown in the right plot of Fig. 5.3: no significant variability is detected during the four years of observation. A fit of the period-by-period (a *H.E.S.S.* observing period is defined as the period between two full moons) light curve with a constant value yields a $\tilde{\chi}^2 = 11.39/9$, with a probability of 25%. The measured normalized excess variance[1] of 0.44 ± 0.71 on the same light-curve yields a 99% confidence level upper limit on the fractional variance of 151%, as calculated using the method of Feldman & Cousins (1998). No variability can be seen either in other time binnings tested (night-by-night or run-by-run).

---

[1] The normalized excess variance is defined as $\sum_i ((x_i - \bar{x})^2 - \sigma_i^2)/N\bar{x}^2$, and represents the variance to the mean value, taking into account the statistical uncertainties. The fractional variance represents the square root of this value (see e.g. Vaughan et al. 2003).

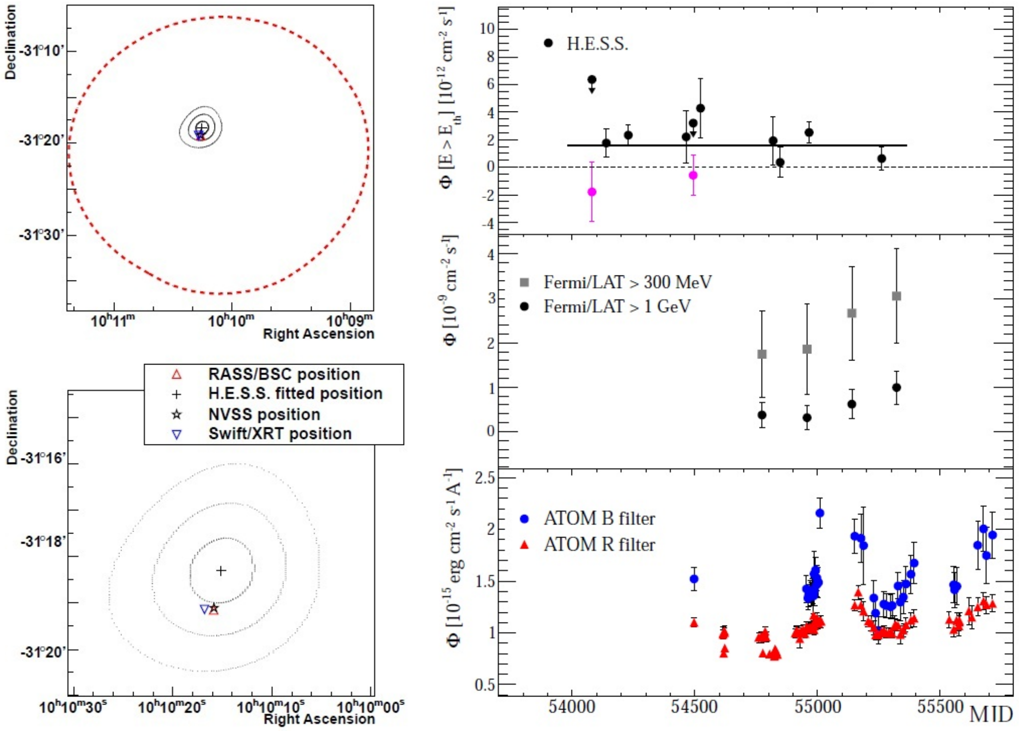

Figure 5.3: *Left* : *Upper panel*: The red dashed line represents the 1 σ significance contour of the *Fermi* detection, while the three black line represent the 1,2, and 3 σ contours of the *H.E.S.S.* detection. *Lower panel*: Zoom on the *H.E.S.S.* fitted position, compared to the radio (*RASS/BSC* and *NVSS*) and X-rays (*Swift-XRT*) positions.
Right: *Upper panel*: Light curve of *H.E.S.S.* observations of *1RXS J101015.9 - 311909* binned with one point per observing period (between two full moons). The black line represents the mean flux measured by *H.E.S.S.*. When no signal is detected (pink points), upper limits (at 99% confidence level) are calculated. *Middle panel*: Light curve of *Fermi* observations of *1RXS J101015.9 - 311909* for the $E > 300$ MeV (grey squares) and $E > 1$ GeV (black dots) thresholds in a 6-month binning. The first two flux points of the $E > 300$ MeV light-curve, and the first three of the $E > 1$ GeV light-curve have $TS < 9$. *Bottom panel* : Light curve of *ATOM* observations of *1RXS J101015.9 - 311909*with R (red points) and B (blue points) filters. Data have been corrected for Galactic extinction assuming $E_{B-V} = 0.104$ (case A, see Section 5.3.2.

5.3 Multi-wavelength data

5.3.1 *Fermi*

As already recalled, a *Fermi-LAT* source from the 2FGL catalog (*2FGL J1009.7-3123*, see The Fermi-LAT Collaboration 2011) has been associated with *1RXS J101015.9 - 311909*. A *Fermi-LAT* analysis has been performed on the publicly available data, spanning the time interval from 2008-08-04 (MJD 54682) to 2011-01-01 (MJD 55562), using the binned likelihood method (Atwood et al. 2009) from the *Science Tools* package *V. v9r23p1*, following the procedure reccommended by the *Fermi-LAT* collaboration [2]. The isotropic model *iso_p7v6source* is used to account for both the extragalactic diffuse emission and residual instrumental background, while the spatial template *gal_2yearp7v6_v0* is used to account for the contribution from the Galactic diffuse emission.

Since *1RXS J101015.9 - 311909* lies at a Galactic latitude of 20.05°, the centre of the region of inter-

---

[2] see `http://fermi.gsfc.nasa.gov/ssc/data/analysis`

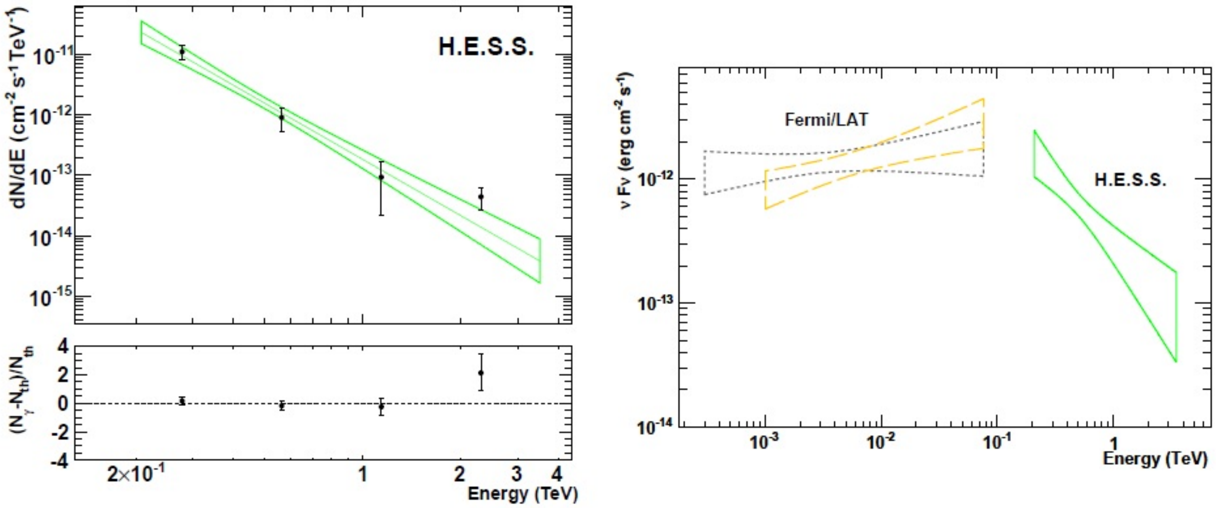

Figure 5.4: *Left panel*: Time-averaged VHE spectrum of *1RXS J101015.9 - 311909* measured by *H.E.S.S.*. The bow-tie represents the 1σ confidence level of the fitted spectrum using a power-law function. The lower panel shows the fit residuals $(N_\gamma - N_{th})/N_{th}$, where N_γ and N_{th} are the number of detected and expected excess events, respectively). *Right panel*: *Fermi* and *H.E.S.S.* bow-ties (expressed in $\nu \cdot F(\nu) = E \cdot F(E)$). The *Fermi* spectra are shown for an energy threshold of 300 MeV and 1 GeV with the dotted black line and the yellow dashed line, respectively.

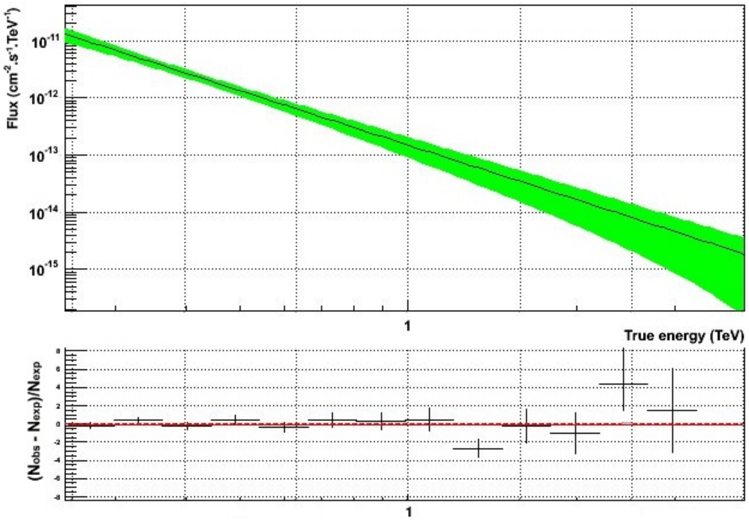

Figure 5.5: Time-averaged VHE spectrum of *1RXS J101015.9 - 311909* measured by *H.E.S.S.*, with the *ParisAnalysis* package. This result represent the cross-check with respect to the published *H.E.S.S.* spectrum. The bow-tie represents the 1σ confidence level of the fitted spectrum using a power-law function. The lower panel shows the fit residuals $N_\gamma - N_{th})/N_{th}$, where N_γ and N_{th} are the number of detected and expected excess events, respectively).

est (RoI) is taken 5° away, in the North-East direction from its nominal position, in order to minimize the contribution from the Galactic diffuse emission. In the analysis presented here, source-class events are considered in a circular RoI of 10° radius, and the *P7V6_SOURCE* instrumental response functions were used. In order to account for potential contribution from sources outside the RoI (due to the relatively large *Fermi-LAT* PSF at low energies) all the neighbouring *2FGL* objects up to a radius of 15° have been included in the model reconstruction.

Using the *gtlike* tool, and assuming a power-law shape for the source spectrum, the Test Statistic (TS, see Mattox et al. 1996) of the analysis is 68.3, corresponding to a significance of $\approx 8.3\sigma$ in the 100 MeV-200 GeV energy range. The corresponding photon index is 2.09 $\pm 0.15_{stat}$ and the highest energy photon from the source direction (i.e. in the 95% containment radius of the PSF at a given energy) has an energy of 76.6 GeV. Other more complex spectral shapes (broken-power-law or log-parabola) do not improve the goodness of the fit, and the power-law function remains the favoured hypothesis. This result is in agreement with the value presented in the *2FGL* catalog, which reports a power-law photon index of 2.24 $\pm 0.14_{stat}$.
However, as shown in Table 5.2, there is evidence for a dependence of the photon index to the chosen low-energy threshold of the data analysis. The source spectrum tends to harden when increasing the threshold, indicating a possible curvature in the spectrum. This curvature is however not seen in the spectral analysis, where curved spectral shapes do not provide a significantly better fit than the simple power-law function. Future observations with *Fermi-LAT* (increasing the significance of the detection) may enable a significant detection of this possible curvature.

To further check these results a test was performed by modelling the Galactic diffuse emission with a power-law spectrum, instead of using a constant flux normalisation for this component (as is recommended by the *Fermi-LAT* team). Such an energy-dependent spectrum would be an indication of a mis-modelling of the Galactic diffuse emission component. When using an energy threshold of 100 MeV, the Galactic diffuse emission normalisation parameter is fitted with a photon index of $\Gamma = 0.07 \pm 0.01$, while the spectral result for *1RXS J101015.9 - 311909* remains fully compatible with the fit performed with a constant Galactic component normalisation. This slight energy-dependence of the spectrum of the Galactic model reflects that the mechanism reponsible for the HE emission from the Milky Way is not yet perfectly understood, but does not affect the results on our source. In addition, while at each of the energy thresholds the count-map of *Fermi-LAT* exhibits a visible gradient due to the Galactic diffuse emission, such gradient is not present in the residual maps (after subtraction of all the modelled components). This shows that the normalization of the Galactic diffuse emission is under control and well-modelled in the analysis.

In the study of the SED of *1RXS J101015.9 - 311909* we adopted the results of the *Fermi-LAT* data analysis obtained using two different energy thresholds, one at 300 MeV, the other at 1 GeV (reported in the right plot of Fig. 5.4). The choice of 300 MeV is done in order to minimize a possible contamination at low energies from neighbouring sources and from the Galactic diffuse emission. This choice takes into account the tendency of the spectrum to harden with increasing energy threshold, while not loosing too many source photons due to this cut. We choose 1 GeV as a second threshold in order to study how the evaluation of the *Fermi-LAT* slope affects the modelling of the SED.
The *Fermi-LAT* data points shown in Fig. 5.12 are computed running *gtlike* in five contiguous energy bins, using the model parameters from the likelihood fit on the energy range 1-200 GeV, where the spectral index of *1RXS J101015.9 - 311909* was fixed to the best value of $\Gamma = 1.71$. When $TS < 9$, an upper limit on the flux is computed.

The *Fermi-LAT* light-curves of *1RXS J101015.9 - 311909* are shown in the left panel of Fig. 5.3, for the two chosen energy thresholds, with a binning of six months. Given the low statistic of the detection, no significan variability is observed in the 25 months of observations. This has been checked using other time-binning ranging from 90 to 180 days.
The *Fermi-LAT* best-fit position of *1RXS J101015.9 - 311909* is found to be $\alpha_{2000} = 10^{h}09^{m}49.51^{s}$ and $\delta_{2000} = -31^{\circ}24'21.9''$, fully consistent with the results presented in the *2FGL* catalog ($\approx 3'$ away). In

E_{th}	Γ	TS	$\phi(E > E_{th}$	E_{dec}
100	2.09 ± 0.15	68.3	11.31 ± 3.83	1929
300	1.92 ± 0.15	62.7	2.54 ± 0.69	3259
500	1.82 ± 0.15	59.8	1.36 ± 0.34	4306
1000	1.71 ± 0.16	55.9	0.70 ± 0.16	5863

Table 5.2: Spectral properties of the *Fermi-LAT* analysis of *1RXS J101015.9 - 311909*. The columns correspond to the energy threshold (E_{th}, in MeV), the photon index (Γ), the test statistic (TS), the integral flux above the threshold energy (in units of 10^{-9} cm^{-2} s^{-1}) and the decorrelation energy (E_{dec}, in MeV). The *Fermi-LAT* systematic uncertainty on the spectral index is 10% at 100 MeV, decreasing to 5% at 560 MeV and increasing again to 10% above 10 GeV.

Fig. 5.3 is reported the 1σ contour computed from the TS map, using the best fit position of the source.

5.3.2 *Swift-XRT*

The X-ray telescope (*XRT*) (Burrows et al. 2005) on board the γ-ray-burst mission *Swift* (Gehrels et al. 2004) observed *1RXS J101015.9 - 311909* three times during 2007-05-17 and 2007-05-18. The first and the third observations were performed in the photon-counting (pc) mode, while the second observation was performed in the windowed-timing (wt) mode. While in the pc-mode the entire CCD camera is read out, in the wt-mode only the central raws of the camera (in which the target is centered) are read, increasing the time-resolution of the detector. Information about the *Swift* observations, including identification numbers and exposures, are given in Table 5.3.

Cleaned event files have been reduced using *HEASoft*[3], version 6.7. Source spectra and light-curves have been extracted using *XSelect*, version 2.4a, and the spectral fitting has been performed using *XSpec*, version 12.5.1. Response matrices and ancillary response files have been provided by the *Swift-XRT* instrument team [4].

The sky-maps of *1RXS J101015.9 - 311909* as seen by *Swift-XRT* are shown in Fig. 5.6. The source count-rate is roughly 0.4 counts s^{-1} for the three observations. A common problem in X-ray astronomy is the so-called *pile-up* effect : if the input flux is too high compared to the detector reading capabilites, more than one photon is collected at once, and the total charge is summed together, leading to both an under-estimation of the source flux and a hardening of the measured spectrum. For *Swift-XRT* the count-rate values above which the pile-up effect become important are 0.6 and 100 counts s^{-1} for the pc and the wt-mode, respectively. While for the wt-mode the flux measured from the *1RXS J101015.9 - 311909* direction is well below this threshold, for the pc-mode a check of the pile-up has been performed, following the prescriptions of the *Swift-XRT* instrument team[5]. The fit of the angular distribution of photons around the maximum of the emission, reported in Fig. 5.7, shows that the pile-up effect does not affect our observations.

The light-curves extracted from the three *Swift-XRT* observations are shown in Fig. 5.8 : as no significant variability is observed, the two observations obtained in the pc-mode have been summed together using

---

[3] `http://heasarc.nasa.gov`

[4] The ancillary reponse file (*.arf*) provided by the *Swift-XRT* team is correct for a point-like source located at the center of the field of view. When the source is off-axis a new response file should be generated using the *xrtmkarf* tool. For *1RXS J101015.9 - 311909*, the difference between the results obtained with the two files is not energy-dependent (i.e. the measurement of the slopes is the same); the only difference is in the overall normalization, but it remains within one sigma

[5] `http://www.swift.ac.uk/pileupthread.shtml`

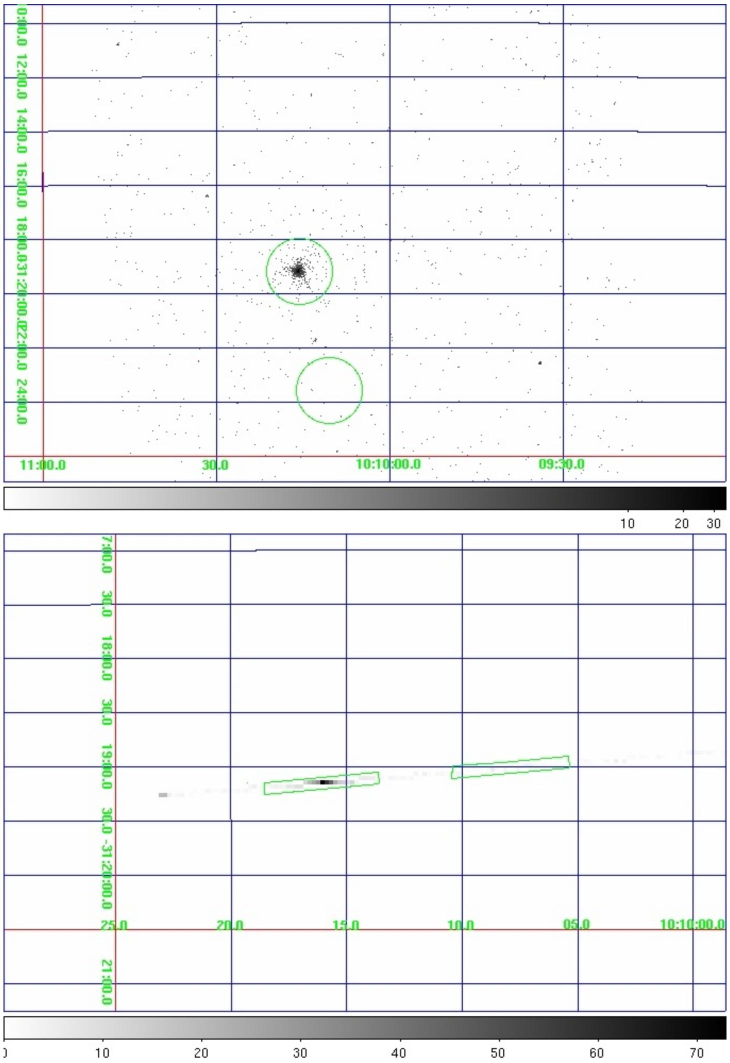

Figure 5.6: Sky-map of *1RXS J101015.9 - 311909* as seen by *Swift-XRT* in photon-counting (Top, first observation, see Table 5.3) or windowed-timing mode (Bottom, second observation). In green are shown the regions used for the extraction of spectra and light-curves for the source and the background.

mathpha, version 4.1.0 and fitted together with the wt-mode observation spectrum. Data below 0.3 keV have not been included in the analysis[6] while the last signifcant bin goes up to $\simeq$ 7 keV. The spectra have been rebinned using *grppha*, version 3.0.1, in order to have a minimum of ten counts per bien. The Galactic column density N_H has been fixed at $7.79{\times}10^{20}\mathrm{cm}^{-2}$, as evaluated by Dickey & Lockman (1990).

A fit perfomed using a simple power-law function with Galactic absorption (model *wabs*powerlaw* in *Xspec*) gives $\Gamma = 2.15 \pm 0.06$ and normalization factor (defined as the number of photons per units of surface, time and energy at $E = 1$ keV) $C_{1\,\mathrm{keV}} = (3.0 \pm 0.1) \times 10^{-3}$ keV^{-1} cm^{-2} s^{-1} (χ^2/d.o.f. = 172/141). The fit is significantly improved (χ^2/d.o.f. = 144/139, corresponding to a F-test statistic equal to $4{\times}10^{-6}$) if a broken power-law function is assumed : the best fit values of the model parameters (the two slopes, the break energy and the normalization factor) are given in Table 5.4; in Fig. 5.9 are shown the ratio of the residuals to the best-fit model. The absorbed flux in the 0.3-7 keV energy band is found to be $(1.04^{+0.04}_{-0.05}) \times 10^{-11}$ erg cm^{-2} s^{-1}.

---

[6] `http://heasarc.gsfc.nasa.gov/docs/heasarc/caldb/swift/docs/xrt/SWIFT-XRT-CALDB-09-v16.pdf`

	ID	Mode	Start	Exposure(s)
obs.1	00030940002	pc	2007-05-17	1744
obs.2	00030940003	wt	2007-05-18	790
obs.3	00030940004	pc	2007-05-18	1981
tot				4515

Table 5.3: *Swift* observations available for *1RXS J101015.9 - 311909*. For each observation is reported the ID number, the observation mode (in the photon-counting (*pc*) mode the entire camera is read-out, while in the windowed-timing (*wt*) mode only the central rows of the camera are read, increasing the time resolution of the instrument), the observing date and the exposure.

The break observed in the X-ray spectrum can either be intrinsic (representing a real break in the blazar synchrotron emission) or external, due to extra-absorption in the source. The most complete work so far on this problem has been performed by Perlman et al. (2005), who analysed *XMM-Newton* spectra of 13 different BL Lac objects, investigating the origin of the spectral curvature, and concluding that, for the majority of the sources, the intrinsic origin is preferred. The hypothesis of an external origin of the break observed in *1RXS J101015.9 - 311909* data has been tested by fitting the *Swift-XRT* spectra with a power-law function absorbed by Galactic material (fixed at the value given by Dickey & Lockman) plus a second absorber located at the redshift of the source (z = 0.143, frozen in the fit) with adjustable column density. The best fit in this case, reported in Table 5.4, is statistically equivalent to the one performed assuming a broken-power-law function, the evaluation of the second absorber column density being $N_H = 9^{+4}_{-3} \times 10^{20}\mathrm{cm}^{-2}$.

The intrinsic origin of the break suggested by Perlman et al. is supported mainly by two arguments : variability and smoothness of the break. If the value of the fitted second-absorbed column-density varies at different epochs, the external origin is clearly strongly disfavoured. Unluckily, *1RXS J101015.9 - 311909* did not vary significantly during the *Swift-XRT* observations, and we cannot use temporal information to disentangle the two scenarios. The other argument proposed by Perlman et al. is that an absorption feature leads to a sharp break, while an intrinsic break in a synchrotron spectrum is smoothed over a relatively large energy band : they thus performed separate power-law fits on narrow energy bands (0.5 – 1.0 keV, 1.0 – 2.0 keV, 2.0 – 4.0 keV and 4.0 – 10.0 keV), showing a smooth evolution of the

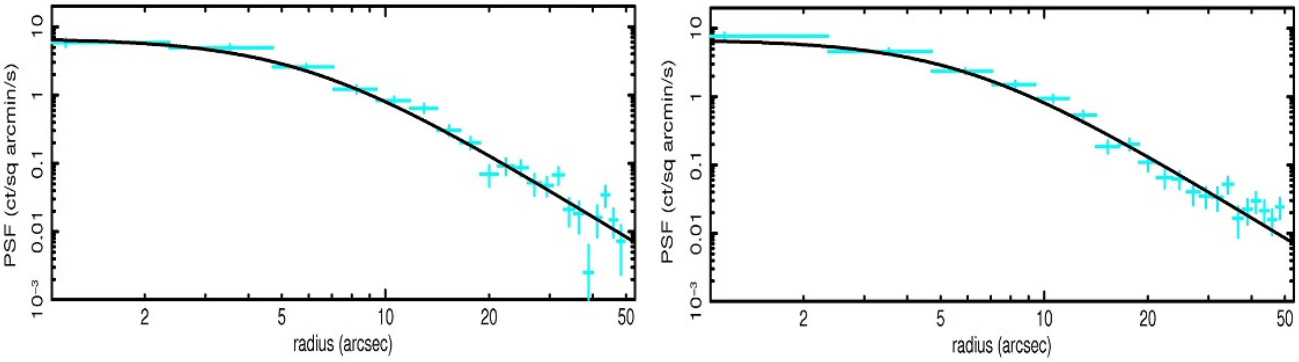

Figure 5.7: Fit of the angular distribution of photons centered on the maximum of the X-ray emission, for the First (Left) and the Third (Right) observation. The fit is performed using a King model for the point-spread-function, and considering only data above 15 arc-seconds, and is then extrapolated towards the central bins.

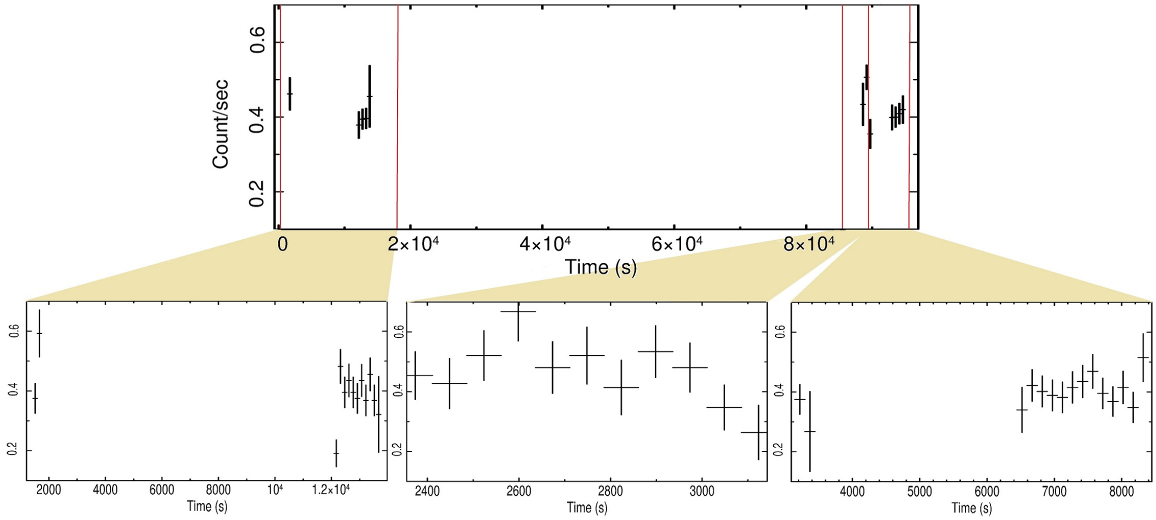

Figure 5.8: *Swift-XRT* light-curve (in counts per second) of *1RXS J101015.9 - 311909*. Top: over-all light-curve, obtained with a time-binning of 550 seconds. Bottom : zoom on the light-curves obtained for each single observation. The time-binning is 150 seconds for the first and the third observations (pc-mode, see Table 5.3), and 75 seconds for the second observation (wt-mode).

best-fit power-law spectral index (see Fig. 3 and Table 4 in their paper). For *1RXS J101015.9 - 311909* we performed the same spectral fitting as Perlman et al. : in our case the evolution of the power-law spectral index is not clear, and our results are still compatible with a sharp break. For these reasons in the study of the SED of *1RXS J101015.9 - 311909* (Section 5.4) we consider and discuss both scenarios.

Another point which is worth to mention is that, given the relatively low redshift of the source, the exact location of the absorber cannot be constrained. A fit performed letting the redshift of the second-absorber free to vary leads only to an upper limit ($z \leq z_{source}$, which is consistent with an absorber located at the source redshift, but not constraining for its exact location). In particular, the same absorption effect could be achieved by multiplying by a factor of two the Galactic column density. However, such a high value of N_H (equal to 16×10^{20} cm^{-2}) is not consistent with the range of N_H measured by Dickey & Lockman in a 1° circle around the nominal position of the object.

The deabsorbed X-ray spectrum of *1RXS J101015.9 - 311909*, assuming either an instrinsic or an external origin of the break is presented in Fig. 5.10.

Case	Γ	E_{break}[keV]	C_{1keV}	$N_{H,free}$	$\chi^2/d.o.f.$
A	$\Gamma_1 = 1.8^{+0.2}_{-0.2}$ $\Gamma_2 = 2.5^{+0.3}_{-0.2}$	$1.4^{+0.5}_{-0.2}$	$3.2^{+0.2}_{-0.2}$		144/139
B	$\Gamma = 2.5^{+0.1}_{-0.1}$		$3.9^{+0.4}_{-0.4}$	9^{+4}_{-3}	147/140

Table 5.4: Best-fit parameters for the two models used for the fitting of the *Swift-XRT* spectra. Case A represents the broken-power-law hypothesis, assuming only absorptiony by our Galaxy, while case B represents the power-law fit, adding an extra-absorber at the redshift of the source. Γ represents the photon index, E_{break} the energy break in case A, $N_{H,free}$ (in units of 10^{20} cm^{-2}) the column density of the second absorber in case B. The normalization C_{1keV} is given in units of 10^{-3} keV^{-1} cm^{-2} s^{-1}

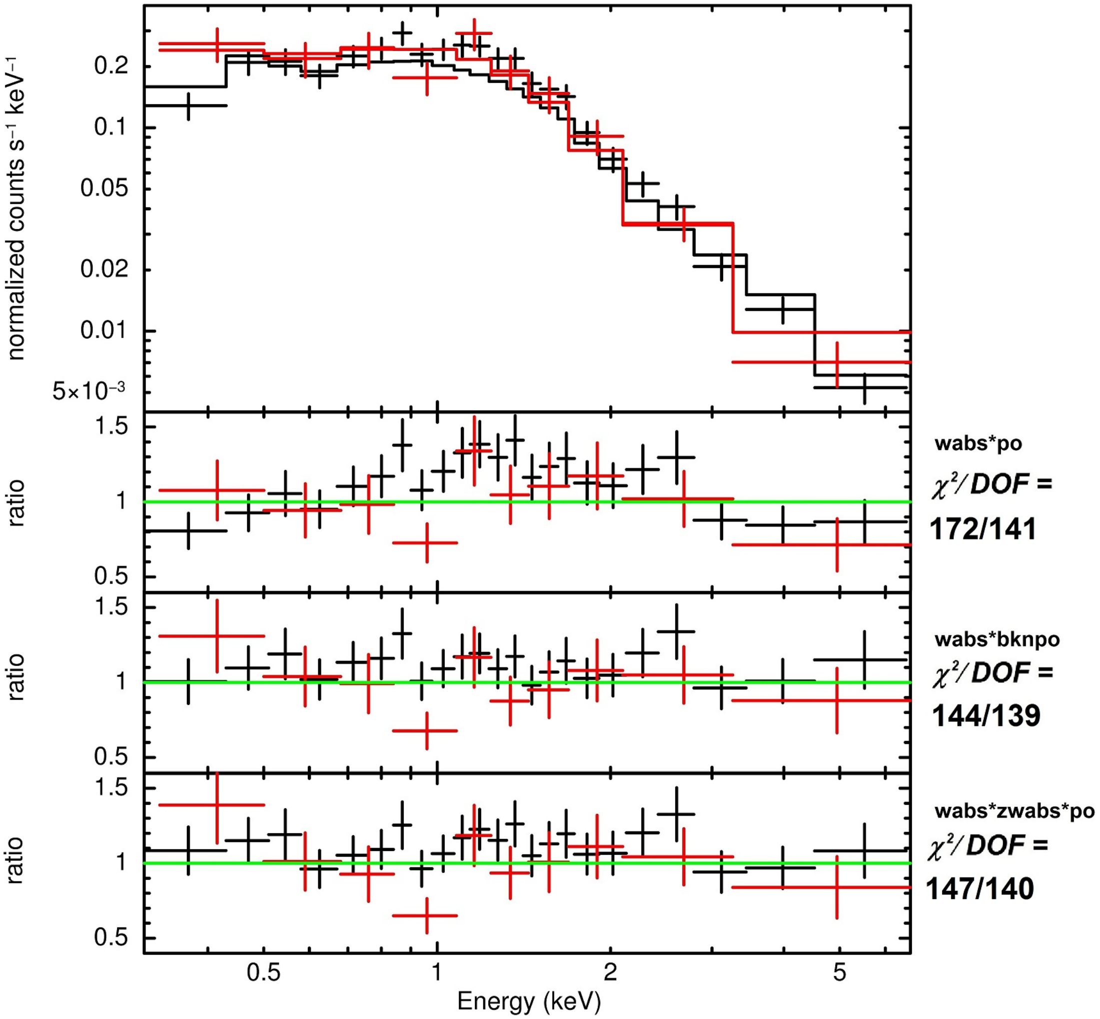

Figure 5.9: *Swift-XRT* spectra have been first fitted with a simple power-law function plus Galactic absorbtion (Top panel, and first ratio plot). The fit is significantly improved if a broken-power-law funcion is assumed (second ratio plot) or if a second absorber is taken into account (third ratio plot). The spectrum from the pc-mode observations is shown in black, while the spectrum from the wt-mode observation is shown in red.

5.3.3 *Swift-UVOT*

The *Swift* satellite carries an Ultra-Violet/Optical telescope (*UVOT*) (Roming et al. 2005) which observed *1RXS J101015.9 - 311909* simultaneously with *XRT*. For each of the three *Swift* observations, *UVOT* observed the source using six different filters : V and B in optical (with central wavelength λ = 5468 and 4382 Å, respectively), and U, UVW1, UVM2, UVW2 in ultraviolet (with λ = 3465, 2600, 2246 and 1928 Å, respectively), in order of increasing frequency (for the exact definition of the *UVOT* filters see Roming et al.). Following the prescriptions given by the *Swift-UVOT* instrument team [7], counts have been extracted in a circular region of 5" radius of aperture for the source, and 15" radius of aperture for the background. The image taken by *UVOT* in the V filter during the first observation is shown in Fig. 5.11.

The conversion from instrumental counts to magnitudes and fluxes has been performed using *uvotmaghist*, version 1.1.

---

[7] `http://www.swift.ac.uk/analysis/uvot/mag.php`

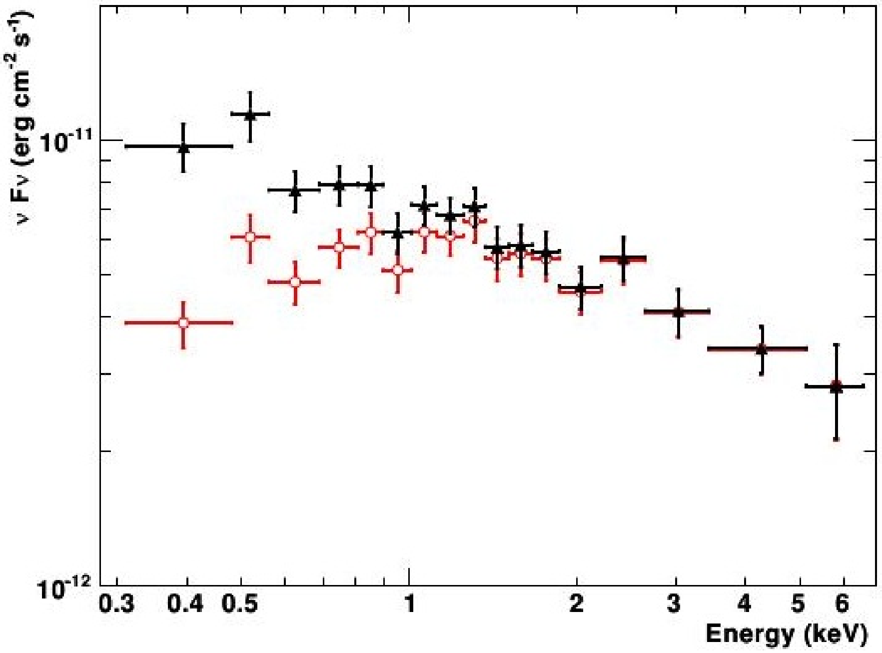

Figure 5.10: The two *Swift-XRT* spectra for case A (broken-power-law) and case B (power-law with extra-absorption), corrected for the respective absorbtions, are shown by the red points and the black triangles, respectively. For simplicity, only the spectrum from the pc-mode observations, rebinned for plotting purposes, is shown.

The correction for Galactic absorption has been done assuming E_{B-V} = 0.104 and E_{B-V} = 0.224 for the two cases A and B, respectively (see Table 5.4). These values have been estimated from the N_H values used in the X-ray analysis (N_H = 7.79 and 16.79 × 10^{20} cm^{-2} for case A and B, respectively, see Section 5.3.2) using the relation $N_H/E_{B-V} = 7.5 \times 10^{21}$ cm^{-2} as given by Jenkins & Savage (1974). Following Roming et al. (2009), the E_{B-V} values are converted to the absorbtion coefficient A_λ for each filter, and the magnitudes have been then de-absorbed according to $m_\lambda = m_\lambda - A_\lambda$.
As in the case of the X-ray observations, no significant variability is observed in the *Swift-UVOT* data, and the mean flux values have been used for the modelling of the SED in section 5.4.

5.3.4 *ATOM*

ATOM (Hauser et al. 2004) is a 75-cm optical telescope located at the *H.E.S.S.* site, developed in order to perform a simultaneous follow-up of the *H.E.S.S.* targets in visible light. *1RXS J101015.9 - 311909* has been regularly observed by *ATOM* since January 2008 and in this Section we report the results of *ATOM* observations up to June 2011. On the 2nd of January 2008 the source has been observed in the I, R and B filters (as defined by Bessell 1990), while the rest of the observations have been performed in the R and B bands only. The magnitudes have been evaluated using a 4” radius of aperture, and the estimation of the errors includes the uncertainty on the absolute calibration (based on known reference stars in the field of view of *1RXS J101015.9 - 311909*). The conversion from magnitudes to flux has been done following Bessell (1990). The correction for Galactic absorption has been done as for the *Swift-UVOT* data, assuming E_{B-V} = 0.104 and E_{B-V} = 0.224 for the case A and B, respectively (the conversion from E_{B-V} to A_λ has been done following Cardelli et al. 1989).
The long-term *ATOM* light-curve of *1RXS J101015.9 - 311909* (plotted in the left part of Fig. 5.3) shows that the source varies significantly in both the B (79 ± 11%, evaluated as the difference between the high-

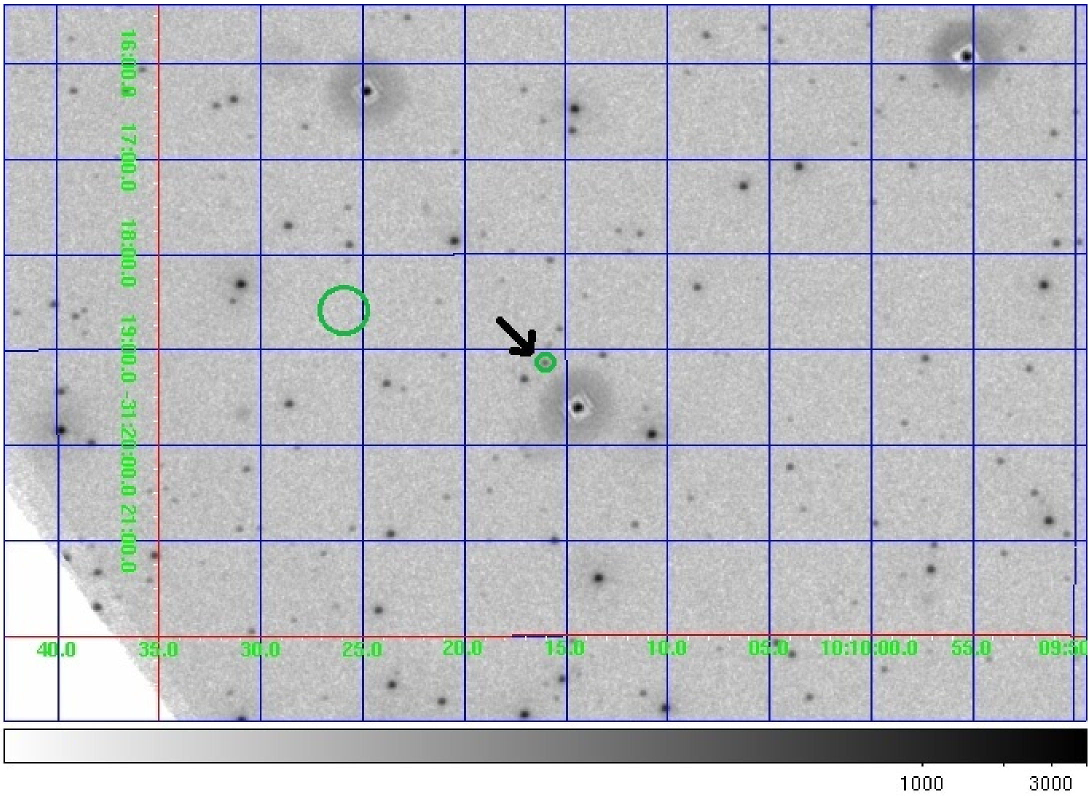

Figure 5.11: Sky-map of *1RXS J101015.9 - 311909* as seen by *Swift-UVOT* in the V filter (first observation). In green are shown the regions used for the extraction of spectra and light-curves for the source (indicated by a black arrow) and the background.

	Case A	Case B
E_{B-L}	0.104 10^{-11}erg cm^{-2} s^{-1}	0.224 10^{-11}erg cm^{-2} s^{-1}
UVOT filters		
V	0.78 ± 0.01	1.10 ± 0.02
B	0.58 ± 0.02	0.92 ± 0.02
U	0.46 ± 0.01	0.80 ± 0.02
UVW1	0.48 ± 0.01	1.00 ± 0.03
UWM2	0.46 ± 0.02	1.31 ± 0.07
UVW2	0.47 ± 0.01	1.18 ± 0.02
ATOM filters		
I	0.63 ± 0.03	0.84 ± 0.04
R	$0.65^{+0.25}_{-0.15}$	$0.90^{+0.35}_{-0.20}$
B	$0.67^{+0.34}_{-0.19}$	$1.05^{+0.52}_{-0.20}$

Table 5.5: Summary of optical and ultra-violet data point of *1RXS J101015.9 - 311909*used for the analysis of the SED, from the *Swift-UVOT* and *ATOM* observations (see Section 5.3.3 and 5.3.4. The $\nu F(\nu)$ values are expressed in 10^{-11}erg cm^{-2} s^{-1} . The error bars of the B and R *ATOM* data points do not represent statistical errors, but the range of variability observed in two years and a half of observation.

est and the lowest flux, over the mean value) and the R (62 ± 8%) energy bands. The estimation of the variability amplitude has been done also by the evaluation of the normalized excess variance (see Section 5.2): the values of 0.014 ± 0.05 and 0.011 ± 0.02 for the B and the R band, respectively, confirm that there is a statistically significant variability in the source. It should be underlined that the variability observed in the B band is significantly higher than that measured in the R band. We will get back on this point in the following Section. The lowest detected variability time-scale is roughly one day, corresponding to the minimum time between two different observations.

For the study of the SED, the mean *ATOM* flux (computed using the entire data set) is used, the error bars representing the variability range measured during the observing period. The *Swift-UVOT* and *ATOM* observations are not simultaneous. However, the flux measured with *Swift-UVOT* in the B band is compatible with the range of variability observed by *ATOM*.

5.4 Modelling of the spectral energy distribution

The results from multi-wavelength observations of *1RXS J101015.9 - 311909*, discussed in Section 5.3 are used to study its spectral energy distribution. The source has been observed in the past in radio, infrared, optical and X-rays. The non-simultaneous SED, including the data analysed in the previous section, and historical data from the NED [8] is shown in Fig. 5.12.

The blazar host galaxy is detected in infra-red and optical, and a study of its contribution is important in order to determine the physical properties of the blazar emission. In order to do this, we used the information from the *2MASS Extended Source* catalog (Jarrett et al. 2000), in which the *1RXS J101015.9 - 311909* host galaxy is included : the effective radius of the galaxy is evaluated at 3.03” in the J band, and the magnitude values measured for different radii of aperture (r>5”) are given. Following Young (1976) we then evaluated the galaxy contribution in the J band in a 4” radius of aperture (to match the *ATOM* results) as $m_{gal} = 14.3$. The estimation of the host galaxy contribution at other wavelengths requires an assumption on the intrinsic galaxy spectrum : for this we used a template of a giant elliptical galaxy spectrum (obtained using *PEGASE* (Fioc & Rocca-Volmerange 1997)), properly rescaled in order to match the flux estimated in the J band.

As shown in Fig. 5.12, the host galaxy dominates the AGN emission in infrared light. This is consistent with the optical spectrum of *1RXS J101015.9 - 311909* studied by Piranomonte et al. (2007) in order to evaluate the redshift of the source : from Fig. 2 and A.1 of their paper, the host galaxy contribution can be evaluated at roughly 3 times the non-thermal continuum in visible light. The estimation of the host galaxy contribution naturally explains the fact that the observed long-term variabilty in *ATOM* data is significantly larger in the B band than in the R band : the host galaxy spectrum shows in fact a cut-off in the B band and the non-thermal continuum start dominating the total emission.

The emission from the active nucleus has been studied using the stationary one-zone SSC code (Katarzyński et al. 2001), described in Chapter 3. The two X-ray spectral hypothesis described in Section 5.3.2 (assuming an intrinsic break, or an additional absorption) have been considered as the lower and the upper limit of the synchrotron emission from the blob. In case A, the synchrotron peak energy corresponds to the observed X-ray break ($E_{break} = 1.4^{+0.5}_{-0.2}$ keV), while in case B the synchrotron peak falls between UV and X-rays. Whereas in case A the emission from the blob cannot describe both the X-rays and the optical/UV data, in case B the synchrotron component, together with the emission from the host galaxy, fully reproduce the observations. In both cases, the historical radio data are not taken

---

[8] NASA/IPAC extra-galactic database, `http://ned.ipac.caltech.edu`

into account in the modelling, as they are more likely generated in the extended jet, and they have been considered as upper limits of the emission.
In order to study how the uncertainty of the *Fermi-LAT* slope affects the modelling of the SED, we studied two cases, for a *Fermi-LAT* threshold equal to 300 MeV and 1 GeV, respectively.
The minimum (maximum) Lorentz factor cannot be constrained by the data : as long as it is low (high) enough, it does not play any role in the overall SED, and it has been thus fixed at 300 (5×10^6). It should be noted, however, that the value of γ_{min} cannot be arbitrarly low, being constrained by the radio data (which are considered as upper limits). The index of the electron distribution after the break α_2 is completely constrained by the measured spectral index of *Swift-XRT* data above the break ($\alpha_2 = 2\Gamma - 1$) and has thus been fixed at 4.0. The value of α_1 is instead constrained by the *Fermi-LAT* photon index (different for the two *Fermi-LAT* spectra considered) and by the optical/UV data (for case B only) : it has been fixed at 2.2 and 2.0 for a *Fermi-LAT* spectrum evaluated above 300 MeV and 1 GeV, respectively.
A good description of the *1RXS J101015.9 - 311909* SED is achieved assuming an angle $\vartheta = 1°$ and a Doppler factor equal to 30 (corresponding to a bulk Lorentz factor of the emitting region equal to 16). The other free parameters (B,R,$\gamma_{e,break}$ and K) are different for the different cases considered, and are given in Table 5.6. We also evaluated the energy densities of electrons ($u_e = mc^2 \int d\gamma_e \gamma_e N(\gamma_e)$) and of the magnetic field ($u_B = B^2/8\pi$) : the u_e/u_B value is higher in case A (intrinsic break) compared to the case B (additional absorption), reflecting the fact that the ratio between the inverse Compton and the synchrotron bump is higher in the first case. The lower limit of the model variability time-scale, evaluated for the emitting region and the Doppler factor assumed ($\tau_{var} = (1+z)R/(c\delta)$) is equal to roughly 1 and 25 hours for the case A and B, respectively, consistent with the variability time-scale observed in the *ATOM* data.
The difference between the *Fermi-LAT* spectra evaluated with two different threshold energies affects the evaluation of the electron-distribution slope before the break (α_1), thus inducing a variation on the normalization factor K and on γ_{break}, modifying the value of the particle energy density inside the emitting region.
As already mentioned, in case A, the emission from the blob, cannot explain the observed flux at low frequencies (infrared to UV) : in this case the observed non-thermal continuum should be associated to another component, most likely the emission from the extended jet, dominating the AGN emission from radio to UV, and being responsible for the *ATOM* variability. On the other hand, in case B, the SSC model alone can fully describe the SED, and the variability observed in *ATOM* data should be ascribed to the blazar component. It should be noted that in this case, the UV data point are slightly under-estimated: to better describe the data the model would require a harder slope α_1 which is inconsistent with the *Fermi-LAT* spectrum. However, the uncertainties (both statistical and systematic) on the evaluation of the GeV slope, as well as on the value of the second absorber in case B (the de-reddening of the data did not take into account the error on the E_{B-V} value, which is almost 20%, and induces a systematic error in the modelling) can still explain this discrepancy.
The two cases A and B are, as mentioned above, considered as lower and upper limit of the blazar emission : the real scenario may be more complex and lie between these two limiting cases.

The paramaters found for the modelling of the SED are typical for a HBL as *1RXS J101015.9 - 311909*. However, several problems affect the study that has been perfomed, in particular the uncertainties on the origin of the observed X-ray break, the non-simultaneity of infrared-to-UV observations and the threshold-dependance of the *Fermi-LAT* spectrum. Future simultaneous multi-wavelength observatios are required, in particular in order to determine whether optical/UV and X-rays photons are produced within the same region, thus constraining the origin of the observed X-ray break.

	$Fermi_{>300MeV}$		$Fermi_{>1GeV}$	
	Case A	Case B	Case A	Case B
$\gamma_{e,break}$	1.08×10^5	9.0×10^4	1.01×10^5	7.8×10^4
α_1	4.0	4.0	4.0	4.0
α_2	2.2	2.2	2.0	2.0
K	5.67×10^4	3.37×10^2	6.6×10^3	4.5×10^1
u_e	5.37×10^{-2}	3.15×10^{-4}	3.42×10^{-2}	2.24×10^{-4}
δ	30	30	30	30
B	0.16	0.025	0.16	0.025
u_B	1.02×10^{-3}	2.49×10^{-5}	1.02×10^{-3}	2.49×10^{-5}
u_e/u_B	52.7	12.7	33.6	9.0
R	2.37×10^{15}	7.0×10^{16}	2.37×10^{15}	7.0×10^{16}
τ_{var}	0.8	24.7	0.8	24.7
L_{jet}	7.6×10^{42}	4.1×10^{43}	4.9×10^{42}	3.0×10^{43}

Table 5.6: Summary of the parameters used for the modelling of the *1RXS J101015.9 - 311909* SED. The modelling has been performed for the two different *Fermi* specta (with threshold above 300 MeV and 1 GeV, respectively, see Section 5.3.1) and for the two cases considered in the analysis of the *Swift-XRT* data (Section 5.3.2). For all the cases considered, the minimum and the maximum Lorentz factors of the electron distribution are $\gamma_{e,min} = 300$ and $\gamma_{e,max} = 5 \times 10^6$, respectively, and the angle to the line of sight has been setted to 1°. The electron-distribution normalization parameter K is in units of cm^{-3}; the magnetic field is in G; the emitting-region size is in cm; the energy densities $u_{e,B}$ are in erg cm^{-3}; the variability time-scale τ_{var} is in hours and the jet luminosity L_{jet} is in erg s^{-1}, and is computed as $\pi R^2 c \Gamma^2 (u_e + u_B + u_p)$, where u_p represents the term of cold protons, computed following Sikora et al. (2009).

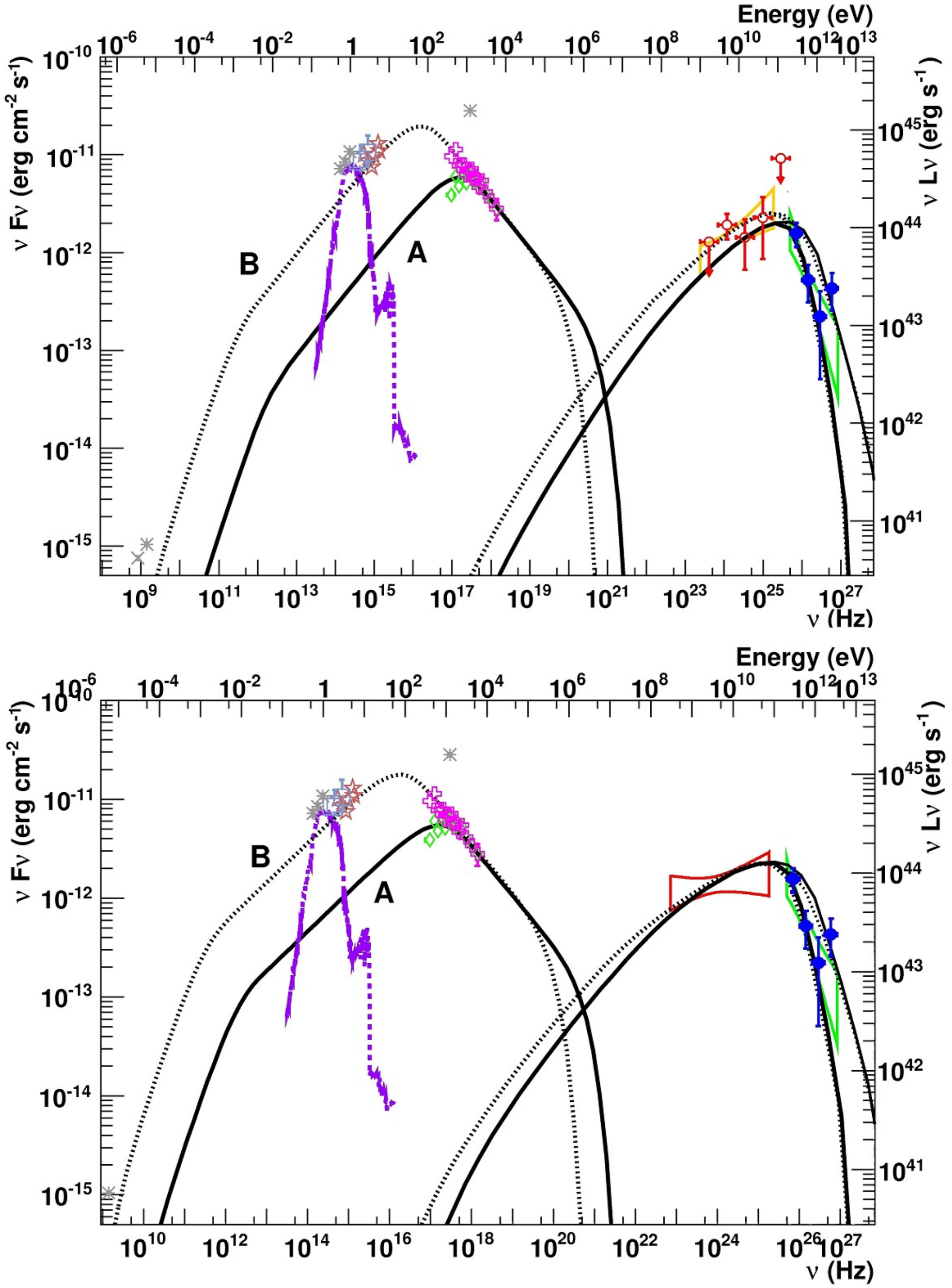

Figure 5.12: SED of *1RXS J101015.9 - 311909* for a *Fermi-LAT* spectrum evaluated using a threshold of 1 GeV (top) or 300 MeV (bottom). The *H.E.S.S.* spectrum (as measured, i.e. not corrected for absorption on the EBL) is represented by the green bow-tie and the blue points. The *Fermi-LAT* spectrum is represented by the orange and red bow-tie (for the two different thresholds). The *Swift-XRT* spectrum in case A is shown with green diamonds, while case B is represented with pink crosses (see Section 5.3.2. *Swift-UVOT* data are shown with light-red stars, while *ATOM* data are shown with light-blue squares. Deabsorbed infrared-to-UV data are plotted for case B only to avoid cluttering. The total SSC emission model (including absorption by the EBL) is represented by the solid line for case A, and by the dashed line for case B (see Table 5.6 for the parameters used in the modelling). The intrinsic emission (corrected for EBL absorption) is plotted as well with thinner lines. The host galaxy contribution is shown by the purple dashed line in the optical regime.

Chapter 6

Constraining the synchrotron-self-Compton model parameters

Contents

6.1 Introduction

In this Chapter we describe the development of a new algorithm for the determination of the best-fit parameters of the synchrotron-self-Compton model. As described in Chapter 3, the one-zone SSC model provides a satisfactorily description of the blazar SED only for high-frequency-peaked BL Lac object. In this sense, the fitting procedure that is described here is intended to be applied only to HBL data.

Before presenting our results, in Section 6.2 we discuss the current minimization algorithms presented in the scientific literature. The details of our algorithm are given in Section 6.3, while in Section 6.4 we show a first application to the SED of *1RXS J101015.9 - 311909*, described in Chapter 5 and to *PKS 0447-439* (see Chapter 4), whose redshift will be constrained in a model-dependent way.

6.2 The current status of the SSC-model constraints

As already discussed in Chapters 3 and 5 (for the particular case of *1RXS J101015.9 - 311909*), the SSC model is under-constrained, in the sense that the number of free parameters is larger than the number of independent observables. In particular, if we consider the primary electron population in the emitting region as being described by a broken power-law function, the free parameters of the model are in total nine:

- six related to the population of electrons responsible of the emission: the two slopes of the electron distribution α_1 and α_2; the three corresponding Lorentz factor γ_{min}, γ_{break} and γ_{Max}, and the normalization factor K
- three for the emitting region : the size R, the magnetic field B and the doppler factor δ

Concerning the independent observables of the system, they are six:

- the position and the luminosity of the synchrotron peak: ν_s and L_s
- the position and the luminosity of the inverse Compton peak: ν_c and L_c
- the spectral index of the X-ray spectrum (i.e. the spectral index of the synchrotron emission after the peak) and of the γ-ray spectrum (i.e. the spectral index of the inverse Compton emission before the peak): Γ_X and Γ_γ

A simple χ^2-minimization algorithm would thus fail in finding a unique solution of the problem. A key is to reduce the number of free parameters or to increase the number of constraints for physical reasons. The first consideration that help us is related to the variability time-scale and in particular to the causality effect. In fact, for a source of size R we expect to see a variability time-scale higher than the crossing-time of the region: $\tau_{var} \geq R/c$.
Taking into account the Doppler factor and the redshift correction, the equation become:

$$\tau_{var} \geq \frac{1+z}{\delta}\frac{R}{c} \tag{6.1}$$

which provides a new constrain (even though it is just an upper limit, not an equality) between the two model parameters R and δ.

To further reduce the difference between numbers of parameters and observables we note that two of the model parameters, namely the two Lorentz factor γ_{min} and γ_{Max} do not play an active role in the modelling as long as they are reasonably low (γ_{min} of the order of 100, or lower) and high ($\gamma_{Max} \gg \gamma_{break}$), respectively. Under this assumption, the number of free parameters is thus reduced to seven, and the number of constraints is increased to six plus an upper-limit related to the variability time-scale.

This approach has been deeply studied by Tavecchio et al. (1998), who provide analytical formulae linking observables and parameters, in order to determine the best solution of the SSC model. Given the importance of this work, we think it is useful to recall here this approach, providing an application to *1RXS J101015.9 - 311909* as a test-case.

We first notice that two pairs parameter-observable are decoupled from the other set of costraints, and they are represented by the two electron distribution indices and the measured X-ray and γ-ray (in the MeV-GeV range) slopes. In particular we have :

$$\begin{aligned} \alpha_1 &= 2\Gamma_\gamma - 1 \\ \alpha_2 &= 2\Gamma_X - 1 \end{aligned} \tag{6.2}$$

These relations are valid only if the conditions on the minimum and maximum electron Lorentz factor are respected, otherwise the synchrotron and the inverse Compton spectrum would show a curvature in the X-ray and γ-ray energies, modifing this result.

Following Tavecchio et al. (1998) we start by providing constraints for the peak energies and luminosities in the Thompson regime. All the equations are written in order to have a constrain in the $B - \delta$ plane.
The relation between the two peak energies provides a first equation:

$$B = \frac{4\nu_s^2}{3\nu_c} \frac{1+z}{3.7 \times 10^6} \frac{1}{\delta} \tag{6.3}$$

where B is expressed in G, and $\nu_{s,c}$ in Hz.
The relation between the two peak luminosity provides a second equation:

$$B \geq (1+z) \left(\frac{2\nu_s^2 L_s^2 f}{c^3 \tau_{var}^2 \nu_c L_c} \right)^{1/2} \frac{1}{\delta^3} \tag{6.4}$$

where $f = f(\Gamma_X, \Gamma_\gamma) = 1/(2 - \Gamma_\gamma) + 1/(\Gamma_X - 2)$, and the inequality comes from equation 6.1.
Considering the uncertainties in the evaluation of the observables, equation 6.3 defines a strip in the $B - \delta$ plane. Following Tavecchio et al. (1998), we can also define a lower limit for the emitting region size, justified by the fact that "we do not want to force δ to be too large"; assuming a low limit size equal to one tenth of the maximum value (Tavecchio et al. (1998) used one third), equation 6.4 defines as well a strip in the $B - \delta$ plane, constraining our parameter space.

The above expressions are correct only if the Compton peak is still produced in the Thompson regime. The threshold for these expressions being valid is

$$\delta \geq \frac{h}{mc^2} \left(\frac{4}{3} g \nu_s \nu_c \right) \tag{6.5}$$

where $g = g(\Gamma_\gamma, \Gamma_X) = \exp(1/(\Gamma_\gamma - 2) + 1/(2(\Gamma_X - \Gamma_\gamma)))$.
If the above condition is not respected, the equations 6.3 and 6.4 have to be corrected using the Klein-Nishina formula, leading to:

$$B = \frac{\nu_s}{\nu_c^2} \left(\frac{mc^2}{h} \right)^2 \frac{g^2}{3.7 \times 10^6} \frac{\delta}{1+z} \tag{6.6}$$

$$B \geq (1+z)^{\Gamma_\gamma - 1} \left(\frac{g}{\nu_s \nu_c} \right)^{(2-\Gamma_\gamma)/2} \left(\frac{2\nu_s^2 L_s^2 f}{c^3 \tau_{var}^2 \nu_c L_c} \right)^{1/2} \left(\frac{3mc^2}{4h} \right)^{2-\Gamma_\gamma} \frac{1}{\delta^{1+\Gamma_\gamma}} \tag{6.7}$$

which are valid as well for B expressed in G, and $\nu_{s,c}$ in Hz.
These equations are enough to constrain an allowed region in the $B - \delta$ plane. In order to narrow further the constraints on the model parameters, other physical relation can be added. First of all, a minimum value of the Doppler factor can be defined through the pair-production opacity in the emitting region (the basic idea is that if we detect a γ-ray photon from the source, the emitting region has to be transparent to $\gamma - \gamma$ pair-production). The expression of δ_{min}, provided by Dondi & Ghisellini (1995) is :

$$\delta \geq \delta_{min} = \left(\frac{\sigma_T}{5hc^2} d_L^2 (1+z)^{2(\beta-1)} \frac{F(\nu_0)}{\tau} \right)^{1/(2+\beta)} \tag{6.8}$$

where d_L is the luminosity distance of the source, $\nu_0 = 1.6 \times 10^{40} / \nu_\gamma$ is the frequency of the target photons and β is the photon index of the target photons (equal to Γ_γ if $\nu_0 < \nu_s$ or to Γ_X if $\nu_0 > \nu_s$).

Up to now, the value of γ_{break} is considered as a free parameter of the model, fully determined by the modelling of the SED of our object. An additional constrain can be added by considering that the break energy corresponds to the energy at which the electron injection and cooling term reach an equilibrium (for more details on this point, see Section 7.2.6). If the cooling is dominated by synchrotron losses, the additional equations are (for the Thompson and Klein-Nishina limit, respectively):

$$B \geq \left(\frac{5 \times 10^{8} (\nu_s/\nu_c)^{1/2} (1+z)}{\tau} \right)^{1/2} \left(\frac{\beta_{esc}}{\delta} \right)^{1/2} \tag{6.9}$$

$$B \geq \left(\frac{5 \times 10^{8}}{\tau} \frac{g\, mc^2}{h} \frac{1}{\nu_c} \right)^{1/2} \beta_{esc}^{1/2} \tag{6.10}$$

where β_{esc} is the electron escape time (which is an unknown parameter, depending on the details of the transport processes in the emitting region; in the following is considered as comprised between 1/3 and 1, see Tavecchio et al. (1998)).
If, instead, the cooling is dominated by the Compton losses, the equations become:

$$B \geq 5.2 \times 10^{-14} \left(\frac{\nu_s L_s\, f}{c^3} \right)^{2.1} \left(\beta_{esc} \left(\frac{\nu_s}{\nu_c} \right)^{1/2} (1+z) \right)^{-8/5} \frac{\tau^{-13/5}}{\delta^{11}} \tag{6.11}$$

in the Thompson limit, and

$$B \geq \xi \left(\frac{\nu_s L_s\, f}{\tau\, \beta_{esc}} \right)^{1/(2-\Gamma_\gamma)} (\nu_c (1+z))^{(3\Gamma_\gamma - 5)/(2-\Gamma_\gamma)}\, \delta^{-6/(2-\Gamma_\gamma)} \tag{6.12}$$

in the Klein-Nishina limit, where

$$\xi = \xi(\Gamma_\gamma, \Gamma_X) = 2 \times 10^{-7} \left(\frac{h}{mc^2} \right)^{(4\Gamma_\gamma - 7)/(2-\Gamma_\gamma)} \left(\frac{f}{5.7 \times 10^{39}} \right)^{1/(2-\Gamma_\gamma)} g^{(5-3\Gamma_\gamma)/(2-\Gamma_\gamma)} \tag{6.13}$$

As a test, we apply these constraints to the SED of *1RXS J101015.9 - 311909* described in Chapter 5 for the two studied X-ray spectra (case A, where the synchrotron peak is located at ≈ 1 keV; and case B, where the intrinsic X-ray spectrum is a power-law, and the synchrotron peak is located in the gap between UV and X-rays).
In order to be consistent with the modelling proposed in Section 5.4, the two indices defining the broken power-law particle distribution have been fixed at 2.0 and 4.0, leading to $\Gamma_\gamma = 1.5$ and $\Gamma_X = 2.5$. The Compton peak frequency has been fixed to $(5.0 \pm 0.5) \times 10^{25}$ Hz and its luminosity (expressed as $\nu L_c(\nu)$) to $(1.0 \pm 0.1) \times 10^{44}$ erg s^{-1}. The synchrotron peak frequency has been fixed to $(2.0 \pm 0.2) \times 10^{17}$ Hz for case A and to $(2.0 \pm 0.2) \times 10^{16}$ Hz for case B; its luminosity has been fixed to $\nu L_{\nu;s} = (3.0 \pm 0.5) \times 10^{44}$ erg s^{-1} for case A and to $\nu L_{\nu;s} = (1.1 \pm 0.3) \times 10^{45}$ erg s^{-1} for case B.

The variability time-scale τ has been fixed to 24 hours (which corresponds to the variability detected in the optical *ATOM* data). As already discussed, we consider a lower-limit to the emitting region size equal to one tenth of the maximum value (equation 6.1), and we consider the β_{esc} parameter comprised in the range 1/3 to 1.
The first thing to be checked is whether the solution is in the Thompson or in the Klein-Nishina limit: for case A the δ_{KN} is equal to 111, while for case B it is equal to 20. Given the value of 30 that has been used in the modelling, we consider for case A the Klein-Nishina approximation, while for case B the Thompson approximation. The minimum value of the Doppler factor, using the condition on the gamma-ray

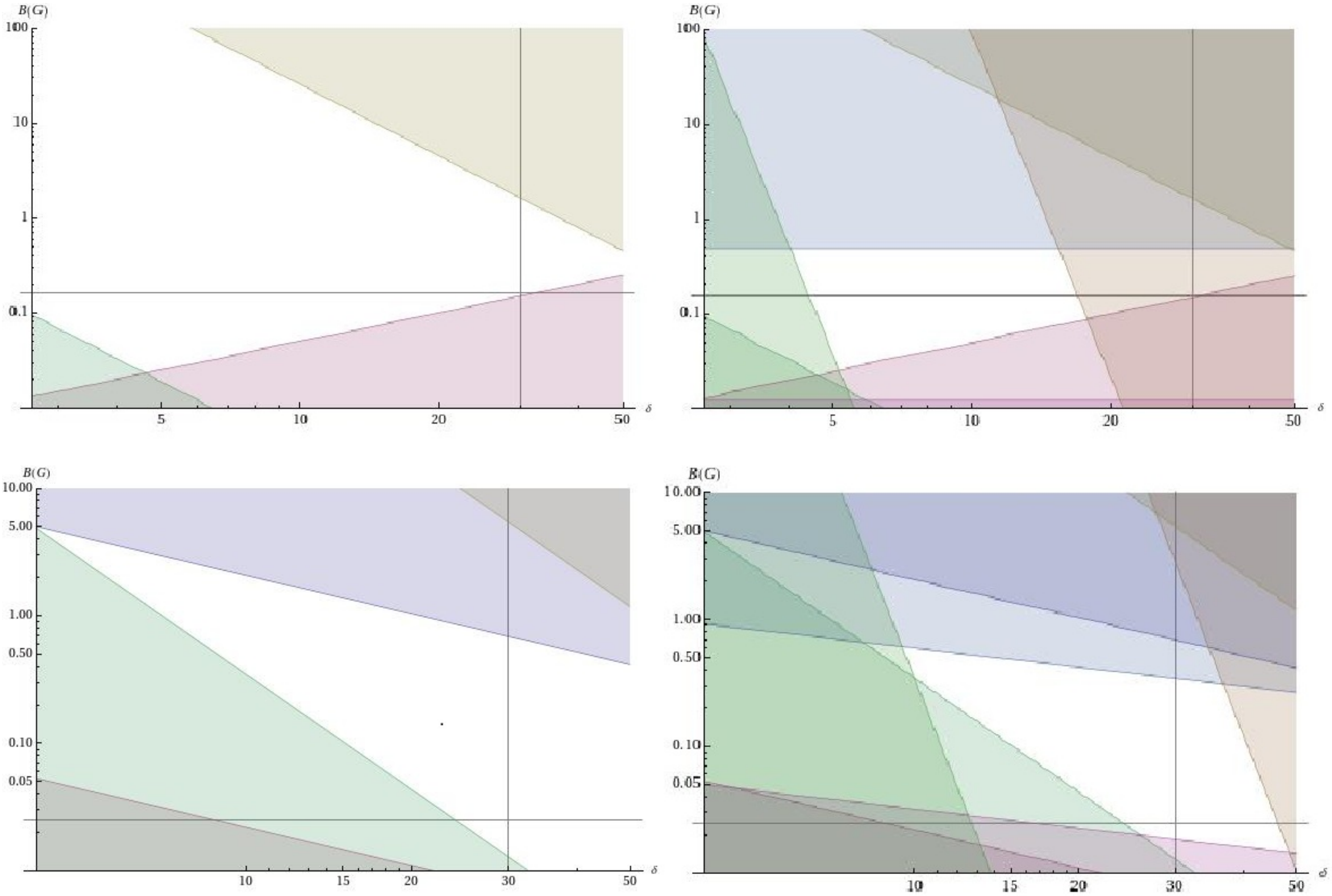

Figure 6.1: *Top:* constraints for the SED of *1RXS J101015.9 - 311909*, in case A (see Section 5.3.2).*Bottom:* constraints for the SED of *1RXS J101015.9 - 311909*, in case B. The left plots have been obtained using only the constraints on the energy and luminosity of the two peaks; the right plots include the additional constraint for the self-consistency of γ_{break} with respect to the synchrotron and Compton cooling. The permitted parameter space is described by the white region; the black lines show the adopted values of B and δ used in the modelling. As described in Section 6.2, for the case A the Klein-Nishina limit has been adopted, while for the case B we used the Thompson limit.

transparency (assuming $\nu_\gamma = 5 \times 10^{26}$ Hz) is $\delta_{min} = 5$ and $\delta_{min} = 8$ for the case A and B, respectively.

In Fig. 6.1 we show the constraints on the $B - \delta$ plane for the case A (top plots) and case B (bottom plots), with (left plots) or without (right plots) the constraint on the consistency of γ_{break} with the expected cooling break. As can be seen by the plots, for the case B the chosen values ($\delta = 30$ and $B = 0.025$) are fully consistent with the constraints, even for the balance between cooling and injection. On the other hand, for case A, the chosen values ($\delta = 30$ and $B = 0.16$) are consistent with the constrain only if we do not consider the balance between cooling and injection (i.e. in this case the chosen value of γ_{break} is not consistent with the expected cooling break). In order to have a fully consistent model, it would have required a lower Doppler factor ($\delta \leq 18$, assuming the same value for the magnetic field). However, as discussed in Chapter 3, the break observed in the synchrotron emission is in general not consistent with a simple synchrotron cooling (given that we observe $\Delta\Gamma > 1$), indicating a more complex situation, and the solution we have here provided remains valid.

The algorithm which will be presented in the next Section can be placed in the framework developed by Tavecchio et al. (1998) : analytical equations are established between observables and parameters, and then the system is solved, providing the best solution of our model.

A valid alternative to this framework is provided by a direct χ^2-minimization algorithm, which determines the best-fit solution of the model to the data. This approach has been studied as well in the scientific literature, and the most representative work has been done by Finke et al. (2008). In the left plot of Fig. 6.2 we report the diagram of the minimization algorithm that they have developed: the main characteristic is that the fit is performed in two steps, one for the synchrotron component, and another for the inverse Compton one. Finke et al. (2008) follow the same approach described above, namely they assume that γ_{min} and γ_{Max} are reasonably low and high, and link the emitting region size to the variability time-scale of the source. They also include in the fitting procedure a minimization of the jet-power, and constrain the observed break to being related to the synchrotron cooling, imposing $\alpha_2 = \alpha_1 + 1$ during the fitting procedure.

In Fig. 6.2 we also show the results obtained by Mankuzhiyil et al. (2011a,b) who also developed a χ^2-minimization algorithm. In the right is shown the diagram of the minimization algorithm which, with respect to the work by Finke et al. (2008), is performed over the overall SED (synchrotron and inverse Compton component) at the same time. As in the other cases, the value of γ_{min} is fixed low enough ($\gamma_{min} = 1$) that it does not play any role in the modelling. However, interestingly, γ_{Max} is consistently fitted, as well as the two slopes α_1 and α_2. The value of γ_{break} is considered as a free parameter, and its consistency with the expected cooling break is studied *a posteriori*.

6.3 A new numerical algorithm

The algorithm that we have developed to constrain the synchrotron-self-Compton model parameters is based on the work done by Tavecchio et al. (1998). The basic idea is to define a set of equations linking parameters and observables, but in our case they are obtained numerically: we generate a grid of synchrotron-self-Compton models (spanning the region of interest of the parameters involved p_j), and for each model we compute the value of the corresponding observable (O_i); we then fitted our grid of models in order to express each observable O_i as $O_i = \sum_j \alpha_j \, p_j$, where α_j is the result of the fit; we then produce a set of equations which is solved for a given set of observables O_i, giving us the solution of our model p_j. If the observables O_i include an intrinsic uncertainty (σ_i), we iteratively solve the system for $O_i \in [O_i - \sigma_i, O_i + \sigma_i]$, thus producing a set of possible solution to our problem.

As already discussed, we reduced the number of free parameters to seven by fixing a reasonably low and high value for γ_{min} (fixed to 100) and γ_{max} (fixed to 5×10^6). The main difference with respect to the work by Tavecchio et al. (1998) is on the choice of the observables: while the synchrotron peak is relatively well constrained (even when it is comprised in the gap between ultra-violet and X-rays, its position and luminosity can be reasonably well guessed by extrapolating the low and high energy data), the position of the Compton peak is much more uncertain. We then decided, instead of using this observable to use the *true* observables we have (in the sense of true observational data): the GeV and TeV spectral slopes, and their flux. This has two advantages with respect to the work done by Tavecchio et al. (1998): first of all we do not have to guess the position of the Compton peak or, better, we considerably reduce the uncertainty on this observable; and second (and more important) we double the number of observables

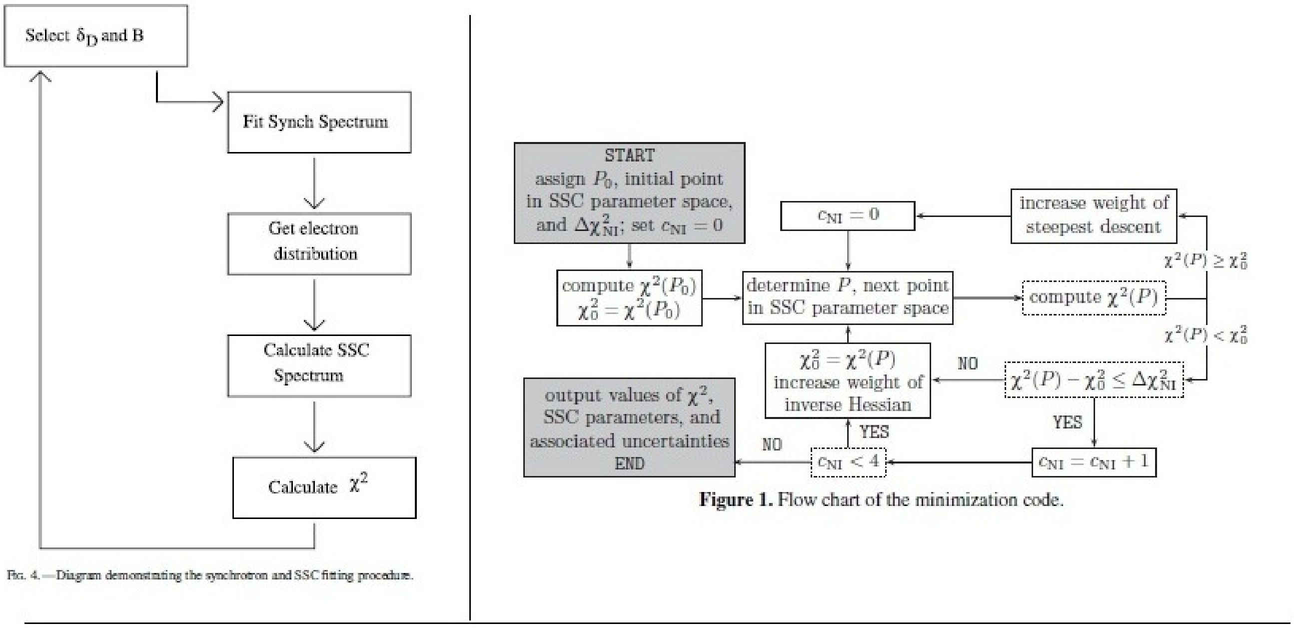

FIG. 4.—Diagram demonstrating the synchrotron and SSC fitting procedure.

Figure 1. Flow chart of the minimization code.

Figure 6.2: Flow diagram for the χ-squared minimization algorithm described in Finke et al. (2008) (left plot) and Mankuzhiyil et al. (2011a) (right plot).

which becomes: $\nu F_{\nu;GeV}$; $\nu F_{\nu;TeV}$; Γ_{GeV} and Γ_{TeV}. It is important to underline that these observables are not degenerate: the shape of the inverse Compton component is *not* symmetrical with respect to its peak, given the fact that the TeV part is affected by the transition to the Klein-Nishina regime, the internal absorption (which depends on the synchrotron emission) and the EBL absortion. It is clear that such a study is much more easily done through a numerical approach (a purely theoretical derivation of the expression of the TeV spectral slope assuming all the effect described above would not be trivial). Another improvement with respect to the Tavecchio et al. (1998) work is that we do not use the simple approximation that the GeV slope is uniquely related to the electron spectral index below the break (when γ_{min} is reasonably low): this approximation is true only if we measure the inverse Compton component well before the peak; if the Compton peak is located at lower energies, the *Fermi-LAT* measured spectrum would be significantly softer.

The model we used in our computation is the SSC code developed by Katarzyński et al. (2001), with the improvements described in Section 7.2. The primary electron population is described as a broken power-law function with two sharp cut-offs at γ_{min} and γ_{max}. Given the low contribution expected from emission from secondary pais coming from internal $\gamma - \gamma$ pair production, the spectrum of secondary pairs is not computed, in order to minimize the computing time. A major modification (used only in this framework, and not in the new code described in chapter 7.2) has been introduced for the definition of the normalization factor K of the electron distribution, which is originally defined as the number density at $\gamma = 1$. The problem of using this definition is that in this case the value of K strongly depends on the value of α_1: in particular, assuming that the model correctly fits the synchrotron peak, but we want to modify α_1, this automatically affects the value of K which has to be modified as well. In the framework of producing a grid of model, this definition is not appropriate, imposing a huge range of values for K. We then decided to redefine K, using the number density for $\gamma = \gamma_{break}$:

$$K' = K\gamma_{break}^{-\alpha_1} \tag{6.14}$$

In this way, if the model correctly describes the synchrotron peak, one can modify the value of α_1 without affecting the other parameters, and, more importantly, the range of values of K' to study becomes narrower.

In order to minimize the computing time, the code has been parallelized using *MPI*, and we run the simulations on a small 16-core machine. The parallelization is not at the level of the computation of the synchrotron and inverse Compton component, but at the higher level of the sampling of the parameter space: more correctly, it is a multi-thread computation, in the sense that each core computes its own SSC model. The distribution of the input parameters per thread is done dynamically, and the communication between threads take place only at the end of each computation, when the results are merged.

A grid of models has been produced, iterating on the values of δ, B, K', R, γ_{break} and α_1. The value of α_2 (the seventh free parameter of the model) is fixed, constrained by the measured X-ray spectral slope (the seventh observable), and equal to 4.0 for the case of *1RXS J101015.9 - 311909*, and 3.6 for *PKS 0447-439*. For the particular case of *PKS 0447-439*, in order to study the redshift of the source, the value of α_1 has been fixed to 2.0, and the new free parameter is z.
For each model we first identify the position of the synchrotron peak and its intensity. To compute the expected fluxes and spectral slopes detected in the GeV and TeV ranges, we simply fit the model in the useful range of the GeV and TeV detection with a power-law function, defining an index $\Gamma_{Fermi;HESS}$, and the two fluxes (of the fitted power-law, not of the model) $\nu F_{\nu;Fermi;HESS}$ at the respective decorrelation energy.
For the two applications which will be presented in the next section, we sampled 5 different values for each free parameter, resulting in a grid of $5^6 = 15625$ models. The spanned range of parameters depends on the two sources, and will be presented in the respective section. As an indication, the computing time on our 16-core machine is roughly one hour.

This grid of models has then been fitted using as dependent variables the six observables, and as independent variables the six free parameters. While for the synchrotron peak frequency and flux the relation between observables and parameters is simple (and consistent with the analytical expression), for the fluxes and slopes measured in the GeV and TeV energy bands, it becomes quite complex. In particular, the simple relation $O_i = \sum_j \alpha_j \, p_j$ does not work any more, and we should consider a more complex relation of the form $O_i = \sum_{k1...k6} \alpha_{k1...k6} \prod_j p_j^{k1...k6}$. More explicitly, we have to perform a fit considering all the possible polynomials composed by our parameters.
The problem is then to find the fitting formula of a dependent variable, function of six other variables, without knowing it *a priori* (nonparametric regression). This problem has been solved using the *root* software[1], namely the *TMultiDim* class. This function provides, for each term of the fit, the fitted coefficient and the weight of the term in the overall fit, allowing a listing of the different terms in order of relative importance.
The computing time for this step is a few seconds for the synchrotron observables and for $\nu F_{\nu;Fermi;HESS}$, while for the *Fermi* and *H.E.S.S.* slopes can be significantly longer, taking up to an hour (each) if we want to study all the possible polynomial functions (in order to be sure not to miss a high-order polynomial

---

[1] `http://root.cern.ch/`

which plays an important role in the fit).

Once we have obtained the six equations relating the six observables to the six free parameters, the system is closed and the problem becomes just solving the system of equations. This task has been solved with the *Mathematica* software, using the numerical *FindInstance* command, reducing the solutions to the real domain. To reduce the computing time, we solve a system of five equations plus two inequalities, corresponding to the minimum and the maximum of Γ_{Fermi}. Another inequality is added to the system, relating the size and the Doppler factor to the variability time-scale (equation 6.1). To take into account the uncertainty on the five remaining observables, we iterate the solution of the system spanning the range $O_i \in [O_i - \sigma_i, O_i + \sigma_i]$, using five values per observable (for a total of $5^5 = 3125$ systems solved), producing a set of solutions (note that, for each solved system, the number of real solutions can vary from zero to two). The computing time of this step depends strongly on the form of the equations in our system. In order to reduce the computing time, we have fixed one of the variables (α_1 for the case of *1RXS J101015.9 - 311909*, and z for the case of *PKS 0447-439*), searching the solutions of our problem for given different values of this frozen variable. For the expressions used for the two applications presented in the next Section, the computing time is roughly 20 hours (we sample four different values of the frozen variable, and we span the five observables four times each, leading to $4^6 = 4096$ systems studied). In order to improve the computing time, we parallelized the *Mathematica* code [2], using all the four cores of our machine, decreasing the computing time to roughly six hours.

The three steps of the analysis (grid-production, grid-fitting and system-solution, resumed in the plot shown in Figure 6.3) can then take a couple of days, and this impose a compromise for the resolution adopted for the grid, the number of terms used in the fit, the number of iterations done in the system solution. It is important to notice that the resolution of the grid does not affect only the computing time of this steps, but also of the fitting of the grid, whose computing-time depends strongly of the number of points.

As a conclusive remark, considering the discussion on the modelling of blazar emission presented in Chapter 3, we recall that our algorithm can be applied only to HBL objects, given the fact that only the synchrotron and SSC component is considered.

6.4 Applications

In this section we present the first application of our numerical algorithm for constraining the SSC-model parameter space to two HBLs: *1RXS J101015.9 - 311909*, a typical HBL presented in Chapter 5, and *PKS 0447-439*, presented in chapter 4, which is an HBL of unknown redshift. For this one we show that the distance of this GeV-TeV detected HBL, can be constrained in a model-dependent way.

---

[2] The parallelization in *Mathematica* is built-in, in the sense that there are parallel-versions of the functions, which automatically distribute the computation over the different threads. However, the outcome of this easy parallelization, is that we do not have control at all on the communication between the different threads, and the declaration of the different variables has to be carefully thought. For example, a simple substitution of the *Do* function with the *ParallelDo* function, results in a doubling (*sic!*) of the computing time. In practice, it is usually worth to rewrite the mono-core version of the code in a parallel-version of the code, minimizing the number of shared-variables. In this case, the parallel-code can effectively run in less than one-third of the mono-core code (using a four-core machine).

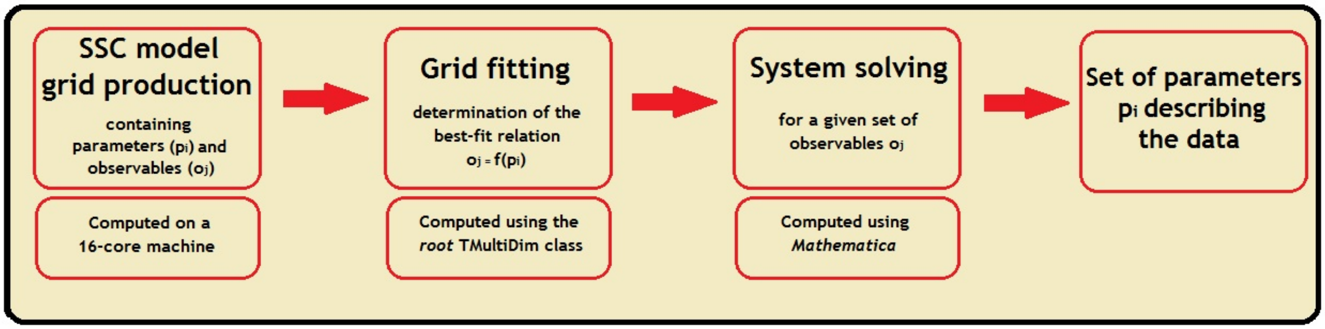

Figure 6.3: Flow diagram for the new numerical algorithm for constraining the SSC model parameters, described in Section 6.3.

6.4.1 *1RXS J101015.9 - 311909*

As a first test, we applied our algorithm to the BL Lac object *1RXS J101015.9 - 311909*, which has been presented in Chapter 5. We concentrate on one of the different spectra considered, in particular we study the SSC modelling for the *Fermi-LAT* spectrum obtained assuming a threshold of 1 GeV, and assuming an intrinsic power-law emission for the X-ray spectrum (case B, in Section 5.3.2), with a synchrotron peak located in beetween UV and X-rays. The value of α_2 is uniquely constrained by the X-ray spectrum measured by *Swift-XRT* ($\Gamma = 2.5$) and it has been fixed at 4.0. The model grid has been produced sampling the other six free parameters in the ranges: $\delta \in [20, 100]$, $B \in [0.001, 0.1]$ G, $\gamma_{break} \in [10^4, 10^5]$, $K' \in [10^{-10}, 10^{-7}]$ cm^{-3} and $R \in [10^{16}, 10^{17}]$ cm. As already said, the grid has been produced sampling five different values for each parameter, logarithmically spaced between the minimum and the maximum. It is important to underline that, if the solution is found *outside* of the sampled grid, its value cannot be trusted, given the fact that the system of equation is non-linear, and the fitted expression of the O_i is appropriate only for the sampled parameter space.

The result of the fits of the model grid for the six different observables is presented in Tables 6.2, 6.3, 6.4 and 6.5. As can be seen, while the expression of ν_s and $\nu f_{\nu;s}$ is simple, and consistent with what is expected from analytical considerations, the expression of the *Fermi* and *H.E.S.S.* observables is more complicated, and we are obliged to consider second-order terms in the fitting polynomial, with the extreme case of Γ_{HESS} which is described satisfactorily using more one hundred terms. In Fig. 6.4 we show the relation between the value of each observable, and its reconstructed value (after fit): in a perfect fit the values should follow exactly the linear relation, represented by the thick blue line.

The system of equations was then solved for four different values of α_1 (equal to 1.6, 1.8, 2.0 and 2.2.) and for four different values of each observable (apart from Γ_{Fermi}, which is defined through two inequalities), spanning from $O_i - \sigma_i$ to $O_i + \sigma_i$. The adopted values are (in logarithm): $\nu_s \in [16.15, 16.25]$, $\nu f_{\nu;s} \in [-10.75, -10.65]$, $\nu f_{\nu;Fermi} \in [-12.0, -11.82]$, $\nu f_{\nu;HESS} \in [-12.36, -12.10]$, $\Gamma_{Fermi} \in [-1.94, -1.48]$ and $\Gamma_{HESS} \in [-3.55, -2.61]$. Please notice that for the γ-ray observables, the considered error does include the systematic error on the observable (summed in quadrature to the statistic one). The system of equation includes an inequality for the variability time-scale ($\tau_{var} = 24$ hours) plus a limit on the value of the Doppler factor ($\delta < 100$, which corresponds to the limit of the sampled grid). Without this last constrain, we could find solutions to our problem with values of δ of the order of 10^2, 10^3, which have to be considered as wrong extrapolations of the fit performed for $\delta < 100$.

The results of our algorithm, defining the range of SSC parameters which correctly fits the data, are shown in Table 6.1 and the histograms are shown in Fig. 6.5 (for all the solutions) and 6.6 (only for the case $\alpha_1 = 2.0$).
It is interesting to see that minimum value of the Doppler factor which solves the system is $\delta \approx 30$, which corresponds to the value adopted in the modelling in Chapter 5. Values lower than this are excluded, mainly by the fact that it would require a harder *H.E.S.S.* slope (as can be seen in Fig. 5.12, the adopted model is indeed at the 1-σ limit of the *H.E.S.S.* slope, being particularly hard). The study of the solutions found for different values of α_1, reveals that the slope of the electron distribution is not so well-constrained as it is usually assumed by looking at the GeV slope, and that the solutions of $\alpha_1 = 1.8$, 2.0 and 2.2 are quite similar. A notable exception is represented by the solutions found for $\alpha_1 = 1.6$, which require $\delta \geq 40$. It is also interesting that there exists a maximum value of the Doppler factor, which is thus nicely constrained. The values adopted in the modelling of *1RXS J101015.9 - 311909* presented in Chapter 5 are consistent with the solutions found with our algorithm, even though the chosen model assumes a Doppler factor which is at the very edge (and slightly above) of the solutions found here.

It is important to underline that the range of solutions found here is a much narrower parameter space than the one allowed with the Tavecchio et al. (1998) approach, showing that this numerical algorithm, through the study of the expected GeV and TeV spectral emission, could permit a significant improvement in our knowledge of the blazar emitting regions.

Several improvements can be made to the algorithm we just presented. First of all, the production of the grid pre-selects a range of solutions: it would be interesting to extend the grid to higher Doppler factors, studying a wider parameter space. Obviously the problem become the computing time of this extended grid.
Another aspect which should be understood concerns the statistics of the found solutions. As can be seen in Fig. 6.5, the solutions are in the form of an asymmetric gaussian: does the peak of the solution sample represent the best-fit value, and the minimum and maximum the variance? Or the minimum and maximum are just a lower and a upper-limit? An easy way to verify this, would be to take the solution sample, recompute the associated model, compute a χ^2 over the data, and determine which is the best solution of our sample.
The last point we would like to stress is the fit of the grid. By cutting the number of adopted term in the fitting polynomials, we make an approximation on the reconstructed value of the observable, and this error should be taken into account when computing the solutions. Qualitatively, we could say that the solutions we provide for *1RXS J101015.9 - 311909* are correct under the assumption that the error done in the fitting procedure is much lower than the error on the observable itself (which is true for the *Fermi* and *H.E.S.S.* slopes, for example, but should be verified for their flux).

Table 6.1: Summary of the constrained parameters for the SSC modelling of *1RXS J101015.9 - 311909*. The solutions have been computed for four different values of α_1, which have been frozen in the solution of the system. For the other five free parameters, we provide the minimum and the maximum value found. The solutions with a Doppler factor higher than 100 have been excluded

α_1	1.6	1.8	2.0	2.2
γ_{break}	$(3.57 - 8.19) \cdot 10^4$	$(4.08 - 10.66) \cdot 10^4$	$(5.850 - 10.96) \cdot 10^4$	$(8.30 - 12.54) \cdot 10^4$
B	0.0124 – 0.0347	0.0117 – 0.0345	0.0122 – 0.0260	0.0071 – 0.0193
K'	$(0.610 - 79.370) \cdot 10^{-8}$	$(0.282 - 48.0) \cdot 10^{-7}$	$(0.187 - 6.057) \cdot 10^{-8}$	$(0.0059 - 0.811) \cdot 10^{-8}$
δ	41.34 – 99.74	30.82 – 90.57	31.43 – 63.86	32.63 – 58.41
R	$(0.53 - 8.02) \cdot 10^{16}$	$(0.60 - 10.35) \cdot 10^{16}$	$(1.59 - 10.63) \cdot 10^{16}$	$(4.11 - 11.11) \cdot 10^{16}$

Table 6.2: Coefficients of the fit performed to obtain an expression of ν_s (left) and $\nu F_{\nu;s}$ (right) for the case of *1RXS J101015.9 - 311909*. The correspondent plots are the top plots of Fig. 6.4. Each line correspond to a term of the fit: the first column gives the total order of the polynomial, the next six columns give, for each model free parameter, the degree considered, and the last column gives the associated coefficient. The terms are listed regarding to the parameters composing each term, and then by increasing degree, *not* by relative weight in the fit. In this case, the value of α_2 has been fixed to 4.0.

Order	γ_{br}	B	K	α_1	δ	R	Coefficient	Order	γ_{br}	B	K	α_1	δ	R	Coefficient
0	-	-	-	-	-	-	6.78265	0	-	-	-	-	-	-	-70.5555
1	1	-	-	-	-	-	2.00171	1	1	-	-	-	-	-	2.99949
1	-	1	-	-	-	-	1.00073	1	-	1	-	-	-	-	2.00001
1	-	-	-	1	-	-	-0.851359	1	-	-	1	-	-	-	1.0
1	-	-	-	-	1	-	0.997387	1	-	-	-	1	-	-	0.218826
								1	-	-	-	-	1	-	3.99999
								1	-	-	-	-	-	1	3.0

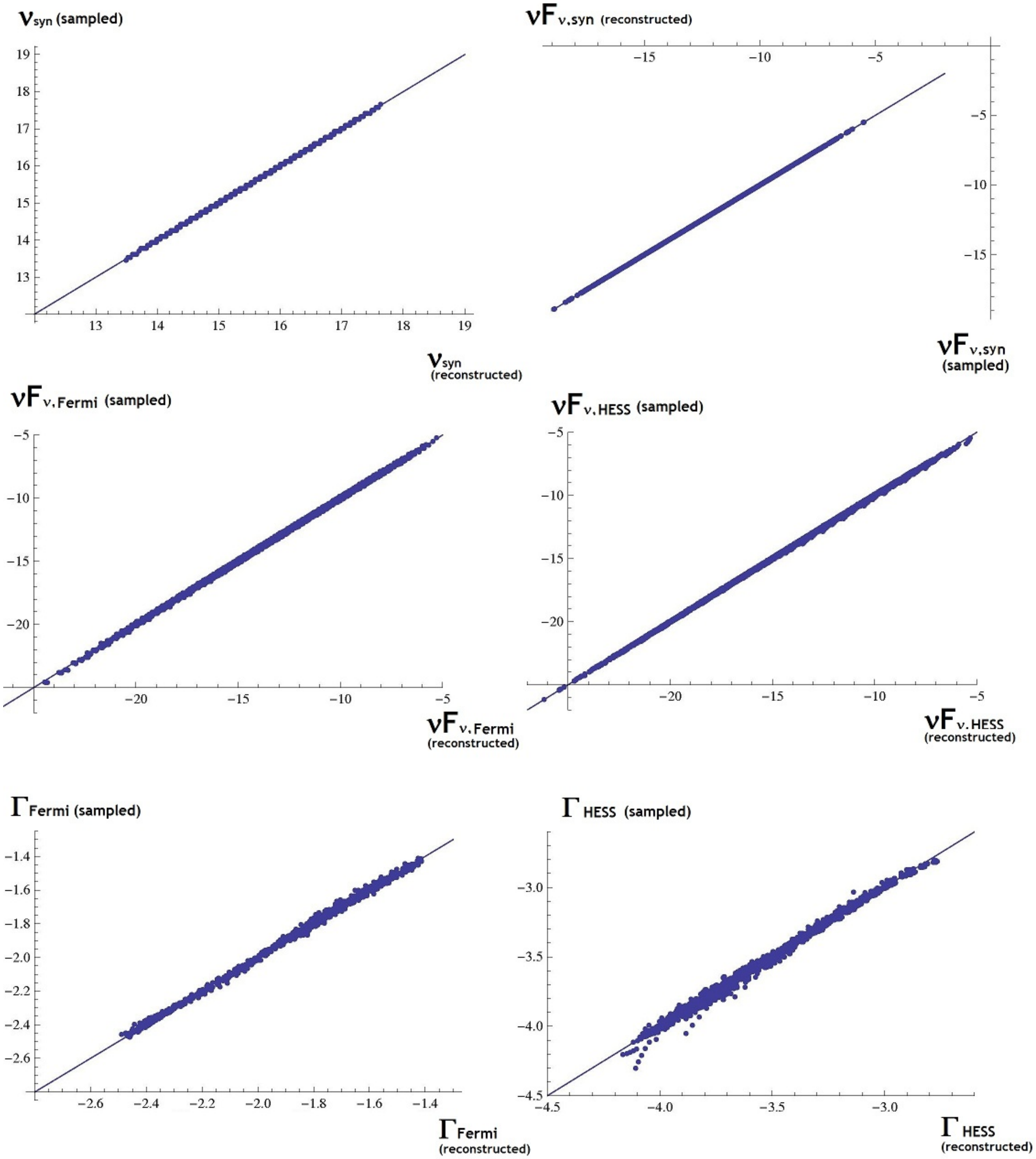

Figure 6.4: Comparison between the sampled values of the six observables considered in this study and their reconstructed value, expressed as a function of the SSC-model parameters, for the case of *1RXS J101015.9 - 311909*. In a perfect fit, the points would follow a linear relation (tiny solid line). The six subplots are in the order (from top to bottom, from left to right): the synchrotron peak frequency; the synchrotron peak flux (expressed as $\nu F_{\nu;s}$); the *Fermi* flux (measured at the decorrelation energy and expressed as $\nu F_{\nu;Fermi}$); the *H.E.S.S.* flux (measured at the decorrelation energy and expressed as $\nu F_{\nu;HESS}$); the measured *Fermi* photon index and the measured *H.E.S.S.* photon index.

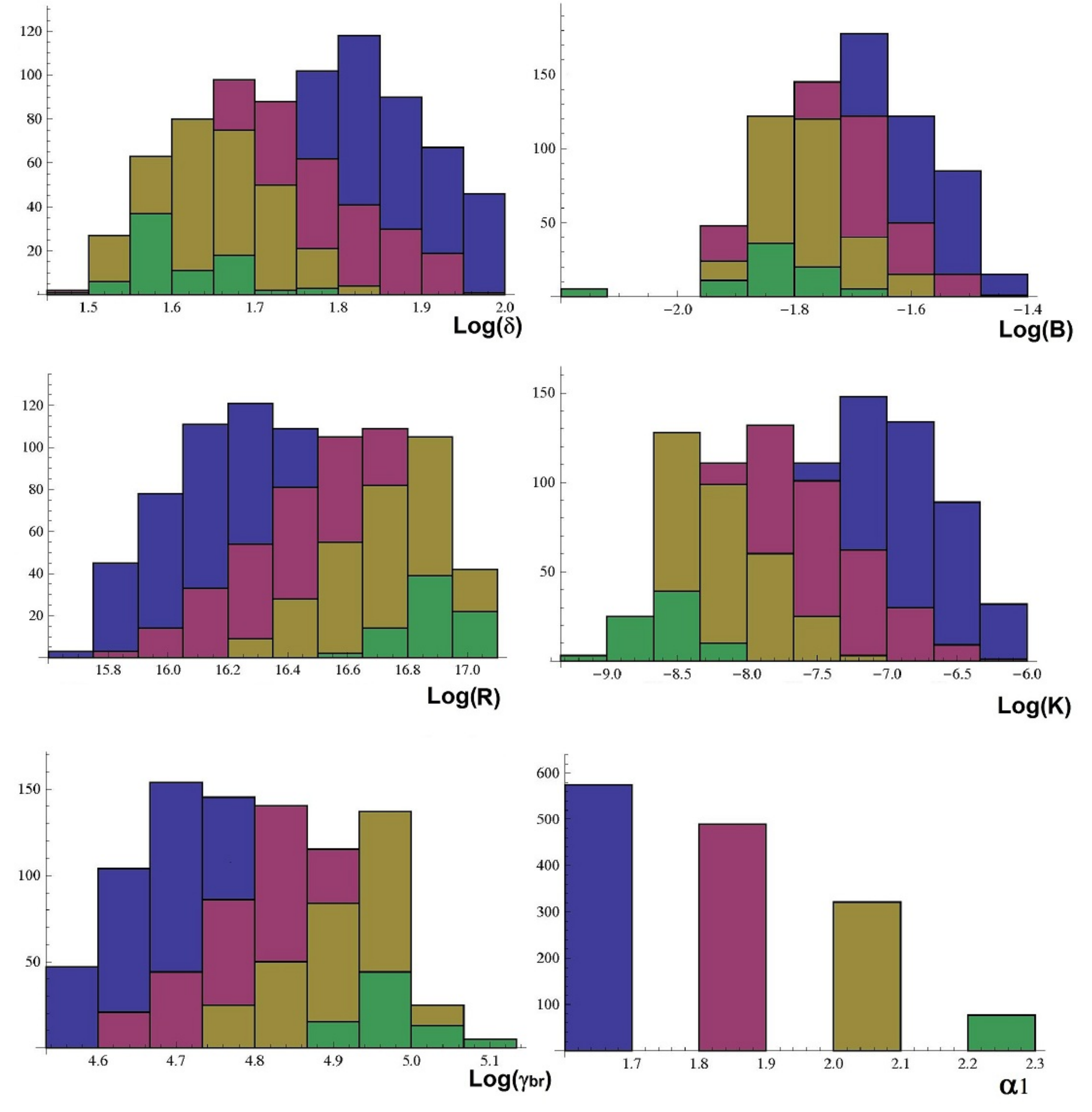

Figure 6.5: Histograms showing the values of the SSC model parameters solved for the case of *1RXS J101015.9 - 311909*. From top to bottom, and left to right, we show the distribution of the solutions for δ, B (in G), R (in cm), K' (in cm^{-3}), γ_{break}, and α_1. Please notice that the value of α_1 is not totally free, but it has been frozen, and studied for four different cases (1.6, 1.8, 2.0 and 2.2). The four colours represent the different solutions for the four values of $alpha_1$ studied.

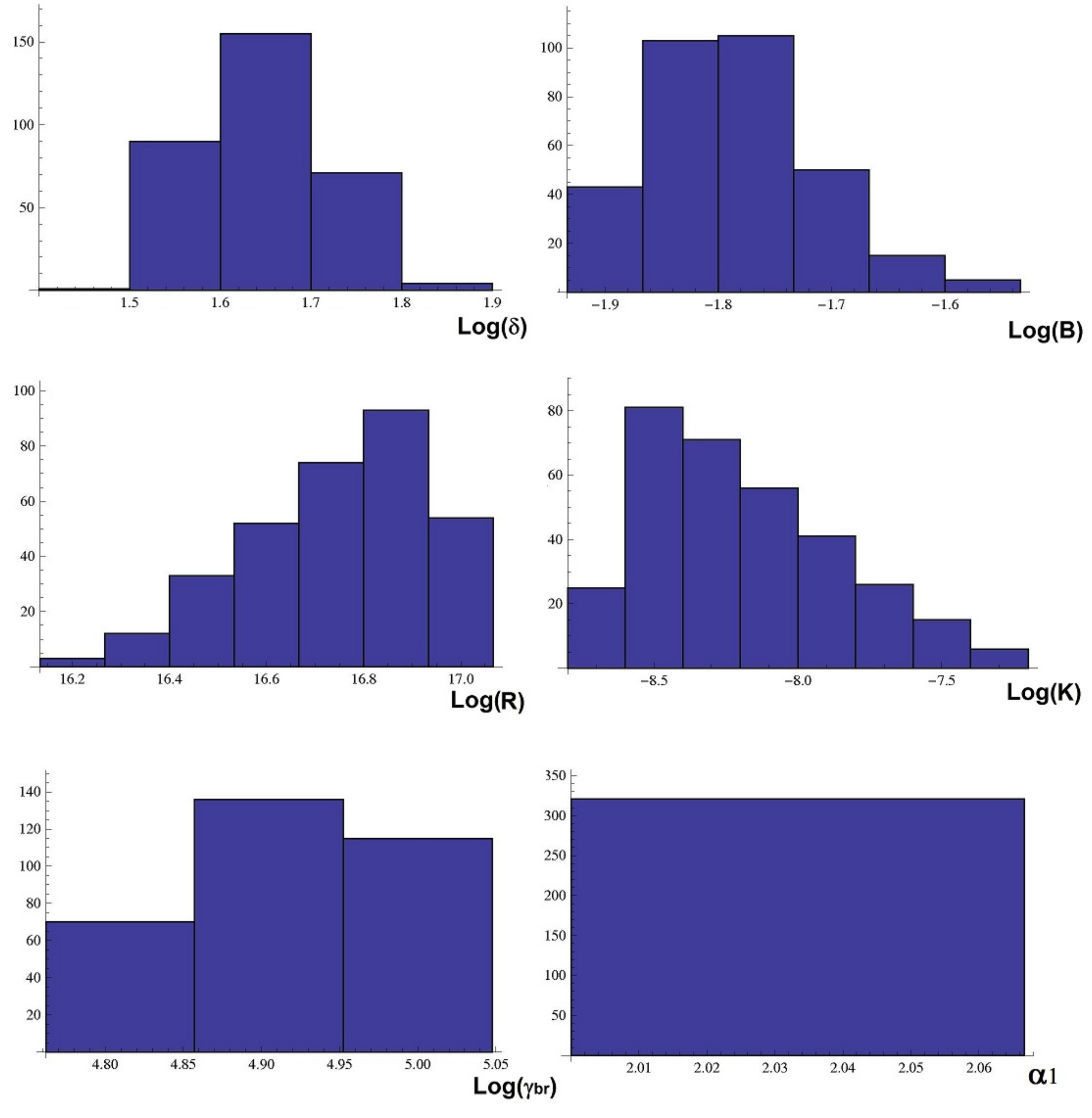

Figure 6.6: Histograms showing the values of the SSC model parameters solved for the case of *1RXS J101015.9 - 311909*. From top to bottom, and left to right, we show the distribution of the solutions for δ, B (in G), R (in cm), K' (in cm^{-3}), γ_{break}, and α_1. In this case only the solutions obtained fixing α_1 equal to 2.0 are shown.

Table 6.3: Coefficients of the fit performed to obtain an expression of $\nu F_{\nu;Fermi}$ (left) and $\nu F_{\nu;HESS}$ (right) for the case of *1RXS J101015.9 - 311909*. The correspondent plots are the central plots of Fig. 6.4. Each line correspond to a term of the fit: the first column gives the total order of the polynomial, the next six columns give, for each model free parameter, the degree considered, and the last column gives the associated coefficient. The terms are listed regarding to the parameters composing each term, and then by increasing degree, *not* by relative weight in the fit. In this case, the value of α_2 has been fixed to 4.0.

Order	γ_{br}	B	K	α_1	δ	R	Coefficient	Order	γ_{br}	B	K	α_1	δ	R	Coefficient
0	-	-	-	-	-	-	-113.002	0	-	-	-	-	-	-	-114.315
1	1	-	-	-	-	-	16.3966	1	1	-	-	-	-	-	14.0846
2	2	-	-	-	-	-	-1.4658	2	2	-	-	-	-	-	-0.938894
1	-	1	-	-	-	-	4.69141	1	-	1	-	-	-	-	4.41682
2	1	1	-	-	-	-	-0.688759	2	1	1	-	-	-	-	-0.532471
1	-	-	1	-	-	-	1.9998	1	-	-	1	-	-	-	1.99864
1	-	-	-	1	-	-	-16.0426	1	-	-	-	1	-	-	-5.11436
2	1	-	-	1	-	-	4.43891	2	1	-	-	1	-	-	1.28344
2	-	1	-	1	-	-	1.07212	1	-	-	-	-	1	-	4.69911
1	-	-	-	-	1	-	3.94107	1	-	-	-	-	-	1	3.99727
1	-	-	-	-	-	1	3.9996								

Table 6.4: Coefficients of the fit performed to obtain an expression of Γ_{Fermi} for the case of *1RXS J101015.9 - 311909*. The correspondent plot is the left bottom plot of Fig. 6.4. Each line correspond to a term of the fit: the first column gives the total order of the polynomial, the next six columns give, for each model free parameter, the degree considered, and the last column gives the associated coefficient. The terms are listed regarding to the parameters composing each term, and then by increasing degree, *not* by relative weight in the fit. In this case, the value of α_2 has been fixed to 4.0.

Order	γ_{br}	B	K	α_1	δ	R	Coefficient	Order	γ_{br}	B	K	α_1	δ	R	Coefficient
0	-	-	-	-	-	-	398.213	2	1	-	-	1	-	-	4.4965
1	1	-	-	-	-	-	-348.795	3	2	-	-	1	-	-	0.309104
2	2	-	-	-	-	-	112.175	2	-	1	-	1	-	-	-0.380824
3	3	-	-	-	-	-	-15.8483	2	-	-	-	2	-	-	-1.68929
4	4	-	-	-	-	-	0.833565	1	-	-	-	-	1	-	-70.9811
1	-	1	-	-	-	-	-68.9286	2	1	-	-	-	1	-	46.4101
2	1	1	-	-	-	-	44.1488	3	2	-	-	-	1	-	-9.87151
3	2	1	-	-	-	-	-9.33914	4	3	-	-	-	1	-	0.688271
4	3	1	-	-	-	-	0.654178	3	1	1	-	-	1	-	0.217057
3	1	2	-	-	-	-	0.087207	4	2	1	-	-	1	-	-0.0467622
4	2	2	-	-	-	-	-0.0195643	2	-	-	-	1	1	-	-0.324303
1	-	-	-	1	-	-	13.6346	2	-	-	-	-	2	-	-0.0738383

Table 6.5: Coefficients of the fit performed to obtain an expression of Γ_{HESS} for the case of *1RXS J101015.9 - 311909*. The correspondent plot is the right bottom plot of Fig. 6.4. Each line correspond to a term of the fit: the first column gives the total order of the polynomial, the next six columns give, for each model free parameter, the degree considered, and the last column gives the associated coefficient. The terms are listed regarding to the parameters composing each term, and then by increasing degree, *not* by relative weight in the fit. In this case, the value of α_2 has been fixed to 4.0.

Order	γ_{br}	B	K	α_1	δ	R	Coefficient	Order	γ_{br}	B	K	α_1	δ	R	Coefficient
0	-	-	-	-	-	-	-3954.35	3	-	1	-	1	1	-	2.38177
1	1	-	-	-	-	-	2163.16	4	1	1	-	1	1	-	-0.643191
2	2	-	-	-	-	-	-290.652	4	1	-	-	2	1	-	0.00172655
3	3	-	-	-	-	-	-0.160449	2	-	-	-	-	2	-	200.785
1	-	1	-	-	-	-	-851.172	3	1	-	-	-	2	-	-153.997
2	1	1	-	-	-	-	983.022	4	2	-	-	-	2	-	37.9658
3	2	1	-	-	-	-	-320.271	5	3	-	-	-	2	-	-3.02415
4	3	1	-	-	-	-	41.0637	3	-	1	-	-	2	-	-25.4177
5	4	1	-	-	-	-	-2.1726	4	1	1	-	-	2	-	11.7392
2	-	2	-	-	-	-	14.8015	5	2	1	-	-	2	-	-1.34305
3	1	2	-	-	-	-	-30.6515	4	1	-	-	-	3	-	0.757704
4	2	2	-	-	-	-	8.67771	5	2	-	-	-	3	-	-0.172364
5	3	2	-	-	-	-	-0.519937	1	-	-	-	-	-	1	545.898
1	-	-	1	-	-	-	-156.652	2	1	-	-	-	-	1	-303.063
2	1	-	1	-	-	-	99.164	3	2	-	-	-	-	1	41.2409
3	2	-	1	-	-	-	-14.7709	2	-	1	-	-	-	1	-37.7498
2	-	1	1	-	-	-	88.8937	3	1	1	-	-	-	1	-10.3761
3	1	1	1	-	-	-	28.549	4	2	1	-	-	-	1	4.65842
4	2	1	1	-	-	-	1.72284	3	-	2	-	-	-	1	1.1598
3	-	2	1	-	-	-	-8.74045	4	1	2	-	-	-	1	0.3104
4	1	2	1	-	-	-	2.40497	5	2	2	-	-	-	1	-0.142019
5	2	2	1	-	-	-	-0.0710192	2	-	-	1	-	-	1	32.2241
2	-	-	2	-	-	-	10.5324	3	1	-	1	-	-	1	-20.1753
3	1	-	2	-	-	-	-6.69355	4	2	-	1	-	-	1	2.98328
4	2	-	2	-	-	-	0.99886	3	-	1	1	-	-	1	-16.1852
3	-	1	2	-	-	-	-5.71583	4	1	1	1	-	-	1	4.59722
4	1	1	2	-	-	-	1.58048	5	2	1	1	-	-	1	-0.172364
5	2	1	2	-	-	-	-0.0499911	4	-	2	1	-	-	1	0.454641
1	-	-	-	1	-	-	100.625	5	1	2	1	-	-	1	-0.109741
2	1	-	-	1	-	-	-89.3943	3	-	-	2	-	-	1	-0.753039
3	2	-	-	1	-	-	24.4512	4	1	-	2	-	-	1	0.459343
4	3	-	-	1	-	-	2.09082	5	2	-	2	-	-	1	-0.0668009
2	-	1	-	1	-	-	-22.027	4	-	1	2	-	-	1	0.291005
3	1	1	-	1	-	-	9.78226	5	1	1	2	-	-	1	-0.0698424
4	2	1	-	1	-	-	-1.04136	3	1	-	-	-	1	1	-0.00357236
1	-	-	-	-	1	-	-1170.29	4	1	1	-	-	1	1	-0.0146785
2	1	-	-	-	1	-	1052.36	3	-	-	1	-	1	1	-0.00710273
3	2	-	-	-	1	-	-341.5	4	-	1	1	-	1	1	0.00271708

Continued on next page

Table 6.5 – continued from previous page

Order	γ_{br}	B	K	α_1	δ	R	Coefficient	Order	γ_{br}	B	K	α_1	δ	R	Coefficient
4	3	-	-	-	1	-	47.3488	5	1	1	1	-	1	1	-0.0017413
5	4	-	-	-	1	-	-2.35472	2	-	-	-	-	-	2	-19.6259
2	-	1	-	-	1	-	288.799	3	1	-	-	-	-	2	10.8947
3	1	1	-	-	1	-	-178.629	4	2	-	-	-	-	2	-1.48254
4	2	1	-	-	1	-	36.2439	3	-	1	-	-	-	2	0.998147
5	3	1	-	-	1	-	-2.39234	4	1	1	-	-	-	2	0.595245
4	1	2	-	-	1	-	0.0860533	5	2	1	-	-	-	2	-0.200008
5	2	2	-	-	1	-	-0.0183176	3	-	-	1	-	-	2	-1.50662
3	1	-	1	-	1	-	0.0303717	4	1	-	1	-	-	2	0.918928
4	1	1	1	-	1	-	0.0406589	5	2	-	1	-	-	2	-0.133628
2	-	-	-	1	1	-	12.3366	4	-	1	1	-	-	2	0.582001
3	1	-	-	1	1	-	-3.11118	5	1	1	1	-	-	2	-0.139682

6.4.2 *PKS 0447-439*

The second test of our numerical algorithm is the BL Lac object *PKS 0447-439*, which has been recently detected by the *H.E.S.S.* collaboration (Zech et al. 2011). As for many blazars, its redshift is unknown (there are no detectable absorption nor emission lines in its optical spectrum), and only a lower limit as been defined ($z > 0.176$, Landt & Bignall 2008). In this Section we show that, in a model-dependent way, and under certain assumptions we can significantly constrain the distance of a HBL with unknown redshift.
In order to have the same number of free parameters, we substitute α_1 with z, which become the new parameter sampled in the production of the model grid (spanning 0.1 to 0.5), while α_1 has been fixed to 2.0. The X-ray spectrum of *PKS 0447-439* constraints the value of α_2 to 3.6. The model grid has then been produced sampling the other six free parameters in the ranges: $\delta \in [20, 100]$, $B \in [0.001, 0.1]$ G, $\gamma_{break} \in [10^4, 10^5]$, $K' \in [10^{-10}, 10^{-7}]$ cm^{-3} and $R \in [10^{16}, 10^{17}]$ cm. Apart from this major modification, we follow the same steps used for the analysis on *1RXS J101015.9 - 311909*: in Fig. 6.7 we show the results of the grid fit, whose parameters are given in Table 6.7, 6.10, 6.8 and 6.9

The system of equations is solved for four different values of z (0.2, 0.25, 0.3, 0.35) iterating (four times) over the values of the observables, which are: $\nu_s \in [15.15, 15.35]$, $\nu f_{\nu;s} \in [-10.33, -10.37]$, $\nu f_{\nu;Fermi} \in [-10.85, -10.61]$, $\nu f_{\nu;HESS} \in [-11.5, -11.3]$, $\Gamma_{Fermi} \in [-2.04, -1.66]$ and $\Gamma_{HESS} \in [-4.43, -3.47]$. In this case as well, the error on the γ-ray observables includes the systematic error (summed in quadrature to the statisitic one). The system of equation includes an inequality for the variability time-scale ($\tau_{var} = 24$ hours) plus a limit on the value of the Doppler factor ($\delta < 100$, which corresponds to the limit of the sampled grid).
The set of solutions found is plotted in Fig. 6.8, and the constrained values are given in Table 6.6.
As can be seen, the system is not solved for $z = 0.35$, providing a strong upper-limit on the redshift of the source, in the framework of the SSC modelling of the broad-band emission. For the other studied redshift values, a solution is found, with a Doppler factor comprised between 30 and 90 (the minimum required Doppler factor increasing with z).

The constraint on the distance of *PKS 0447-439* can be better determined by sampling more redshift values to study: we then considered 15 different values of z, from 0.2 to 0.35, and we found that the first value of redshift for which no solutions exist is 0.33, which can then be defined as the z_{Max} of this object (assuming that the SSC modelling is a good description of the SED, that the EBL model by Franceschini et al. (2008) is correct, and that the primary electron distribution has a first slope equal to 2.0). However, the high Doppler factor required for the solutions found for $z \geq 0.2$, favours a relatively low redshift, comprised between 0.176 and 0.2.

A tentative measurement of the redshift of this source ($z = 0.205$) was made by Perlman et al. (1998), whose result was however not confirmed by further studies. Recently, a tentative measurement of the redshift of this source has been proposed by Landt (2012), who proposed $z \geq 1.246$. However, this value is preasumeably affected by an uncorrect substraction of the atmospheric absorption, as shown by Pita et al. (2012).
Prandini et al. (2012) recently proposed a redshift value of $z = 0.20 \pm 0.05$, using an empirical approach which makes use of the GeV and TeV photon index (see Prandini et al. 2010, for details), consistent with our result.

Table 6.6: Summary of the constrained parameters for the SSC modelling of *PKS 0447-439*. The solutions have been computed for four different values of z, which have been frozen in the solution of the system. For the other five free parameters, we provide the minimum and the maximum value found. The solutions with a Doppler factor higher than 100 have been excluded

z	0.18	0.2	0.25	0.3
γ_{break}	$(2.32 - 3.44) \cdot 10^4$	$(1.61 - 4.46) \cdot 10^4$	$(2.27 - 5.53) \cdot 10^4$	$(4.77 - 6.40) \cdot 10^4$
B	0.0112 – 0.0231	0.0026 – 0.0165	0.0016 – 0.0123	0.0013 – 0.0018
K'	$(2.55 - 20.0) \cdot 10^{-7}$	$(0.601 - 117.80) \cdot 10^{-7}$	$(0.271 - 33.76) \cdot 10^{-7}$	$(0.203 - 0.398) \cdot 10^{-7}$
δ	36.66 – 42.99	69.38 – 99.99	68.84 – 99.95	89.22 – 99.68
R	$(3.50 - 8.33) \cdot 10^{16}$	$(1.39 - 13.60) \cdot 10^{16}$	$(2.14 - 18.12) \cdot 10^{16}$	$(16.7 - 19.4) \cdot 10^{16}$

Table 6.7: Coefficients of the fit performed to obtain an expression of ν_s (left) and $\nu F_{\nu;s}$ (right) for the case of *PKS 0447-439*. The correspondent plots are the top plots of Fig. 6.7. Each line correspond to a term of the fit: the first column gives the total order of the polynomial, the next six columns give, for each model free parameter, the degree considered, and the last column gives the associated coefficient. The terms are listed regarding to the parameters composing each term, and then by increasing degree, *not* by relative weight in the fit. In this case, the value of α_1 has been fixed to 2.0, and α_2 to 3.6.

Order	γ_{br}	B	K	z	δ	R	Coefficient	Order	γ_{br}	B	K	z	δ	R	Coefficient
0	-	-	-	-	-	-	6.45829	0	-	-	-	-	-	-	-72.221
1	1	-	-	-	-	-	2.00352	1	1	-	-	-	-	-	2.99977
1	-	1	-	-	-	-	1.00058	1	-	1	-	-	-	-	2.00001
1	-	-	-	1	-	-	-0.19414	1	-	-	1	-	-	-	1.0
1	-	-	-	-	1	-	1.00095	1	-	-	-	1	-	-	-2.08905
								1	-	-	-	-	1	-	3.99998
								1	-	-	-	-	-	1	3.0

Table 6.8: Coefficients of the fit performed to obtain an expression of Γ_{Fermi} for the case of *PKS 0447-439*. The correspondent plot is the right bottom plot of Fig. 6.7. Each line correspond to a term of the fit: the first column gives the total order of the polynomial, the next six columns give, for each model free parameter, the degree considered, and the last column gives the associated coefficient. The terms are listed regarding to the parameters composing each term, and then by increasing degree, *not* by relative weight in the fit. In this case, the value of α_2 has been fixed to 2.0, and α_2 to 3.6.

Order	γ_{br}	B	K	z	δ	R	Coefficient	Order	γ_{br}	B	K	z	δ	R	Coefficient
0	-	-	-	-	-	-	571.705	4	1	1	1	-	1	-	-2.04576
1	1	-	-	-	-	-	-468.723	2	-	-	-	1	1	-	0.0198501
2	2	-	-	-	-	-	105.05	2	-	-	-	-	2	-	-0.0529074
3	3	-	-	-	-	-	-9.22313	1	-	-	-	-	-	1	-18.9231
4	4	-	-	-	-	-	0.421236	2	1	-	-	-	-	1	16.3116
1	-	1	-	-	-	-	-39.9937	3	2	-	-	-	-	1	-2.11782
2	1	1	-	-	-	-	-81.452	2	-	1	-	-	-	1	8.44413

Continued on next page

Table 6.8 – continued from previous page

Order	γ_{br}	B	K	z	δ	R	Coefficient	Order	γ_{br}	B	K	z	δ	R	Coefficient
3	2	1	-	-	-	-	20.0101	3	1	1	-	-	-	1	4.30282
4	3	1	-	-	-	-	-0.330335	4	2	1	-	-	-	1	-1.10718
2	-	2	-	-	-	-	-47.3667	3	-	2	-	-	-	1	2.35097
3	1	2	-	-	-	-	11.2108	4	1	2	-	-	-	1	-0.430701
1	-	-	1	-	-	-	20.1031	5	2	2	-	-	-	1	0.0297321
2	1	-	1	-	-	-	-23.3041	2	-	-	1	-	-	1	-1.54343
3	2	-	1	-	-	-	3.80504	3	1	-	1	-	-	1	1.80569
2	-	1	1	-	-	-	-33.4641	4	2	-	1	-	-	1	-0.250805
3	1	1	1	-	-	-	2.38955	3	-	1	1	-	-	1	2.71644
4	2	1	1	-	-	-	0.983436	4	1	1	1	-	-	1	-0.0882339
3	-	2	1	-	-	-	-15.7716	5	2	1	1	-	-	1	-0.0807291
4	1	2	1	-	-	-	5.57224	4	-	2	1	-	-	1	0.0857171
5	2	2	1	-	-	-	-0.433953	5	1	2	1	-	-	1	-0.291479
3	1	-	2	-	-	-	0.113397	6	2	2	1	-	-	1	0.020913
3	-	1	2	-	-	-	0.517243	4	1	-	2	-	-	1	-0.00702387
4	1	1	2	-	-	-	-0.058539	4	-	1	2	-	-	1	-0.0320156
1	-	-	-	1	-	-	-0.216484	5	1	1	2	-	-	1	0.00362036
2	1	-	-	1	-	-	0.0178506	2	-	-	-	-	1	1	7.52994
2	-	-	-	2	-	-	-0.0484962	3	1	-	-	-	1	1	1.79391
1	-	-	-	-	1	-	29.3559	3	-	1	-	-	1	1	-3.62135
2	1	-	-	-	1	-	35.1506	4	1	1	-	-	1	1	0.863516
3	2	-	-	-	1	-	-14.6849	3	-	-	1	-	1	1	1.10886
4	3	-	-	-	1	-	1.1132	4	1	-	1	-	1	1	0.264333
2	-	1	-	-	1	-	29.3506	4	-	1	1	-	1	1	0.532573
3	1	1	-	-	1	-	7.15172	5	1	1	1	-	1	1	0.127085
4	2	1	-	-	1	-	-5.02861	3	1	-	-	-	-	2	-0.0947857
5	3	1	-	-	1	-	0.395586	3	-	1	-	-	-	2	-0.431792
4	1	2	-	-	1	-	0.00317698	4	1	1	-	-	-	2	0.0488131
2	-	-	1	-	1	-	17.8503	4	1	-	1	-	-	2	-0.0140932
3	1	-	1	-	1	-	-4.25576	4	-	1	1	-	-	2	-0.0642827
3	-	1	1	-	1	-	8.57179	5	1	1	1	-	-	2	0.00727777

Table 6.9: Coefficients of the fit performed to obtain an expression of Γ_{HESS} for the case of *PKS 0447-439*. The correspondent plot is the left bottom plot of Fig. 6.7. Each line correspond to a term of the fit: the first column gives the total order of the polynomial, the next six columns give, for each model free parameter, the degree considered, and the last column gives the associated coefficient. The terms are listed regarding to the parameters composing each term, and then by increasing degree, *not* by relative weight in the fit. In this case, the value of α_2 has been fixed to 2.0, and α_2 to 3.6.

Order	γ_{br}	B	K	z	δ	R	Coefficient	Order	γ_{br}	B	K	z	δ	R	Coefficient
0	-	-	-	-	-	-	-17009.0	2	-	-	-	-	2	-	-2.46037

Continued on next page

Table 6.9 – continued from previous page

Order	γ_{br}	B	K	z	δ	R	Coefficient	Order	γ_{br}	B	K	z	δ	R	Coefficient
1	1	-	-	-	-	-	6795.57	3	1	-	-	-	2	-	0.567358
2	2	-	-	-	-	-	-824.788	1	-	-	-	-	-	1	1374.23
3	3	-	-	-	-	-	24.4175	2	1	-	-	-	-	1	-433.961
1	-	1	-	-	-	-	-14813.0	3	2	-	-	-	-	1	32.9607
2	1	1	-	-	-	-	6659.01	2	-	1	-	-	-	1	980.643
3	2	1	-	-	-	-	-998.348	3	1	1	-	-	-	1	-341.7
4	3	1	-	-	-	-	44.7119	4	2	1	-	-	-	1	37.9328
2	-	2	-	-	-	-	-4539.53	5	3	1	-	-	-	1	-1.31569
3	1	2	-	-	-	-	2628.93	3	-	2	-	-	-	1	255.377
4	2	2	-	-	-	-	-518.352	4	1	2	-	-	-	1	-139.899
5	3	2	-	-	-	-	31.5486	5	2	2	-	-	-	1	27.2703
1	-	-	1	-	-	-	-1342.73	6	3	2	-	-	-	1	-1.60802
2	1	-	1	-	-	-	486.557	5	1	3	-	-	-	1	0.00479986
3	2	-	1	-	-	-	-50.5161	2	-	-	1	-	-	1	106.894
2	-	1	1	-	-	-	-655.843	3	1	-	1	-	-	1	-24.2438
3	1	1	1	-	-	-	190.492	5	3	-	1	-	-	1	0.201401
4	2	1	1	-	-	-	-2.78315	3	-	1	1	-	-	1	33.676
5	3	1	1	-	-	-	3.72404	5	2	1	1	-	-	1	-2.70421
3	-	2	1	-	-	-	-141.914	6	3	1	1	-	-	1	0.412083
4	1	2	1	-	-	-	95.3309	5	1	2	1	-	-	1	-2.25164
5	2	2	1	-	-	-	-20.5401	6	2	2	1	-	-	1	0.812849
6	3	2	1	-	-	-	0.65831	6	1	3	1	-	-	1	0.00260742
5	1	3	1	-	-	-	-0.0561336	3	-	-	2	-	-	1	-0.8503
2	-	-	2	-	-	-	30.1288	5	2	-	2	-	-	1	0.056178
3	1	-	2	-	-	-	-7.78144	5	1	1	2	-	-	1	-0.309632
3	-	1	2	-	-	-	7.07657	6	2	1	2	-	-	1	0.0726727
5	2	1	2	-	-	-	-0.540777	5	-	2	2	-	-	1	0.021954
5	1	2	2	-	-	-	-0.727234	6	1	2	2	-	-	1	0.0197914
6	2	2	2	-	-	-	0.071911	2	-	-	-	-	1	1	1.10437
1	-	-	-	1	-	-	-7.1227	4	2	-	-	-	1	1	-0.484547
2	1	-	-	1	-	-	1.22876	4	1	1	-	-	1	1	-1.06297
3	2	-	-	1	-	-	-0.148402	5	2	1	-	-	1	1	-0.317501
2	-	-	-	2	-	-	31.235	5	1	2	-	-	1	1	-0.712116
3	-	-	-	3	-	-	56.2458	5	2	-	1	-	1	1	-0.0690995
4	-	-	-	4	-	-	26.8421	5	1	1	1	-	1	1	-0.218396
1	-	-	-	-	1	-	-9.25675	6	2	1	1	-	1	1	-0.0388661
2	1	-	-	-	1	-	-0.551168	6	1	2	1	-	1	1	-0.111363
3	2	-	-	-	1	-	7.64413	2	-	-	-	-	-	2	25.6867
2	-	1	-	-	1	-	7.61672	3	1	-	-	-	-	2	5.23634
3	1	1	-	-	1	-	11.9078	4	2	-	-	-	-	2	-9.84735
4	2	1	-	-	1	-	6.949	5	2	1	-	-	-	2	0.39262
5	3	1	-	-	1	-	-0.203086	5	1	2	-	-	-	2	-0.303493
4	1	2	-	-	1	-	12.0218	6	2	2	-	-	-	2	0.0335561

Continued on next page

Table 6.9 – continued from previous page

Order	γ_{br}	B	K	z	δ	R	Coefficient	Order	γ_{br}	B	K	z	δ	R	Coefficient
5	2	2	-	-	1	-	-0.0899831	3	-	-	1	-	-	2	-1.76337
2	-	-	1	-	1	-	0.552169	5	2	-	1	-	-	2	0.07035
4	2	-	1	-	1	-	1.10517	5	1	1	1	-	-	2	-0.343158
4	1	1	1	-	1	-	3.72724	6	2	1	1	-	-	2	0.0621977
5	2	1	1	-	1	-	0.59914	5	-	2	1	-	-	2	0.383695
5	1	2	1	-	1	-	1.81552	6	1	2	1	-	-	2	-0.11387
3	1	-	-	1	1	-	-0.00820909	4	-	1	1	-	-	2	0.00934371

Table 6.10: Coefficients of the fit performed to obtain an expression of $\nu F_{\nu;Fermi}$ (left) and $\nu F_{\nu;HESS}$ (right) for the case of *PKS 0447-439*. The correspondent plots are the central plots of Fig. 6.7. Each line correspond to a term of the fit: the first column gives the total order of the polynomial, the next six columns give, for each model free parameter, the degree considered, and the last column gives the associated coefficient. The terms are listed regarding to the parameters composing each term, and then by increasing degree, *not* by relative weight in the fit. In this case, the value of α_1 has been fixed to 2.0, and α_2 to 3.6.

Order	γ_{br}	B	K	z	δ	R	Coefficient	Order	γ_{br}	B	K	z	δ	R	Coefficient
0	-	-	-	-	-	-	-92.8526	0	-	-	-	-	-	-	-101.595
1	1	-	-	-	-	-	5.16212	1	1	-	-	-	-	-	6.25028
1	-	1	-	-	-	-	1.78842	1	-	1	-	-	-	-	1.84784
1	-	-	1	-	-	-	1.99857	1	-	-	1	-	-	-	1.95925
1	-	-	-	1	-	-	-2.06028	1	-	-	-	1	-	-	-11.0249
1	-	-	-	-	1	-	3.83702	2	-	-	-	2	-	-	-8.6787
1	-	-	-	-	-	1	3.99748	3	-	-	-	3	-	-	-3.12142
								1	-	-	-	-	1	-	4.57725
								1	-	-	-	-	-	1	3.9185

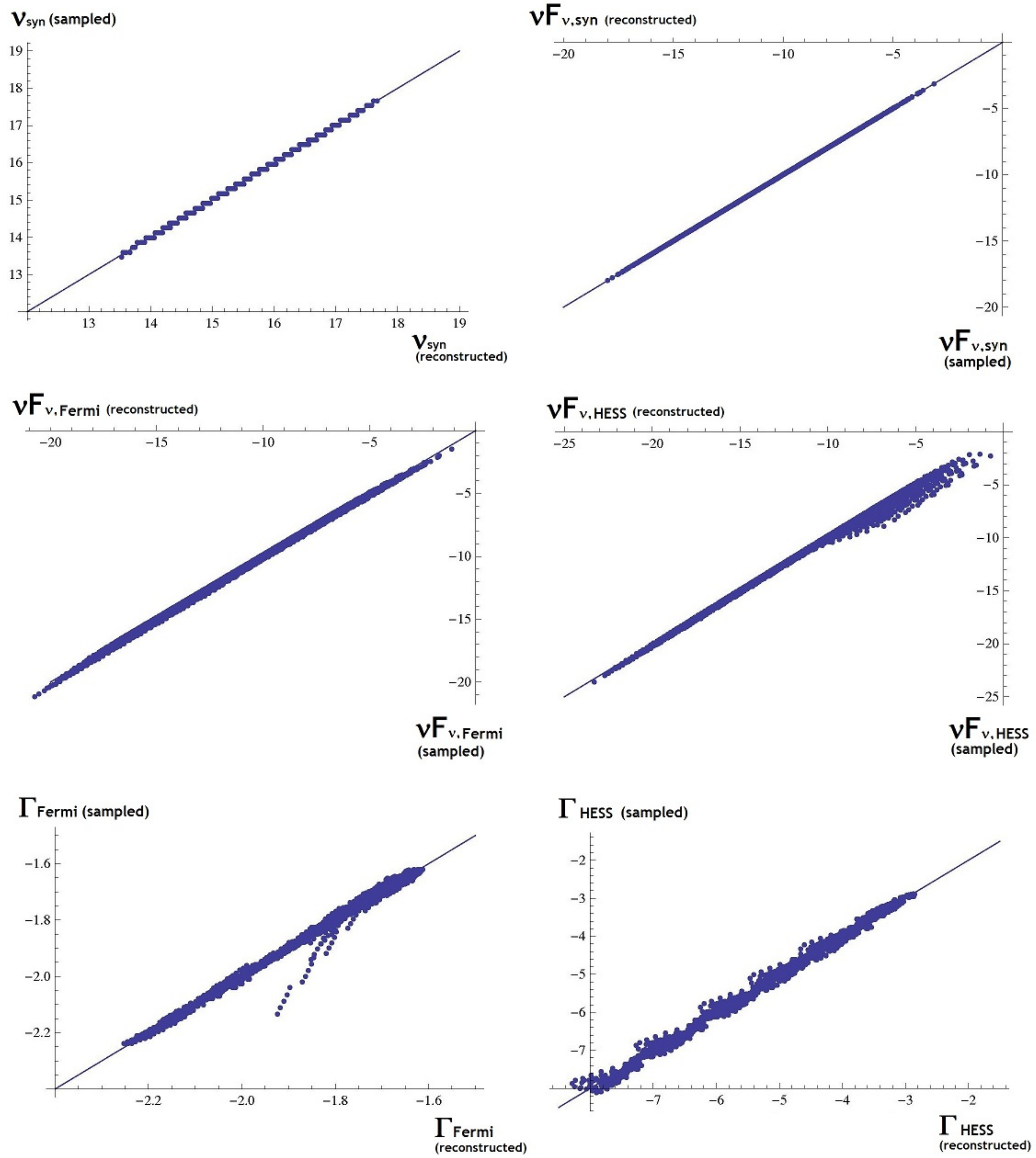

Figure 6.7: Comparison between the sampled values of the six observables considered in this study and their reconstructed value, expressed as a function of the SSC-model parameters, for the case of *PKS 0447-439*. In a perfect fit, the points would follow a linear relation (tiny solid line). The six subplots are in the order (from top to bottom, from left to right): the synchrotron peak frequency; the synchrotron peak flux (expressed as $\nu F_{\nu;s}$); the *Fermi* flux (measured at the decorrelation energy and expressed as $\nu F_{\nu;Fermi}$); the *H.E.S.S.* flux (measured at the decorrelation energy and expressed as $\nu F_{\nu;HESS}$); the measured *Fermi* photon index and the measured *H.E.S.S.* photon index.

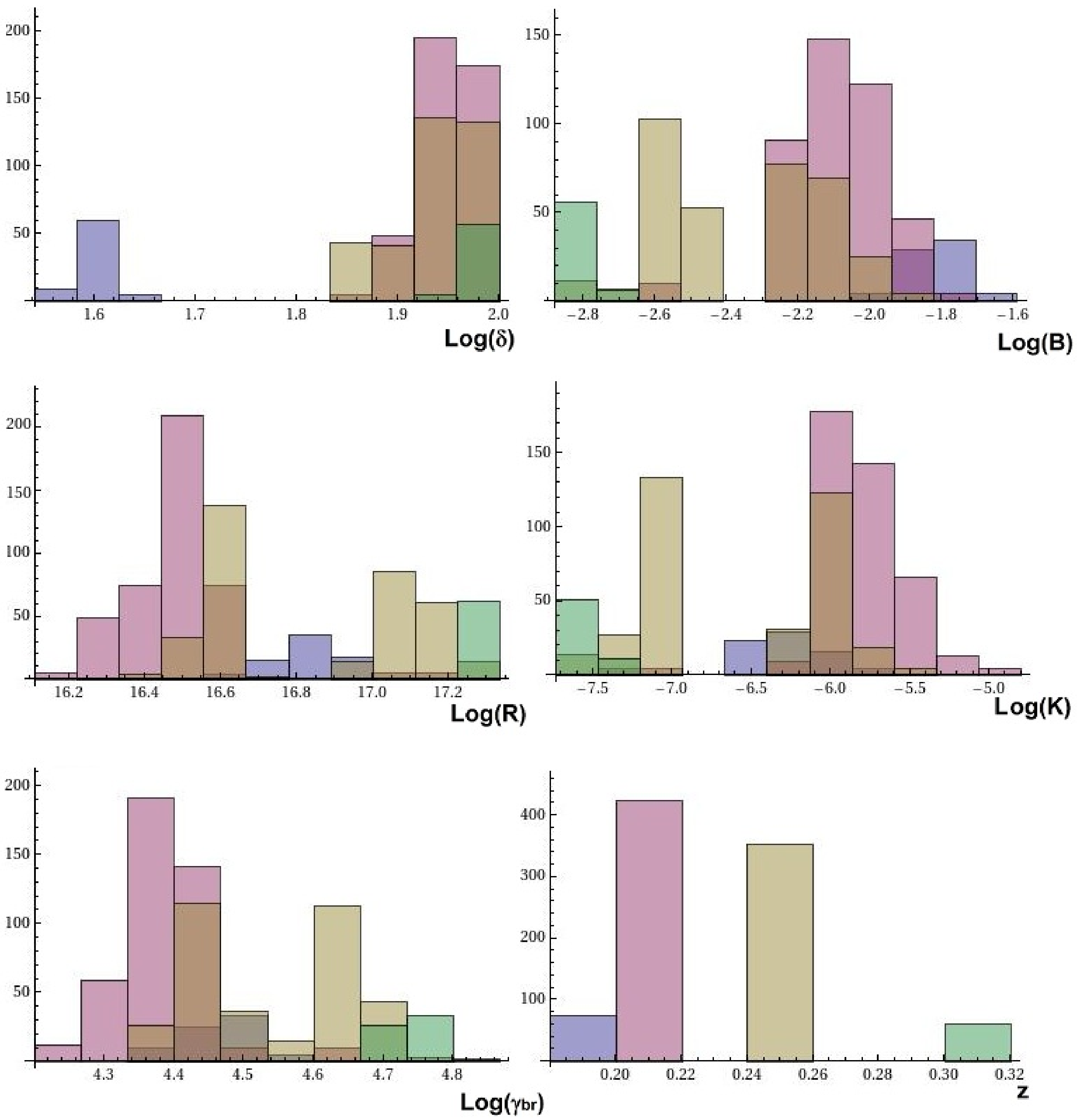

Figure 6.8: Comparison between the sampled values of the six observables considered in this study and their reconstructed value, expressed as a function of the SSC-model parameters, for the case of *PKS 0447-439*. In a perfect fit, the points would follow a linear relation (tiny solid line). The six subplots are in the order (from top to bottom, from left to right): the synchrotron peak frequency; the synchrotron peak flux (expressed as $\nu F_{\nu;s}$); the *Fermi* flux (measured at the decorrelation energy and expressed as $\nu F_{\nu;Fermi}$); the *H.E.S.S.* flux (measured at the decorrelation energy and expressed as $\nu F_{\nu;HESS}$); the measured *Fermi* photon index and the measured *H.E.S.S.* photon index.

Chapter 7

Development of a new lepto-hadronic code

Contents

7.1 Introduction

In this Chapter we describe the development of a new lepto-hadronic code, which computes all the relevant emission processes for the modelling of blazar emission in leptonic (see Section 3.3) and hadronic (see Section 3.4) scenarios.
This work represents an evolution of the original code developed by Katarzyński et al. (2001). In the aim of including hadronic processes, several modification have been performed to the SSC code (see Section 7.2). The description of the coding of hadronic processes is given in Section 7.3.

We first test our code using the SED of the BL Lac object *Mrk 421*, comparing our results to previous hadronic code (Section 7.5.1). In Section 7.5.2 we then tested our code on the SED of *PKS 2155-304* from the multiwavelength campaign of 2008 (Aharonian et al. 2009b, where the source was found to be in a low state). Apart from the standard SSC scenario and proton-synchrotron scenario, the code permits the study of interesting mixed lepto-hadronic scenarios, in which both components contribute significantly in the high energy emission bump.

7.2 Leptonic processes

In this section we describe the improvements to the leptonic part of the code, with the aim of including hadronic processes. The modifications to the original code by Katarzyński et al. (2001) are:

- Primary electron distribution : addition of an exponential cut-off
- Synchrotron emissivity : exact integration over the pitch angles
- Inverse Compton emissivity : improvement of the integration algorithm
- Linear interpolation over the computed emission components
- Pair-production absorbtion coefficient : modification of the cross-section
- Pairs produced : injection and evaluation of the stationary state

In Sections from 7.2.2 to 7.2.6 we describe in details each improvement, providing a numerical evaluation of the effect on the SSC code. The input parameters used as test case correspond to the leptonic model of *PKS 2155-304*, described in Section 7.5.2, whose values are given in Table 7.1.

7.2.1 Primary electron distribution

In the code developed by Katarzyński et al. (2001), the primary electron distribution was described as a broken power-law function, defined between the two Lorentz factor $\gamma_{e;min}$ and $\gamma_{e;Max}$. Above $\gamma_{e;Max}$ the electron function was simply zero. We modified this definition, introducing an exponential cut-off instead of the original Heaviside step function. The new electron distribution thus becomes:

$$N_e(\gamma_e) = \begin{cases} K_e \, \gamma_e^{-\alpha_1} \, e^{-\gamma_e/\gamma_{e;Max}} & \text{if } \gamma_{e;min} \leq \gamma_e < \gamma_{e;break} \\ K_{e;2} \, \gamma_e^{-\alpha_2} \, e^{-\gamma_e/\gamma_{e;Max}} & \text{if } \gamma_{e;break} \leq \gamma_e \end{cases} \tag{7.1}$$

where $K_{e;2} = K_e \, \gamma_{e;break}^{\alpha_2-\alpha_1}$ as in Katarzyński et al. (2001).
The exponential cut-off is more physical, in the sense that the acceleration mechanism at the origin of the injected electron population (not studied here) is stochastic, and the value of $\gamma_{e;Max}$ does not represent a sharp threshold.

7.2.2 Synchrotron emissivity

In the original version of the code, Katarzyński et al. (2001) used a simplified version of the synchrotron emissivity, in which the exact integration over the pitch angles between the particles and the magnetic field lines is replaced by a simple analytical fitted formula. The main reason of this approximation was to gain computation time. However, in order to include the hadronic processes, and in particular for the computation of the synchrotron spectrum from protons and muons, and for a correct evolution of the electro-magnetic cascade (see Section 7.3.2), this approximation was not sufficient any more, the error induced being too important. With the evolution of the computation capabilities in the last decade, we can now easily perform the exact calculus in an acceptable amount of time. In the following we describe the formula used in the new version of the code (for a reference on the radiative processes of relativistic particles, see e.g. Rybicki & Lightman (1979)).

The power $P(\nu,\gamma,\vartheta)$ emitted by a charged particle in a homogeneous magnetic field (where ν is the frequence of the emitted photon, $\gamma = E/mc^2$ is the Lorentz factor of the emitting particle, and ϑ is the angle between the particle momentum and the magnetic field line) is expressed (in units of $ergs^{-1}cm^{-3}Hz^{-1}sterad^{-1}$) as

$$P(\nu,\gamma,\vartheta) = \frac{\sqrt{3}e^3 B\sin\vartheta}{mc^2}\frac{\nu}{\nu_c}\int_{\frac{\nu}{\nu_c}}^{\infty} dx\, K_{5/3}(x) \tag{7.2}$$

where $\nu_c = \frac{3eB}{4\pi mc^2}\gamma^2\sin\vartheta$, and $K_j(x)$ is the modified Bessell function of the second kind of order j. By using the new variable $t = \frac{\nu}{3\gamma^2\nu_B}$ (where $\nu_B = \frac{eB}{2\pi mc}$ is the gyro-frequence), the equation 7.2 can be rewritten as :

$$P(t,\vartheta) = \frac{\sqrt{3}e^3 B}{mc^2}2t\int_{\frac{2t}{\sin\vartheta}}^{\infty} dx\, K_{5/3}(x) \tag{7.3}$$

The synchrotron emissivity (defined as the energy density per unit time, volume, frequency and solid angle, in units of $ergs^{-1}cm^{-3}Hz^{-1}sterad^{-1}$) is given by the integral over γ of the power emitted, multiplied by the particle distribution $N(\gamma)$:

$$j(\nu,\vartheta) = \frac{1}{4\pi}\int_{\gamma_{min}}^{\gamma_{Max}} d\gamma\, N(\gamma)P(\nu,\gamma,\vartheta) \tag{7.4}$$

After substitution:

$$j(\nu,\vartheta) = \frac{e^3 B}{4\pi mc^2}\sqrt{\frac{\nu}{\nu_B}}\int_{t_{min}}^{t_{Max}} dt\, N(\sqrt{\frac{\nu}{3t\nu_B}})t^{-1/2}\int_{\frac{2t}{\sin\vartheta}}^{\infty} dx\, K_{5/3}(x) \tag{7.5}$$

The total emissivity $j(\nu)$ is thus obtained by computing the mean value over an isotropic distribution of angles ϑ :

$$j(\nu) = \frac{1}{2}\int_0^{\pi} d\vartheta\ \sin\vartheta\, j(\nu,\vartheta) \tag{7.6}$$

The formula for the synchrotron emissivity as a function of ν is thus :

$$j(\nu) = \frac{e^3 B}{8\pi mc^2}\sqrt{\frac{\nu}{\nu_B}}\int_{t_{min}}^{t_{Max}} dt\, N(\sqrt{\frac{\nu}{3t\nu_B}})t^{-1/2}\int_0^{\pi} d\vartheta\ \sin\vartheta\int_{\frac{2t}{\sin\vartheta}}^{\infty} dx\, K_{5/3}(x) \tag{7.7}$$

The (self-)absorption coefficient $\mu(\nu,\vartheta)$ is given by the equation:

$$\mu(\nu,\vartheta) = -\frac{c^2}{8\pi\nu^2}\int_{E_{min}}^{E_{Max}} dE\, P(\nu,E,\vartheta)E^2\frac{d}{dE}\left(\frac{N(E)}{E^2}\right) \tag{7.8}$$

which is equal to

$$\mu(\nu, \vartheta) = -\frac{1}{8\pi m\nu^2} \int_{\gamma_{min}}^{\gamma_{Max}} d\gamma\, P(\nu, \gamma, \vartheta)\gamma^2 \frac{d}{d\gamma}\left(\frac{N(\gamma)}{\gamma^2}\right) \tag{7.9}$$

By substituting to $P(\nu, \gamma, \vartheta)$ its expression, we get

$$\mu(\nu, \vartheta) = -\frac{\sqrt{3}e^3 B}{12\pi m^2 c^2 \nu_B} \frac{1}{\nu} \int_{\gamma_{min}}^{\gamma_{Max}} d\gamma\, \frac{d}{d\gamma}\left(\frac{N(\gamma)}{\gamma^2}\right) \int_{\frac{2\nu}{3\nu_B \sin\vartheta\gamma^2}}^{+\infty} dx\, K_{5/3}(x) \tag{7.10}$$

The final absorption coefficient is given, as for the emissivity, by computing the mean value over an isotropic distribution of angles ϑ:

$$\mu(\nu) = -\frac{\sqrt{3}e^3 B}{24\pi m^2 c^2 \nu_B} \frac{1}{\nu} \int_{\gamma_{min}}^{\gamma_{Max}} d\gamma\, \frac{d}{d\gamma}\left(\frac{N(\gamma)}{\gamma^2}\right) \int_0^{\pi} d\vartheta\, \sin\vartheta \int_{\frac{2\nu}{3\nu_B \sin\vartheta\gamma^2}}^{+\infty} dx\, K_{5/3}(x) \tag{7.11}$$

If the particle distribution is described by a power-law function ($N(\gamma) = K\gamma^{-p}$), the formula can be simplified as

$$\mu(\nu) = -\frac{K\sqrt{3}e^3 B}{24\pi m^2 c^2 \nu_B} \frac{1}{\nu} \int_{\gamma_{min}}^{\gamma_{Max}} d\gamma\, \frac{p+2}{\gamma^3} N(\gamma) \int_0^{\pi} d\vartheta\, \sin\vartheta \int_{\frac{2\nu}{3\nu_B \sin\vartheta\gamma^2}}^{+\infty} dx\, K_{5/3}(x) \tag{7.12}$$

In the original version of the code Katarzyński et al. (2001) used the following analytical approximation:

$$\frac{1}{2}\int_0^{\pi} d\vartheta \sin\vartheta\, t \int_{2t/\sin\vartheta}^{\infty} dx\, K_{5/3}(x) \approx C_1 t^{C_2} e^{-C_3 t} \tag{7.13}$$

where $C_1 = 0.78$, $C_2 = 0.25$ and $C_3 = 2.175$.
The synchrotron emissivity is thus expressed as

$$j(\nu) = \frac{3\sigma_T c u_B}{8\pi\nu_B} \sqrt{\frac{\nu}{\nu_B}} C_1 \int_{t_{min}}^{t_{Max}} dt\, N\left(\sqrt{\frac{\nu}{3t\nu_B}}\right) t^{C_2 - 3/2} e^{-C_3 t} \tag{7.14}$$

where σ_T is the Thomson cross-section and $u_B = B^2/8\pi$ is the magnetic energy density.
In Fig. 7.1 we show the synchrotron and the associated SSC spectrum evaluated using the approximation by Katarzyński et al. (2001) and the exact evaluation of the integral over the pitch angles. This figure (as well as the followings) has been computed for the leptonic model of *PKS 2155-304* described in Section 7.5.2.

7.2.3 Inverse Compton emissivity

The inverse Compton emissivity $j_C(\nu)$ can be expressed as :

$$j_C(\nu) = \frac{h}{4\pi}\varepsilon q(\varepsilon) \tag{7.15}$$

where ε is the adimensional photon energy, equal to $h\nu/m_e c^2$, and $q(\varepsilon)$ is the differential production rate of inverse Compton photons, function of the soft photon and electron densities:

$$q(\varepsilon) = \int d\varepsilon'\, n_{\varepsilon'}(\varepsilon') \int d\gamma\, N(\gamma) C(\varepsilon, \varepsilon', \gamma) \tag{7.16}$$

where $C(\varepsilon, \varepsilon', \gamma)$ is the Compton kernel as given by Jones (1968).
The original version of the code used a Gauss-Legendre integration algorithm for the evaluation of the first integration over γ, while the integration over the synchrotron photons was performed using a simple trapezoidal rule. We improved the precision of the code by computing a double integration using the Gauss-Legendre algorithm.

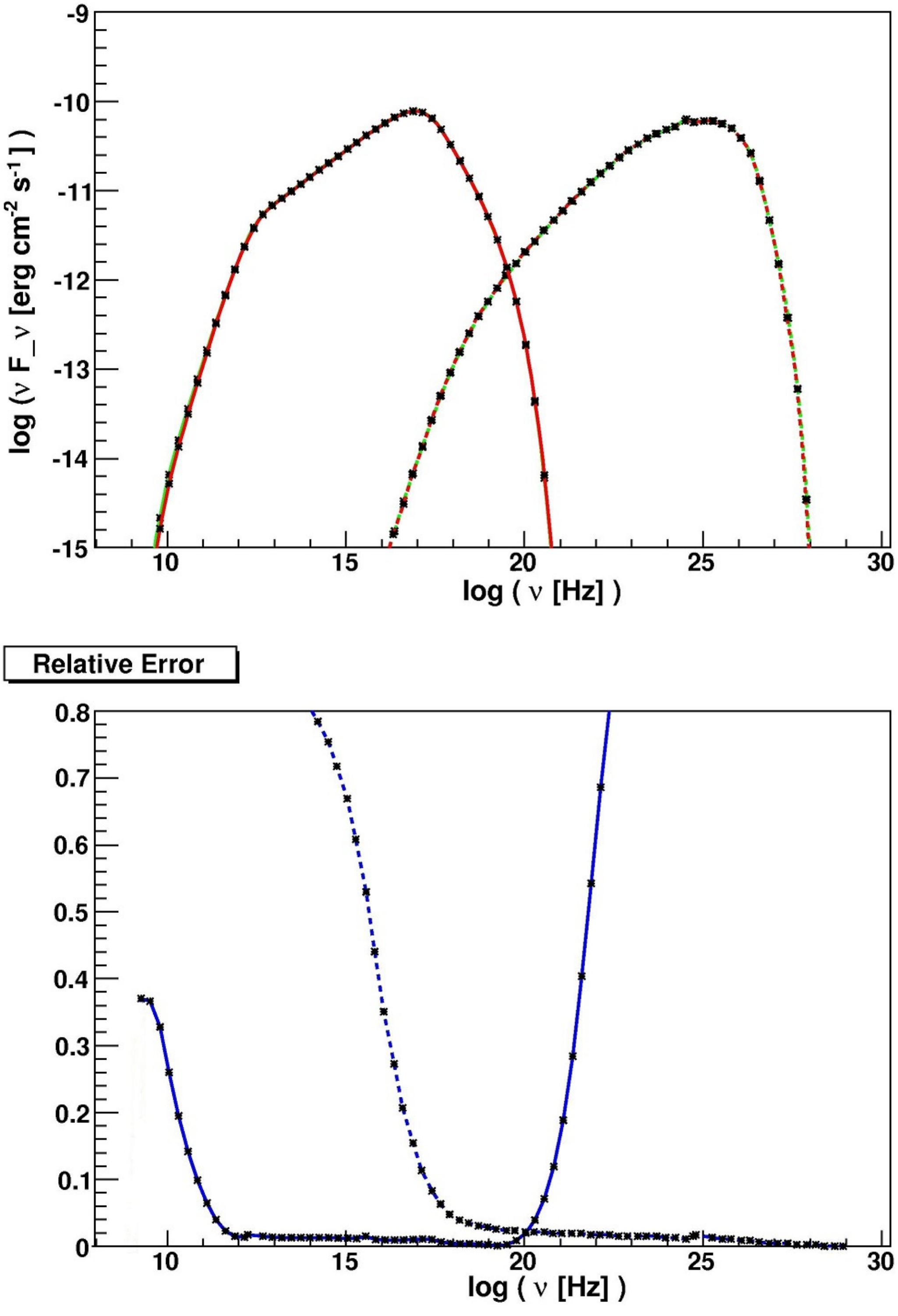

Figure 7.1: *Top:* Synchrotron and inverse Compton emission for the leptonic modelling of *PKS 2155-304* described in Section 7.5.2. The red and the green lines show the computation done using the approximation by Katarzyński et al. (2001) or the exact integration over the pitch angle, respectively (see Section 7.2.2). *Bottom:* relative error of the two different computed spectra for the synchrotron (bold line) and inverse Compton (dotted line) component.

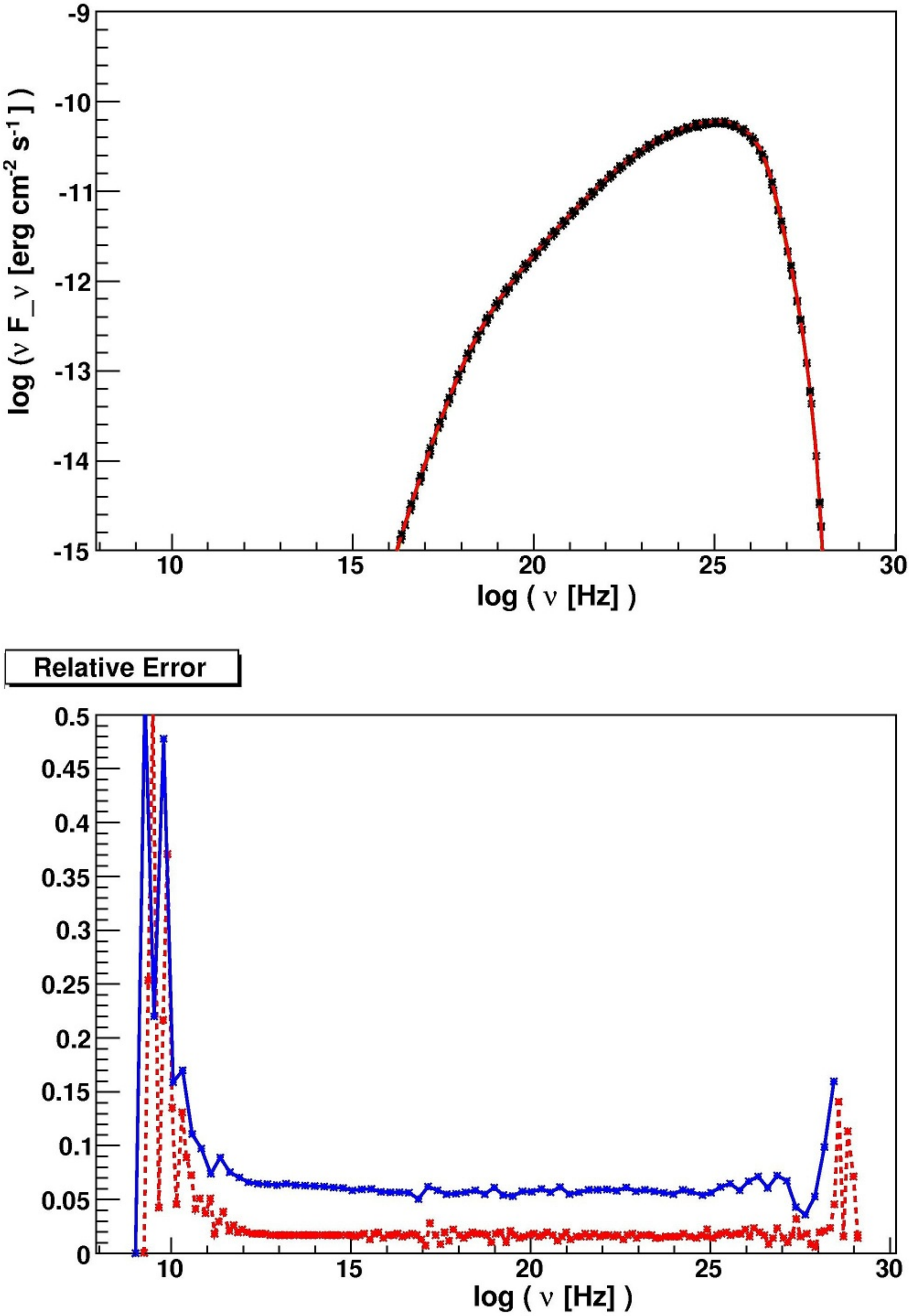

Figure 7.2: *Top:* inverse Compton emission for the leptonic modelling of *PKS 2155-304* described in Section 7.5.2. The red and the green lines show the computation done using the exact calculation for the inverse Compton emission or the linear interpolation approximation (see Section 7.2.4). *Bottom:* relative error of the two different computed spectra for the inverse Compton component, using vectors of 100 (blue line) or 200 (red line) points.

7.2.4 Linear interpolation

The computation of the inverse Compton emission needs the information about the soft photons produced by the synchrotron emission. This term is called by a Gauss-Legendre integration algorithm and the sampling needed is different from the sampling with which the synchrotron intensity is stored.
For this reason, the original version of the code calls the synchrotron subroutine for each frequency needed in the computation of the integral. This method is a good solution if the synchrotron intensity needs to be called just once, but with the modification we apported to the code we would need to call the synchrotron subroutine once for the inverse Compton emissivity, once for the $\gamma - \gamma$ absorption coefficient, three times more for the computation of the pair spectra (for the synchrotron emissivity, the inverse Compton emissivity and the $\gamma - \gamma$ absorption), and a last time for the computation of the pair synchrotron emission. Such a high number of calls makes the computation time of the code considerably longer (expecially in the aim of including hadronic processes).
For this reason we decided to modify the code in order that the synchrotron and inverse Compton spectra are calculated only once at the very beginning of the code and stored in a vector. The inverse Compton subroutine (as well as the $\gamma - \gamma$ pair production, and the pair-injection ones) reads the vector which contains the synchrotron intensity and performs a linear interpolation between the vector points.

It is impotant to note that for the inverse Compton subroutine, a linear interpolation on the synchrotron intensity vector is the same as performing the integration with the trapezoidal rule (instead of the Gauss-Legendre algorithm described in Section 7.2.3). In this case the ”linear interpolation” calculus is thus simply the original version of the subroutine. In Fig. 7.2 we show the error done by using the ”linear interpolation” computation. As expected, the error depends on the spectral resolution used for the sampling of the synchrotron emission: while for a 100-bins computation the error is almost 7%, it decreseas below the 2% for a 200-bins computation.

7.2.5 Pair-production absorption coefficient

The interaction between a high-energy SSC photon with adimensional energy $\varepsilon = h\nu/mc^2$ and a low energy synchrotron photon with adimensional energy $\varepsilon' = h\nu'/mc^2$ leads to the production of a leptonic pair e^+-e^-, if the total available energy ($\simeq h\nu$) is higher than $2mc^2$. The absorption coefficient for this process is :

$$\kappa_{\gamma\gamma}(\varepsilon) = \int_{\varepsilon'} d\varepsilon' \; n_s(\varepsilon')\sigma_{\gamma\gamma}(\varepsilon, \varepsilon') \tag{7.17}$$

where $n_s(\varepsilon')$ is the number density of synchrotron photons, and $\sigma_{\gamma\gamma}$ the pair-production cross-section. The number density of photons can be easily evaluated from the intensity $I(\nu)$ using the formula:

$$n_s(\varepsilon') = \frac{4\pi}{hc}\frac{I(mc^2\varepsilon'/h)}{\varepsilon'} \tag{7.18}$$

For an isotropic photon field, the pair-production cross-section can be expressed as (see Aharonian et al. 2008d):

$$\sigma_{\gamma\gamma}(s = \varepsilon\varepsilon') = \frac{3\sigma_T}{2s^2}\left[\left(s + \frac{1}{2}\log s - \frac{1}{6} + \frac{1}{2s}\right)\log(\sqrt{s} + \sqrt{s-1}) - \left(s + \frac{4}{9} - \frac{1}{9s}\right)\sqrt{1 - \frac{1}{s}}\right] \tag{7.19}$$

The original version of the code used as pair-production cross-section the Dirac-δ approximation :

$$\sigma_{\gamma\gamma} \simeq 0.2\sigma_T\delta(\varepsilon' - \frac{1}{\varepsilon})\frac{1}{\varepsilon} \tag{7.20}$$

which leads to

$$\kappa_{\gamma\gamma} \simeq 0.2\sigma_T \frac{n_s(1/\varepsilon)}{\varepsilon} \tag{7.21}$$

As shown in Fig. 7.3, the difference between the two approximation is quite small (for the particular model chosen), being less than 1% (in relative error).

7.2.6 Pair injection and cooling of secondary particles

The electron-positron pairs produced in the $\gamma - \gamma$ interaction represent a secondary generation of leptons which is injected in the emitting region. The injection function can be expressed as (Aharonian et al. 1983):

$$\begin{aligned} Q(\gamma) = & \frac{3\sigma_T c}{32} \int_{\gamma}^{\infty} d\varepsilon \, \frac{n_\varepsilon(\varepsilon)}{\varepsilon^3} \int_{\frac{\varepsilon}{4\gamma(\varepsilon-\gamma)}}^{\infty} d\varepsilon' \, \frac{n_{\varepsilon'}(\varepsilon')}{\varepsilon'^2} \cdot \\ & \cdot \left[\frac{4\varepsilon^2}{\gamma(\varepsilon-\gamma)} \ln\left(\frac{4\gamma\varepsilon'(\varepsilon-\gamma)}{\varepsilon}\right) - 8\varepsilon\varepsilon' + \frac{2\varepsilon^2(\varepsilon\varepsilon'-1)}{\gamma(\varepsilon-\gamma)} - \left(1 - \frac{1}{\varepsilon\varepsilon'}\right)\left(\frac{\varepsilon^2}{\gamma(\varepsilon-\gamma)}\right)^2 \right] \end{aligned} \tag{7.22}$$

where ε and ε' are defined as in the previous section, and $n_\varepsilon(\varepsilon)$ and $n_{\varepsilon'}(\varepsilon')$ are the number densities of the synchrotron and the Compton photons, respectively.
The injection function has to be converted into a stationary spectrum in order to compute the stationary synchrotron emission from secondary pairs. The stationary spectrum is given by the balance between the injection, the adiabatic losses and the synchrotron cooling (which depends on the energy of the particles). The differential equation which describes the process is :

$$\frac{\partial}{\partial t} N(\gamma) = \frac{\partial}{\partial \gamma}\left[\gamma \, \frac{N(\gamma)}{\tau_c(\gamma)}\right] + Q(\gamma) - \frac{N(\gamma)}{\tau_{ad}} \tag{7.23}$$

where $\tau_{ad} \approx R/(0.5\ c)$ is the advection time (see Mücke & Protheroe 2001) and

$$\tau_c(\gamma) = \frac{3 m_e c}{4(u_B + u_{soft})\sigma_T} \frac{1}{\gamma} \tag{7.24}$$

is the radiative cooling time, including both synchrotron losses (u_B being the magnetic energy density, equal to $B^2/8\pi$) and inverse-Compton losses (in the Thomson regime; u_{soft} being the synchrotron photon energy density). By imposing $\frac{\partial}{\partial t}N(\gamma) = 0$, we can explicitely give the integral expression of the stationary state (following Inoue & Takahara 1996):

$$N_e(\gamma_e) = e^{-\gamma_e^*/\gamma_e} \frac{\gamma_e^* \tau_{ad}}{\gamma_e^2} \int_{\gamma_e}^{\infty} d\zeta \; Q_e(\zeta) e^{+\gamma_e^*/\zeta} \tag{7.25}$$

with

$$\gamma_e^* = \frac{3 m_e c^2}{8(u_B + u_{soft})\sigma_T R} \tag{7.26}$$

representing the Lorentz factor at which $\tau_c(\gamma_e) = \tau_{ad}$.

In Fig. 7.4 we show two examples of the effect of cooling on a power-law distribution of injected particles (with the characteristic spectral break of one) and on the specific case of the leptonic model of *PKS 2155-304* described in Section 7.5.2. In the final version of the code, in order to improve the computing time, the integration given in Eq. 7.25 is solved only for the values of γ_e affected by synchrotron losses. In particular, if $\gamma_e << \gamma_e^*$ the solution is given simply by $Q_e(\gamma)\ \tau_{ad}$.

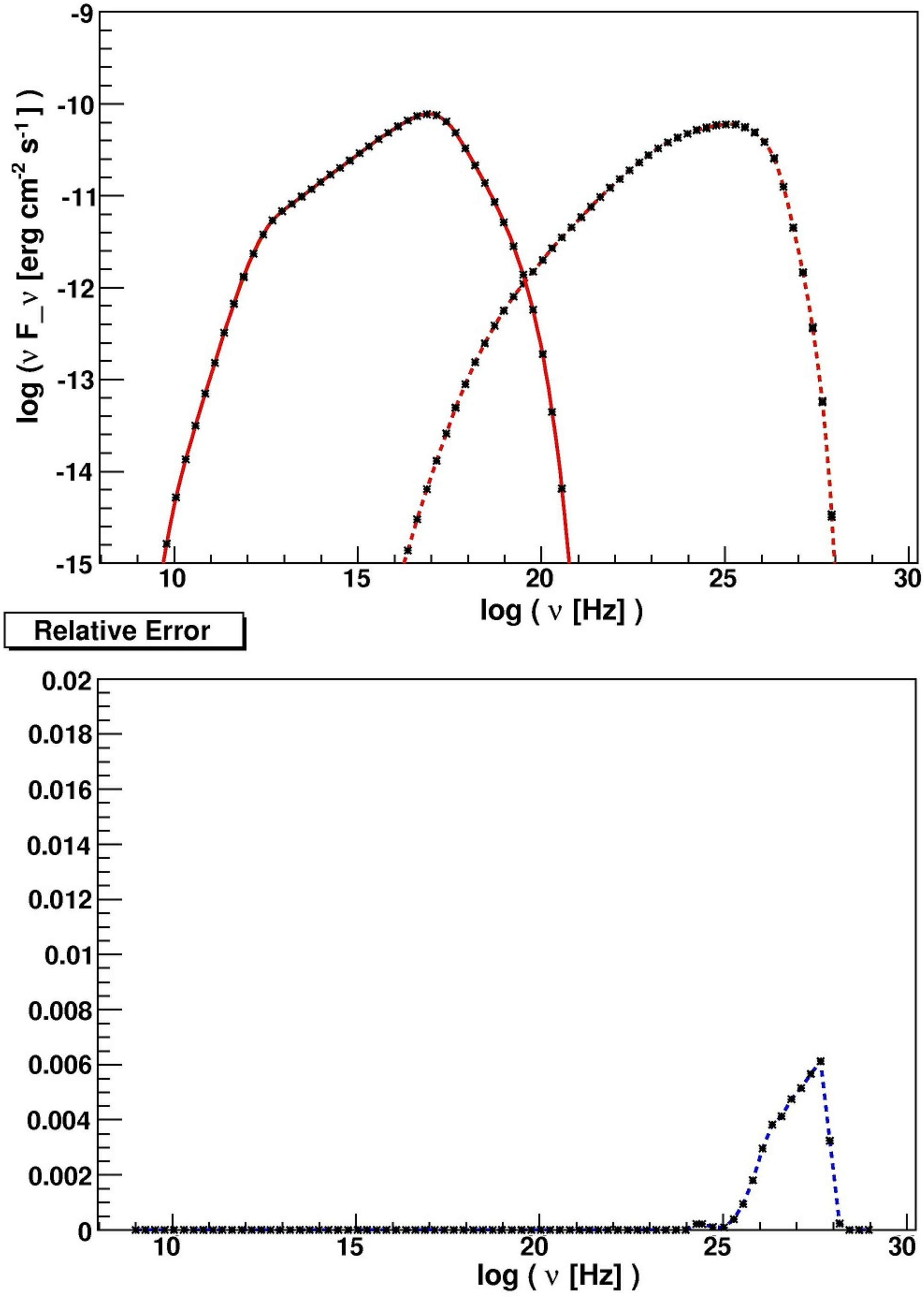

Figure 7.3: *Top:* Synchrotron and inverse Compton emission for the leptonic modelling of *PKS 2155-304* described in Section 7.5.2. The red and the green lines show the computation done using the δ-function cross-section or the formula given by Aharonian et al. (2008d) (see Section 7.2.5). *Bottom:* relative error of the two different computed spectra for the inverse Compton (dotted line) component.

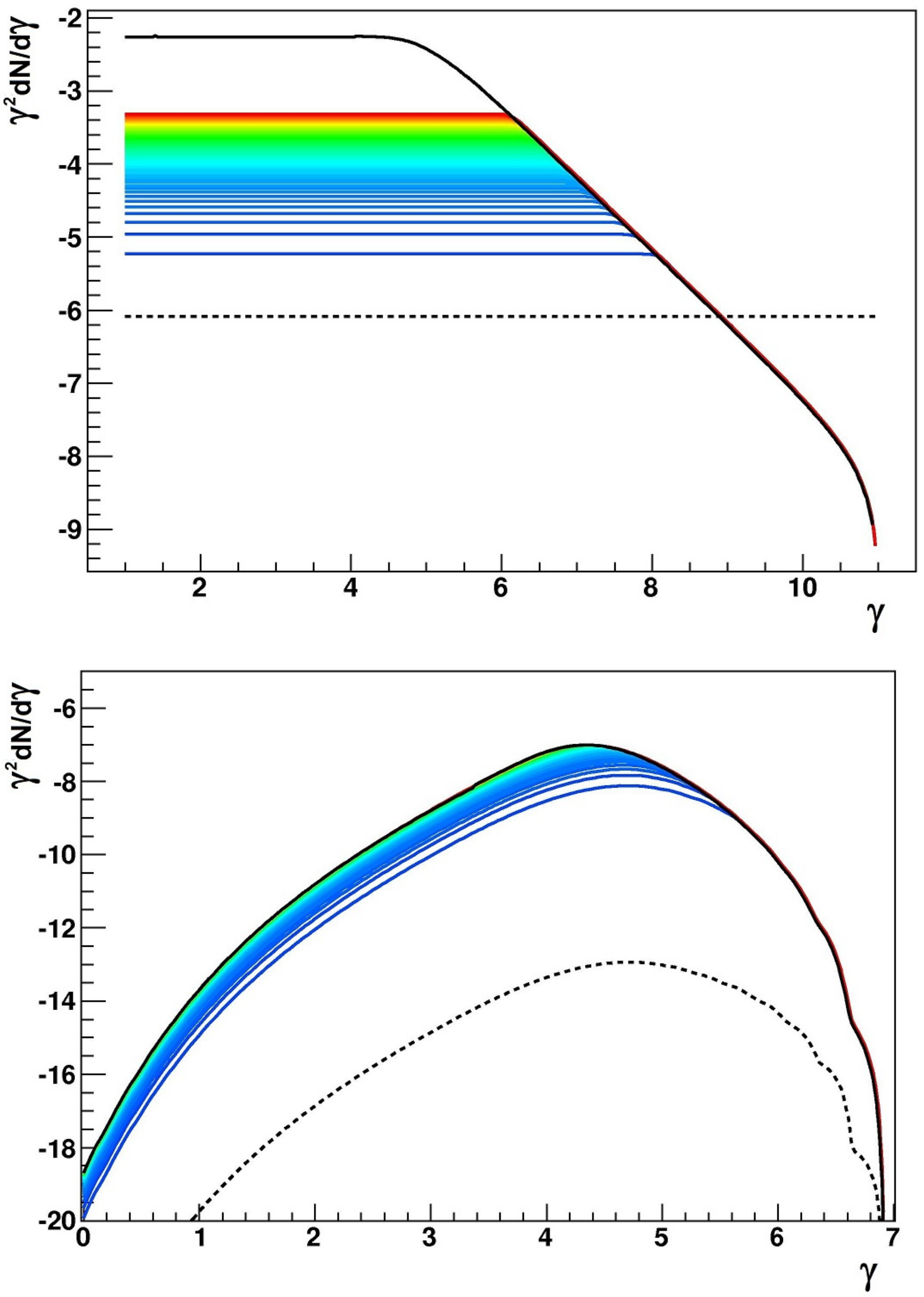

Figure 7.4: *Top:* effect of cooling on a power-law distribution of injected electrons with $\alpha = 2$ (dotted black-line). The rainbow lines represent the solution of equation 7.23 for different times, while the black solide line represent the integral solution (equation 7.25). A magnetic field of 1 G and an emitting region size of 10^{14} cm have been used (in this case, only the synchrotron cooling is included). *Bottom:* same as the top plot but for the injection spectrum of secondary pairs corresponding to the leptonic model of *PKS 2155-304* described in Section 7.5.2.

7.3 Hadronic processes

The emitting region is assumed to be filled with a stationary population of relativistic protons. By analogy with the electron population, the proton distribution $N_p(\gamma_p = E_p/m_pc^2)$ is described by a power-law function with index α_p, defined above $\gamma_{p;min}$ and with an exponential cut-off at $\gamma_{p;Max}$. The normalization factor at $\gamma_p = 1$ is $K_p = \eta K_e$, the η factor representing the ratio between the number density of protons and electrons at $\gamma_p = \gamma_e = 1$. No break is assumed to be present in the proton distribution, given the fact that the maximum proton energy is supposed to be lower than the value at which the cooling terms become important (see Section 7.4).

The proton synchrotron emission is evaluated using equation 7.7. In hadronic models, proton synchrotron emission is assumed to be responsible of the high energy bump (reaching TeV energies): thus it suffers γ - γ absorption from both internal photons and EBL. The γ - γ absorption and the emission from the secondary population of the produced pairs is evaluated in analogy with what is done for the inverse Compton emission for the leptonic part of the code.

The proton population in the emitting region interacts with the low energy photons through the photo-meson process

$$p + \gamma \rightarrow p' + n^0\pi^0 + n^+\pi^+ + n^-\pi^- + \ldots \tag{7.27}$$

and the electron-positron pair production (also called Bethe-Heitler process)

$$p + \gamma \rightarrow p' + e^+ + e^- \tag{7.28}$$

7.3.1 Implementation of *SOPHIA*

The photo-meson interaction has been evaluated using the publicly available Monte-Carlo code *SOPHIA* (Mücke et al. 2000) which computes N_{iter} interactions of a proton of energy E_p with a low-energy photon field. The outputs are the distributions (expressed as $E\frac{dN}{dE} = \gamma\frac{dN}{d\gamma}$) of the stable particles produced ($e^\pm$, γ, p, n, $\nu_{e,\mu}$ and $\bar{\nu}_{e,\mu}$). As the study of the neutrino emission from blazars is beyond the purposes of this work, they will not be considered in the following. We notice however, that the neutrino emission is automatically produced by our code, in the sense that the information about the neutrino spectra is stored in the associate vectors in our code, and its study would represent a natural extension of this work. The low-energy photon field is given by the synchrotron emission from the primary electron population in the jet, which represents by far the dominant component at low energies. We modified the *SOPHIA* code so that it can accept as input photon-field any numerical function (instead of just a power-law or a black-body function as in the original version of the code). We call *SOPHIA* for 50 different proton energies, equally spaced by 0.1 $\log\gamma_p$, using for each call $N_{iter} = 10^4$. For the i-th call, the proton Lorentz factor is thus:

$$\log(\gamma_{p;i}) = \log(\gamma_{p;Max}) - i \cdot 0.1 \tag{7.29}$$

The energy of the proton before interaction is modified in order to take into account the synchrotron losses (following Mücke & Protheroe 2001) which can occour before the proton-photon collision :

$$E'_p \simeq \frac{E_p}{1 + \frac{r_{p,syn}(E_p)}{r_\pi(E_p)}} \tag{7.30}$$

where $r_{p,syn}$ represents the mean synchrotron loss rate, sampled from an exponential distribution with mean value:

$$r_{p,syn}(E_p) = \frac{4}{3}\left(\frac{m_e}{m_p}\right)^2 \frac{\sigma_T u_B c}{(m_p c^2)^2}\, E_p \tag{7.31}$$

and r_π represents the mean pion-production interaction rate, given by:

$$\begin{aligned} r_\pi(E_p) =& \frac{c}{2}\int_{\varepsilon'_{th}}^{\infty} d\varepsilon'\; n_{\varepsilon'}(\varepsilon') \int_0^{\pi} d\vartheta\; \sin\vartheta \cdot \\ & \cdot (1-\beta_p\cos\vartheta)\; \sigma_\pi(s_p) \end{aligned} \tag{7.32}$$

where $c\beta_p = c(1 - 1/\gamma_p^2)^{1/2}$ is the proton velocity, ϑ is the angle of the proton-photon interaction, $s_p = m_p^2c^4 + 2E_p\varepsilon'(1-\beta_p\cos\vartheta)$ (with $\sqrt{s_p} > 1.08\mathrm{GeV}$) is the energy squared in the centre-of-momentum frame, $\varepsilon'_{th} = ((1.08\mathrm{GeV})^2 - m_p^2c^4)/2(E_p + \gamma_p\beta_p m_p c^2)$ is the photon energy threshold, and σ_π is the pion production cross-section (evaluated using *SOPHIA*).

The 50 *SOPHIA* outputs are summed together and, in order to be consistent with the framework of our code, renormalized as follow: for each kind of particle, the *SOPHIA* outputs, expressed as $\gamma\frac{dN}{d\gamma}$, are divided by γ, multiplied by $\int_{\gamma'_{p;i}}^{\gamma'_{p;i+1}} d\gamma'_p\; N_p(\gamma'_p)$ (i.e. the number of protons in the emitting region with energy comprised between $\gamma'_{p;i}$ and $\gamma'_{p;i+1}$, where $\gamma'_p = E'_p/m_pc^2$ is defined according to equation 7.30) and multiplied by r_π/r_{tot} (the ratio of the pion-production interaction rate over the total interaction rate, given by $r_\pi + r_{BH} + c(0.5/R)$, where r_{BH} represents the Bethe-Heitler interaction rate (see equation 2.2 in Chodorowski et al. 1992) and $c/(0.5R)$ the rate of adiabatic losses). As discussed by Mücke & Protheroe (2001), in this stationary framework the protons are assumed to be confined in the emitting region, and multiple p-γ interactions can occour. This effect is taken into account by multipling all the *SOPHIA* outputs by a factor of 2.01.

7.3.2 Pair cascade

Photons coming from the π^0 decay and the synchrotron emission from $e^\pm$ coming from the $\pi^\pm$ channel can reach energies up to $m_pc^2\gamma_{p;Max}$: interacting with the low-energy photon field they trigger an electromagnetic cascade, supported by synchrotron emission.

The evaluation of the stationary state of the cascade emission has been evaluated as follow : the first generation of pairs injected in the emitting region has been computed as for the leptonic part of the code, computing the injection rate, the stationary state of pair distribution and the associated synchrotron emission. In this case however, the synchrotron photons from pairs are still energetic enough to produce a second generation of pairs, which as well can produce a third generation, and so on; we then iterate the process until the j-th generation of pairs gives a negligible contribution with respect to the sum of the previous generations (as a general remark, for the physical parameter used in the following sections, the spectrum computed including 5 generations of pairs already provide a good description of the cascade). During the computation of the cascade spectrum, the low energy photon field is considered as being represented only by the synchrotron emission of primary electrons, neglecting the emission from the cascade itself (i.e. we assume that the cascade is not self-supported, and we verify *a posteriori* that this condition is respected).

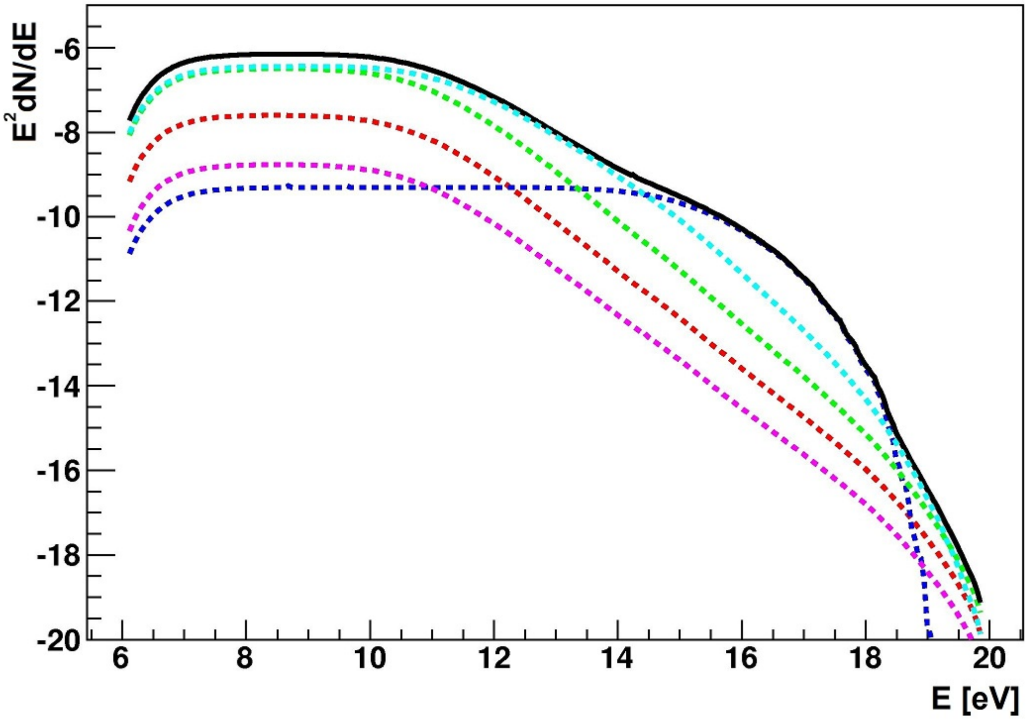

Figure 7.5: Spectrum of the pairs composing the cascade triggered by photons coming from the π^0 decay for the hadronic modelling of *PKS 2155-304* described in Section 7.5.2. The different dotted lines show the cascade generations: blue-one, light blue-two, green-three, red-four and violet-five. The solid black line show the total emission

In Fig. 7.5 is shown the spectrum of the cascade triggered by photons coming from the π^0 decay for the hadronic modelling of *PKS 2155-304* described in Section 7.5.2 (which assume a magnetic field of 80 G).

7.3.3 Synchrotron emission from muons

The public version of the *SOPHIA* code consider as output particles only the stable ones. However, in highly magnetized environments, the synchrotron emission from pions and muons before decay can be important, affecting as well the resulting spectra of electrons and positrons. Following Mücke & Protheroe (2001), we then modified the spectra of kaons, pions and muons before decay :

$$E'_{K,\pi,\mu} \simeq \frac{E_{K,\pi,\mu}}{\sqrt{1+\frac{2\ r_{K,\pi,\mu;syn}(E_{K,\pi,\mu})}{r_{K,\pi,\mu;dec}(E_{K,\pi,\mu})}}} \tag{7.33}$$

where $r_{K,\pi,\mu;syn}$ represents the synchrotron loss rate of kaons, pions and muons, respectively (sampled from an exponential distribution with mean value evaluated following equation 7.31) and $r_{K,\pi,\mu;dec}$ represents the decay rate, sampled from an exponential distribution with mean value equal to $1/\gamma\tau_{dec}$ (where τ_{dec} is the decay time in the co-moving frame, equal to 1.24×10^{-8}, 2.6×10^{-8} and 2.2×10^{-6} seconds for kaons, pions and muons, respectively).

Synchrotron emission from muons can significantly contribute to the overall SED for magnetic fields of the order of tens of Gauss. We then retrieved the muon ($\mu^{\pm}$) spectra from *SOPHIA before* their decay

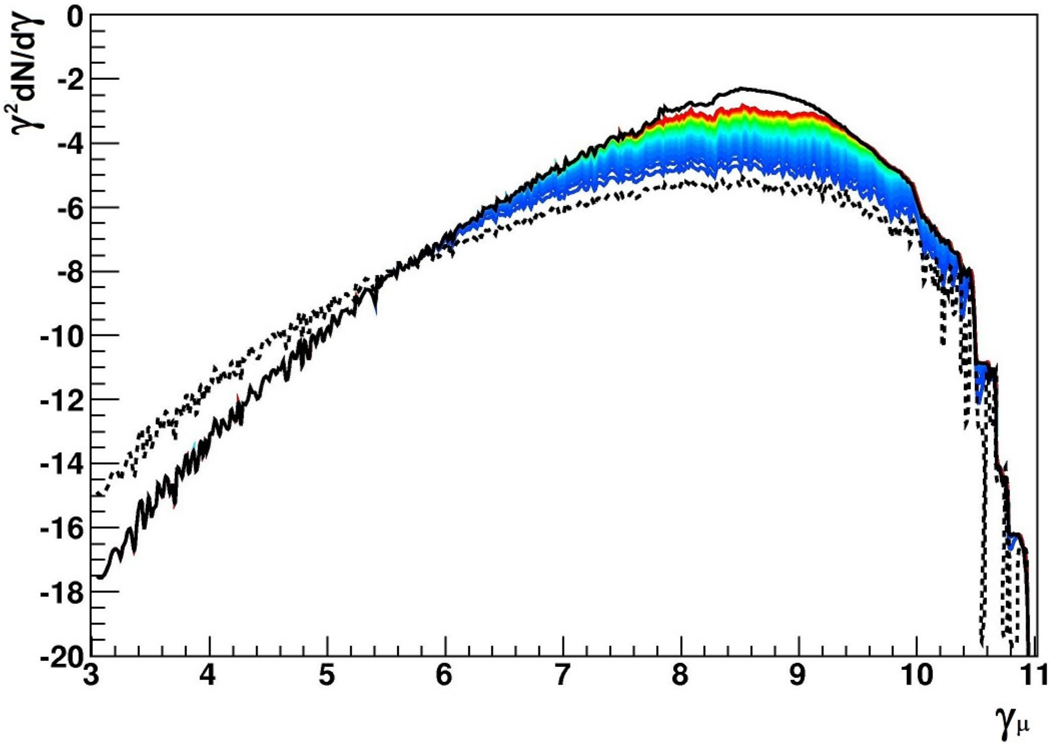

Figure 7.6: Effect of cooling and decay on the population of muons in the emitting region. The black dotted line represents the distribution of injected muons for the hadronic model of *PKS 2155-304* described in Section 7.5.2. The rainbow lines represent the solution of equation 7.34 for different times, while the black solide line represent the integral solution (equation 7.35).

into electrons and positrons, and we treat them as all the other *SOPHIA* outputs. The only difference occours in the evaluation of the stationary state distribution : for non-stable particles as muons, we need to add the decay term (equal to $-N(\gamma)/\gamma\tau_{dec}$) in the equation 7.23, which becomes :

$$\frac{\partial}{\partial t}N(\gamma) = \frac{\partial}{\partial \gamma}\left[\gamma\,\frac{N(\gamma)}{\tau_c(\gamma)}\right] + Q(\gamma) - \frac{N(\gamma)}{\tau_{ad}} - \frac{N(\gamma)}{\gamma\tau_{dec}} \tag{7.34}$$

The integral solution (equation 7.25) is then modified as follow :

$$\begin{aligned} N_\mu(\gamma_\mu) = {} & \exp\left[-\frac{\gamma^*_\mu}{\gamma_\mu} - \gamma^*_\mu\frac{\tau_{ad}}{2\gamma^2_\mu\tau_{dec}}\right]\frac{\gamma^*_\mu\tau_{ad}}{\gamma^2_\mu}\cdot \\ & \cdot\int_{\gamma_\mu}^{\infty} d\zeta\;\; Q_\mu(\zeta)\exp\left[+\frac{\gamma^*_\mu}{\zeta} + \gamma^*_\mu\frac{\tau_{ad}}{2\zeta^2\tau_{dec}}\right] \end{aligned} \tag{7.35}$$

where $Q_\mu(\gamma_\mu)$ is represented by the *SOPHIA* output, and γ^*_μ is the Lorentz factor at which $\tau_c(\gamma_\mu) = \tau_{ad}$ (as in equation 7.26).

It is worth mentioning that a valid alternative to the direct use of the *SOPHIA* code is the work done by Kelner & Aharonian (2008), in which an analytical expression of the secondary particle distributions produced in the p-γ interactions is given. However, the main issue of using these results is the fact that an analytical expression for muons is not presented, and that in highly magnetized environments synchrotron losses can significantly affect the distribution of secondary electrons and positrons.

7.3.4 Bethe-Heitler pair production

As discussed above, a competitive interaction with respect to the photo-meson channel is the Bethe-Heitler process (which is not included in the *SOPHIA* package). This process refers to the pair-production of low-energy photons in the field of a high-energy charged particle: the emerging particles are a pair of leptons plus the original proton (whose energy and momentum are modified). The cross-section of this process is higher than for the photo-meson interaction, and thus it is important to take into account this effect when renormalizing the *SOPHIA* outputs (see Section 7.3.1). However, the energy of the outcoming leptons is lower than the energy produced in the photo-meson interactions (because the proton is not lost in the interaction, and still carries a significant amount of energy). The pair injected in the emitting region through this process have been computed using the analytical formulae of Kelner & Aharonian (2008) (in which the Bethe-Heitler cross-section is expressed following the work by Blumenthal 1970). In the same was as for the other injected pairs, we first compute the stationary particle distribution, then their associated synchrotron emission.

7.4 Physical constraints

In hadronic models, the fact of considering protons in the emitting region is represented in the model by four more free parameters (with respect to the simple leptonic scenario): the two Lorentz factor $\gamma_{p;min}$ and $\gamma_{p;Max}$, the slope of the proton power-law distribution α_p, and the normalization factor η.
The value of $\gamma_{p;min}$ however does not affect the modelling as long as it is low enough, so it can be considered as a *false* free parameter. It impacts however the value of the particle energy density in the emitting region (expecially if the proton-distribution slope is softer than two).

The value of $\gamma_{p;max}$ is constrained by physical consideration on acceleration and cooling time-scales. In particular, assuming that the acceleration take place in relativistic shocks, the most general expression of the acceleration time-scale is

$$\tau_{acc} = \frac{1}{\eta} \frac{m_p}{e\, B}\, \gamma_p \tag{7.36}$$

where η represents the efficiency of the schok acceleration, and has been fixed at $1/10$. The cooling terms are represented by the adiabatic losses ($\tau_{ad} = R/(0.5c)$), the synchrotron losses (the inverse of Equation 7.31) and the photo-meson losses (expressed analytically following Sikora et al. 2009). The equation of the acceleration term with the lowest of the cooling term provide thus an upper-limit of the value of $\gamma_{p;Max}$. In Fig. 7.7 we show an example of this calculation for the hadronic model shown in Fig. 7.9. For the other model presented, the value of $\gamma_{p;Max}$ adopted is always consistent with its upper-limit evaluation. An additional constraint is provided by the gyroradius of the protons with $\gamma_{p;Max}$, equal to (in cgs untis)

$$\sqrt{\gamma_{p;Max}^2 - 1}\, \frac{m_p c^2}{eB} \approx \gamma_{p;Max}\, \frac{m_p c^2}{eB} \tag{7.37}$$

which is required to be lower than the emitting region size, in order to avoid energy-dependent escape from the emitting region.

The value of α_p can be constrained assuming that electrons and protons share the same acceleration mechanism, and thus the same particle distribution. The proton-distribution slope has been thus fixed equal to the electron-distribution slope *before* the break (assuming that the cooling affects the electron distribution after the break only, and that before the break the electron distribution is representative of the injection spectrum).

The last proton-distribution free parameter is the ratio between protons and electrons (η) in the emitting region. In this case a firm constraint cannot be provided: a simple neutrality consideration cannot be applied given the fact that we do not know what is the pair content of the primary electron distribution (i.e. how many of these ”electrons” are indeed positrons) nor the content of cold protons (other than the relativistic population of protons that we model). This parameter is thus left as a true free parameter in the following applications.

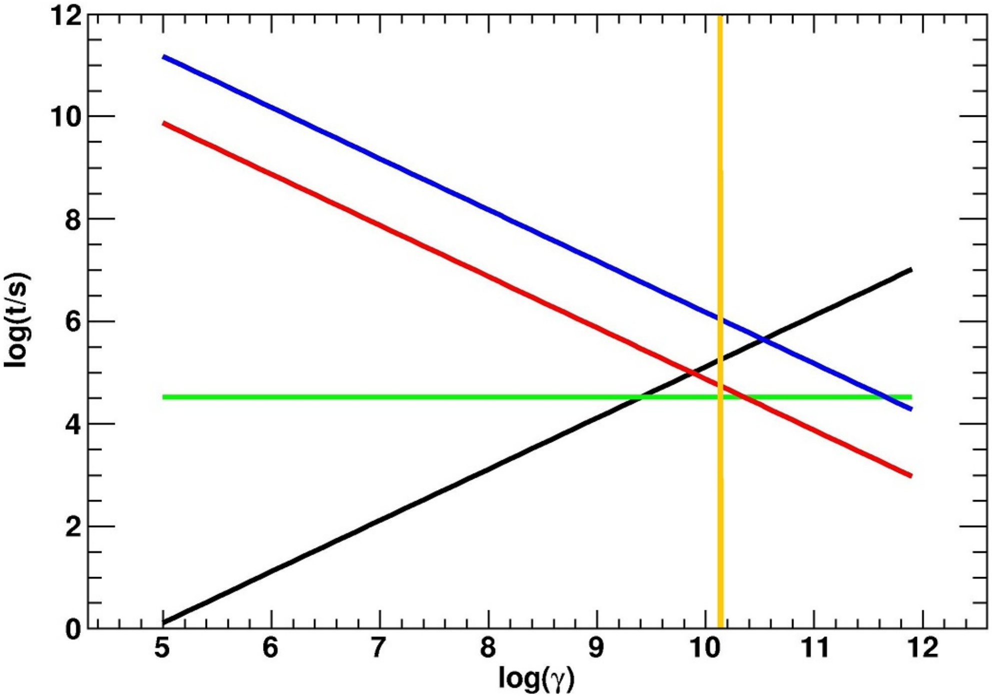

Figure 7.7: Acceleration and cooling time-scales for the hadronic modelling of *PKS 2155-304* described in Section 7.5.2. The black solid line represents the acceleration time-scale (see Eq. 7.36); the green line represents the adiabatic time-scale; the red line represents the synchrotron-cooling time-scale and the blue line the $p-\gamma$ cooling time-scale; the organge line represents the Lorentz factor at which the gyroradius is equal to the region size. The corresponding maximum value of the proton Lorentz factor is 2.57×10^9.

7.5 Applications

In this Section we present the first application of our code to two well-known BL Lac objects, *Mrk 421* and *PKS 2155-304*. For *Mrk 421* we present a comparison of our code with the work done by Mücke & Protheroe (2001), while for *PKS 2155-304* we study the SED measured in 2008 during a multiwavelength campaign led by *H.E.S.S.*, and we present a modelling in a leptonic and hadronic scenario, discussing mixed lepto-hadronic models as well.
In all the applications we use the EBL model by Franceschini et al. (2008), which is in agreement with the constraints putted by VHE observations (see e.g. Aharonian et al. 2006d). The original version of the code used the model by Stecker & de Jager (1998).

7.5.1 *Mrk 421*

The BL Lac object *Mrk 421* has been presented in Chapter 4, among the BL Lac objects detected by the *H.E.S.S.* telescope array (Aharonian et al. 2005b). It is one of the brightest TeV blazar (indeed the very first AGN observed at TeV energies, Punch et al. 1992) and it is also visible for the *MAGIC* and *VERITAS* collaborations (Albert et al. 2007a; Acciari et al. 2009b; Abdo et al. 2011b). In their original work on proton-synchrotron models, Mücke & Protheroe (2001) provided an application to this object, and in this context we present in Fig. 7.8 the modelling of *Mrk 421* in a proton synchrotron scenario, comparing our results with the work of Mücke & Protheroe (2001).

The main difference arises from the low-energy part of the SED: while in our code it is treated in a consistent way, in the original paper the synchrotron bump was only parametrised. The second difference come from the input spectrum used to compute the p-γ interactions: while we use the synchrotron emission modelled to the low-energy bump, Mücke & Protheroe (2001) used an asymptotic power-law (which can be seen as a thin, dashed line in the left plot of Fig. 7.8). This affects of course the computation of the secondary particles, given the fact that in our case we take into account the high-energy cut-off of the synchrotron photons (while for Mücke & Protheroe (2001) there are just no photons after the synchrotron peak): when computing the *SOPHIA* Monte-Carlo simulation, the sampled energy of the photon is thus shifted towards higher energies, increasing the energy of the secondary particles as well. A third difference is on the spectral distribution of the primary protons, which, comparing the two plots, seems to present a steeper cut-off (super-exponential) in Mücke & Protheroe (2001). The last two point can explain the higher contribution from secondary particles in our code, with respect to Mücke & Protheroe (2001) (effect that can be estimated by looking at the cascade contribution above the TeV). Another important difference is in the internal absorption, which present a clear minimum in our simulation, while it becomes more and more important in the code by Mücke & Protheroe (2001) (who used a simple δ-function to express the γ-γ cross-section).

The most recent result on *Mrk 421* comes from the multi-wavelength campaign performed in 2009 (Abdo et al. 2011b), in which the γ-ray spectrum is well constrained thanks to the *Fermi-LAT* and *MAGIC* measurements. Abdo et al. (2011b) studied as well a hadronic scenario, modelled using the code described in Mücke & Protheroe (2001) (see bottom-left plot of Fig. 7.8). In this case, the magnetic field is assumed to be 50 G, and the emitting region size equal to 4×10^{14} cm. The primary proton distribution is described by a power-law with index 1.9, which represents as well the index of the injection function of primary electrons. However, as discussed by Abdo et al. (2011b), the cooling-break of the electron distribution is located below the adopted value of $\gamma_{e;min} = 700$, and the stationary distribution is thus described by a single-powerlaw function with index 2.9.

In the bottom-right plot of Fig. 7.8 we show the modelling of the 2009 SED of *Mrk 421* using our code. The main difference compared to the work presented by Abdo et al. (2011b) comes from the constraint on the proton maximum Lorentz factor, which is lower than what they used (7.1×10^8 compared to 2.3×10^9, and comes from the fact that Mücke & Protheroe (2001) use as acceleration term a more efficient acceleration by oblique shocks). In order to reach the highest energies, we adopt then a higher Doppler factor (21 instead of 12), and, to compensate for the increase in the overall normalization given by the higher value of δ, we use a lower emitting region size (2.2×10^{14} instead of 4.0×10^{14}). The high-energy bump is well described in this hadronic scenario: it is important to underline that the emission is not due to a single component, but to a superposition of synchrotron emission by protons, muons and cascade from π^0 and secondary $e^{\pm}$.

We underline here the presence of the SSC component (green line), which turns out to be as important

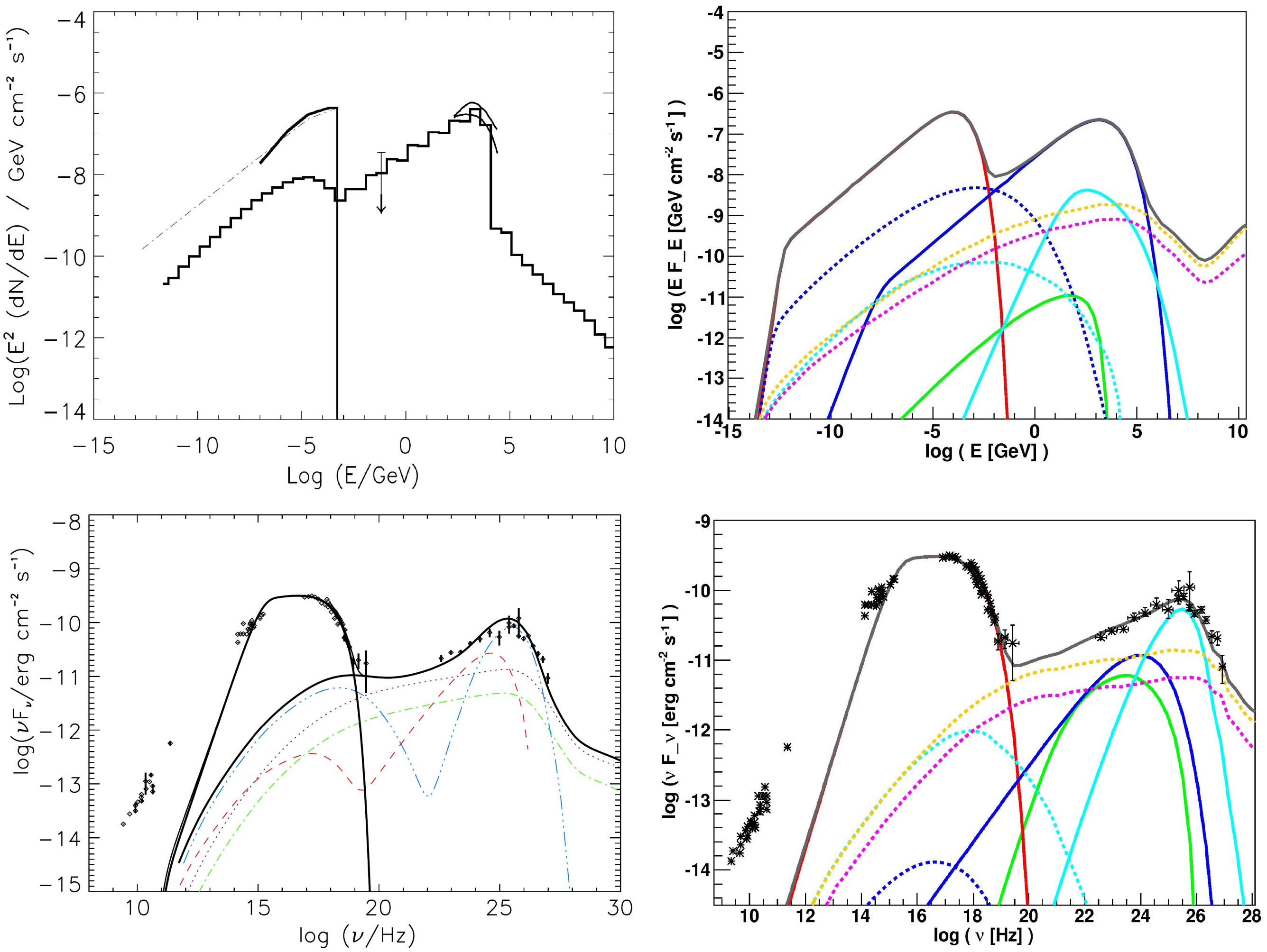

Figure 7.8: *Top left*: proton-synchrotron modelling of *Mrk 421* as proposed in the original paper by Mücke & Protheroe (2001). The black histogram represents the *total* emission from hadronic processes, namely the proton synchrotron emission (strongest component), the associated emission from secondary pairs (low energy bump), and the emission from the cascade triggered by photons from π_0 decay and electrons and positrons from $\pi^{\pm}$ decay (shoulder at very high energies). The low-energy bump is not modelled; the dotted line represent the input photon field used by *SOPHIA*. *Top right*: modelling of *Mrk 421* with our code, using the same input parameters as Mücke & Protheroe (2001). The colour-code is as follow: red-primary electron synchrotron emission; green-inverse Compton emission; blue-proton synchrotron emission; ligh blue-muon synchrotron emission; brown-photons from π^0 decay; pink-synchrotron emission from secondary $e^{\pm}$ coming from $\pi^{\pm}$ decay. The emission from the associated electromagnetic cascade is shown by the dotted curves (same colour). *Bottom left*: hadronic modelling of the SED of *Mrk 421* observed in 2009 (Abdo et al. 2011b). The colour-code is as follow: red-proton synchrotron emission; blue: muon synchrotron emission; violet: cascade from π^0 photons; green: cascade from secondary $e^{\pm}$ coming from $\pi^{\pm}$; black: primary electron synchrotron emission and total emission. *Bottom right*: modelling of *Mrk 421* with our code. The colour code is the same as in the *Top right* figure. In all models, the TeV data have been corrected for the EBL absorption, which is thus not included in the modelling.

as the proton synchrotron emission (and which was neglected in the modelling described by Abdo et al. (2011b)).

7.5.2 *PKS 2155-304*

PKS 2155-304 is one of the brightest BL Lac objects in the sky (see Chapter 4), and one of the most studied. It is classified as a HBL at a redshift of 0.117 (Charles et al. 1979). This source is in particular one of the brightest in the TeV sky and in 2006 an exeptional flare was observed by the *H.E.S.S.* telescope array (Aharonian et al. 2007b), which measured an integrated flux above 200 GeV equal to seven times the Crab nebula. In 2008 the *H.E.S.S.* collaboration led a multi-wavelength (MWL) campaign on *PKS 2155-304* (Aharonian et al. 2009b) succesfully achieving a full characterization of its SED, with simultaneous data from radio to TeV. In particular, thanks to the *Fermi* satellite, the high energy bump of the SED could be nicely constrained. During this campaign the source was found to be in a low state. The data from this MWL campaign will be used in the following as a test-bank for our lepto-hadronic code.

In this section, the radio and optical data will be considered as upper limit of the blazar emission. While the radio emission is generally ascribed to the external part of the jet (and not to the high-energy emitting region that we are modelling), the origin of the optical emission is not clear. Recently the *H.E.S.S.* collaboration published a long-term MWL study of *PKS 2155-304* (Abramowski et al. 2012a), showing that no clear correlation exists beween the optical and the high-energy behaviour, suggesting that the low energy emission could come from a different emitting region (i.e. the emission from the extended jet plus contamination from the host galaxy). According to this result, in the following we explicitely do not model the optical data.

SSC scenario

As first test, we model the SED of *PKS 2155-304* in a purely leptonic scenario: in this case, the η parameter (the proton-to-electron ratio) is set to zero, and the computation of the hadronic processes is skipped. Apart from the improvement in the leptonic part described in Section 7.2, the code is thus the same as in Katarzyński et al. (2001). The SSC model has been widely discussed in Chapters 3, 5 and 6. In the following we do not apply the algorithm to constrain the SSC model parameters that we have presented, but we follow the standard modelling, (i.e. we simply find a good solution among several others, remarking that this solution is not unique). As a reminder, the free parameters of the model are nine: the two slopes (α_1 and α_2), the three Lorentz factors ($\gamma_{e;min}$,$\gamma_{e;break}$ and $\gamma_{e;Max}$) and the normalization factor K_e which describe the primary electron distribution; and B, δ and R which describe the emitting region. However, as long as $\gamma_{e;min}$ is low enough, it does not play any role in the modelling (we can just set a lower limit provided by the radio data point), and it has been fixed at $\gamma_{e;min} = 500$. The two slopes α_1 and α_2 are constrained respectively by the measured slope in the GeV band and in the X-rays, and they have been fixed at 2.4 and 4.32, respectively. The X-ray spectrum show a hint of curvature which can be well reproduced by modifying the high energy cut-off $\gamma_{e;Max}$. The size of the emitting region is partially constrained by the causality principle which sets an upper-limit as a function of the variability time-scale

$$R < \frac{\delta}{1+z} c\tau_{var} \tag{7.38}$$

with, in this case, $\tau_{var} \approx 1$ day (Aharonian et al. 2009b). A good description of the SED can be achieved assuming a doppler factor of 30, a magnetic field equal to 0.065 G and an emitting region size equal to 1.7×10^{16} cm (corresponding to a six hours variability time-scale).

In Fig. 7.9 we show the modelling of the *PKS 2155-304* SED in this leptonic scenario, and in table 7.1 we summarize the model parameters, including the energy budget of the emitting region. The region is far from equipartition, with an electron energy density ($u_e = m_e c^2 \int d\gamma_e N_e(\gamma_e)$) 35 times larger than the magnetic energy density ($u_B = B^2/8\pi$). The total power of the emitting region is 5.3×10^{43} erg s^{-1}, quite far from the Eddington luminosity of the AGN, which is comprised between 10^{46} and 10^{47} erg s^{-1}, if we consider a SMBH mass comprised between 10^8 and 10^9 $M_\odot$ (see e.g. Zhang et al. 2005; Aharonian et al. 2007b). The synchrotron emission by pairs is totally negligible for the parameters used in this modelling, being more than four orders of magnitude lower than the emission from primary electrons.

Hadronic scenario

In the proton synchrotron scenario the high energy bump of the SED of *PKS 2155-304* is ascribed entirely to a hadronic compononent, namely the synchrotron emission from protons and from muons. For these two components to be dominant, the magnetic field needs to be much higher than in the SSC case, of the order of tens of gauss. The electron density in the emitting region is lower than in the SSC scenario (it compensates the increase in the synchrotron emission from electrons due to the increase of the magnetic field), suppressing the inverse Compton emission which is negligible compared to the emission from hadrons and from secondary particles coming from p-γ interactions. The emission from electrons and positrons coming from the $\pi^\pm$ decay, and from photons coming from the π^0 decay is completely reprocessed in the synchrotron-supported electro-magnetic cascade, resulting in an almost-flat spectrum from X-rays to TeV.

A good solution is found for a doppler factor of 30, a proton distribution slope α_p=2.0, an electron distribution slope before and after break $\alpha_{e;1}$ and $\alpha_{e;2}$ equal to 2.0 and 4.32, respectively, a magnetic field of 80 G, and a emitting region size of 5.2×10^{14} cm (corresponding to a 11-minutes variability time-scale). The model parameters are reported in table 7.1, and the SED modelling is shown in Fig. 7.9.
The importance of muon synchrotron emission in this kind of model has been already pointed out by Mücke & Protheroe (2001). In the recent MWL campaing on Mrk 421 (Abdo et al. 2011b), the hadronic scenario which is discussed presents as well this particular behaviour, with two differnt components for the GeV and TeV energy bands. It is worth to underline that at energies of the order of several TeV the emissions from the π^0 and from the secondary $e^\pm$ cascades become important, producing a significant hardening of the spectrum.
Concerning the energy budget of the emitting region, the system is closer to equipartition than the SSC model (u_p/u_B=1.5), while the total luminosity is much higher (due to the presence of hadrons in the emitting region), reaching 4.2×10^{45} erg s^{-1} (but still lower than the Eddington luminosity of the source).

Lepto-hadronic scenario

Our code permits the study of mixed lepto-hadronic scenarios, in which both the SSC and the hadronic components contribute to the high-energy bump. We present here two different mixed models, the first characterised by a low magnetic field (equal to the one used in the simple SSC scenario), the second by a higher magnetic field (equal to 5 G), which lies in between the typical values required by the SSC and the proton-synchrotron scenarios.

In the first scenario, shown in the top plot of Fig. 7.11, we consider indeed the same parameters used in the SSC scenario, with a magnetic field of 0.065 G. We add however a population of primary protons,

characterised by the same index of the electron distribution before break ($\alpha_p = 2.4$). Given the low magnetic field, the synchrotron emission by protons and muons is totally negligible. However, the secondary electrons and positrons coming from the $\pi^{\pm}$ decay can provide a contribution to the highest energies (in the VHE range).
This scenario implies a hardening of the VHE emission above the TeV, with respect to the spectrum expected from a pure inverse-Compton component, and is interesting for CTA. In particular, if we consider that the flaring states of *PKS 2155-304* are due to leptonic processes, this scenario could be tested by triggering low-states of the source, and looking to a spectral hardening of the TeV emission as a function of the flux.
The main problem of this scenario comes from the energy budget of the emitting region: in this case the power of the emitting region starts becoming of the same order of the Eddington luminosity of the source, implying a total conversion of the accreting material into the outflow. However, the proton energy density is dominated by the low-energy protons, and depends strongly on the adopted value of α_p: the used value of 2.4 implies infact a huge population of midly-relativistic protons. The total proton energy density can thus be decreased using harder injection functions, even though arbitrarly hard values cannot be used, given the constraints provided by *Fermi*.

The second scenario, shown in the bottom plot of Fig 7.11, assumes a magnetic field of 5 G, in between the 0.065 G used in the SSC scenario, and the 80 G used in the proton-synchrotron scenario. In this case as well, the high energy bump is due to the SSC component and the synchrotron emission from secondary electrons and positrons coming from p-γ interactions. Interestingly, the GeV and TeV components are due to two separate components, which could be observationally tested as a lack of correlation between the two energy bands. In this case as well, the energy budget of the emitting region is higher than the proton-synchrotron scenario, but less-critical than the previous scenario.
In Table 7.1 we report the parameters used for the two scenarios here discussed.

Table 7.1: Parameters used for the SSC and the hadronic modelling of *PKS 2155-304*. The luminosity of the source has been calculated as $L_{jet} = \pi R_{src}^2 c \Gamma_{bulk}^2 (u_B + u_e + u_p)$. For the SSC scenario, we included the term $u_{p,cold}$, which represents the contribution of cold protons in the emitting region, estimated using Sikora et al. (2009).

	SSC	Hadronic	Mixed 1	Mixed 2
ϑ	1°	1°	1°	1°
δ	30	30	30	30
Γ_{bulk}	16	16	16	16
$\gamma_{e,min}$	5×10^2	1	5×10^2	1×10^2
$\gamma_{e,break}$	1.5×10^5	4×10^3	1.5×10^5	1.7×10^4
$\gamma_{e,max}$	3×10^6	6×10^4	2.5×10^6	3×10^5
$\alpha_{e,1}$	2.4	2.0	2.4	2.0
$\alpha_{e,2}$	4.32	4.32	4.32	4.32
K_e [cm^{-3}]	7.5×10^4	6.0×10^2	6.3×10^4	6×10^5
u_e [erg cm^{-3}]	5.9×10^{-3}	2.2×10^{-3}	5.1×10^{-3}	1.4
$\gamma_{p,min}$	-	1	10^5	1
$\gamma_{p,max}$	-	1×10^9	8×10^7	6×10^7
α_p	-	2.0	2.4	2.0
$\eta = K_p/K_e$	-	20	10	1.0
u_p [erg cm^{-3}]	-	3.7×10^2	22	1.6×10^4
R_{src} [cm]	1.7×10^{16}	5.2×10^{14}	1.8×10^{16}	2×10^{14}
$\tau_{var}[h]$	5.9	0.18	6.2	0.07
B [G]	0.065	80	0.065	5
u_B [erg cm^{-3}]	1.7×10^{-4}	2.5×10^2	1.7×10^{-4}	1.0
u_e/u_B	35	8.5×10^{-6}	29	1.4
u_p/u_B	-	1.5	1.3×10^5	1.6×10^4
L_{jet} [erg s^{-1}]	4.3×10^{43}	4.2×10^{45}	1.7×10^{47}	1.5×10^{46}

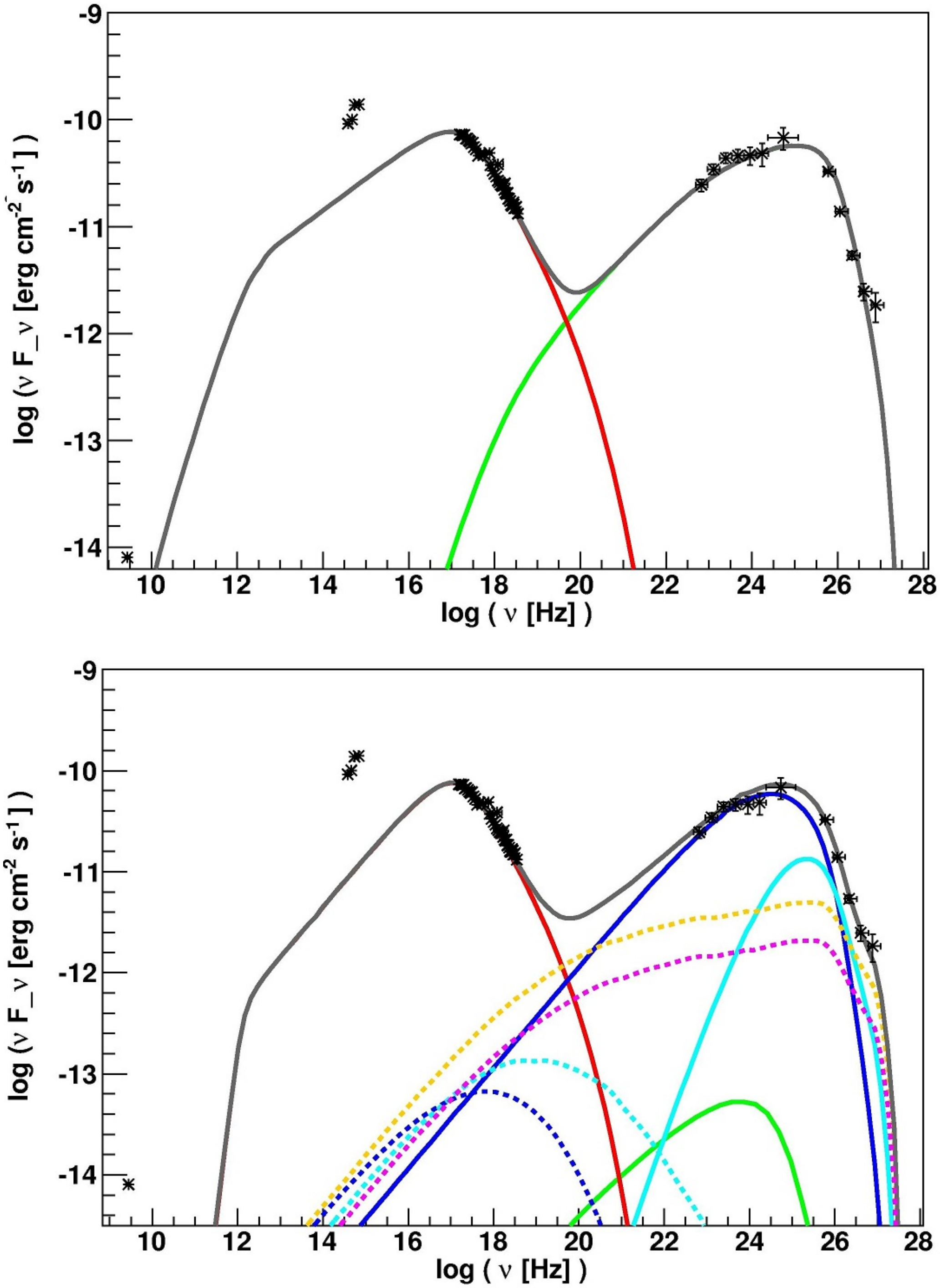

Figure 7.9: *Top:* modelling of *PKS 2155-304* in a synchrotron-self-Compton scenario. *Bottom:* modelling of *PKS 2155-304* in a hadronic scenario. The colour-code is as follow: red-primary electron synchrotron emission; green-inverse Compton emission; blue-proton synchrotron emission; light blue-muon synchrotron emission; brown-photons from π^0 decay; pink-synchrotron emission from secondary $e^{\pm}$ coming from $\pi^{\pm}$ decay. The emission from the associated electro-magnetic cascade is shown by the dotted curves (same colour).

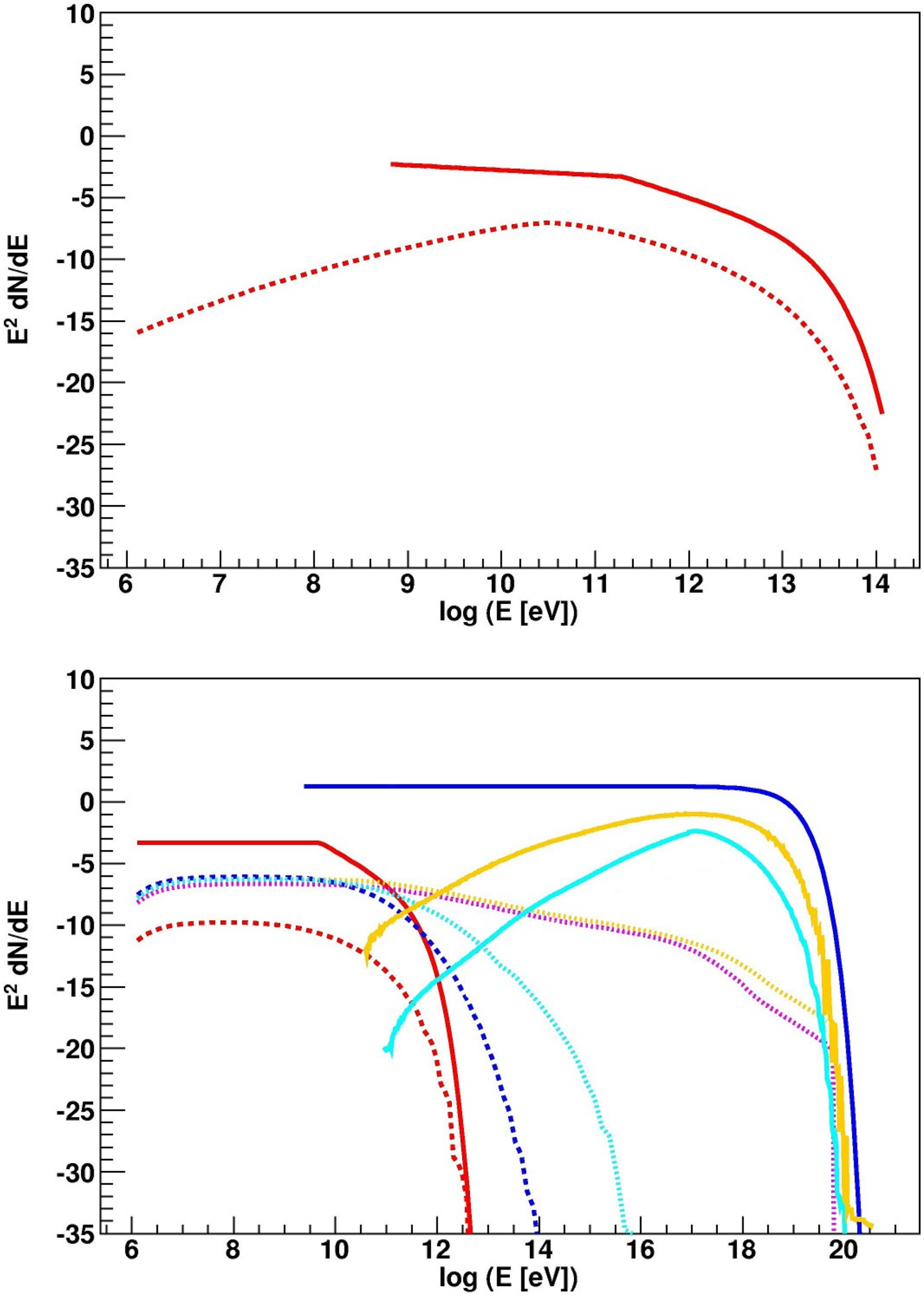

Figure 7.10: *Top:* particle distribution (expressed as $E^2\ dN/dE$) associated to the model presented in the top plot of Fig. 7.9 *Bottom:* The same for the bottom plot of Fig. 7.9. The colour-code is as follow: red-primary electrons; blue-primary protons; light blue-muons; brown-photons from π^0 decay; pink-secondary $e^{\pm}$ coming from $\pi^{\pm}$ decay. The spectrum of associated pairs (from $\gamma - \gamma$ pair-production) is shown by the dotted curves (same colour; the dotted red line correspond to the pairs coming from the SSC component).

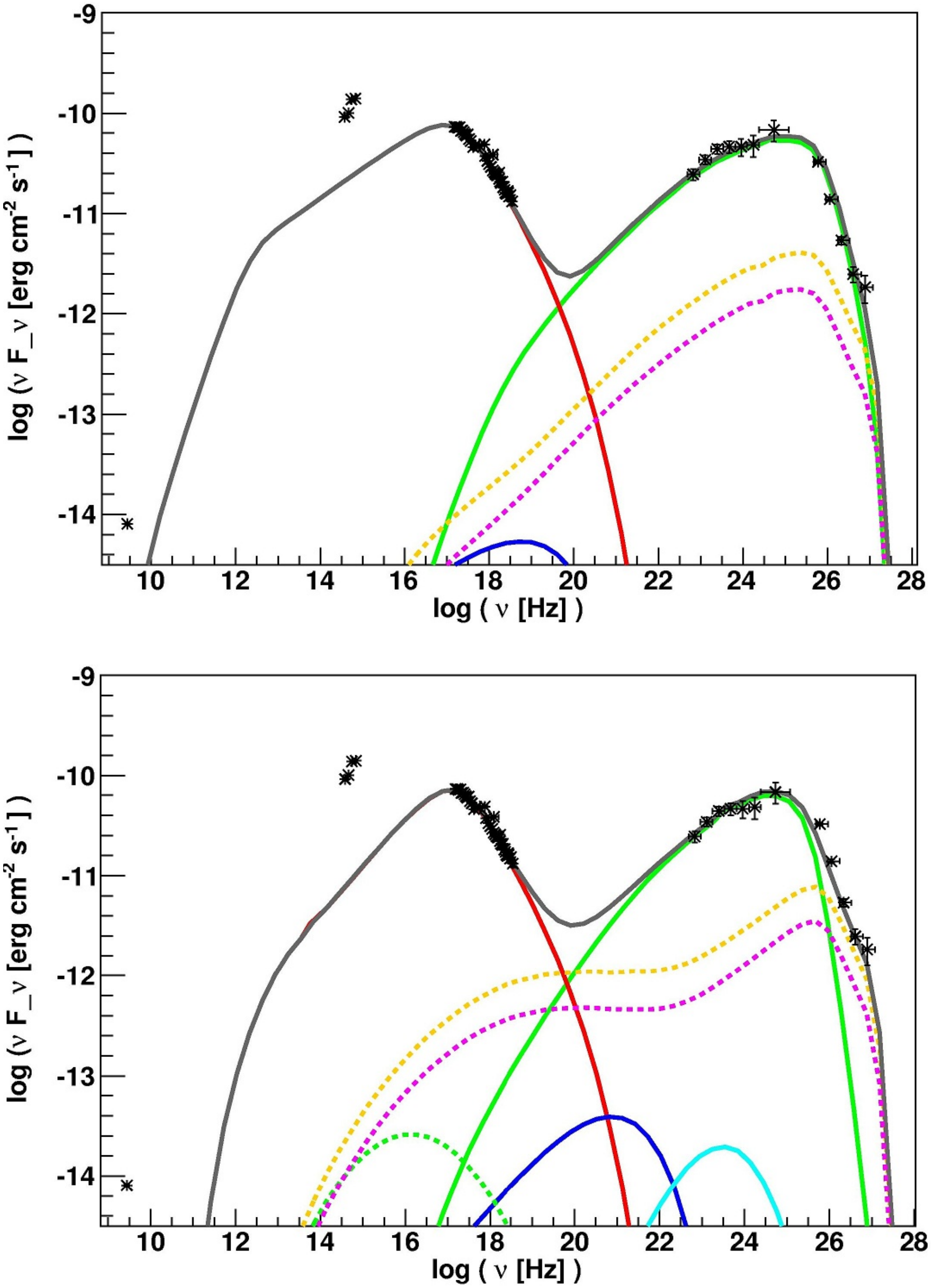

Figure 7.11: *Top:* modelling of *PKS 2155-304* in a mixed lepto-hadronic scenario (first case, B = 0.065G). *Bottom:* modelling of *PKS 2155-304* in a mixed lepto-hadronic scenario (second case, B = 5G.) The colour-code is as follow: red-primary electron synchrotron emission; green-inverse Compton emission; blue-proton synchrotron emission; light blue-muon synchrotron emission; brown-photons from π^0 decay; pink-synchrotron emission from secondary $e^{\pm}$ coming from $\pi^{\pm}$ decay. The emission from the associated electro-magnetic cascade is shown by the dotted curves (same colour).

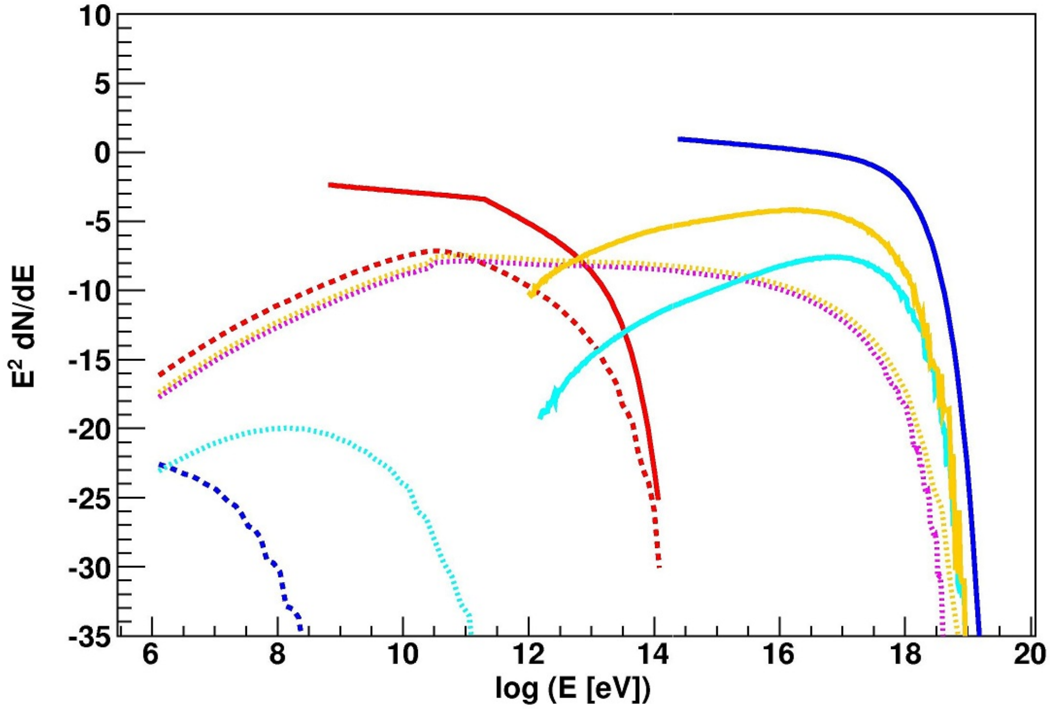

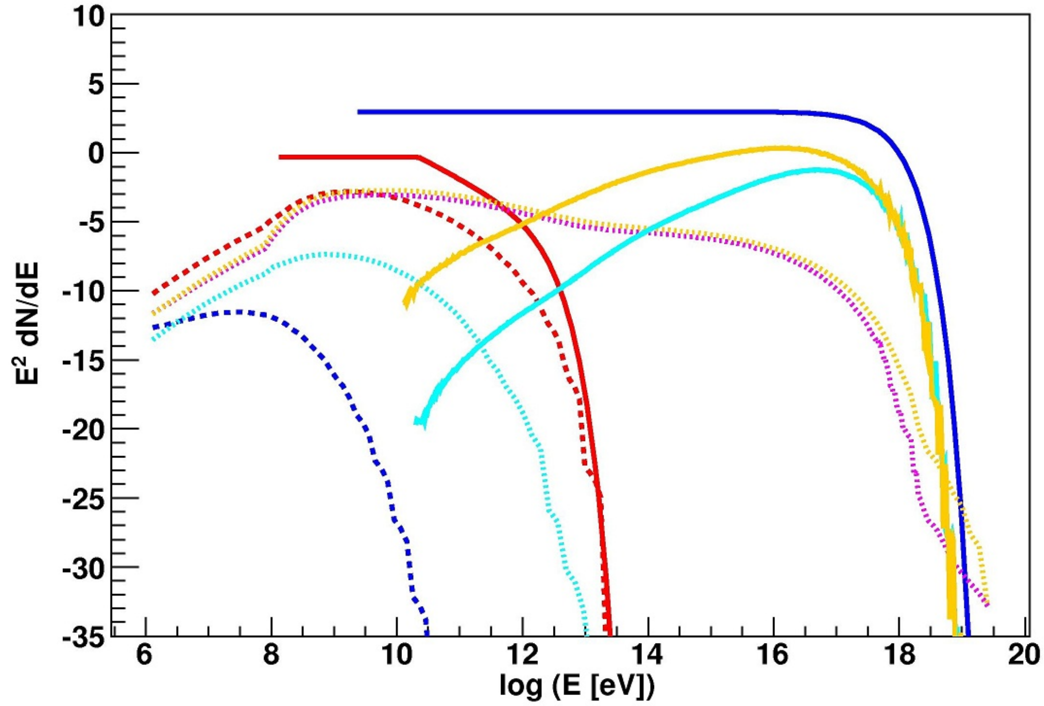

Figure 7.12: *Top:* particle distribution (expressed as $E^2\ dN/dE$) associated to the model presented in the top plot of Fig. 7.11 *Bottom:* The same for the bottom plot of Fig. 7.11. The colour-code is as follow: red-primary electrons; blue-primary protons; light blue-muons; brown-photons from π^0 decay; pink-secondary $e^{\pm}$ coming from $\pi^{\pm}$ decay. The spectrum of associated pairs (from $\gamma - \gamma$ pair-production) is shown by the dotted curves (same colour; the dotted red line correspond to the pairs coming from the SSC component).

Chapter 8

On the spectral break in the GeV spectrum of *3C 454.3*

Contents

8.1 Introduction

In this Chapter we discuss the observations of the FSRQ *3C 454.3*, and in particular the spectral break observed in the GeV energy range with the *Fermi* telescope (Section 8.2).

The SED is modelled by an external-inverse-Compton scenario, considering as soft photons the reprocessed emission of broad lines observed in the optical spectrum: the details of the modelling are provided in Section 8.3 and the results in Section 8.4.

This work represents the preliminary result of a collaboration with Charles Dermer.

8.2 The *Fermi-LAT* result

3C 454.3, observed for the first time as a radio source (Bennett 1962) and located at a redshift of 0.859 (see Burbidge 1967), showed historically an extreme variability behaviour with several flares observed at all wavelengths (Kinman et al. 1968; Gómez et al. 1999). The γ-ray emission from *3C 454.3* was first observed with *EGRET* (Hartman et al. 1993).

Among the recent outbursts, it is worth mentioning the one that occured in 2005 (Villata et al. 2006; Pian et al. 2006; Fuhrmann et al. 2006), and the one in 2007 (Ghisellini et al. 2007; Vercellone et al. 2008; Raiteri et al. 2008; Vercellone et al. 2009; Donnarumma et al. 2009). Since the launch of the *Fermi* mission, *3C 454.3* has been monitored in the GeV energy band, providing the first continuous long-term light-curve in γ-rays (see Fig. 8.1): since 2008, the source showed two major flares, in 2009 and 2010 (Ackermann et al. 2010; Abdo et al. 2010c; Vercellone et al. 2011).

The most unexpected result from the *Fermi-LAT* observations comes from the spectral distribution of γ-ray photons: the spectrum does not follow a pure power-law, but presents instead a clear break at an

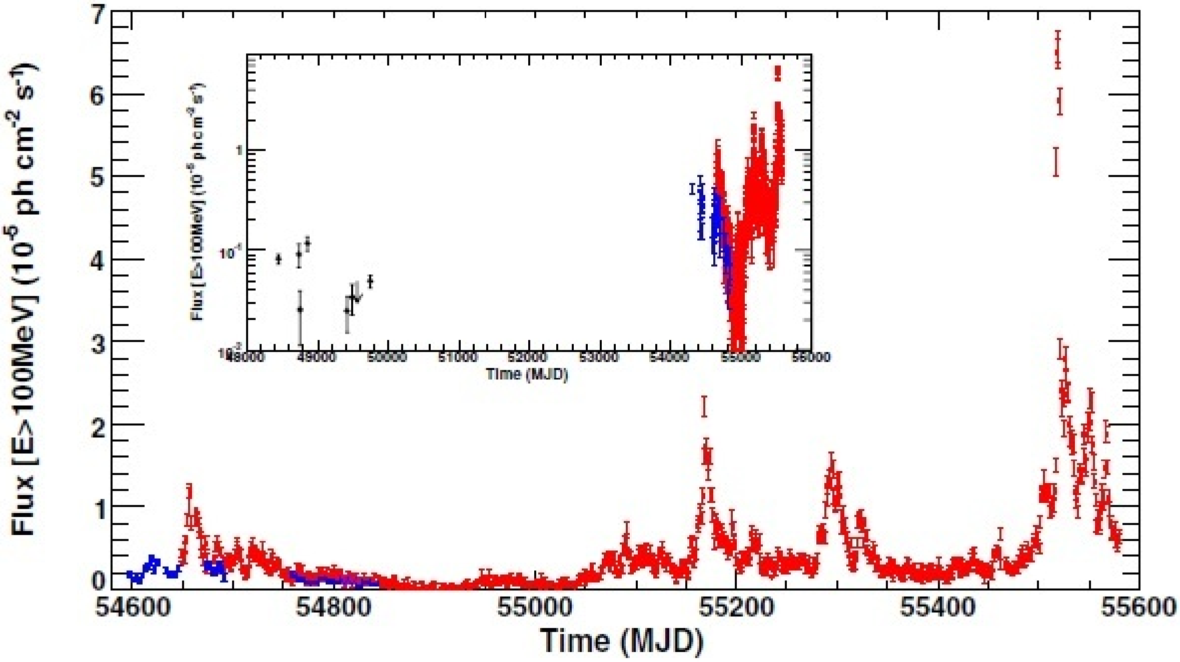

Figure 8.1: The *Fermi-LAT* lightcurve of *3C 454.3*, with clearly visible the giant flare occoured in 2010. The inset shows the historical γ-ray lightcurve. Taken from Abdo et al. (2011a).

energy of a few GeVs (see Fig. 8.2). More interestingly, the energy of the break is constant despite the strong flux variations.
It is important to notice that, while the presence of a break is statistically significant, the statistics is still too low to differentiate between a broken power-law model or a curved function, as a power-law with a cut-off or a log-parabolic distribution.

Various theoretical models have been developed to explain such a break: its constancy, in particular, favours an origin related to physical process. Stern & Poutanen (2011) proposed that it is due to an absorption effect, generated by γ-γ pair production over the broad optical emission lines. This model has been succesfully applied to several *Fermi* FSRQs (Poutanen & Stern 2010). An alternative is that it could be due to the onset of Klein-Nishina effects in the Compton scattering of soft photons coming from the BLR on the high energy electrons in the emitting region. This scenario has been originally proposed by Ackermann et al. (2010) but, as can be seen in Fig. 8.3, a simple power-law electron distribution scattering the Lyα photons (at 10.2 eV, the dominant emission line in the optical spectrum) results in a spectrum too hard with respect to the data. Finke & Dermer (2010) proposed a different scenario in which the *Fermi-LAT* spectrum is ascribed to two different components: an EIC over the accretion disc (dominating the soft part of the spectrum), and an EIC over the Lyα emission line (dominating the emission after the break).

In the next Section we start from the idea discussed in Ackermann et al. (2010) (break due to the transition to the Klein-Nishina regime), including a curvature in the electron distribution in order to describe the data. We then study the overall SED, providing a set of parameters which can satisfactorly describe both the low energy emission (visible and X-rays) and the peculiar GeV spectrum.

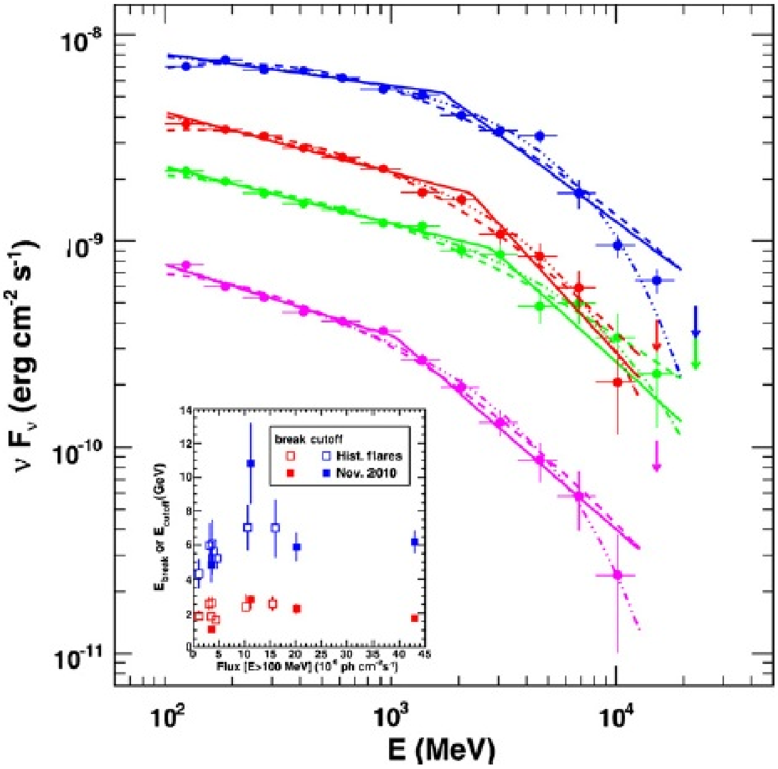

Figure 8.2: The *Fermi-LAT* spectrum of *3C 454.3*, computed for different flux values. The data have been fitted with both a broken power-law function (solid line) a log-parabola (dashed line) and a power-law with exponential cut-off (dashed-triple-dotted line). The inset show the best-fit values of the break energy (red) and the cut-off energy (blue), which remains constant during the flare. Taken from Abdo et al. (2011a).

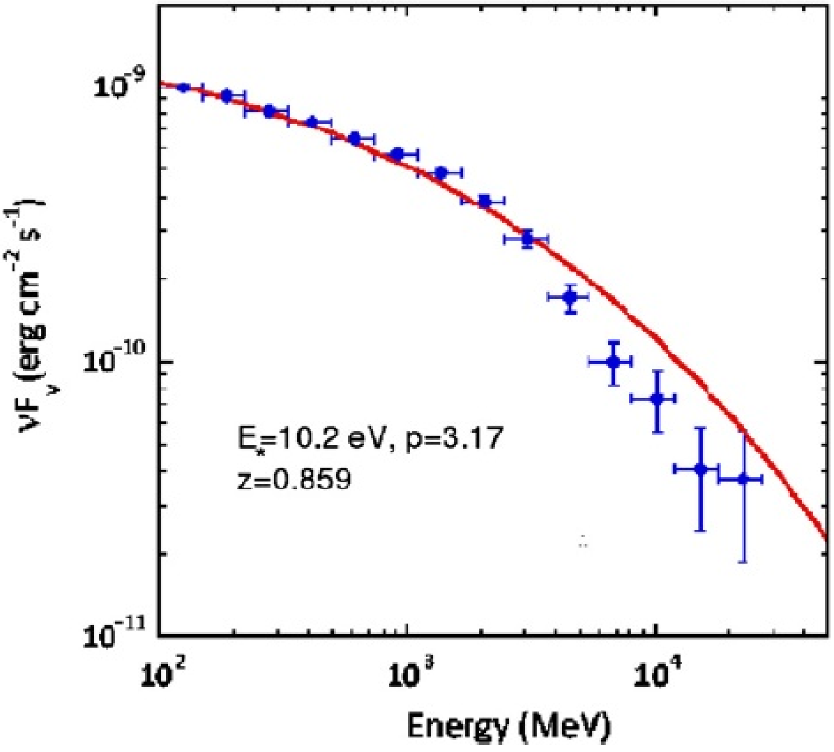

Figure 8.3: The *Fermi-LAT* spectrum of *3C 454.3*, modelled in a EIC scenario: a power-law distribution of electrons scatters photons from the BLR. The break observed comes from the transition to the Klein-Nishina regime of the inverse Compton scattering. Taken from (Ackermann et al. 2010).

8.3 External inverse Compton on the Lyα line

The external inverse Compton emission over the Lyα line has been computed considering that the external radiation field is isotropic and monochromatic (with an adimensional energy $\varepsilon_\star = E_\star/m_e c^2$, and $u_\star(\varepsilon_\star)$ representing the energy density of soft photons). In this case, the expected flux (as a function of $\varepsilon = h\nu/m_e c^2$) can be expressed as (see Dermer & Menon 2009)

$$\varepsilon f_\varepsilon(\varepsilon) = \frac{3\, c\sigma_T}{16\pi d_L^2} \frac{\varepsilon_s^2}{\varepsilon_\star^2} \delta^3 u_\star(\varepsilon_\star) \int_{\gamma_{min}}^{\gamma_{Max}} d\gamma\, \frac{N'(\gamma/\delta)}{\gamma^2} F_C(q, \Gamma_e) \tag{8.1}$$

where

$$\begin{aligned} \gamma &= \delta\gamma' \\ \varepsilon_s &= (1+z)\varepsilon \\ q &= \frac{\varepsilon_s/\gamma}{\Gamma_e(1-\varepsilon_s/\gamma)} \\ \Gamma_e &= 4\gamma\varepsilon_\star \\ F_C(q,\Gamma_e) &= 2q\ln q + (1+2q)(1-q) + \frac{(\Gamma_e q)^2}{2(1+\Gamma_e q)}(1-q) \\ \gamma_{min} &= \frac{\varepsilon_s}{2}\left(1 + \sqrt{1 + 1/\varepsilon_s\varepsilon_\star}\right) \end{aligned} \tag{8.2}$$

Note that all quantities are given in the rest frame of the observer, apart from γ' and N'.
The expression of $u_\star$ depends on the geometry of the emitting region. We used the expression provided by Finke & Dermer (2010): we consider the BLR as a spherical shell which extends between a minimum inner radius to a maximum outer one from the central black hole ($r_{BLR;min}$ and $r_{BLR;Max}$). The γ-ray emitting region is located at a radius r_γ. The intensity of the emission depends also on the mass of the SMBH ($M_\bullet$), the ratio of the Eddington luminosity reprocessed into the BLR ($l_{Edd} = L^\dagger/L_{edd}$, where L_{Edd} represents the Eddington luminosity of the SMBH, and $L^\dagger$ represents the reprocessed luminosity), the optical depth of the BLR (τ_{BLR}) and the index of the BLR density (Γ_{BLR}. We assume in this case a BLR density distribution in the form $n_{BLR}(r) \propto r^{\Gamma_{BLR}}$).
For a value of $\Gamma_{BLR} = -2.0$, and a γ-ray emitting region located inside the BLR ($r_{BLR;min} < r_\gamma < r_{BLR;Max}$) we have:

$$\frac{L^\dagger \tau_{BLR}}{8\pi c} \frac{1}{r_\gamma r_{BLR;min}} \left(\frac{r_\gamma}{r_{BLR;min}}\right)^{-2} \tag{8.3}$$

As can be seen, in this case, the expression does not depend on $r_{BLR;Max}$.

We include some modifications to the model discussed by Ackermann et al. (2010): first, in order to describe the break observed in the *Fermi* data, we include a curvature in the electron distribution; second, we consider the overall SED, constraining the parameters of the electron population using the low energy data; third, we have considered the EIC over the most important broad lines observed in the optical spectrum, instead of only the Lyα line.

The log-parabolic function represents the most simple way to introduce a curvature in a power-law. It is simply defined as a parabola in the logarithmic space. It is characterised by the following expression (see e.g. Massaro et al. 2004)

$$N(\gamma) = K\left(\frac{\gamma}{\gamma_1}\right)^{-(\alpha+\beta\log\gamma/\gamma_1)} \tag{8.4}$$

At $\gamma = \gamma_1$ the log-parabola is reduced to a power-law with index α. Alternatively, it can be used as a reference to the value of the peak, which is related to γ_1 by $\gamma_p = \gamma_1\ 10^{(2-\alpha)/2\beta}$.
The log-parabola is not just a mathematical expression of an intrinsic curvature: Massaro et al. (2004) showed that a log-parabolic distribution can in fact be produced in a simple statistical acceleration mechanism, in which the probability of acceleration depends on the particle energy.
The log-parabolic function has been integrated as a possible parametrization of the primary electron distribution in our leptonic code, described in Section 7 (No hadronic interactions will be considered here).

We used the data from Abdo et al. (2009b) for the overall SED, as in the study by Finke & Dermer (2010). In this work are presented the results of a multiwavelength campaign on *3C 454.3*, including data from the *Effelsberg* and *IRAM* radio telescopes, from the UV and X-ray observatory *Swift*, and from *Fermi*.

As mentionned above, we included in our model the computation of EIC over several emission lines. The strength of the lines are expressed as a ratio with respect to the Lyα intensity ($u_\star$), and are fixed: we used in particular the ratio estimation by Telfer et al. (2002). We tested other different line-ratio combinations (Osterbrock 1989; Francis et al. 1991), wich provide similar results and do not significantly modify the modelling.
We also tested a more correct integration over a Gaussian function of soft photons: this more precise computation results in a negligible modification with respect to the result achieved assuming monochromatic photons (as in Eq. 8.1). In the following we will thus show the results achieved using Eq. 8.1.

8.4 Modelling of the SED

The SED of *3C 454.3* is shown in Fig. 8.4 (taken from Abdo et al. 2009b). The radio data are considered in this case as well as upper limits. The UV data are modelled as the decreasing part of the synchrotron component, which thus is expected to peak at lower energies (infrared).
The X-rays data represents, on the other hand, the rising part of the high-energy bump, and in this scenario their origin is ascribed to the SSC component. The different EIC components contribute to produce the γ-rays observed by *Fermi-LAT*.

The modelling is strongly constrained by the X-ray and γ-ray data. In particular, in order to fit the X-rays, we need to blue-shift the model, and then to increase the magnetic field up to a value of 2 G. The Doppler factor is equal to 20, and the emitting region size is equal to 1.5×10^{16} cm (the same order of magnitude of the values of δ and R adopted in the description of HBLs in Chapters 5 and 6).
The electron distribution is described by a log-parabola, with $\gamma_1 = 100$, $\alpha = 2.1$ and $\beta = 0.65$ (contrained by the *Fermi-LAT* spectrum). The other parameters are reported in Table 8.1.
It is worth to underline that the magnetic field used is significantly higher than the one used in the leptonic modelling of HBLs (see Chapters 5, 6, 7), but in agreement with the EIC modelling presented by Bonnoli et al. (2011). The system is thus closer to equipartition with respect to the SSC modelling of HBLs, with a u_e/u_B ratio equal to 0.6.
In our scenario we have ignored the EIC over the soft photons coming from the accretion disc: this component is expected to contribute significantly in the gap between the SSC and the EIC over the emission lines, and should affect the hard-X-ray and the low-γ-ray part of the SED. However, the lack of observations in this energy band prevent us from constraining this second EIC component.

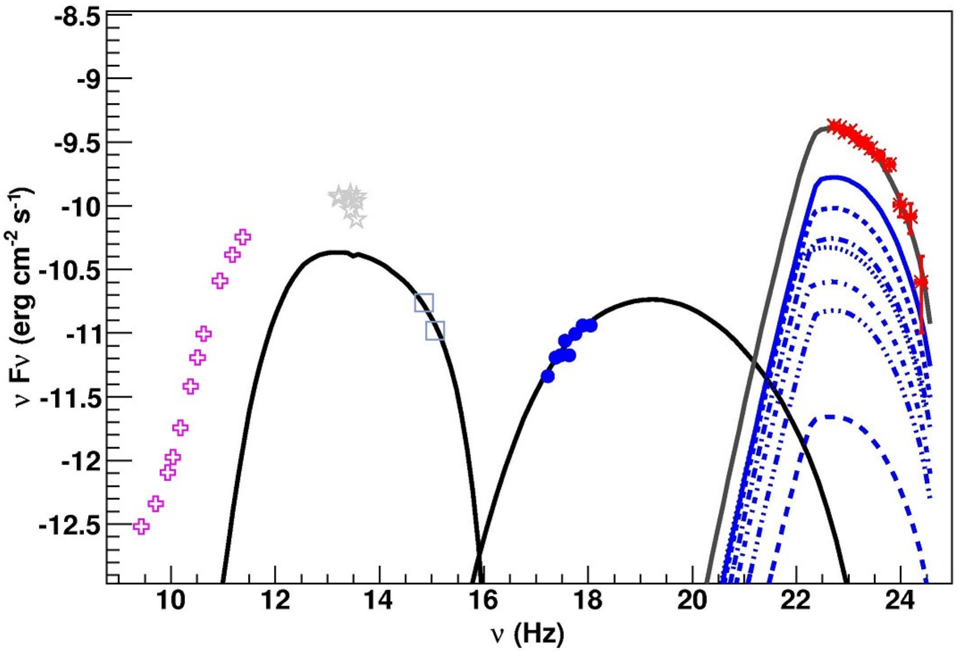

Figure 8.4: Modelling of the SED of *3C 454.3* in a EIC scenario. The data points are taken from Abdo et al. (2009b) (the grey data at 10^{14} Hz are not simultaneous). The different components are, from low to high energies, the synchrotron emission by primary leptons, the SSC component and the external Compton over the lines from the BLR (each line contribution is represented by the blue lines, while the black line represent the total EIC emission).

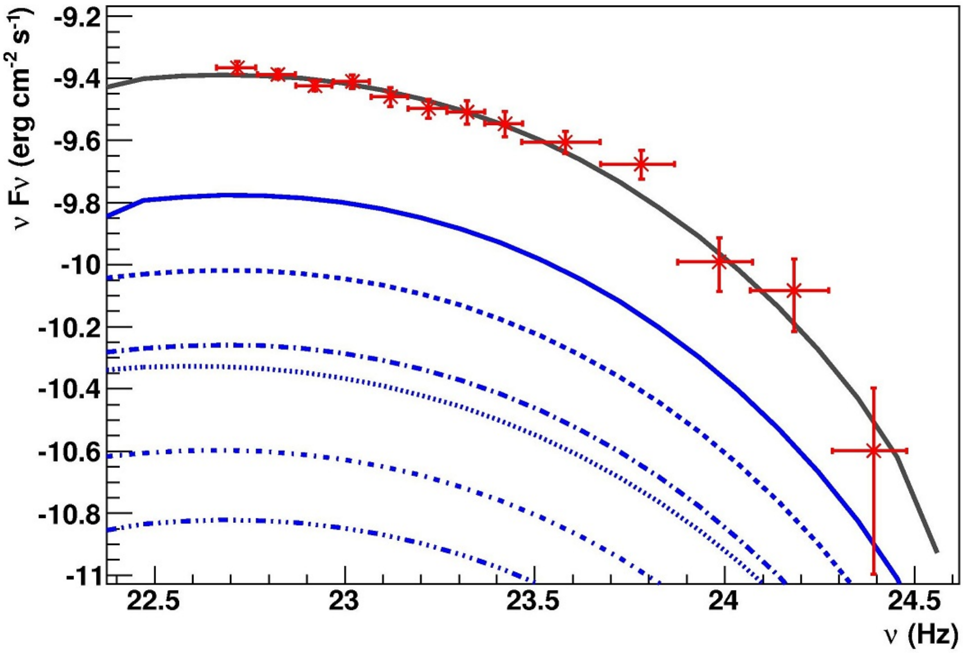

Figure 8.5: Modelling of the SED of *3C 454.3* in a EIC scenario. Zoom on the GeV part of the SED shown in Fig. 8.4.

Table 8.1: Parameters used for the EIC modelling of *3C 454.3*.

ϑ	1°
δ	20
Γ_{bulk}	10
γ_{min}	1.25×10^{2}
γ_{max}	4.50×10^{3}
γ_1	100
α	2.1
β	0.65
K_e [cm^{-3}]	10
u_e [erg cm^{-3}]	1.03×10^{-1}
R_{src} [cm]	1.5×10^{16}
$\tau_{var}[h]$	12.9
B [G]	2.0
u_B [erg cm^{-3}]	1.59×10^{-1}
u_e/u_B	0.65
$r_{BLR;min}$ [$\mathrm{r_G}$]	5.0×10^{2}
r_γ [$\mathrm{r_G}$]	1.0×10^{3}
$r_{BLR;Max}$ [$\mathrm{r_G}$]	5.0×10^{5}
τ_{BLR}	0.05
$M_\bullet[\mathrm{M_\odot}]$	1.4×10^{9}
l_{Edd}	0.03
Γ_{BLR}	-2
L_{jet} [erg s^{-1}]	5.96×10^{44}

Conclusions

In this work we have presented and discussed the results of observations and modelling of high-energy emission (X-ray and γ-rays) of active galactic nuclei (AGN). The thesis covers two different aspects: the X-ray emission of Seyfert 1 galaxies (part I) and the γ-ray emission of blazars (part II).

In the first part we have presented, after a short introduction on the X-ray emission of radio-quiet AGNs (Chapter 1), the results of observations with the *Suzaku* telescope of two Seyfert 1 galaxies (*Mrk 509* and *Mrk 841*, Chapter 2). The study deals in particular with the problem of the origin of the soft-excess emission observed in this kind of AGN. We have investigated three different scenarios proposed to explain the soft-excess: a double-Comptonisation, a blurred reflection over the accretion disk, and a smeared absorption by a relativistic wind. While for *Mrk 841* none of the models can be excluded on the basis of *Suzaku* observations, in the case of *Mrk 509* we have disfavoured the reflection scenario.

In the second part we have studied the γ-ray emission of blazars, making use in particular of data from the atmospheric Cherenekov telescope system *H.E.S.S.* (Chapter 4).
We have then analysed in detail the typical BL Lac object *1RXS J101015.9 - 311909* (Chapter 5): the analysis of *H.E.S.S.* data, as well as a multi-wavelength study (using the *ATOM*, *Swift* and *Fermi* telescopes), allows the study of the spectral energy distribution (SED) of the source. The emission has been then modelled in a standard leptonic scenario (synchrotron-self-Compton, SSC).

The study of the leptonic modelling of blazar emission is studied more deeply in Chapter 6 in which we have presented a new numerical algorithm to constrain the parameters of the SSC model. This method, which can be applied to any GeV-TeV detected high-frequency-peaked BL Lac object (HBL), is tested for the specific case of *1RXS J101015.9 - 311909*, showing that the parameter space can be significantly narrowed with respect to previous analytical constrains. A second application to the BL Lac object *PKS 0447-439* show that, under certain hypothesis, this algorithm can be used to constrain the distance of a TeV-deteted HBL with unknown redshift.
An alternative to leptonic blazar models, is represented by hadronic models, in which the high-energy part of the SED is dominated by emission processes associated to protons. We have then developped a new code (Chapter 7), which computes the most important leptonic and hadronic emission processes: the code allows the modelling of blazar SED in both leptonic and hadronic scenarios, and allows the study of interesting mixed lepto-hadronic scenarios, in which the high-energy emission is ascribed to both components.

The theoretical interpretation of blazar emission is completed by the study of the FSRQ *3C 454.3* (Chapter 8): in FSRQs the bright soft photon field (associated mainly to the emission lines produced in the broad-line-regions, the accretion disk and the dusty torus) is Compton scattered by the leptons in the emitting region, producing an External-Inverse-Compton (EIC) component in γ-rays. In this Chapter (preliminar to a further study) we put a particular emphasis to the spectral break observed in the GeV spectrum of *3C 454.3*.

The current generation of Cherenkov telescopes (*H.E.S.S.*, *MAGIC* and *VERITAS*), together with the *Fermi* space telescope, has provided a new view of the γ-ray emission of radio-loud AGNs, increasing the number of sources detected and measuring the spectral energy distribution with an excellent resolution. The new *H.E.S.S. II* telescope (which has taken the first light during the summer 2012), thanks to the lower energy threshold with respect to the current *H.E.S.S.* array, will allow to overlap the *Fermi* and IACT measurements, putting stronger constrains on the γ-ray emission of blazars.
In perspective, the scientifical community is currently working on the development of the next generation Cherenkov telescope array, *CTA*. The project is currently in its preparatory phase, and the first telescope protoypes are on construction (as for example the GATE project, at the Paris Observatory). In this context, we have performed a study of prediction of detection of high-redshift blazar with *CTA*, presented in Appendix A.

Appendix A

Perspectives of detection of high redshift blazars with CTA

Contents

A.1 Introduction

In this Chapter are presented predictions of observations with CTA, the next generation IACT (see Introduction), in particular the study of the detectability of high-redshift blazars, both in low-state (see Section A.2) and in flaring-state (see Section A.3).[1]

The work has been done using the scripts developed by the high-energy astrophysics group (GAE) in the Complutense University of Madrid.[2]
The tool permits the estimation of the CTA detection of a simulated source, as a function of different input parameters:

- The integral *Fermi* flux between 1 and 100 GeV ($F_{1-100\ \mathrm{GeV}}$), which will be extrapolated into the CTA energy range
- The spectral index
- The redshift of the source z
- The integrated observation time
- The EBL absorption model

---

[1] The work has been done by Bolo Thiam during her one-month internship (*stage de licence*, for the French reader) in the LUTh, under my supervision.

[2] For details on the prediction algorithm, see `http://cta.gae.ucm.es/cta-observatory-files/static/pdf_files/forecastingcta.pdf`, or Hassan et al. (2011)

- The CTA array configuration

The basic idea of the study is to simulate a *typical* blazar spectrum, vary the redshift of the source and test the capability of detection with CTA. Given the fact that the final configuration of CTA has not been chosen yet, this study also helps in determining the best configuration for this particular scientific aspect. The configurations studied in this context are three: NA (North-A: compact with large-size telescopes, LSTs), C (extended without LSTs) and I (extended with LSTs).
In the following we used the EBL model by Franceschini et al. (2008) (as for the rest of this thesis).

A.2 Detection of steady-state blazars

The first study is the detection of non-flaring blazars. In this case we consider as *typical* low-state source, a blazar with a flux corresponding to 10% of the Crab nebula (Aharonian et al. 2006a), located at a redshift of $z = 0.1$. The spectral index in the TeV range (intrinsic, i.e. before absorption by the EBL) is assumed to be equal to $\Gamma = 3.0$. These values correspond roughly to the ones observed for *1RXS J101015.9 - 311909* (see Chapter 5).
The flux is rescaled for different redshift values (from 0.1 to 0.5), and the expected significance is then computed, considering 50 hours of observation time. The results of the simulation are given in Table A.1 and plotted in Fig. A.1. As can be seen, CTA will be able to detect ($\sigma > 5$) a source with the characteristics of *1RXS J101015.9 - 311909* up to a redshift of 0.4. For lower redshifts, the significance of the detection is huge, implying a high number of γ-ray photons and thus the possibility of performing interesting spectral and variability studies.

The results also show the importance of the LSTs for the study of high-redshift sources: the configuration C (the only one without LSTs) provides in fact a lower significance. This comes from the higher sensitivity provided by the LSTs in the low-energy band, where the absorption by the EBL is not so strong, permitting thus the detection of distant blazars.

A.3 Detection of flaring blazars

We studied then the case of a flaring blazar: in this case we consider a bright source (with a flux equal to 10 times the Crab nebula, at $z = 0.1$), with a spectral index of 2.5 (similar to the one measured for the flare of *PKS 2155-304*, see Aharonian et al. (2007b)). We consider a rapid flare, lasting only 3 hours, and we test the capability of detection with CTA as a function of the redshift.
The results are given in Table A.2 and plotted in Fig. A.2. In this case, a 5σ detection can be achieved up to a redshift of 1.0, significantly extending the horizon of sources detected at VHE. This result is interesting in the perspective of ToO (target of opportunity)[3] observations, showing that in the case of such a flare it will be worth to observe even sources located at $z = 1.0$.
In this case as well, the configurations which include LSTs are more efficient in the detection: the array C results in fact in a maximum redshift significantly lower, and equal to 0.75.

---

[3] In this case the observation is triggered by the detection of a flare at other wavelengths.

	Array NA	Array I	Array C
z	Significance (in σ, for 50h)		
0.10	190.1	174.3	135.7
0.20	49.6	45.4	33.8
0.25	31.1	28.4	20.3
0.30	21.0	19.1	13.0
0.35	15.0	13.6	8.9
0.40	11.2	10.2	6.4
0.45	<5	<5	<5
0.50	<5	<5	<5

Table A.1: Simulation of detection of low-state blazars with CTA, as a function of the redshift. We considered a source flux equal to the 10% of the Crab nebula at a redshift of 0.1, with a spectral index of 3.0

	Array NA	Array I	Array C
z	Significance (in σ, for 3h)		
0.10	529.7	496.0	441.4
0.20	206.6	192.4	173.0
0.25	144.3	133.6	119.2
0.30	105.0	96.4	84.1
0.35	79.5	73.0	62.9
0.40	61.6	56.6	47.7
0.45	48.6	44.6	36.4
0.50	38.9	35.8	28.0
0.60	26.3	24.2	18.1
0.75	15.8	14.5	9.8
1.00	7.7	7.0	<5
1.50	<5	<5	<5

Table A.2: Simulation of detection of flaring blazars with CTA, as a function of the redshift. We considered a source flux equal to ten times the Crab nebula at a redshift of 0.1, with a spectral index of 2.5

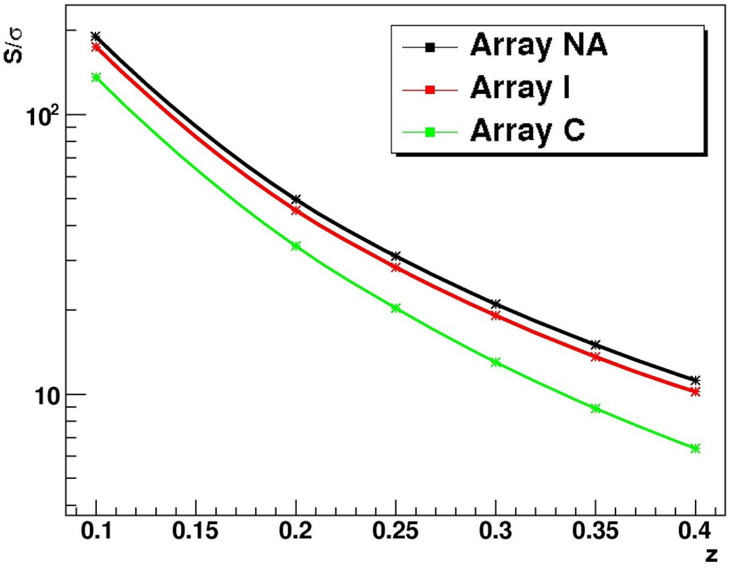

Figure A.1: Simulation of detection of low-state blazars with CTA, as a function of the redshift. Data are from Table A.1

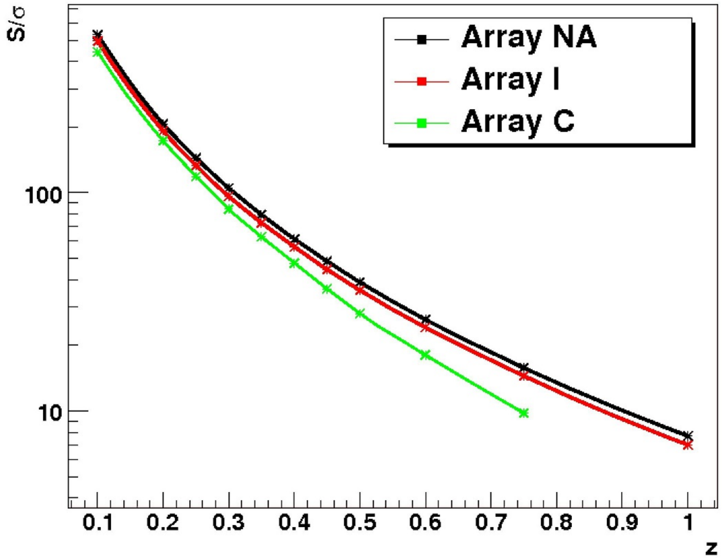

Figure A.2: Simulation of detection of flaring blazars with CTA, as a function of the redshift. Data are from Table A.2

Appendix B

List of publications

Refereed papers:

First author and Corresponding author:

- Cerruti, M.; Ponti, G.; Boisson, C.; Costantini, E.; Longinotti, A. L.; Matt, G.; Mouchet, M.; Petrucci, P. O. : *" Suzaku broad-band observations of the Seyfert 1 galaxies Mrk 509 and Mrk 841"* 2011A&A...535A.113C
- The HESS Collaboration : *"Discovery of very-high-energy gamma-ray emission and multi-wavelength study of the BL Lac object 1RXS J101015.9-311909"*,
  Accepted for publication; corresponding authors: Y.Becherini, M.Cerruti, J.P.Lenain
  2012arXiv1204.1964H

Co-author:

- The HESS Collaboration : *"Discovery of VHE emission towards the Carina arm region with the H.E.S.S. telescope array: HESS J1018-589"*
  2012A&A...541A...5H
- The HESS Collaboration : *" Search for Dark Matter Annihilation Signals from the Fornax Galaxy Cluster with H.E.S.S"*
  2012arXiv1202.5494H
- The HESS Collaboration : *"A multi-wavelength view of the flaring state of PKS 2155-304 in 2006"*
  2012arXiv1201.4135H
- The HESS Collaboration : *"Discovery of hard-spectrum gamma-ray emission from the BL Lac object 1ES 0414+009"*
  2012arXiv1201.2044T
- The HESS Collaboration : *"Discovery of extended VHE γ-ray emission from the vicinity of the young massive stellar cluster Westerlund 1"*
  2012A&A...537A.114A
- The CTA Consortium : *"Design concepts for the Cherenkov Telescope Array CTA: an advanced facility for ground-based high-energy gamma-ray astronomy"*
  2011ExA....32..193A

- The HESS Collaboration : *"The 2010 very high energy gamma-ray flare & 10 years of multi-wavelength observations of M 87"*
  2011arXiv1111.5341T
- The HESS Collaboration : *"Simultaneous multi-wavelength campaign on PKS 2005-489 in a high state"*
  2011A&A...533A.110H
- The HESS Collaboration : *"Discovery of the source HESS J1356-645 associated with the young and energetic PSR J1357-6429"*
  2011A&A...533A.103H
- The HESS Collaboration : *"H.E.S.S. Observations of the Globular Clusters NGC 6388 and M15 and Search for a Dark Matter Signal"*
  2011ApJ...735...12A
- The HESS Collaboration : *"Very-high-energy gamma-ray emission from the direction of the Galactic globular cluster Terzan 5"*
  2011A&A...531L..18H
- The HESS Collaboration: *"A new SNR with TeV shell-type morphology: HESS J1731-347"*
  2011A&A...531A..81H
- The HESS Collaboration : *"HESS J1943+213: a candidate extreme BL Lacertae object"*
  2011A&A...529A..49H
- The HESS Collaboration : *"Search for a Dark Matter Annihilation Signal from the Galactic Center Halo with H.E.S.S."*
  2011PhRvL.106p1301A
- The HESS Collaboration : *"Search for Lorentz Invariance breaking with a likelihood fit of the PKS 2155-304 flare data taken on MJD 53944"*
  2011APh....34..738H
- The HESS Collaboration : *"Detection of very-high-energy gamma-ray emission from the vicinity of PSR B1706-44 and G 343.1-2.3 with H.E.S.S."*
  2011A&A...528A.143H
- The HESS Collaboration : *"H.E.S.S. constraints on dark matter annihilations towards the sculptor and carina dwarf galaxies"*
  2011APh....34..608H
- The HESS Collaboration : *"Revisiting the Westerlund 2 field with the HESS telescope array"*
  2011A&A...525A..46H

Conference proceedings:

- Cerruti, M., for the H.E.S.S Collaboration *"Recent H.E.S.S. results on extra-galactic sources"*, Proceeding from the ICRC 2011 conference 2011arXiv1110.2119C
- Cerruti, M., Zech, A., Boisson, C. and Inoue, S. *"Lepto-hadronic modelling of blazar emission"*, Proceeding from the SF2A 2011 conference 2011sf2a.conf..555C
- Becherini, Y.; Behera, B.; Biteau, J.; Cerruti, M.; Giebels, B.; Lenain, J. -P.; de Naurois, M.; Punch, M.; Raue, M.; Sanchez, D.; Volpe, F.; A. Zech on behalf of the H. E. S. S. Collaboration ; *"New AGNs discovered by H.E.S.S."*,
  Proceeding from the 25th Texas Symposium on Relativistic Astrophysics 2011arXiv1105.5243B

Papers in preparation:

- Cerruti, M., Zech, A., Boisson, C. and Inoue, S. *"Lepto-hadronic modelling of blazar emission"*, in preparation
- H. Sol et al. for the CTA consortium *"AGN under the scrutiny of CTA"*,
  to be submitted to Astroparticle Physics

Presentations:

Oral:

- "γ-CR-nu" Workshop, Meudon 2010 *"Lepto-hadronic modeling of blazar emission"*
- H.E.S.S. Collaboration Meeting , Hamburg 2010
- H.E.S.S. AGN WG Meeting , Paris 2010
- H.E.S.S. Collaboration Meeting, Stockholm 2010
- H.E.S.S. AAC WG Meeting, Paris 2011
- H.E.S.S. AGN WG Meeting, Hamburg, 2011
- H.E.S.S. Collaboration Meeting, Innsbruck, 2011
- ICRC 2011, Beijing, 2011 *"Recent H.E.S.S. results on extragalactic sources"*, on behalf of the H.E.S.S. Collaboration
- H.E.S.S. AGN WG Meeting, Paris, 2011
- H.E.S.S. Collaboration Meeting, Paris, 2011
- CTA AGN Meeting, Paris, 2011

- "Journée des Jeunes Chercheurs", Meudon, 2010-2011-2012
- "Elbereth", Paris, 2011

Poster:

- "Understanding Relativistic Jet" Meeting, Krakow, 2011 *"Lepto-hadronic modeling of blazar emission"*
- "SF2A 2011" Meeting, Paris, 2011 *"Lepto-hadronic modeling of blazar emission"*
- "GAMMA 2012" Meeting, Heidelberg, 2012 *"A mixed lepto-hadronic scenario for PKS 2155-304"*

Afterword

Bibliography

Abdo, A. A., Ackermann, M., Agudo, I., et al. 2010a, ApJ, 716, 30

Abdo, A. A., Ackermann, M., Ajello, M., et al. 2010b, ApJ, 715, 429

Abdo, A. A., Ackermann, M., Ajello, M., et al. 2011a, ApJL, 733, L26

Abdo, A. A., Ackermann, M., Ajello, M., et al. 2009a, ApJS, 183, 46

Abdo, A. A., Ackermann, M., Ajello, M., et al. 2009b, ApJ, 699, 817

Abdo, A. A., Ackermann, M., Ajello, M., et al. 2010c, ApJ, 710, 810

Abdo, A. A., Ackermann, M., Ajello, M., et al. 2009c, ApJL, 707, L142

Abdo, A. A., Ackermann, M., Ajello, M., et al. 2011b, ApJ, 736, 131

Abramowski, A., Acero, F., Aharonian, F., et al. 2012a, A&AP, 539, A149

Abramowski, A., Acero, F., Aharonian, F., et al. 2012b, ApJ, 746, 151

Acciari, V. A., Aliu, E., Arlen, T., et al. 2009a, Science, 325, 444

Acciari, V. A., Aliu, E., Aune, T., et al. 2009b, ApJ, 703, 169

Acero, F., Aharonian, F., Akhperjanian, A. G., et al. 2009, Science, 326, 1080

Ackermann, M., Ajello, M., Allafort, A., et al. 2011, ApJ, 743, 171

Ackermann, M., Ajello, M., Baldini, L., et al. 2010, ApJ, 721, 1383

Actis, M., Agnetta, G., Aharonian, F., et al. 2011, Experimental Astronomy, 32, 193

Ageron, M., Aguilar, J. A., Al Samarai, I., et al. 2011, Nuclear Instruments and Methods in Physics Research A, 656, 11

Aharonian, F., Akhperjanian, A. G., Anton, G., et al. 2010, A&AP, 521, A69

Aharonian, F., Akhperjanian, A. G., Anton, G., et al. 2009a, A&AP, 502, 749

Aharonian, F., Akhperjanian, A. G., Anton, G., et al. 2009b, ApJL, 696, L150

Aharonian, F., Akhperjanian, A. G., Anton, G., et al. 2009c, ApJL, 695, L40

Aharonian, F., Akhperjanian, A. G., Aye, K.-M., et al. 2005a, Science, 307, 1938

Aharonian, F., Akhperjanian, A. G., Aye, K.-M., et al. 2005b, A&AP, 437, 95

Aharonian, F., Akhperjanian, A. G., Aye, K.-M., et al. 2005c, A&AP, 436, L17

Aharonian, F., Akhperjanian, A. G., Aye, K.-M., et al. 2005d, A&AP, 430, 865

Aharonian, F., Akhperjanian, A. G., Aye, K.-M., et al. 2004, Astroparticle Physics, 22, 109

Aharonian, F., Akhperjanian, A. G., Barres de Almeida, U., et al. 2007a, A&AP, 473, L25

Aharonian, F., Akhperjanian, A. G., Barres de Almeida, U., et al. 2008a, A&AP, 477, 481

Aharonian, F., Akhperjanian, A. G., Barres de Almeida, U., et al. 2008b, A&AP, 478, 387

Aharonian, F., Akhperjanian, A. G., Barres de Almeida, U., et al. 2008c, A&AP, 481, L103

Aharonian, F., Akhperjanian, A. G., Bazer-Bachi, A. R., et al. 2007b, ApJL, 664, L71

Aharonian, F., Akhperjanian, A. G., Bazer-Bachi, A. R., et al. 2006a, A&AP, 457, 899

Aharonian, F., Akhperjanian, A. G., Bazer-Bachi, A. R., et al. 2006b, A&AP, 455, 461

Aharonian, F., Akhperjanian, A. G., Bazer-Bachi, A. R., et al. 2006c, A&AP, 448, L19

Aharonian, F., Akhperjanian, A. G., Bazer-Bachi, A. R., et al. 2006d, Nature, 440, 1018

Aharonian, F., Akhperjanian, A. G., Bazer-Bachi, A. R., et al. 2005e, A&AP, 442, 895

Aharonian, F., Akhperjanian, A. G., Bazer-Bachi, A. R., et al. 2005f, A&AP, 441, 465

Aharonian, F., Akhperjanian, A. G., Bazer-Bachi, A. R., et al. 2007c, A&AP, 470, 475

Aharonian, F., Akhperjanian, A. G., Bazer-Bachi, A. R., et al. 2006e, Science, 314, 1424

Aharonian, F. A., Atoian, A. M., & Nagapetian, A. M. 1983, Afz, 19, 323

Aharonian, F. A., Coppi, P. S., & Voelk, H. J. 1994, ApJL, 423, L5

Aharonian, F. A., Khangulyan, D., & Costamante, L. 2008d, MNRAS, 387, 1206

Akiyama, M., Ueda, Y., Ohta, K., Takahashi, T., & Yamada, T. 2003, ApJS, 148, 275

Albert, J., Aliu, E., Anderhub, H., et al. 2007a, ApJ, 663, 125

Albert, J., Aliu, E., Anderhub, H., et al. 2007b, ApJL, 666, L17

Aleksić, J., Alvarez, E. A., Antonelli, L. A., et al. 2012, A&AP, 539, L2

Aleksić, J., Antonelli, L. A., Antoranz, P., et al. 2010, ApJL, 723, L207

Aleksić, J., Antonelli, L. A., Antoranz, P., et al. 2011, ApJL, 730, L8

Aliu, E., Anderhub, H., Antonelli, L. A., et al. 2009, ApJL, 692, L29

Anderhub, H., Antonelli, L. A., Antoranz, P., et al. 2009, ApJL, 704, L129

Angel, J. R. P. & Stockman, H. S. 1980, ARA&A, 18, 321

Antonucci, R. 1993, ARA&A, 31, 473

Antonucci, R. R. J. & Miller, J. S. 1985, ApJ, 297, 621

Aretxaga, I., Joguet, B., Kunth, D., Melnick, J., & Terlevich, R. J. 1999, ApJL, 519, L123

Arévalo, P., Papadakis, I., Kuhlbrodt, B., & Brinkmann, W. 2005, A&AP, 430, 435

Arnaud, K. A., Branduardi-Raymont, G., Culhane, J. L., et al. 1985, MNRAS, 217, 105

Atwood, W. B., Abdo, A. A., Ackermann, M., et al. 2009, ApJ, 697, 1071

Baldwin, J. A., Phillips, M. M., & Terlevich, R. 1981, PASP, 93, 5

Barkov, M. V., Aharonian, F. A., Bogovalov, S. V., Kelner, S. R., & Khangulyan, D. 2012, ApJ, 749, 119

Barrau, A., Bazer-Bachi, R., Beyer, E., et al. 1998, Nuclear Instruments and Methods in Physics Research A, 416, 278

Bauer, F. E., Condon, J. J., Thuan, T. X., & Broderick, J. J. 2000, ApJS, 129, 547

Bautista, M. A. & Kallman, T. R. 2001, ApJS, 134, 139

Becherini, Y., Behera, B., Biteau, J., et al. 2011a, ArXiv e-prints

Becherini, Y., Boisson, C., & Cerruti, M. f. t. H. C. 2012, in preparation

Becherini, Y., Djannati-Ataï, A., Marandon, V., Punch, M., & Pita, S. 2011b, APh, 34, 858

Bennett, A. S. 1962, MemRAS, 68, 163

Bessell, M. S. 1990, PASP, 102, 1181

Bianchi, S., Matt, G., Haardt, F., et al. 2001, A&AP, 376, 77

Blumenthal, G. R. 1970, PhRD, 1, 1596

Boldt, E. & Leiter, D. 1987, ApJL, 322, L1

Boller, T., Brandt, W. N., & Fink, H. 1996, A&AP, 305, 53

Bonnoli, G., Ghisellini, G., Foschini, L., Tavecchio, F., & Ghirlanda, G. 2011, MNRAS, 410, 368

Boutelier, T., Henri, G., & Petrucci, P.-O. 2008, MNRAS, 390, L73

Brun, F. 2012, PhD thesis

Burbidge, E. M. 1967, ARA&A, 5, 399

Burrows, D. N., Hill, J. E., Nousek, J. A., et al. 2005, Space Sci. Rev., 120, 165

Caccianiga, A. & Marchã, M. J. M. 2004, MNRAS, 348, 937

Camenzind, M. 2005, MmSAI, 76, 98

Cannon, A. 2010, The Astronomer's Telegram, 2591, 1

Cappi, M., Panessa, F., Bassani, L., et al. 2006, A&AP, 446, 459

Cardelli, J. A., Clayton, G. C., & Mathis, J. S. 1989, ApJ, 345, 245

Carone, T. E., Peterson, B. M., Bechtold, J., et al. 1996, ApJ, 471, 737

Cawley, M. F., Fegan, D. J., Harris, K., et al. 1990, Experimental Astronomy, 1, 173

Cerruti, M., Ponti, G., Boisson, C., et al. 2011, A&AP, 535, A113

Cerruti, M. f. t. H. C. 2011, ArXiv e-prints

Charles, P., Thorstensen, J., & Bowyer, S. 1979, Nature, 281, 285

Chaves, R. C. G., de Oña Wilhemi, E., & Hoppe, S. 2008, in American Institute of Physics Conference Series, Vol. 1085, American Institute of Physics Conference Series, ed. F. A. Aharonian, W. Hofmann, & F. Rieger, 219–222

Chevallier, L., Collin, S., Dumont, A., et al. 2006, A&AP, 449, 493

Chodorowski, M. J., Zdziarski, A. A., & Sikora, M. 1992, ApJ, 400, 181

Cohen, R. D., Puetter, R. C., Rudy, R. J., Ake, T. B., & Foltz, C. B. 1986, ApJ, 311, 135

Condon, J. J., Helou, G., Sanders, D. B., & Soifer, B. T. 1996, ApJS, 103, 81

Cooke, B. A., Ricketts, M. J., Maccacaro, T., et al. 1978, MNRAS, 182, 489

Costamante, L. & Ghisellini, G. 2002, A&A, 384, 56

Crummy, J., Fabian, A. C., Gallo, L., & Ross, R. R. 2006, MNRAS, 365, 1067

Cusumano, G., La Parola, V., Segreto, A., et al. 2010, A&AP, 524, A64+

Czerny, B., Nikołajuk, M., Różańska, A., et al. 2003, A&AP, 412, 317

Dadina, M., Cappi, M., Malaguti, G., Ponti, G., & de Rosa, A. 2005, A&AP, 442, 461

Danforth, C. W., Keeney, B. A., Stocke, J. T., Shull, J. M., & Yao, Y. 2010, ApJ, 720, 976

Davies, J. & Cotton, E. 1957, Journal of Solar Energy Science and Engineering, 1, 16

de Angelis, A., Roncadelli, M., & Mansutti, O. 2007, PhRD, 76, 121301

de La Calle Pérez, I., Longinotti, A. L., Guainazzi, M., et al. 2010, A&AP, 524, A50+

de Naurois, M. & Rolland, L. 2009, APh, 32, 231

De Rosa, A., Piro, L., Matt, G., & Perola, G. C. 2004, A&AP, 413, 895

Dermer, C. D. & Atoyan, A. 2001, ArXiv Astrophysics e-prints

Dermer, C. D. & Menon, G. 2009, High Energy Radiation from Black Holes: Gamma Rays, Cosmic Rays, and Neutrinos

Dermer, C. D., Murase, K., & Takami, H. 2012, ArXiv e-prints

Detmers, R. G., Kaastra, J. S., Costantini, E., et al. 2010, A&AP, 516, A61+

Dickey, J. M. & Lockman, F. J. 1990, ARA&A, 28, 215

Dole, H., Lagache, G., Puget, J.-L., et al. 2006, A&AP, 451, 417

Domínguez, A., Primack, J. R., Rosario, D. J., et al. 2011, MNRAS, 410, 2556

Dondi, L. & Ghisellini, G. 1995, MNRAS, 273, 583

Done, C., Gierliński, M., & Kubota, A. 2007, A&APR, 15, 1

Donnarumma, I., Pucella, G., Vittorini, V., et al. 2009, ApJ, 707, 1115

Dreyer, J. L. E. 1888, MemRAS, 49, 1

Ebrero, J., Costantini, E., Kaastra, J. S., et al. 2010, A&AP, 520, A36+

Edge, D. O., Shakeshaft, J. R., McAdam, W. B., Baldwin, J. E., & Archer, S. 1959, MemRAS, 68, 37

Eisenhauer, F., Genzel, R., Alexander, T., et al. 2005, ApJ, 628, 246

Falomo, R. & Ulrich, M.-H. 2000, A&AP, 357, 91

Fanaroff, B. L. & Riley, J. M. 1974, MNRAS, 167, 31P

Feldman, G. J. & Cousins, R. D. 1998, PhRD, 57, 3873

Finke, J. D. & Dermer, C. D. 2010, ApJL, 714, L303

Finke, J. D., Dermer, C. D., & Böttcher, M. 2008, ApJ, 686, 181

Fioc, M. & Rocca-Volmerange, B. 1997, A&A, 326, 950

Fisher, K. B., Huchra, J. P., Strauss, M. A., et al. 1995, ApJS, 100, 69

Fortin, P., Fegan, S., Horan, D., et al. 2010, in 25th Texas Symposium on Relativistic Astrophysics

Fossati, G., Maraschi, L., Celotti, A., Comastri, A., & Ghisellini, G. 1998, MNRAS, 299, 433

Franceschini, A., Rodighiero, G., & Vaccari, M. 2008, A&AP, 487, 837

Francis, P. J., Hewett, P. C., Foltz, C. B., et al. 1991, ApJ, 373, 465

Fugmann, W. 1988, A&AP, 205, 86

Fuhrmann, L., Cucchiara, A., Marchili, N., et al. 2006, A&AP, 445, L1

Funk, S. 2012, ArXiv e-prints

Gabanyi, K. E., Dubner, G., Giacani, E., et al. 2011, ArXiv e-prints

Gehrels, N., Chincarini, G., Giommi, P., et al. 2004, ApJ, 611, 1005

George, I. M., Nandra, K., Fabian, A. C., et al. 1993, MNRAS, 260, 111

George, I. M., Nandra, K., Turner, T. J., & Celotti, A. 1994, ApJL, 436, L59

Ghisellini, G., Celotti, A., Fossati, G., Maraschi, L., & Comastri, A. 1998, MNRAS, 301, 451

Ghisellini, G., Foschini, L., Tavecchio, F., & Pian, E. 2007, MNRAS, 382, L82

Ghisellini, G., Maraschi, L., & Tavecchio, F. 2009, MNRAS, 396, L105

Ghisellini, G., Maraschi, L., & Treves, A. 1985, A&AP, 146, 204

Ghisellini, G., Tavecchio, F., Foschini, L., & Ghirlanda, G. 2011, MNRAS, 414, 2674

Gierliński, M. & Done, C. 2004, MNRAS, 349, L7

Giommi, P., Padovani, P., Polenta, G., et al. 2012, MNRAS, 420, 2899

Giommi, P., Piranomonte, S., Perri, M., & Padovani, P. 2005, A&A, 434, 385

Gómez, J.-L., Marscher, A. P., & Alberdi, A. 1999, ApJ, 522, 74

Gondek, D., Zdziarski, A. A., Johnson, W. N., et al. 1996, MNRAS, 282, 646

Gross, E. & Vitells, O. 2010, European Physical Journal C, 70, 525

Guy, J. 2003, PhD thesis

Haardt, F. & Maraschi, L. 1993, ApJ, 413, 507

Harrison, F. A., Boggs, S., Christensen, F., et al. 2010, in Society of Photo-Optical Instrumentation Engineers (SPIE) Conference Series, Vol. 7732, Society of Photo-Optical Instrumentation Engineers (SPIE) Conference Series

Hartman, R. C., Bertsch, D. L., Dingus, B. L., et al. 1993, ApJL, 407, L41

Hassan, T., Mirabal, N., Contreras, J. L., & CTA Consortium. 2011, in AGN Physics in the CTA Era (AGN 2011)

Hauser, M., Möllenhoff, C., Pühlhofer, G., et al. 2004, Astronomische Nachrichten, 325, 659

HEGRA Collaboration, Konopelko, A., Hemberger, M., et al. 1999, Astroparticle Physics, 10, 275

H.E.S.S. Collaboration, Abramowski, A., Acero, F., et al. 2011a, A&AP, 529, A49

H.E.S.S. Collaboration, Abramowski, A., Acero, F., et al. 2012a, ArXiv e-prints

H.E.S.S. Collaboration, Abramowski, A., Acero, F., et al. 2012b, A&AP, 538, A103

H.E.S.S. Collaboration, Abramowski, A., Acero, F., et al. 2012c, A&AP, 542, A94

H.E.S.S. Collaboration, Abramowski, A., Acero, F., et al. 2011b, Astroparticle Physics, 34, 738

H.E.S.S. Collaboration, Abramowski, A., Acero, F., et al. 2011c, A&AP, 533, A110

H.E.S.S. Collaboration, Abramowski, A., Acero, F., et al. 2010a, A&AP, 516, A56

H.E.S.S. Collaboration, Abramowski, A., Acero, F., et al. 2010b, A&AP, 520, A83

Hillas, A. M. 1985, in International Cosmic Ray Conference, Vol. 3, International Cosmic Ray Conference, ed. F. C. Jones, 445–448

Hinton, J. A. & Hofmann, W. 2009, ARA&A, 47, 523

Hofmann, W. 2010a, The Astronomer's Telegram, 2743, 1

Hofmann, W. 2010b, The Astronomer's Telegram, 3007, 1

Hofmann, W. 2012, The Astronomer's Telegram, 4072, 1

Hubble, E. 1929, Proceedings of the National Academy of Science, 15, 168

IceCube Collaboration, Achterberg, A., Ackermann, M., et al. 2006, Astroparticle Physics, 26, 155

Inoue, S. & Takahara, F. 1996, ApJ, 463, 555

Jaffe, W., Ford, H. C., Ferrarese, L., van den Bosch, F., & O'Connell, R. W. 1993, Nature, 364, 213

Janiuk, A., Czerny, B., & Madejski, G. M. 2001, ApJ, 557, 408

Jarrett, T. H., Chester, T., Cutri, R., et al. 2000, AJ, 119, 2498

Jenkins, E. B. & Savage, B. D. 1974, ApJ, 187, 243

Jones, D. H., Read, M. A., Saunders, W., et al. 2009, MNRAS, 399, 683

Jones, F. C. 1968, PhRv, 167, 1159

Kaastra, J. S., Petrucci, P.-O., Cappi, M., et al. 2011, A&AP, 534, A36

Kahn, S. M., von-Ballmoos, P., & Sunyaev, R. 2005, High-Energy Spectroscopic Astrophysics (Springer)

Katarzyński, K., Ghisellini, G., Tavecchio, F., Gracia, J., & Maraschi, L. 2006, MNRAS, 368, L52

Katarzyński, K., Lenain, J.-P., Zech, A., Boisson, C., & Sol, H. 2008, MNRAS, 390, 371

Katarzyński, K., Sol, H., & Kus, A. 2001, A&AP, 367, 809

Katarzyński, K., Sol, H., & Kus, A. 2003, A&AP, 410, 101

Kaufmann, S., Wagner, S. J., Tibolla, O., & Hauser, M. 2011, A&AP, 534, A130

Kellermann, K. I., Sramek, R., Schmidt, M., Shaffer, D. B., & Green, R. 1989, AJ, 98, 1195

Kelner, S. R. & Aharonian, F. A. 2008, PhRD, 78, 034013

Kembhavi, A. K. & Narlikar, J. V. 1999, Quasars and active galactic nuclei : an introduction

Khachikian, E. Y. & Weedman, D. W. 1974, ApJ, 192, 581

Kinman, T. D., Lamla, E., Ciurla, T., Harlan, E., & Wirtanen, C. A. 1968, ApJ, 152, 357

Kneiske, T. M. & Dole, H. 2010, A&AP, 515, A19

Konigl, A. 1981, ApJ, 243, 700

Koyama, K., Tsunemi, H., Dotani, T., et al. 2007, PASJ, 59, 23

Krivonos, R., Tsygankov, S., Revnivtsev, M., et al. 2010, A&AP, 523, A61+

Landt, H. 2012, MNRAS, 423, L84

Landt, H. & Bignall, H. E. 2008, MNRAS, 391, 967

Laor, A. 1991, ApJ, 376, 90

Le Bohec, S., Degrange, B., Punch, M., et al. 1998, Nuclear Instruments and Methods in Physics Research A, 416, 425

Leahy, D. A. & Tian, W. W. 2012, A&AP, 539, A128

Leahy, J. P. & Perley, R. A. 1991, AJ, 102, 537

Lemoine-Goumard, M., Degrange, B., & Tluczykont, M. 2006, Astroparticle Physics, 25, 195

Lenain, J.-P., Boisson, C., Sol, H., & Katarzyński, K. 2008, A&AP, 478, 111

Li, T.-P. & Ma, Y.-Q. 1983, ApJ, 272, 317

Longair, M. S. 1994, High energy astrophysics. Vol.2: Stars, the galaxy and the interstellar medium

Longinotti, A. L., Costantini, E., Petrucci, P. O., et al. 2010, A&AP, 510, A92+

Lyutikov, M. & Lister, M. 2010, ApJ, 722, 197

Madejski, G. M., Sikora, M., Jaffe, T., et al. 1999, ApJ, 521, 145

Magdziarz, P., Blaes, O. M., Zdziarski, A. A., Johnson, W. N., & Smith, D. A. 1998, MNRAS, 301, 179

Magdziarz, P. & Zdziarski, A. A. 1995, MNRAS, 273, 837

MAGIC Collaboration, Albert, J., Aliu, E., et al. 2008, Science, 320, 1752

Mankuzhiyil, N., Ansoldi, S., Persic, M., & Tavecchio, F. 2011a, ApJ, 733, 14

Mankuzhiyil, N., Ansoldi, S., Persic, M., & Tavechhio, F. 2011b, eprint arXiv:1111.0265

Mannheim, K. 1993, A&AP, 269, 67

Maraschi, L., Ghisellini, G., & Celotti, A. 1992, ApJL, 397, L5

Markarian, B. E. 1967, Afz, 3, 24

Marscher, A. P. & Gear, W. K. 1985, ApJ, 298, 114

Massaro, E., Giommi, P., Leto, C., et al. 2009, A&AP, 495, 691

Massaro, E., Perri, M., Giommi, P., & Nesci, R. 2004, A&AP, 413, 489

Mattox, J. R., Bertsch, D. L., Chiang, J., et al. 1996, ApJ, 461, 396

Mazzarella, J. M. & Balzano, V. A. 1986, ApJS, 62, 751

Messier, C. 1781, Connaissance des Temps, 1, 227

Middleton, M., Done, C., & Gierliński, M. 2007, MNRAS, 381, 1426

Miller, J. S. & Goodrich, R. W. 1990, ApJ, 355, 456

Miniutti, G. & Fabian, A. C. 2004, MNRAS, 349, 1435

Miniutti, G., Ponti, G., Greene, J. E., et al. 2009, MNRAS, 394, 443

Miyazawa, T., Haba, Y., & Kunieda, H. 2009, PASJ, 61, 1331

Moore, R. L. & Stockman, H. S. 1981, ApJ, 243, 60

Morini, M., Lipani, N. A., & Molteni, D. 1987, ApJ, 317, 145

Mücke, A., Engel, R., Rachen, J. P., Protheroe, R. J., & Stanev, T. 2000, CoPhC, 124, 290

Mücke, A. & Protheroe, R. J. 2001, APh, 15, 121

Murray, N. & Chiang, J. 1997, ApJ, 474, 91

Mushotzky, R. F., Done, C., & Pounds, K. A. 1993, ARA&A, 31, 717

Nandra, K., George, I. M., Mushotzky, R. F., Turner, T. J., & Yaqoob, T. 1997, ApJ, 477, 602

Narayan, R. & Piran, T. 2012, MNRAS, 420, 604

Neronov, A. & Vovk, I. 2010, Science, 328, 73

Nieppola, E., Valtaoja, E., Tornikoski, M., Hovatta, T., & Kotiranta, M. 2008, A&AP, 488, 867

Ohm, S., van Eldik, C., & Egberts, K. 2009, Astroparticle Physics, 31, 383

Osterbrock, D. E. 1989, Astrophysics of gaseous nebulae and active galactic nuclei

Osterbrock, D. E. & Pogge, R. W. 1985, ApJ, 297, 166

Owen, F. N., Ledlow, M. J., Eilek, J. A., et al. 2000, ArXiv Astrophysics e-prints

Padovani, P. 1992, MNRAS, 257, 404

Padovani, P. & Giommi, P. 1995, ApJ, 444, 567

Padovani, P., Giommi, P., Ábrahám, P., Csizmadia, S., & Moór, A. 2006, A&AP, 456, 131

Padovani, P., Giommi, P., & Fiore, F. 1997, MNRAS, 284, 569

Padovani, P., Giommi, P., & Rau, A. 2012, MNRAS, L423

Padovani, P., Perlman, E., Landt, H., Giommi, P., & Perri, M. 2003, Chinese Journal of Astronomy and Astrophysics Supplement, 3, 147

Palmeri, P., Mendoza, C., Kallman, T. R., Bautista, M. A., & Meléndez, M. 2003, A&AP, 410, 359

Patrick, A. R., Reeves, J. N., Porquet, D., et al. 2011, MNRAS, 411, 2353

Pearson, T. J., Unwin, S. C., Cohen, M. H., et al. 1981, Nature, 290, 365

Perlman, E. S., Madejski, G., Georganopoulos, M., et al. 2005, ApJ, 625, 727

Perlman, E. S., Padovani, P., Giommi, P., et al. 1998, AJ, 115, 1253

Perola, G. C., Matt, G., Fiore, F., et al. 2000, A&AP, 358, 117

Peterson, B. M. 1997, An Introduction to Active Galactic Nuclei

Petrucci, P. O., Ponti, G., Matt, G., et al. 2007, A&AP, 470, 889

Pian, E., Foschini, L., Beckmann, V., et al. 2006, A&AP, 449, L21

Piconcelli, E., Jimenez-Bailón, E., Guainazzi, M., et al. 2005, A&AP, 432, 15

Piranomonte, S., Perri, M., Giommi, P., Landt, H., & Padovani, P. 2007, A&A, 470, 787

Piron, F. 2000, PhD thesis

Piron, F., Djannati-Atai, A., Punch, M., et al. 2001, A&AP, 374, 895

Pita, S., Goldoni, P., Boisson, C., et al. 2012, in preparation

Ponti, G., Cappi, M., Vignali, C., et al. 2009, MNRAS, 394, 1487

Ponti, G., Miniutti, G., Cappi, M., et al. 2006, MNRAS, 368, 903

Pounds, K. & Reeves, J. 2002, ArXiv:astro-ph/0201436, Proceedings of the Symposium on 'New Visions of the X-ray Universe in the XMM-Newton and Chandra Era', 26-30 November 2001, ESTEC, The Netherlands

Pounds, K., Reeves, J., O'Brien, P., et al. 2001, ApJ, 559, 181

Pounds, K. A., Nandra, K., Fink, H. H., & Makino, F. 1994, MNRAS, 267, 193

Poutanen, J. & Stern, B. 2010, ApJL, 717, L118

Prandini, E., Bonnoli, G., Maraschi, L., Mariotti, M., & Tavecchio, F. 2010, MNRAS, 405, L76

Prandini, E., Bonnoli, G., & Tavecchio, F. 2012, A&AP, 543, A111

Pravdo, S., Nugent, J., Nousek, J., et al. 1981, ApJ, 251, 501

Punch, M., Akerlof, C. W., Cawley, M. F., et al. 1992, Nature, 358, 477

Raiteri, C. M., Villata, M., Chen, W. P., et al. 2008, A&AP, 485, L17

Rector, T. A., Stocke, J. T., & Perlman, E. S. 1999, ApJ, 516, 145

Reeves, J., Done, C., Pounds, K., et al. 2008, MNRAS, 385, L108

Reimer, A., Protheroe, R. J., & Donea, A.-C. 2004, A&AP, 419, 89

Reynolds, C. S. 1997, MNRAS, 286, 513

Reynoso, M. M., Medina, M. C., & Romero, G. E. 2011, A&AP, 531, A30

Rieger, F. M. & Aharonian, F. A. 2008, A&AP, 479, L5

Rieger, F. M. & Volpe, F. 2010, A&AP, 520, A23

Roming, P. W. A., Kennedy, T. E., Mason, K. O., et al. 2005, Space Sci. Rev., 120, 95

Roming, P. W. A., Koch, T. S., Oates, S. R., et al. 2009, ApJ, 690, 163

Ross, R. R. & Fabian, A. C. 2005, MNRAS, 358, 211

Ross, R. R., Fabian, A. C., & Young, A. J. 1999, MNRAS, 306, 461

Rybicki, G. B. & Lightman, A. P. 1979, Radiative processes in astrophysics (Wiley-Interscience)

Salamon, M. H. & Stecker, F. W. 1998, ApJ, 493, 547

Sazonov, S., Revnivtsev, M., Krivonos, R., Churazov, E., & Sunyaev, R. 2007, A&AP, 462, 57

Schliesser, A. & Mirzoyan, R. 2005, Astroparticle Physics, 24, 382

Schmidt, M. 1963, Nature, 197, 1040

Schurch, N. J. & Done, C. 2006, MNRAS, 371, 81

Schurch, N. J. & Done, C. 2008, MNRAS, 386, L1

Seyfert, C. K. 1943, ApJ, 97, 28

Shakura, N. I. & Sunyaev, R. A. 1976, MNRAS, 175, 613

Shaw, M. S., Romani, R. W., Cotter, G., et al. 2012, ApJ, 748, 49

Sikora, M., Begelman, M. C., & Rees, M. J. 1994, ApJ, 421, 153

Sikora, M., Stawarz, Ł., Moderski, R., Nalewajko, K., & Madejski, G. M. 2009, ApJ, 704, 38

Sim, S. A., Miller, L., Long, K. S., Turner, T. J., & Reeves, J. N. 2010, MNRAS, 404, 1369

Singh, K. P., Garmire, G. P., & Nousek, J. 1985, ApJ, 297, 633

Singh, K. P., Westergaard, N. J., Schnopper, H. W., Awaki, H., & Tawara, Y. 1990, ApJ, 363, 131

Smith, H. E., Burbidge, E. M., Baldwin, J. A., et al. 1977, ApJ, 215, 427

Smith, R. A. N., Page, M. J., & Branduardi-Raymont, G. 2007, A&AP, 461, 135

Sobolewska, M. A. & Done, C. 2007, MNRAS, 374, 150

Stecker, F. W. & de Jager, O. C. 1998, A&AP, 334, L85

Stein, W. A., Odell, S. L., & Strittmatter, P. A. 1976, ARA&A, 14, 173

Stern, B. E. & Poutanen, J. 2011, MNRAS, 417, L11

Strittmatter, P. A., Serkowski, K., Carswell, R., et al. 1972, ApJL, 175, L7

Su, M., Slatyer, T. R., & Finkbeiner, D. P. 2010, ApJ, 724, 1044

Takahashi, T., Abe, K., Endo, M., et al. 2007, PASJ, 59, 35

Takahashi, T., Mitsuda, K., Kelley, R., et al. 2010, in Society of Photo-Optical Instrumentation Engineers (SPIE) Conference Series, Vol. 7732, Society of Photo-Optical Instrumentation Engineers (SPIE) Conference Series

Tanaka, Y., Nandra, K., Fabian, A. C., et al. 1995, Nature, 375, 659

Tavecchio, F., Becerra-Gonzalez, J., Ghisellini, G., et al. 2011, A&AP, 534, A86

Tavecchio, F., Maraschi, L., & Ghisellini, G. 1998, ApJ, 509, 608

Tavecchio, F., Roncadelli, M., Galanti, G., & Bonnoli, G. 2012, ArXiv e-prints

Taylor, A. M., Vovk, I., & Neronov, A. 2011, A&AP, 529, A144

Tchekhovskoy, A., Narayan, R., & McKinney, J. C. 2010, ApJ, 711, 50

Telfer, R. C., Zheng, W., Kriss, G. A., & Davidsen, A. F. 2002, ApJ, 565, 773

The Fermi-LAT Collaboration. 2011, ArXiv e-prints

Thomas, H.-C., Beuermann, K., Reinsch, K., et al. 1998, A&Alq, 335, 467

Thorne, K. S. 1974, ApJ, 191, 507

Trippe, M. L., Crenshaw, D. M., Deo, R. P., et al. 2010, ApJ, 725, 1749

Turner, T. J. & Miller, L. 2009, A&APR, 17, 47

Urry, C. M. & Padovani, P. 1995, PASP, 107, 803

Vaughan, S., Edelson, R., Warwick, R. S., & Uttley, P. 2003, MNRAS, 345, 1271

Vercellone, S., Chen, A. W., Giuliani, A., et al. 2008, ApJL, 676, L13

Vercellone, S., Chen, A. W., Vittorini, V., et al. 2009, ApJ, 690, 1018

Vercellone, S., Striani, E., Vittorini, V., et al. 2011, ApJL, 736, L38

Vernet, J., Dekker, H., D'Odorico, S., et al. 2011, A&AP, 536, A105

Véron-Cetty, M. P. & Véron, P. 2000, A&APR, 10, 81

Villata, M., Raiteri, C. M., Balonek, T. J., et al. 2006, A&AP, 453, 817

Voges, W., Aschenbach, B., Boller, T., et al. 1999, A&A, 349, 389

Völk, H. J. & Bernlöhr, K. 2009, Experimental Astronomy, 25, 173

Wagner, S. J. & H.E.S.S. Collaboration. 2010, in AAS/High Energy Astrophysics Division, Vol. 11, AAS/High Energy Astrophysics Division #11, #27.06

Walton, D. J., Reis, R. C., & Fabian, A. C. 2010, MNRAS, 408, 601

Watanabe, C., Ohta, K., Akiyama, M., & Ueda, Y. 2004, ApJ, 610, 128

Weekes, T. C. 2003, Very high energy gamma-ray astronomy (Iop)

Weekes, T. C., Cawley, M. F., Fegan, D. J., et al. 1989, ApJ, 342, 379

Wouters, D., Lenain, J.-P., Harris, J., et al. 2012, in preparation

Young, P. J. 1976, AJ, 81, 807

Zech, A., Behera, B., Becherini, Y., et al. 2011, ArXiv e-prints

Zhang, Y. H., Treves, A., Celotti, A., Qin, Y. P., & Bai, J. M. 2005, ApJ, 629, 686

Życki, P. T., Done, C., & Smith, D. A. 1999, MNRAS, 309, 561